The constrained admissible region multiple hypothesis filter tested for real-world measurements

A Master of Science Thesis

R.P. Rikken

TU Delft

The constrained admissible region multiple hypothesis filter tested for real-world measurements

A Master of Science Thesis

by

R.P. Rikken

to obtain the degree of Master of Science
at the Delft University of Technology,
to be defended publicly on Tuesday July 26, 2022 at 13:00.

Student number:	4206738	
Project duration:	January, 2020 – July, 2022	
Supervisors :	Dr. ir. E. J. O. Schrama,	TU Delft
	Dr. T. P. G. Wijnen,	TU Delft

An electronic version of this thesis is available at `http://repository.tudelft.nl/`.

TU Delft

Preface

This research has taught me about research, myself, and not giving up. From the start of my master Aerospace engineering, Master track spaceflight, I knew that my master thesis would be my biggest hurdle. For this reason I am glad I had the opportunity to join an active research, which also had close ties to Royal Netherlands Air Force.

The corona pandemic did not make it easy for me to finish my master thesis. Working at home has a lot of distractions for someone that finds it hard to focus for a long period. Hopefully the pandemic is resolved quickly so the celebration can begin.
I want to thank my supervisor Thomas Wijnen for his dedication. I have to imagine it was not easy to supervise me as his first master student candidate. Your enthusiasm, time, effort, and dedication is immeasurable. Despite failing to deliver deadline after deadline I hope you can forgive me.

I want to thank Ernst Schrama for being the link between the research and the TU Delft. To ensure that the final product complies with the requirements set by the Delft university of technology.
This master thesis confirmed that research is not my cup of tea. I lost count the number of times wanted to quit, or though I was unable to deliver the quality required for a master thesis. I want to thank my parents, sisters, and friends who helped me push forward at times I was to desperate.

The lovely discussion about the subject with Rimsky Wolfs I will never forget. After each conversation I found new ideas and inspiration. After each conversation I was able to recognise the fundamental challenges for which I had selected this topic. I want to thank Stijn Temmen and Chantal Gerritsen for offering the guidance to put me back on track to finish my thesis.

I am glad I was able to come in contact with the RNLAF and experience the wonderful work atmosphere and opportunities within the organisation. This made the choice to join the RNLAF an easy one. Currently I am working at Woensdrecht at the 981 squadron and love every day of it.

Without this experience, only God would knows where I would be today.

R.P. Rikken
Deventer, July 2022

Abstract

My research investigates the (initial) orbit determination (IOD) problem for short-arc angle-only optical observations of satellites. The method is an adaptation of the Constrained Admissible Region Multiple Hypothesis Filter (CAR-MHF) method, as developed by DeMars et al. This adapted method is tested on data obtained from telescopes, where publications by DeMars only tested the method on simulated data. The adapted method of the CAR-MHF was only able to perform IOD for single observation arcs due to the use of the EKF. The CAR-MHF is compared to Gauss's method, for 582 satellites which had an observation arc with a minimum of 3 data points, the minimum number of observations required. The accuracy performance of both methods are comparable. The CAR-MHF was able to find an IOD solution for 242 satellite, almost 20% more than Gauss's method. This research is a stepping stone to improve the CAR-MHF method for real-world data applications.

Contents

List of Abbreviations

Abbreviation	Definition
AFSPC	Air Force Space Command
AoP	Argument of Periapsis
CAR	Constrained Admissible Region
CAR-MHF	Constrained Admissible Region Multiple Hypothesis Filter
CSpcOC	Combined Space Operations Centre
CSV	Comma Separated Value
ECEF	Earth-Centred Earth-Fixed
ECI	Earth Centred Inertial
EKF	Extended Kalman Filter
EOP	Earth Orientation Parameter
EQ	Equation of the Equinoxes
ESA	European Space Agency
FOTOS	Feasibility study for Optical Tracking of Orbiting Satellites
FoV	Field of View
GEO	geosynchronous equatorial orbit
GST	Greenwhich Sidereal Time
IERS	International Earth Rotation and reference systems service
ISS	International Space Station
IOD	Initial Orbit Determination
IPA	Image Processing Algorithm
JD	Julian Day
LEO	Low Earth Orbit
LST	Local Sidereal Time
MASCARA	Multi-site All-Sky Camera
MEME	Mean Equator Mean Equinox
MEO	Medium Earth Orbit
MHF	Multiple Hypothesis Filter
NORAD	North American Aerospace Defence Command
OD	Orbit Determination
RAAN	Right Ascension of the Ascending Node
RCS	Radar Cross Section
RKF45	Runge-Kutta-Felberg method
RNLAF	Royal Netherlands Air Force
SCC	Space Security Center
SGP4	Standard General Perturbations Satellite Orbit Model 4
SRP	Solar Radiation Pressure
STK	Systems Tool Kit
TAI	Internaltional Atomic Time
TDT	Terrestrial Dynamical Time
TEC	Topocentric Equatorial Coordinate
TEME	True Equator Mean Equinox
TLE	Two-line Elements
TT	Terrestrial Time
UKF	Uncented Kalman Filter
UT	Universal Time
UTC	Coordinated Universal time
WGS 72	World Geodetic system 1972

List of Symbols

a	Semi-major axis	$[m]$
d	residual/mahalanobis distance	$[-]2$
e	eccentricity	$[-]$
f	Flattening factor	$[-]$
h	specific angular momentum	$[m^2 s^{-1}]$
H	altitude from the Earth reference surface	$[m]$
$J2, J3, J4$	Earth gravity model zonal terms	$[-]$
K	Kalman gain	$[-]$
P	State covarience matrix	$[-]$
r	Position vector	$[km]$
R	frame transformation matrix	$[km]$
R_e	Earth radius at the equator	$[km]$
R_p	Earth radius at the pole	$[km]$
Q	dynamical model uncertainty	$[rad^2]$
s	scaling factor	$[-]$
S	Model uncertainty	$[-]$
T	Reference frame transformation matrix	$[rad]$
v	velocity vector	$[km/s]$
$\boldsymbol{X}$	State vector	$[m\&m/s]$
Z_m	measured observation	$[rad]$
α	Right ascension	$[degrees]$
$\dot{\alpha}$	Right ascension	$[degrees/s]$
δ	Declination	$[degrees]$
$\dot{\delta}$	Declination	$[degrees/s]$
ϵ	Mean obliquity of the ecliptic at J2000	$[rad]$
ϵ	Specific orbital energy	$[m^2 s^{-2}]$
$\delta\epsilon$	Nutation in obliquity	$[rad]$
θ	Sidereal time	$[rad]$
λ	Longitude	$[degrees]$
μ	Gravitational parameter of Earth	$[m^3 s^{-2}]$
ρ	range	$[m]$
$\dot{\rho}$	range rate	$[m/s]$
ϕ	Geodetic latitude	$[degrees]$
ϕ	state transition matrix	$[-]$
$\Delta\psi$	Equation of the Equinoxes	$[rad]$
ω_m	Longitude of the ascending node of the mean lunar orbit	$[rad]$
ω_E	Earth rotation rate	$[rad/s]$

List of Figures

List of Tables

1

Introduction

This chapter introduces the background of this research, presented in section 1.1. Different initial orbit determination techniques are introduced with their advantages and disadvantages are discussed in section 1.2. The added information value for using real world observations for this research is discussed in section 1.3. The goal of this research is discussed in section 1.4. Finally, the structure of the report is discussed in section 1.5.

1.1. Backgrounds

On the 4th of October 1957, the fist satellite, the Sputnik 1, was launched by the former Soviet Union in the middle of the Cold War. Four months later, the United States launched their first satellite in space, the Explorer 1. From that moment on more and more satellites were launched for both civil and military parties. This evolution of the number of satellites in orbit around Earth over time can be seen in figure 1.1.

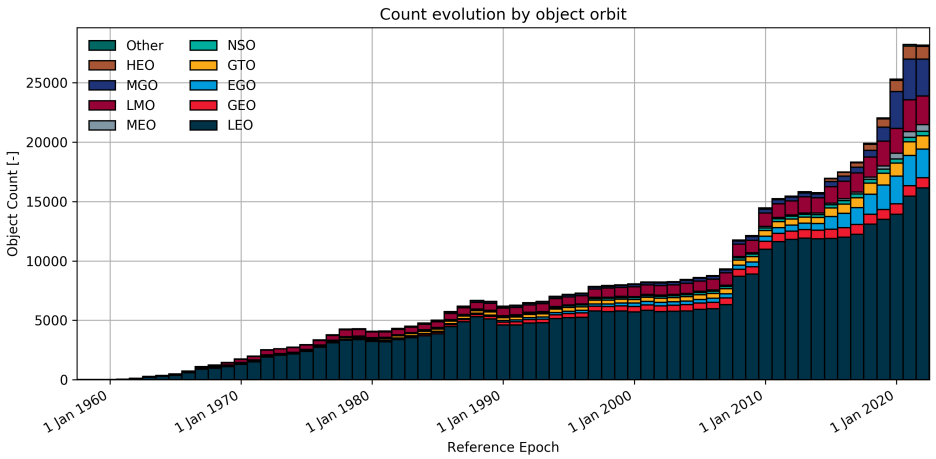

Figure 1.1: Evolution of the number of objects orbiting Earth per orbit type (Copyright **ESA**) [24]

Of the more then 36,500 objects greater then 10 cm orbiting the Earth currently, about 5800 of these are operational satellites[25]. And these numbers will increase significantly over the next few years with projects like Starlink, which has approval to launch and operate 12,000 satellites for a constellation to provide global internet [23]. Of these satellites, more then 20% is launched already.

These operational satellites have resulted in significant benefits. A few example are watching television, world-wide fast communication, navigation, weather forecast, google maps [1]. There are also drawbacks to these developments like the Kessler Effect, which states that when a certain critical particle density is reached in orbit, a collision will start a chain reaction of collisions, generating more debris, making a shell a around

the Earth which makes it unsafe to launch any satellite in orbit. [4].

Another disadvantage of launching more and more satellites, and in particular the Starlink constellation, is the light pollution for astronomers [22]. The satellites pass through their observations and when, for example, taking images in the visual spectrum, satellites can be observed by the reflected sunlight of the satellite.

For astronomers every satellite track is seen as a loss of data that polluted the observations. The Space Security Center of the Royal Netherlands Air Force (RNLAF) want to investigate if it is possible to use the telescopes astronomers are using to observe the satellite population to generate space situational awareness.

1.1.1. FOTOS feasibility study

The Defense Space Security Center (DSSC) of the RNLAF commissioned a feasibility study at Leiden University called Feasibility study for Optical Tracking of Orbiting Satellites (FOTOS). In this study it was explored if it is possible to use satellite tracks in astronomical data to automatically detect satellites and determine their orbit. Resulting from the FOTOS study it was found that it is possible to automatically detect and determine orbits, for Low Earth Orbit (LEO) satellites [33].

The FOTOS study started with astronomical data in which satellites can be seen and had as goal to find out if it is possible to determine the orbit of the observed satellites in LEO. For this study the following steps were developed to achieve this goal:

- An algorithm to automatically detect the satellite tracks in the images.
- Expressing the observed satellites track end points as two angles, the right ascension and declination, with their observed time. This is called an observation.
- The method of Gauss to approximate the state of the satellite based on three sets of observations.
- A batch least square method to improve the quality of the approximated state when more then three observations are available.

Following the successful conclusion of the feasibility study resulted in a follow-up study called FOTOS2. One goal of this study focuses on improving the quality of the satellite detection and improve the quality of the orbit determination results. The research presented in this report is part of the FOTOS2 study and will focus on investigating the initial orbit determination solution and investigate the type of satellites that are detected in the data.

The goal of this research is to find improvements on the Initial Orbit determination (IOD) approach used for FOTOS. This research is written as part of a master thesis for the study Aerospace engineering, spaceflight track. Based on this background it was determined to not focus on the first 2 steps, which consist of image processing. This research is dedicated to improve the quality of the solution by investigating an orbit determination techniques for angle-only observations, called the Constrained admissible region multiple hypotheses filer.

1.2. Initial orbit determination techniques

Prior to this research a literature study was performed to investigate alternative methods to solve the angle-only IOD problem [26]. Following from this literature study it is found that the Method of Gauss has multiple problems. Two of these problems are discussed. The first problem is that Gauss's method is a mathematical based model based on a Kepler orbit, where it is not possible to take perturbations into account. The second problem is the mathematical basis itself. In order to solve the method a polynomial of the eighth order needs to be solved resulting in multiple root solutions [12]. Gauss' method selects one of these roots without being able to know if that is the best solution. This peaks the interest to investigate if another IOD algorithm can out perform Gauss' method.

The Constrained Admissible Region Multiple Hypothesis Filter (CAR-MHF) is using another approach compared to the mathematical basis of Gauss's method [26]. The CAR-MHF determines all possible solutions in

the admissible region for the observed satellite based on an observed angle and angle-rate. The possible solutions are reduced by adding constraints to the admissible region. The constraints are based on a maximum and/or minimum expected value for the expected semi-major axis, and eccentricity.

The remaining possible solutions found in the constrained admissible region are then quantified as hypotheses. An hypothesis is a state vector consisting of a position and velocity vector of the satellite. In order to find the correct hypothesis from the set of hypotheses, a Kalman Filter is used. Each hypothesis is propagated to the next epochs at which an observation is available. When an hypothesis differs to much from the observations the hypothesis is eliminated. This process continues until a single hypothesis remains, which is called the solution of the CAR-MHF IOD problem[10].

The CAR-MHF has a few advantages over Gauss's method and will be listed below:

- Able to take a perturbed orbit model into account
- Investigates the whole range of possible solutions

The Kalman filter used in the CAR-MHF enables the user to implement a dynamical model as complex as one requires, therefore possibly increasing the accuracy of the solution. By investigating the whole range of possible solutions, no viable solution is eliminated in advance. It also enables the algorithm to select the solution based on additional observations.

This last advantage also results in its disadvantage, shown below:

- requiring more then three measurements to find the solution for the IOD problem.
- Tested only on simulated experiments [10].

The CAR-MHF has as drawback that it requires more then three observations to find a solution. The method of Gauss is able to find an approximate solution based on only three sets of observations, a set of observations contains an observed orientation of the satellite described by a right ascension and declination angles. The CAR-MHF has only been tested on simulated experiments, therefore it is still unknown how well the method works when using observations that are not taken under ideal conditions. Using data from real observations can result in gaps in the data due to lighting conditions of the satellite, weather conditions like clouds, the position of the ground station, or the orbit of the satellite.

1.3. Observed satellites

The data used for the research comes from real-world observations, therefore more information can be obtained from the data, then only IOD solutions. Astronomy cameras at different locations and orientations are used to gather data for this research. For this reason a statistical analysis of the observed satellites for each camera can give an insight in the best viewing direction. Analysing the observed satellites can also reveal if specific types of orbits, looking at the semi-major axis, eccentricity, or inclination, can be detected more easily.

Also statistical analysis can be performed to find out the percentage of satellite that are observed in the data versus all satellites orbiting the Earth. The FOTOS line detection algorithm is developed for detecting satellite in LEO. With the available data it can be investigated if only satellite in LEO are detected. Or that satellites in other orbits are also detected despite that the algorithm is not configured for satellites in those orbit regimes. An indications for the minimum required surface area of a satellite to be observed will be analysed with the data available for this research.

1.4. Research proposal

This research starts from the bases developed during the FOTOS study [33] and has as goal to further investigate the observed satellite and investigate another IOD algorithm. The observations of the Multi-site All-Sky CAmeRA (MASCARA) and bRing are used for this research.

1.4.1. Aim

The aim of the research presented in this report can be summarised by the following statement:

Investigating the limitations of the MASCARA optical instrument for the detection & orbit determination of LEO satellites with the constrained admissible region multiple hypothesis filter.

1.4.2. Research goals

The aim of this research can be split up in two research goals in order to have clear objectives. These research goals are given below:

1. Compare the accuracy performance of the CAR-MHF with the accuracy performance of Gauss' method.
2. Analyse the detected satellites as a function of the following characteristics: orbital parameters, orbit type, and Observability.

1.5. Structure of the report

The report starts of with the methodology in chapter 2. In this chapter a detailed description of the methods used for this research are presented. Chapter 3 discusses, based on the theory presented in the methodology, the algorithms used for this research. These algorithms are also validated in that chapter. The results are presented in chapter 4. These results are then discussed in chapter 5, the discussion. Finally a conclusion and recommendation for this research is presented in chapter 6.

2
Methodology

The research presented in this work focuses on two separate analyses. The first analysis is an Initial Orbit Determination (IOD) problem, following the first research goal. Here the Constrained Admissible Region Multiple Hypotheses Filter (CAR-MHF) is used to perform IOD with angle-only observations. The second analysis is statistical, following from the second research goal. The satellite observations from the image processing algorithm are analysed to find out if there are trends in the observed satellites.

Images with satellite tracks will be reduced in order to determine the projected position of the satellite against the night sky. This will result in a set of, right ascension and declination angle. These angle observations can then be used as input for the CAR-MHF. The CAR-MHF uses these input to develop the constrained admissible region from which hypotheses are generated. The hypotheses will be filtered using successive observations until a single hypothesis remains.

The first section, section 2.1, discusses the basic concepts used during the research. Next, the Image Processing Algorithm (IPA) used to identify tracks in images is discussed in section 2.2. This algorithm is developed during a feasibility study called FOTOS, in which it was shown that it is possible to automatically recognise satellite tracks in images taken by an existing all-sky camera system [33]. The same algorithm is used in this research. The output obtained from the IPA, used for this research, is discussed in section 2.3.

The Constrained Admissible Region (CAR) is a method that limits the possible satellite states based on constraints on orbit parameters. The remaining satellite states, the admissible region, can then be sampled to discretise the region and then used to formulate multiple hypotheses. These hypotheses are initial state estimates. This is discussed in section 2.4. These hypotheses can then be filtered until a single hypothesis remains, this process is called the Multiple Hypotheses Filter (MHF), which is discussed in section 2.5. After convergence to a single hypothesis, the IOD problem is solved, thereby concluding the first analysis. In case there are more observations available, the IOD solution can be further improved, transforming in to an Orbit Determination (OD) problem.

The second, statistical analysis investigates if patterns can be recognised for the observed satellites. The background information and method used for this analysis will be discussed in section 2.6.

2.1. Introductory knowledge

Before elaborating on the methods used for this research, some basic concepts used in this research will be discussed. The following elements will be discussed: time notations, coordinate systems, frame transformations, dynamic model, integrator model, and the SGP4 model

2.1.1. Time

The measurements used during this research are all given in Julian days in coordinated universal time (UTC). UTC is based on the International Atomic Time (TAI). Both time definitions use the SI definition of a second. To keep UTC in conjunction with the apparent position of the Sun and the other stats, leap seconds are intro-

duced [1]. The last time a leap second was introduced was on December 31, 2016.

Universal Time (UT) is based on the mean solar second, which is defined as the mean solar day by 86400 seconds. This time indication is based on observations. To make the time independent of the observer location, the UT is corrected for the polar motion, called UT1. [32] Most frame transformation algorithms used in this research use UT1 as input. [2].

In order to converge UTC to UT1 a correction needs to be applied. This correction is caused by the fact that UT1 is based on the mean solar second and UTC is based on the SI definition of a second. The leap seconds are applied to keep the difference within ± 0.9 seconds. The exact correction term between UTC en UT1 is published by the EIRS and is given for every day.

Terrestrial time (TT), formally called Terrestrial Dynamical Time (TDT), is equal to the TAI, plus 32.184 seconds. TT is also based on the SI definition of a second, therefore this difference is constant over time. The relation between UTC, UT1, and TT is shown in equations 2.1 [30, 32]. These relations are used in the different Matlab scripts for reference frame transformations created by Vallado [3].

$$\begin{aligned} UT1 &= UTC + \Delta UT1 \\ TAI &= UTC + \Delta AT \\ TT &= TAI + 32.184 \end{aligned} \tag{2.1}$$

where:

- $UT1$: universal time.
- UTC: coordinates universal time.
- $\Delta UT1$: less then ± 0.9 second correction between UTC and UT1.
- TAI: Atomic time.
- ΔAT: leap seconds.
- TT: Terrestrial time.

2.1.2. Coordinates system

This section discusses the different coordinate systems, in which a state of an object is defined, and how these coordinate systems relate to one another.

Oblate spheroidal Earth model

The oblate spheroidal Earth model is used to approach the shape of the Earth. The earth is not a perfect sphere, but is elliptically shaped with its semi-major axis towards the equator and the semi-minor axis towards the pole. The flattening factor is defined as the ratio between these two orthogonal dimensions, given in equation 2.2.

$$f = \frac{R_e - R_p}{R_e} \tag{2.2}$$

- R_e: Earth radius at the equator.
- R_p: Earth radius at the pole.
- f: flattening factor

The factor is measured at 1/298.26 according to the World Geodetic System 1984 (WGS 72) model. The WGS 72 is a model describing the shape of the Earth, nominal mean angular velocity, and Geocentric gravitational constant. The WGS 72 model defines the Earth equatorial radius as 6378135.0 meters. [3].

[1] `https://www.nist.gov/pml/time-and-frequency-division/atomic-standards/leap-second-and-ut1-utc-information` accessed at 23-9-2020

[2] `https://celestrak.com/software/vallado-sw.php`, accessed at 23-9-2020

[3] `https://apps.dtic.mil/sti/pdfs/ADA110165.pdf`, accessed at 11-7-2022

Reference frame

This section discusses the reference frames most commonly used in this work.

Earth-centred Earth-fixed coordinate system The Earth-centred Earth-fixed (ECEF) reference frame is a coordinate system that is centred in the centre of mass of the Earth and is fixed to the Earth. The x-axis points towards the Greenwich prime meridian, the z-axis is pointing along the rotation axis of the Earth, and the y-axis follows from the x & z-axis following the standard three axis system.

This reference frame will be used to express the position of the observer in both Cartesian and geographic coordinates. The geographic coordinate system expresses the position in the ECEF reference frame by a geodetic latitude, longitude and altitude from the Earth reference surface, as described in section 2.1.2. The latitude is defined in the degrees from the x-y plane in the direction of the z-axis. The northern hemisphere is defined as positive and the southern hemisphere is defined as negative. The longitude is expressed in degrees and is defined in the x-y plane, The longitude is 0 degrees when pointing in the direction of the x-axis and moves positive when moving east.

J2000-inertial reference frame The J2000 Earth Centred Inertial (ECI) reference frame is a reference frame that is non-rotating with the Earth. This inertial reference frame is the reference frame in which the state of satellites is expressed, in general, in this research. The J2000 reference frame is also called a mean equator mean equinox (MEME), with its origin at the centre of the Earth. The x-axis points towards the mean equinox defined at 12:00 terrestrial time, on the first of January 2000. The z-axis aligns with the Earth spin axis, perpendicular to the equatorial plane. The orientation of the Earth spin axes, as it was at 12:00 terrestrial time, on the first of January 2000 is used as the definition for the J2000 reference frame.

Topocentric equatorial coordinate The Topocentric Equatorial Coordinate (TEC) reference frame does not have its origin at the centre of the Earth, but can be appointed in any position. In this research the origin of the TEC reference frame is defined at the position of the camera stations. The axis coincide with the axis of the J2000 inertial reference frame.

The TEC reference frame is used to express observations from the observer, at the Earth surface, to the projected sky position of the satellite. These observations are expressed in two angles, right ascension and declination. The right ascension is defined in the x-y plane, and is the angle between the x-axis and the projected position of the satellite on the x-y plane. The declination is the angle between the x-y plane and the satellite position. These angles are dependent on the location of the observer, and therefore frame transformations need to be performed when combining observations from different observer locations.

Fully defining a state of a satellite in the TEC reference frame is defined by the following six elements: Right ascension (α), declination (δ), range (ρ), time rate of change of the right ascension ($\dot{\alpha}$), time rate of change of the declination ($\dot{\delta}$), and time rate of change of the range ($\dot{\rho}$).

True equator mean equinox reference frame The True Equator Mean Equinox (TEME) reference frame is used for the two-line elements (TLE) generated by the Combined Space Operations Centre (CSpOC). These TLE's are used by programs like Standard General Perturbations Satellite Orbit Model 4 (SGP4) that can be used to propagate the state of a satellite to a given time. The TLE and the SGP4 model will be further explained in section 2.1.5. The satellite state vectors calculated by the SGP4 theory, based on TLE's are expressed in the TEME reference frame.

The true equator is defined as the mean equator corrected for the nutation and precession effects for a given date. These effects will be further elaborated on in section 2.1.2. Generally, the equinox is defined as the intersection of the equatorial and the ecliptic plane. This is called the mean equinox before correcting for nutation and it called the true equinox after correcting for nutation[27] .

The TEME reference frame uses a different definition for the mean equinox. The mean equinox, also called the uniform equinox for the TEME reference frame, is defined as the true equinox minus the Equation of the Equinoxes (EQ). The EQ is given in equation 2.3.

$$EQ = \Delta\psi \cos(\epsilon + \Delta\epsilon) \tag{2.3}$$

where:

- EQ: Equation of the Equinoxes
- $\Delta\psi$: nutation in longitude
- ϵ: mean obliquity of the ecliptic at J2000
- $\Delta\epsilon$: nutation in obliquity

The relation between the mean, true and uniform equinox are schematically presented in figure 2.1. Due to this definition the definition of the equinox in the TEME reference frame does not match with the equinox in the J2000 reference frame.

The True equator, as defined in the TEME reference frame, is obtained by correcting the nominal rotation pole of the Earth (mean equator) for nutation and precession. This is also called the uniform equinox. This does follow standard definitions of mean and true equator.

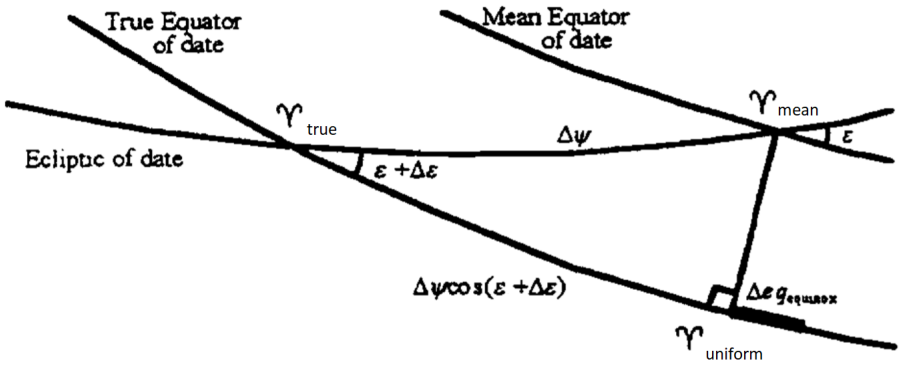

Figure 2.1: The Mean, True, and Uniform equinoxes, as viewed from outside the Celestial Sphere . (reproduced with permission [27])

The TEME reference frame aligns its x-axis with the mean equinox. The z-axis is defined as perpendicular to the true equatorial plane and the y-axis follows from the standard 3-axis system.

Frame transformation

This section discusses the different frame transformations used for the research presented in this work.

Geographic to Cartesian in the ECEF reference frame The location of the observation cameras are given in the geographic coordinate system. These need to be transformed to Cartesian coordinates. For this transformation it is important to take in to account the oblate shape of the Earth. The relation between the latitude, longitude and altitude with respect to their Cartesian counterparts are given in equation 2.4. The relation between the Local Sidereal Time (LST), Greenwhich Sidereal Time (GST), and latitude λ is shown in figure 2.2. The Greenwich sidereal time is the hour angle between Greenwich and the vernal equinox.

$$\boldsymbol{R} = \begin{bmatrix} x \\ y \\ z \end{bmatrix} = \begin{bmatrix} \left[\frac{R_e}{\sqrt{1-(2f-f^2)\sin^2\phi}} + H\right]\cos\phi\cos\lambda \\ \left[\frac{R_e}{\sqrt{1-(2f-f^2)\sin^2\phi}} + H\right]\cos\phi\sin\lambda \\ \left[\frac{R_e(1-f)^2}{\sqrt{1-(2f-f^2)\sin^2\phi}} + H\right]\sin\phi \end{bmatrix} \tag{2.4}$$

The Cartesian position in the ECEF depends on the following parameters:

- R_e: Equatorial radius of the Earth according to the WGS 84 model.
- f: Flattening factor according to the WGS 84 model.
- λ: Longitude.
- ϕ: Geodetic latitude.
- H: Altitude from Earth reference surface.

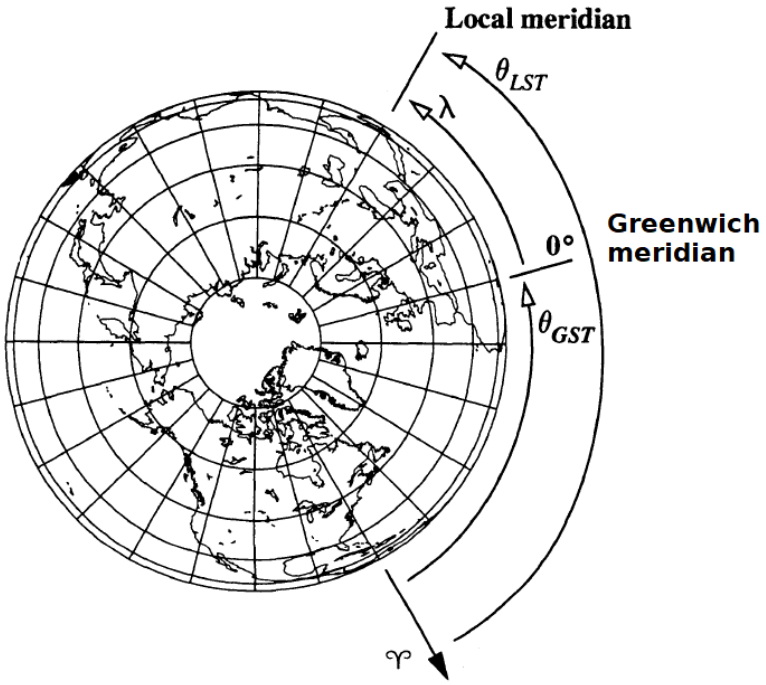

Figure 2.2: Relation between the local sidereal time θ_{LST} , Greenwich mean sidereal time θ_{GST}, and the latitude λ. (reproduced with permission [30])

polar motion The North pole is changing location with respect to the celestial ephemeris pole over time. The celestial ephemeris pole is the Earth rotation axis. The movement of the North pole has a maximum amplitude of 9 meters in any direction. The displacement of the north pole is expressed in angles x_{pm} and y_{pm}, positive in the south direction along the 0 and 270 degrees meridians, respectively. Equation 2.5 expresses the transformation matrix between the ECEF reference frame to the ECEF reference frame without polar motion. Here the $ROT_x(\theta)$, $ROT_y(\theta)$, and $ROT_z(\theta)$ are the standard rotation matrices with angle θ. Equation 2.6 shows the transformation to account for polar motion [30].

$$\boldsymbol{T_{pm}} = ROT_x(y_{pm})ROT_y(x_{pm}) \tag{2.5}$$

$$\boldsymbol{R}_{ECEFw/oPM} = T_{pm}\boldsymbol{R}_{ECEF} \tag{2.6}$$

Sidereal time The sidereal time transformation results in general in the largest transformation. The Sidereal time transformation accounts for the rotation of the Earth so that the reference frame's x-axis no longer points towards Greenwich, but towards the equinox. This transformation makes the reference frame non co-rotating with the Earth. The rotation angle is the angle between the vernal equinox and Greenwich, as shown in figure 2.2. The angle is calculated in the ECEF reference frame and is expressed as mean sidereal time, based on

the mean pole of the Earth. Therefore the angle needs needs to be converted to the apparent sidereal time. Applying nutation of the Earth's pole from the mean position to the true position. This conversion is shown in equation 2.7.

$$\theta_{AST} = \theta_{GST} + EQ + 0.00264\frac{\pi}{3600 \cdot 180}\sin(\Omega_m) + 0.000063\frac{\pi}{3600 \cdot 180}\sin(2\Omega_m) \tag{2.7}$$

where:

- θ_{AST}: Greenwich Apparent sidereal time
- θ_{GST}: Greenwich mean sidereal time, shown in figure 2.2
- EQ: Equation of the equinoxes, shown in equation 2.3
- Ω_m: Longitude of the ascending node of the mean lunar orbit.

Equation 2.7 calculates the apparent sidereal time, expressed in radians. This element is then used to calculate the transformation matrix, given in equation 2.8. Where the apparent sidereal time angle is rotated around the z-axis so that the x-axis points towards the true equinox.

$$T_{st} = ROT_z(-\theta_{AST}) \tag{2.8}$$

The sidereal time transformation matrix, as shown in equation 2.9, transforms the ECEF reference frame without polar motion to an inertial true of date reference frame.

$$\boldsymbol{R}_{ECI_{TOD}} = T_{st}\boldsymbol{R}_{ECEFw/oPM} \tag{2.9}$$

Nutation Nutation is mainly caused by the Moon's gravity and is a periodic effect. This effects causes the difference between the true equator of date to the mean equator of date. The nutation transformation matrix is given in equation 2.10. The transformation transforms the True of date inertial reference frame to a mean of date inertial reference frame, as can be seen in equation 2.11.

$$T_n = ROT_x(-\epsilon)ROT_z(\Delta\psi)ROT_x(\epsilon + \Delta\epsilon) \tag{2.10}$$

where:

- $\Delta\psi$: Nutation in longitude [obtained from the IERS]
- $\Delta\epsilon$: Nutation in obliquity [obtained from the IERS]
- ϵ: True obliquity of the ecliptic [obtained from the IERS]

$$\boldsymbol{R}_{ECI_{MOD}} = T_n\boldsymbol{R}_{ECI_{TOD}} \tag{2.11}$$

Precession Precession results from perturbations from the Moon, Sun, and the major planets in our solar system. The effects of precession are expressed using three rotating angles, ξ_p, z_p, and θ_p. The angles are shown in figure 2.3. To transform the mean of date inertial reference frame to the mean equinox of J2000 inertial reference frame. Equation 2.12 shows the transformation matrix and equation 2.13 shows the transformation from the mean of date inertial reference frame to the J2000 inertial reference frame.

$$T + p = ROT_z(\xi_p)ROT_y(-\theta_p)ROT_z(z_p) \tag{2.12}$$

$$\boldsymbol{R}_{J2000} = T_p\boldsymbol{R}_{ECI_{MOD}} \tag{2.13}$$

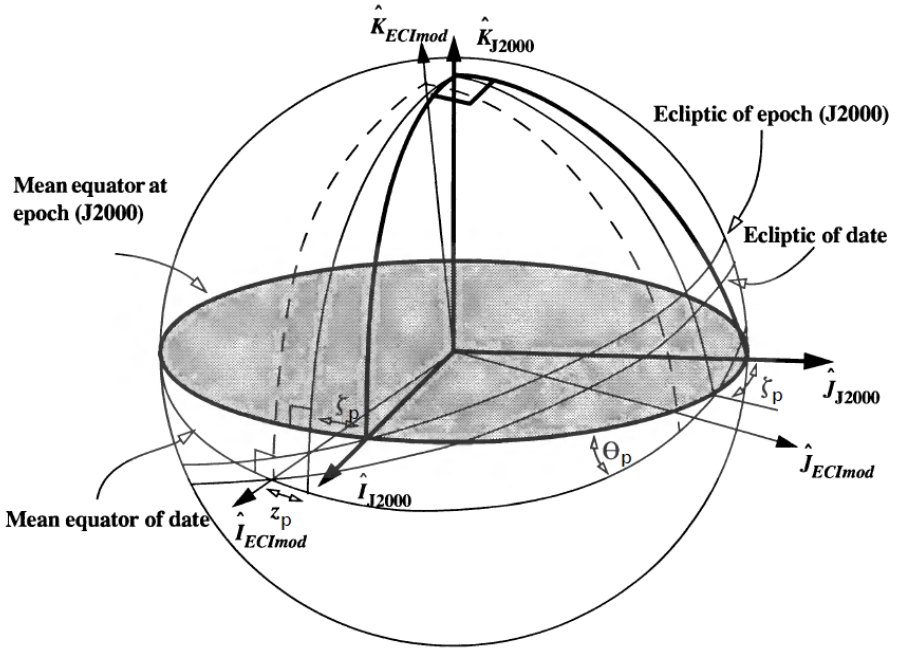

Figure 2.3: Three rotation angles, ξ_p, z_p, and θ_p, to rotate a reference frames to account for precession. (reproduced with permission [30])

ECEF to J2000 reference frame The observations angles, are observed in the TEC reference frame, which is a J2000 reference reference frame with its origin translated to the observers location. The position of the observer needs to be expressed in the Earth centred J2000 reference frame in order to be able to do vector operations to express the observations in an Earth centred J2000 reference frame. This transformation has consist of four elements: precession, nutation, sidereal time, and polar motion [30]

The transformation matrices needed for this transformation are described in the previous paragraphs. The required rotation angles are published by the international Earth Rotation and reference systems service (IERS). This service provides data on the Earth's orientation on a day by day bases. The relation between the position and velocity in the ECEF and the J2000 reference frame is given in equations 2.14 and 2.15.

$$\boldsymbol{R}_{J2000} = T_p T_n T_{st} T_{pm} \boldsymbol{R}_{ECEF} \tag{2.14}$$

$$\boldsymbol{V}_{J2000} = T_p T_n T_{st} (T_{pm} V_{ECEF} + \omega_E \times (T_{pm} \boldsymbol{R}_{ECEF})) \tag{2.15}$$

where:

- ω_E: Angular rotation speed of the Earth

TEME to J2000 reference frame Both TEME and the J2000 reference frame are inertial reference frames, yet differently defined. To convert the TEME reference frame to the J2000 reference frame requires two operations. Convert the mean equinox to the true equinox, since the mean (uniform) equinox of the TEME reference frame is not equal to the mean equinox of the J2000 reference frame. The true equator and true equinox then need to be converted to the J2000 reference frame.

The conversion from uniform equinox to true equinox is performed by a rotation matrix around the z-axis with an angle given by equation 2.3, the Equation of the Equinoxes. Next the true of date inertial reference frame transformed by precession and nutation in order to calculate the state vector in the J2000 reference frame. This is shown in equation 2.16 and 2.17.

$$\boldsymbol{R}_{J2000} = ROT_z(EQ)\, T_n T_p \boldsymbol{R}_{TEME} \tag{2.16}$$

$$\boldsymbol{V}_{J2000} = ROT_z(EQ)\,T_n\,T_p\,\boldsymbol{V}_{TEME} \tag{2.17}$$

2.1.3. Dynamic model

The dynamics model used for propagation is discussed in this section. The model can range from a simple point mass gravity model of Earth, to a model with all third body perturbations from bodies in the solar system, solar & atmospheric drag and a high fidelity model of the Earth's gravity field. Figure 2.4 shows the acceleration normalised with respect to sea level gravity for the different forces. From this is can be seen that the primary gravity and the J2, J3 & J4 are dominant for an altitude higher then 200 km altitude. These terms will be taken into account for the dynamic model. In the research of S.T. Aghav [5] an expression was given for these forces in terms of Cartesian coordinates. This expression can then be used to calculate the Jacobian to determine the state transition matrix for the Extended Kalman Filter. Also the next major force is the J5 effect, This is roughly one order of magnitude smaller then the J4 effect, therefore seen as small enough to neglect.

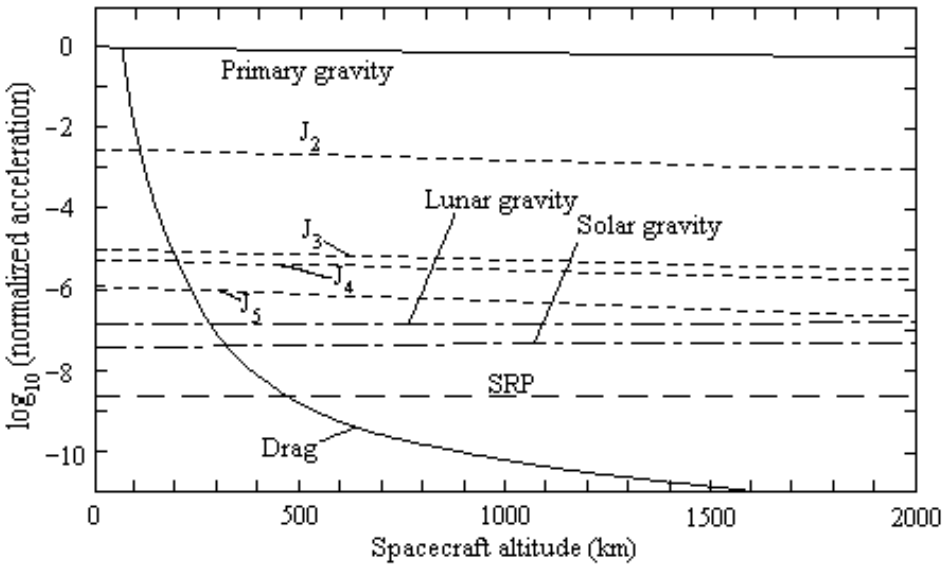

Figure 2.4: Acceleration effects for perturbing forces for LEO satellites normalised with respect to sea level gravitational acceleration. Where the primary gravity, drag, third body perturbations, Earth gravity models, and Solar Radiation Pressure (SRP) (reproduced with permission [14])

The acceleration based on the central gravity and the J2, J3 & J4 effect are expressed as a function of the satellite's position [5]. This relation is shown in equation 2.18,2.19 & 2.20:

$$\ddot{\mathbf{x}} = \frac{-\mu \boldsymbol{x}}{r^3}\left[1 + J_2\left(\frac{R_e}{r}\right)^2 \frac{3}{2}\left(1 - 5\frac{z^2}{r^2}\right) + J_3\left(\frac{R_e}{r}\right)^3 \frac{5}{2}\left(3 - 7\frac{z^2}{r^2}\right)\frac{z}{r} - J_4\left(\frac{R_e}{r}\right)^4 \frac{5}{8}\left(3 - 42\frac{z^2}{r^2} + 63\frac{z^4}{r^4}\right)\right] \tag{2.18}$$

$$\ddot{\mathbf{y}} = \frac{-\mu \boldsymbol{y}}{r^3}\left[1 + J_2\left(\frac{R_e}{r}\right)^2 \frac{3}{2}\left(1 - 5\frac{z^2}{r^2}\right) + J_3\left(\frac{R_e}{r}\right)^3 \frac{5}{2}\left(3 - 7\frac{z^2}{r^2}\right)\frac{z}{r} - J_4\left(\frac{R_e}{r}\right)^4 \frac{5}{8}\left(3 - 42\frac{z^2}{r^2} + 63\frac{z^4}{r^4}\right)\right] \tag{2.19}$$

$$\ddot{\mathbf{z}} = \frac{-\mu \boldsymbol{z}}{r^3}\left[1 + J_2\left(\frac{R_e}{r}\right)^2 \frac{3}{2}\left(3 - 5\frac{z^2}{r^2}\right) + J_3\left(\frac{R_e}{r}\right)^3 \frac{5}{2}\left(6 - 7\frac{z^2}{r^2}\right)\frac{z}{r}\right] + \frac{\mu}{r^2} J_3\left(\frac{R_e}{r}\right)^3 \frac{3}{2} + \frac{\mu \mathbf{z}}{r^4} J_4\left(\frac{R_e}{r}\right)^4 \frac{5}{8}\left(15 - 70\frac{z^2}{r^2} + 63\frac{z^4}{r^4}\right) \tag{2.20}$$

where:

- μ: gravitational parameter of Earth, equal to $3.98{\cdot}10^{14} m^3 s^{-2}$ [32]
- r: magnitude of the distance of the satellite with respect to the centre of the Earth
- $J2$: Earth gravity model zonal term J2, equal to $1082.6{\cdot}10^{-6}$ [32]

- $J3$: Earth gravity model zonal term J3, equal to -2.53·10^{-6} [32]
- $J4$: Earth gravity model zonal term J4, equal to -1.62·10^{-6} [32]

2.1.4. Runge-kutta-Fehlberg 4(5) integrator

The Runge-Kutta-Felberg method (RKF45) is a variable step size integrator to optimise computational cost while still achieving the desired accuracy. The RKF45 integrates the dynamics, as shown in section 2.1.3. For the RKF45 method this dynamical model is represented by the sign f. The RKF45 method integrates once with the Runge-Kutta method of the order 4, shown in equation 2.22 and once with the order 5, shown in equation 2.23. These integrators require the values given in equation 2.21. These two solutions are compared to each other. If the difference does not agree to a specified tolerance, the step size is reduced. If the difference agree to more significant digits than required to the specified tolerance, the step size is increased. This is shown in equation 2.24. The scaling factor s is then multiplied with given step size, h, which is the optimal step size for the next propagation. The propagated state solution is given by equation 2.22, the RKF_4 solution is calculated with the optimal step size obtained either from the given first step size when it is the first propagation step, or the calculated step size during the previous propagation. This is repeated until the epoch for which the state needs to be known is reached [21].

$$
\begin{aligned}
k_1 &= hf(t_k, y_k) \\
k_2 &= hf(t_k + \frac{1}{4}h, y_k + \frac{1}{4}k_1) \\
k_3 &= hf(t_k + \frac{3}{8}h, y_k + \frac{3}{32}k_1 + \frac{9}{32}k_2) \\
k_4 &= hf(t_k + \frac{12}{13}h, y_k + \frac{1932}{2197}k_2 - \frac{7200}{2197}k_2 + \frac{7296}{2197}k_3) \\
k_5 &= hf(t_k + h, y_k + \frac{439}{216}k_1 - 8k_2 + \frac{3680}{513}k_3 - \frac{845}{4104}k_4) \\
k_6 &= hf(t_k + \frac{1}{2}h, y_k - \frac{8}{27}k_1 + 2k_2 - \frac{3544}{2565}k_3 + \frac{1859}{4104}k_4 - \frac{11}{40}k_5)
\end{aligned}
\tag{2.21}
$$

$$
RKF_4 = y_{k+1} = y_k + \frac{25}{216}k_1 + \frac{1408}{2565}k_3 + \frac{2197}{4101}k_4 - \frac{1}{5}k_5 \tag{2.22}
$$

$$
RKF_5 = y_k + \frac{16}{135}k_1 + \frac{6656}{12825}k_3 + \frac{28561}{56430}k_4 - \frac{9}{50}k_5 + \frac{2}{55}k_6 \tag{2.23}
$$

$$
s = \left(\frac{tol\, h}{2|RKF_5 - RKF_4|} \right)^{\frac{1}{4}} \tag{2.24}
$$

where:

- $tol\, h$: The given tolerance
- RKF_5: The solution from the RKF of order 5.
- RKF_4: The solution from the RKF of order 4.
- s: scaling factor.
- f: dynamical force model for orbital mechanics.
- t_k: time at current epoch.
- y_k: state vector at current epoch.
- y_{k+1}: state vector at next epoch.

For the research presented in this work a RKF45 integrator from mathworks file exchange was used [4].

[4] `https://nl.mathworks.com/matlabcentral/fileexchange/73881-runge-kutta-fehlberg-rkf45`, accessed at 14-10-2020

2.1.5. SGP4

The SGP4 algorithm computes the state of a satellite analytically, based on a given TLE, without the need for numerical propagators and integrators. TLE's are made available by the CSpOC of all observable non classified objects that orbit the Earth. A TLE contains general information about the satellite like catalogue number and launch year. The TLE also contains information to determine and model the state of the object by providing the following parameters: inclination, right ascension of the Ascending node, eccentricity, argument of perigee, mean anomaly, mean motion, drag term, and date for which the TLE is made. The orbital elements in the TLE are orbital average elements and can therefore not directly be used to compute a Kepler orbit, which consist of osculating orbital elements[5].

The SGP4 theory uses a TLE of an object as input to calculate a state vector of the object for a given epoch in Cartesian coordinates in the TEME reference frame. The SGP4 theory is an analytical method that takes an approximation of the following perturbing forces in to account: Earth oblateness, solar and lunar third body perturbations, gravitational resonance effect, solar radiation, and atmospheric drag. According to the research of Wei Dong et al. [13] the officials providing the mathematical models do not provide modal accuracy and the related references are very few. Therefore they analysed 1120 space objects, representing the full range of satellites, in order to access the accuracy of the last available SGP4 model in 2010. Since the references for similar research are so few, this is the best found reference to have an indication for the SGP4 model uncertainty. In this research it was found that the orbit determination accuracy is in the order of magnitude of 100 meters, and is related to the orbital altitude, where the lower the altitude the larger the orbit determination error becomes. This is for the epoch at which the TLE is given. The maximum orbit prediction accuracy for a one day prediction is between 2 km and and 10 km, depending on orbital height. The maximum orbit prediction error for predictions of three days is between 10 and 40 km. To minimise the error, the TLE available at the date of the observation will be used to determine SGP4 reference data. Depending on the update frequency of the TLE, which vary from satellite to satellite, it can cause SGP4 model inaccuracies of the magnitude between 1 and 10 km. The maximum SGP4 model uncertainty for this research is therefore set to 10 km. If results should become smaller than this model uncertainty, then no hard conclusions about the true position of the satellite can be made.

The SGP4 theory in combination with TLE's is accepted method of calculating spacecraft position by software programs like Systems Tool Kit (STK) [18]. Finally it is with respect to computation time and development time cheaper to calculate the position of the satellites with this in Maltab available tool SGP4, then using Tudat, a TU Delft developed orbit propagation software. Tudat is written in an other programming language in which I am not proficient. This makes setting up a validated program for all satellites of interest time consuming and complex.

In this thesis the SGP4 reference state should not be seen as the exact true, the inherent uncertainty in initial state and model errors will cause deviations from the true state. The orbit determination method in this work could result in a better estimation of the true state then the SGP4 reference state, due to the extra information of observations. The SPG4 theory shows an approximate initial error of 1 km and increases with 1-3 km a day, so depending on the time of observation and the time at which the TLE described, the error can be in the order of magnitude of kilometres. When the error between the SGP4 reference state and the orbit determination is within this magnitude, it is impossible to state which solution is more correct, showing the accuracy limits for this research.

2.2. Image processing algorithm

The image processing algorithm developed by T.P.G Wijnen in 2019 [33] is the first step in this research. This algorithm detects line segments in images and determines the endpoints of these lines. The endpoints will then be compared to the position of the satellites, which are based on the TLE and SGP4 theory. The observed track is linked to a known satellite when both endpoints of the track matches the sgp4-based position of a satellite within a 10 pixel margin. For the identified tracks the projected position ,with the corresponding time, of the observed satellites are stored and are later to be used in the CAR-MHF method.

The FOTOS study showed that it is possible to automatically link observed satellite tracks to the correspond-

[5] `https://www.space-track.org/documentation#/tle` accessed at 14-10-2020

ing satellite from a database with known satellites. Secondly, it is found that it is possible to perform IOD operations on the detected satellite track. The algorithm is developed during a feasibility study and there are still possibilities for optimisation in this area. The automatic track detection and identification developed will be used as is.

The steps taken in the algorithm are presented in this section, starting with the information on the cameras used to obtain the data, discussed in section 2.2.1. The operations to increase the contrast of the satellite track versus the background are discussed in section 2.2.2. The Hough transform is then used to detect the lines, which is discussed in section 2.2.3. The RANSAC method is used to improve the detected lines and is discussed in section 2.2.4. The end-point detection is performed on the detected line and is discussed in section 2.2.5. This is followed by the identification process of the satellite track which is elaborated on in section 2.2.6.

2.2.1. Camera & observation information

The images recorded, from which the data for this research is obtained from, are taken with a Multi-site All-Sky CameRA [29] station and two bRing stations [28]. These cameras have a field of view of 53x74 degrees, each, and the pixel resolution is approximately 0.02 degrees.

The MASCARA station consists of five identical cameras that cover the sky down to 20 degrees from the horizon. The data used during this research is taken at the MASCARA station in La Silla. The setup can be seen in figure 2.5[6]. The five cameras are points in the following five directs: north, east, south, west, zenith in. This station provided data for the days of January the 2nd and 3rd, in the year of 2020.

Figure 2.5: MASCARA setup in La Silla

The bRing stations consist of two camera, one pointing east and one pointing west. During the time the data was gathered the west pointing cameras on both bRing stations were out of order, therefore we only have data from the bRing eastward facing cameras. The bRing stations are located in South Africa and Australia. These two stations provided data for the days of January 3rd and 4th, in the year 2020.

The information of the cameras are summarised in the table 2.1, including their location in the geographic coordinates system in the ECEF reference frame.

2.2.2. track contrast improvement

Each camera from the MASCARA [29] and bRing [28] set-up takes pictures from the night sky. These cameras are instruments for astronomers with a main objective to detect exoplanet transits [29]. The bRing camera will record images with an alternating exposure time of 2.5 seconds and 6.4 seconds, at a cadence of 12.8 seconds [28]. The MASCARA cameras use an exposure time of 6.4 seconds. For the IPA, only the recorded images

[6] `https://www.eso.org/public/netherlands/images/eso1722b/?lang`, accessed at 13-01-2021

Table 2.1: Summary of the camera station information and observation dates

Camera name	latitude [degrees]	longitude [degrees]	altitude [m]	Camera ID	02/01/2020	03/01/2020	04/01/2020
La Silla North	-29.257124	-70.738	2369.4	LSN	X	X	
La Silla East				LSE	X	X	
La Silla South				LSS	X	X	
La Silla West				LSW	X	X	
La Silla Centre				LSC	X	X	
South Africa East	-32.3812	20.8102	1798.0	SAE		X	X
Australia East	-31.272189	149.062150	1165	AUE		X	X

with an exposure time of 6.4 seconds are used.

The images with an exposure time of 6.4 seconds from the bRing camera are used in this algorithm. Two consecutive images are subtracted from each other to remove common objects from the image. Figure 2.6 shows a part of an image after subtracting two images. Here one can already clearly see two satellite tracks from two images that are subtracted from one another. The star and moon locations in the images are masked with the median pixel value of the whole image. This step removes most of the leftover light sources that vary in brightness between the two images. The pixels that have a value 2.5 standard deviations above the mean pixel value of the whole image, and have a minimum of 6 pixels with a value of at least one standard deviation above the mean pixel value of the image adjacent are marked as interesting light source. All the pixels that do not meet these requirements are replaced with a zero value to enhance the contrast between bright lines and the background. The resulting contrast can be seen in the right image in figure 2.7.

The MASCARA instrument has all 6.4 second exposure time images, compared to the bRing images, which have an alternating exposure time per image. Yet, the same algorithm for the bRing images is used to process the MASCARA images. This results in only using the odd numbered images from the mascara data. For this reason not all data is used and therefore it can be improved in the future. For this research it was noticed too late into the analysis that the even and odd databases can be compared. The skipping of an image results in a similar gap as for the bRing analysis, as seen in figure 2.6, between the two tracks.

The even and odd image number database can be used to improve the results. Since the end of the track at image number one, is equal to the start of the track of image number two. Computing the projected position of track end at image number one, and the beginning of the track at image number two, gives an indication of the reliability of the observed position. This can then be used as a weighting factor in the orbit determination algorithm.

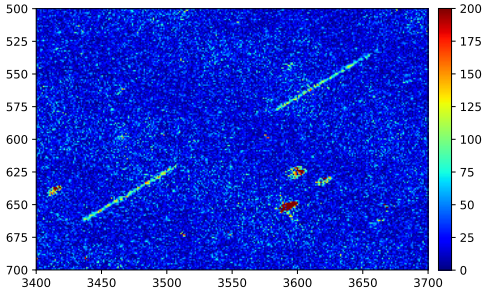

Figure 2.6: Two consecutive bRring images stacked and subtracted from each other. This subtraction removes common light sources. (reproduced with permission [33])

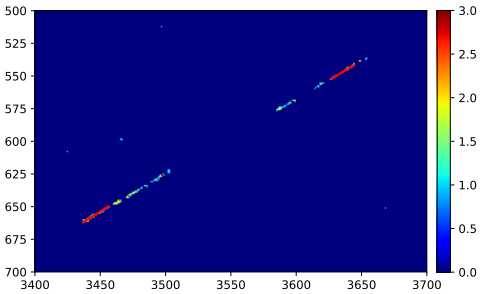

Figure 2.7: Two consecutive bRIng images stacked and sub tracked from each other. Followed with a contract increasing algorithm where all pixels that do not have a pixel value of 2.5 above the mean pixel value with a minimum of 6 pixels around it with a pixel value of 1 standard deviation above the mean pixel value are set to a pixel value of zero. (reproduced with permission [33])

2.2.3. Hough transform

The satellite tracks with improved contrast makes it possible to have an improved performance of the Hough transform. The Hough transform draws multiple reference lines though each data point, at fixed angles which rotate around each data point (blue lines in figure 2.8). Next a support line (orange) is set from the origin to the support line, so that the reference line and the support line have a 90 degree corner with respect to each other. This process is then repeated for each data point. When multiple data points are on a straight line, the length of the support line and the angle between the reference frame and the support line are similar. Hence straight lines can be found in the data set.

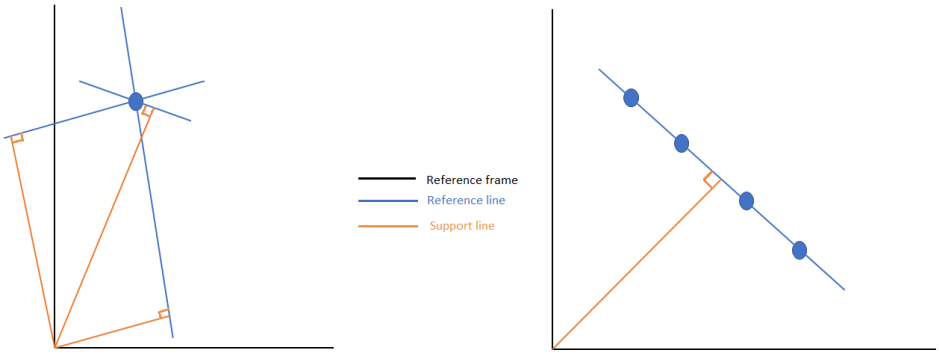

Figure 2.8: Schematic representation of the Hough transform. The black lines define a reference frame in which the reference line and support line are drawn. The reference lines are drawn at fixed angles around a data point. The support line is is drawn perpendicular to the reference line, to the origin on the reference frame.

To reduce the computational load the probabilistic Hough transform , from the cv2 python package, is used for recognise the satellite track [16]. The computational load is decreased due to the fact that this method does not draw lines though every data point but a random set of data points. This can be justified due to the fact that a subset of data points can be sufficient to detect the track.

The Hough transform can further be tuned by setting a minimum line length and maximum gap length in the line segments. The minimum line length is a very important parameter when trying to detect LEO satellites. The larger the semi-major axis, the longer the orbital period of a satellite is. For a fixed exposure time of the camera, the satellites with a larger semi-major axis will result in shorter tracks. For this reason a minimum track length is set and this selects only LEO satellites. The maximum gap parameter lets you overcome small measurement error due to local pixel variations or brightness variations of the satellite. For the current algorithm the minimum line length is set to 20 pixels and the maximum line gap is set to 3 pixels. The Hough transform finds finite line segments, therefore the RANSAC method is used to detect the full length of the track.

2.2.4. RANSAC method

The RANSAC method is applied on the track found by the Hough transform, in a restricted domain, based on the line found by the Hough transform. The RANSAC method distinguishes between inliers and outliers. It uses the inliers, to randomly find a straight line with the best fit. The other data points, the ourliers, are not used to fit the line. The disadvantage of using a random generator is that not always the same results is produced for the same dataset.

The advantage of the RANSAC method over the Hough transform is that it finds infinite lines independent of the gaps in the data points. These gaps can occur due to noise or a masked star which coincides with the satellite track. The RANSAC method is used to find the endpoints of the satellite track.

2.2.5. Endpoint detection

The next step is to determine the endpoints of the found tracks. This process starts at the pixel, along the line found by the RANSAC method, with the highest pixel value. From this point a cost function will follow the

RANSAC line in each opposite direction. This cost function will cumulatively add the consecutive pixel values minus the local mean pixel value plus one standard deviation of the local pixel values. The cost function will continue until the edge of the restricted domain, as defined in the beginning of the RANSAC method. The pixel at which the cost function is maximal is defined as the endpoint of the satellite track.

2.2.6. Satellite Identification

The endpoints of the satellite tracks are known but they need to be identified. After identifying which satellite is observed for a given satellite track, the end points of the track, and the corresponding times will be stored. All observations from a single satellite will later be used to perform orbit determination for that satellite, if enough data is available.

Each image has a time stamp. This is at approximately halfway in during the exposure time. With this information a time stamps can be given to each endpoint of the satellite track; time at which the image is taken plus or minus half the exposure time.

Identifying the satellite track will also determine which time stamps corresponds to the start point, and which to the endpoint of a track. The position of all satellites, given in the North American Aerospace Defence Command (NORAD) database, updated by CSpOC, are computed. The TLE's from the database are used to compute the position of these satellite at the two possible time stamps for a given satellite track. For accurate determination of the satellite's position, a TLE needs to be used with its date as close to the observed date as possible. The two positions are calculated with *Pyephem python package*, based on the SGP4 theory, and are given in the TEC reference frame, in projected sky positions.

All satellites which are above the horizon, observed from the position of the camera, are selected. For these satellites, the projected sky positions are transformed to pixel position, for the image in which the satellite is in the field of view. This is performed with the *world2pix* based on the *astrometry python package*.

The pixel position of the endpoints and the pixel positions of all satellites above the horizon are know for the following time stamps; plus and minus halve the exposure time. The pixel positions of the endpoints are compared to the pixel positions of the satellites, hereby the chronological order of the endpoints can be determined. When both endpoints are within 10 pixels of a satellite its pixel positions, the track is identified.

After identification the data is stored per satellite and used for later research. An advantage of this identification is the fact that the time stamps of the track's endpoints are known. For satellite tracks that cannot be identified it is not yet possible to determine which endpoint corresponds to what time. Those unidentified endpoints are not used in this research.

2.3. Data

This section discusses the observational data and its format used for this research.

2.3.1. Data format

The IPA is written in the Python programming language and the thesis research is coded in Matlab, therefore the data has to be transferred from python to the Matlab environment. The data is output in a Comma Separated Value (CSV) file, since both programming languages are able to read and write those files.

For each observation, each endpoint of a track linked to a satellite, an entry is made. Each line segment will therefore result in two observations, and thus entries. An example of such an entry is given in table 2.2.
Table 2.2 shows 14 parameters output for each endpoint and will be elaborated on below:

- **Satellite ID number:** The NORAD assigned ID number of the satellite which was linked to the observation.

- **Right ascension:** The right ascension of the, by the cost function determined, endpoint of the observed track. The right ascension is defined in the TEC reference frame and is given in degrees.

Table 2.2: Example of the data format used for the research

Local sidereal time [hours]	Satellite ID number	Right ascension [deg]	Declination [deg]	SGP4 right ascension [deg]
3.72	27601U	213.45	-81.86	213.61
SGP4 declination [deg]	X pixel position	Y pixel position	SGP4 X pixel position	SGP4 Y pixel position
-81.88	1119	2474	1120.10	2475.36
Camera ID	Date	Image Number	Julian Day	
SAE	20200104	34655144	2458853.30	

- **Declination:** The declination of the, by the cost function determined, endpoint of the observed track. The declination is defined in the TEC reference frame and is given in degrees.
- **SGP4 right ascension:** The right ascension of the, by the SGP4-based, endpoint of the observed track. The right ascension is defined in the TEC reference frame and is given in degrees.
- **SGP4 declination:** The declination of the, by the SGP4-based, endpoint of the observed track. The declination is defined in the TEC reference frame and is given in degrees.
- **X pixel position:** The x pixel value of the, by the cost function determined, endpoint of the observed track. The X value refers to a pixel in the observed image.
- **Y pixel position:** The Y pixel value of the, by the cost function determined, endpoint of the observed track. The Y value refers to a pixel in the observed image.
- **SGP4 X pixel position:** The x pixel value of the, by the SGP4-based, endpoint of the observed track. The X value refers to a pixel position value, which can be sub-pixel level.
- **SGP4 Y pixel position:** The Y pixel value of the, by the SGP4-based, endpoint of the observed track. The Y value refers to a pixel position value, which can be sub-pixel level.
- **Camera ID:** The camera ID indicates which camera recorded the image from which the endpoints were taken. The first two letters indicate the station and the last letter indicates the direction the camera is facing, more information can be found in section 2.2.1.
- **Date:** The date refers to the date at which the camera started recording that day. Therefore recording observations after midnight will still be marked with the data of the previous day. The data is formatted as follows; the first four digits is the year, the fifth and sixth digit represents the month of the year, and the last digit represents the day of the month.
- **Image number:** Each recorded image is marked with an image identification number, which allows the endpoints to be traced to the original image in which it was detected.
- **JD:** JD represents the Julian Day (JD) of the observed endpoint of the track. A Julian day is a count of the number of solar days started from noon UTC, on Monday, January 1, 4713 BC. This corresponds the date and time at which the endpoint of the track is observed.
- **lst:** The Local Sidereal Time represents the local sidereal time, as represented in equation 2.2.

2.4. Constrained admissible region

The constrained admissible region is the first part of the CAR-MHF. The CAR-MHF used in this research is based on the work of Demars & Jah [9] and DeMars et al.[10]. The admissible region is expressed as a range & range rate domain, as defined by DeMars. This domain is constructed for a given observation angles and angle rates. These values are obtained from the observations.

In order to establish the admissible region, the angle rates need to be calculated. The angle rates are derived from angles and their timing, and is discussed in section 2.4.1. The admissible region and its constraints are further elaborated on in section 2.4.2. The constrained admissible region is then used to quantify hypotheses, which is discussed in section 2.4.3. These hypotheses are the stepping stone to determine the satellite position with orbit determination algorithms.

2.4.1. Angle rate derivation

The right ascension and declination of the observation is directly given by the data. The angles rates need to be derived in order to establish a constrained admissible region.
The angle rates are calculated through three consecutive observations. To acquire an accurate approximation, by interpolation, of the angle rates, the three consecutive observation can not be too far apart. The time between each observation is set to be smaller then 20 seconds. This time span is set to prevent the software of calculating an angle rates with data from multiple observation arcs. The 20 seconds means that in the 6 next potential observation windows, or next 3 images, no satellite is detected. When the first three observations of a set of observations for a satellite do not meet the earlier stated requirement, data points two till four is used, and so forth. If no observations are found that meet the requirement, then the admissible region can not be constructed.

The right ascension and declination and the corresponding times of the three consecutive observations are interpolated, using a polynomial of degree two. Resulting in a function which approximates the right ascension as a function of time, and the declination as a function of time, for the given time span of the three consecutive observations.

The derivative with respect to time of these two function is then taken to obtain the angle rates, as a function of time, for the time span of the three observations. These functions are evaluated at the time of the second observation. This results in the approximate angle rates at the second observation. The angle rates, in combination with the measured observation angles, results in all the required inputs to construct the constrained admissible region, at the second observation.

The second order polynomial is used instead of the first order polynomial to obtain a better fit of the data, due to the fact that a linear interpolation would result in constant angle rates.

2.4.2. Admissible Region constraints

DeMars showed that it is possible to express the range rate ($\dot{\rho}$) as a function of range (ρ), right ascension (α), declination (δ), time rate of change of the right ascension ($\dot{\alpha}$), the time rate of change of the declination ($\dot{\delta}$), and the specific orbital energy (ε). The relation will be used to formulate constraints for the admissible region. This section presents the derivations from DeMars, to construct these constraints.
The derivation starts with the vis-viva equation for a two-body system, given in equation 2.25.

$$\varepsilon = \frac{\|\boldsymbol{v}_{obj}\|^2}{2} - \frac{\mu}{\|\boldsymbol{r}_{obj}\|} \tag{2.25}$$

where:

- ε: Specific orbital energy
- r_{obj}: Position of the object with respect to the planet centre.
- v_{obj}: Velocity of the object with respect to the planet centre.
- μ: gravitational parameter of the body that the object is orbiting.

The position of the cameras are known in a ECEF reference frame and are given by a latitude, a longitude and a altitude. This position is then transformed to Cartesian coordinates and transformed to the J2000 reference frame. The observations, discussed in section 2.3, are defined in an TEC reference frame with the origin at the location of the camera. Based on these two position definitions it it possible to derive equation 2.26. Here the position of the object in the J2000 reference frame,$\boldsymbol{r}_{obj}$, is equal to the position of the camera in the J2000 reference frame, $\boldsymbol{r}_{cam}$, plus the position vector from the camera to the object, $\boldsymbol{r}_{obj/cam}$, in the TEC reference frame.

A similar relation for the velocity is given in equation 2.27. The velocity of the camera in the ECEF reference frame is zero. This vector is then transformed to the J2000 reference frame. The velocity vector from the camera to the object is defined in the TEC reference frame and is given by $\boldsymbol{v}_{cam}$. The velocity of the object,$\boldsymbol{v}_{obj}$, in the J2000 reference frame is expressed as the velocity of the camera in the J2000 reference frame, $\boldsymbol{v}_{cam}$, plus

the velocity of the object as observed from the camera, $\boldsymbol{v}_{obj/cam}$, in the TEC reference frame. A schematic representation of these vectors are given in figure 2.9

$$\boldsymbol{r}_{obj} = \boldsymbol{r}_{cam} + \boldsymbol{r}_{obj/cam} \tag{2.26}$$

$$\boldsymbol{v}_{obj} = \boldsymbol{v}_{cam} + \boldsymbol{v}_{obj/cam} \tag{2.27}$$

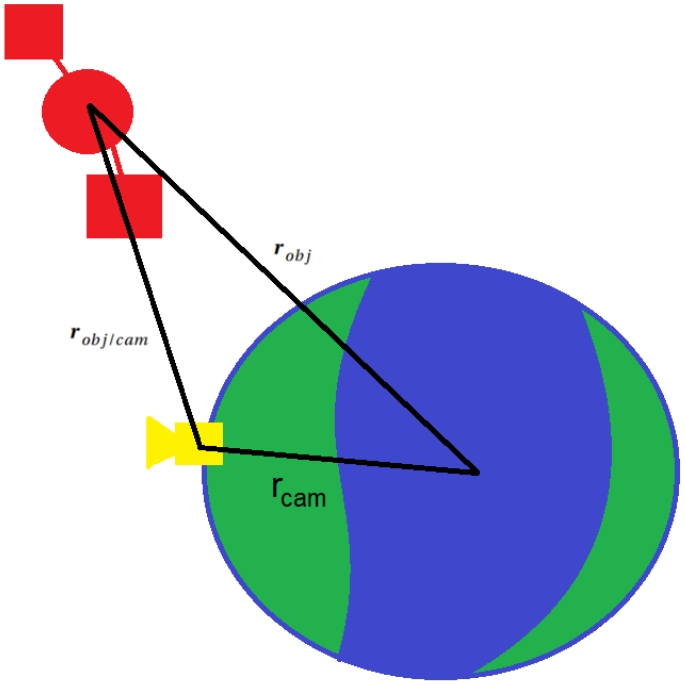

Figure 2.9: Schematic representation of the position vector of the object (red) and the camera (yellow) with respect to the centre of the Earth and to each other

The position and velocity vector between the object and the camera is partially defined by the α & δ, and $\dot{\alpha}$ & $\dot{\delta}$, respectively. The expression for these vectors are given in equation 2.28 & 2.29.

$$\boldsymbol{r}_{obj/cam} = \rho \boldsymbol{u}_{\rho} \tag{2.28}$$

$$\boldsymbol{v}_{obj/cam} = \dot{\rho}\boldsymbol{u}_{\rho} + \rho\dot{\alpha}\boldsymbol{u}_{\alpha} + \rho\dot{\delta}\boldsymbol{u}_{\delta} \tag{2.29}$$

with:

$$\boldsymbol{u}_{\rho} = \begin{bmatrix} \cos\alpha\cos\delta \\ \sin\alpha\cos\delta \\ \sin\delta \end{bmatrix} \tag{2.30}$$

$$\boldsymbol{u}_{\alpha} = \begin{bmatrix} -\sin\alpha\cos\delta \\ \cos\alpha\cos\delta \\ 0 \end{bmatrix} \tag{2.31}$$

$$\boldsymbol{u}_{\delta} = \begin{bmatrix} -\cos\alpha\sin\delta \\ -\sin\alpha\sin\delta \\ \cos\delta \end{bmatrix} \tag{2.32}$$

where:

- ρ: range in the TEC reference frame
- α: right ascension in the TEC reference frame

- δ: declination in the TEC reference frame
- $\dot{\rho}$: time rate of change of the range in the TEC reference frame
- $\dot{\alpha}$: time rate of change of the right ascension in the TEC reference frame
- $\dot{\delta}$: time rate of change of the declination in the TEC reference frame

Setting a set of scalar values will result in cleaner equations further on in the derivations. The set of scalar values are given below:

$$w_0 = \|\boldsymbol{r}_{cam}\|^2 \tag{2.33}$$

$$w_1 = 2(\boldsymbol{v}_{cam} \cdot \boldsymbol{u}_\rho) \tag{2.34}$$

$$w_2 = \dot{\alpha}^2 \cos^2\delta + \dot{\delta}^2 \tag{2.35}$$

$$w_3 = 2\dot{\alpha}(\boldsymbol{v}_{cam} \cdot \boldsymbol{u}_\alpha) + 2\dot{\delta}(\boldsymbol{v}_{cam} \cdot \boldsymbol{u}_\delta) \tag{2.36}$$

$$w_4 = \|\boldsymbol{v}_{cam}\|^2 \tag{2.37}$$

$$w_5 = 2(\boldsymbol{r}_{cam} \cdot \boldsymbol{u}_\rho) \tag{2.38}$$

The position and velocity vector in the J2000 reference frame, with the substituted scalar values, are given in equation 2.39 & 2.40, respectively. This position and velocity of the object is called its state.

$$\|\boldsymbol{r}_{obj}\|^2 = \rho^2 + w_5\rho + w_0 \tag{2.39}$$

$$\|\boldsymbol{v}_{obj}\|^2 = \dot{\rho}^2 + w_1\dot{\rho} + w_2\rho^2 + w_3\rho + w4 \tag{2.40}$$

Substituting these expressions in equation 2.25 will result in the relation between range rate and the range for a given observation angle and angular velocity. This relation is given in equation 2.41, where equation 2.42 if a function of all range dependent variables.

$$\dot{\rho}^2 + W_1\dot{\rho} + f(\rho) - 2\varepsilon = 0 \tag{2.41}$$

$$f(\rho) = w_2\rho^2 + w3\rho + w_4\frac{2\mu}{\sqrt{\rho^2 + w_5\rho + w_0}} \tag{2.42}$$

Solving the quadratic equation, equation 2.41, will result in an expression for the range rate. This expression can be seen in equation 2.43

$$\dot{\rho} = -\frac{w_1}{2} \pm \sqrt{\left(\frac{w_1}{2}\right)^2 - f(\rho) + 2\varepsilon} \tag{2.43}$$

The admissible region can be defined for any satellite orbiting Earth. This results in a specific orbital energy that is smaller then zero. For a given station location, angles and angle rates from measurements, it is possible to define the admissible region. A schematic representation can be seen in figure 2.10, where the grey area below the blue line is the admissible region. The graph shown in figure 2.10 is a illustration to describe the method. Appendix B shows six similar graphs of the con trained admissible region with the different con trains, including the input data used to compute these graphs.

The admissible region can be constrained when the type of orbit is known. In the followings section the range, semi-major axis and eccentricity constraints are discussed.

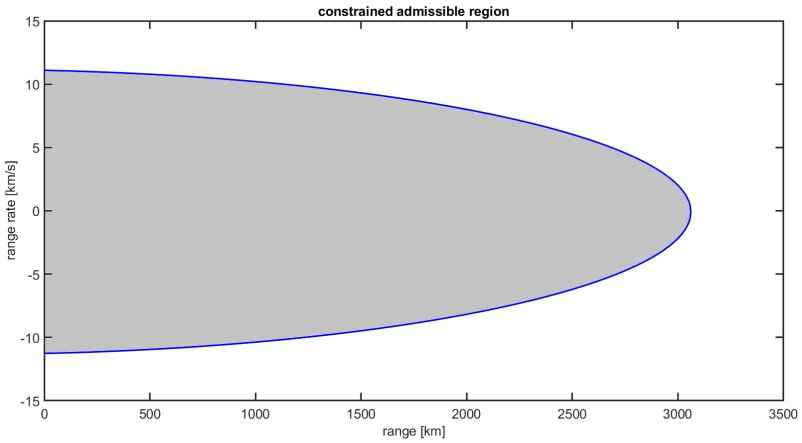

Figure 2.10: schematic representation of the admissible region illustrating the CAR method, appendix B provide the data and graphs to reproduce this method.

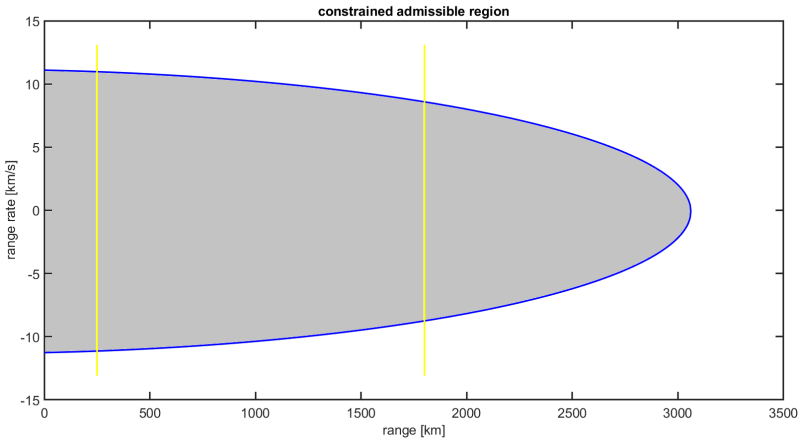

Figure 2.11: Schematic representation of the range constrained admissible region, between the yellow lines. Appendix B provide the data and graphs to reproduce this method.

Range

The range constrained, contrary to the semi-major axis and eccentricity constraints which will be discussed in the next sections, was self developed. The semi-major axis and eccentricity constraints are developed by DeMars [10].

The track length of the observed satellite gives an indication of the maximum range between the observer and the satellite. The further the satellite is away from the observer the shorter the observed track will be. The minimum range constraint is a given input. The maximum range constraint is calculated for a given track length, based on a relation which will be further explained in this section. The range constraints will be a straight lines in the admissible region. A schematic representation of these constraints are shown in figure 2.11.

The minimum range constraint is set to 250 km. This is the orbital height at which satellites de-orbit within a few days. Also the satellites should be directly overhead, otherwise the range would already be larger. This can only occur on the La Silla central camera. Therefore this constraint is lenient, and is almost never the limiting constraint.

The maximum range constraint is determined by the relation between the track length in pixels and the range between the observer and the satellite. Equation 2.44 shows the relation between the angular velocity, veloc-

ity and the range in the general form.

For this constraints we disregard the relation between the orbital velocity and semi-major axis, because the latter is unknown. Without this assumption it is not possible to establish this relation because the semi-major axis is unknown. A LEO satellite with a circular orbit with a a semi-major axis of 6478 (100 km above the earth surface) has a velocity of 7.8 km/s and a LEO satellite with a circular orbit with a semi-major axis of 8378 km (2000 km above the earth surface) has a velocity of 6.9 km/s. This is a 12% decrease in velocity. Secondly, since the observer is positioned on the Earth surface and not at the centre of the Earth, the relative velocity is different and changes over time, depending on the position of the satellite. The time of a single observation is relative short, therefore the chance in velocity caused by this effect is negligible. The velocity of the satellite during a single observation is assumed to be constant. The error resulting from these assumption will be addressed to later in this section.

$$\omega = \frac{v}{(\rho + R_O)} \tag{2.44}$$

where:

- ω: angular velocity [rad/s].
- v: velocity [m/s].
- ρ: range between the observer and the satellite [m].
- R_O: Position of the observer [m]

Equation 2.45 shows the relation between angular velocity, angle and time. Substituting equation 2.44 and 2.45 results in equation 2.46.

$$\omega = \frac{\theta}{t} \tag{2.45}$$

- θ: angle between the start and end of the track as seen from the observer [rad]
- t: time [s]

$$\theta = \frac{vt}{(\rho + R_O)} \tag{2.46}$$

The velocity is assumed to be constant and the time for which the satellite track is observed is also constant. The observed angle, θ, has a direct correlation with the length of the track due to the fact that the distance between the lens and the surface at which the image is captured is constant, so $L_{pixel} \propto \theta$. Using this relation and rewriting equation 2.46 result in the following relation, equation 2.47.

$$\rho = \frac{vt}{L_{pixel}} + R_O \tag{2.47}$$

where:

- L_{pixel}: number of pixels [m]

Equation 2.47 shows the relation $\rho \propto L_{pixel}$, since the velocity and time is constant. From this theoretical relation, equation 2.48 is set as fit function for the observed data

$$\rho_{max} = \frac{a}{L_{pixel}} + b \tag{2.48}$$

where a and b are variables to find the best fit for the given data. The b variable is introduced since the observer is standing on the Earth surface, and not at the centre of the Earth.

The track length and the range to the observer is plotted for 1031 LEO satellites, which can be seen in figure 2.12 as blue circles. These 1031 LEO satellites are all observed LEO satellites with more then two observations for this research. From this it can be seen that the track length increases when the range decreases. Fitting

equation 2.48 through the data results in the red line. This line represents the best fit (mean) relation between track length and range and the formula is given in equation 2.49.

$$\rho_{mean} = \frac{8.8 \cdot 10^7}{L_{pixel}} + 3.1 \cdot 10^5 \tag{2.49}$$

In order to construct a maximum range constraint, it is necessary to transpose the line so that all data points are below the line. The transposed relation is the yellow line in figure 2.12 and the formula is given in equation 2.50, in meters. Where the formula is transposed 20 pixels to the right and 600 km upwards.

$$\rho_{max} = \frac{8.8 \cdot 10^7}{L_{pixel} - 20} + 3.1 \cdot 10^5 + 6.0 \cdot 10^5 \tag{2.50}$$

For a given track length from an observed satellite, the maximum possible range between the observer and the satellite can now be computed with the relation. Together with the minimum range constraint, they can constrain the admissible region.

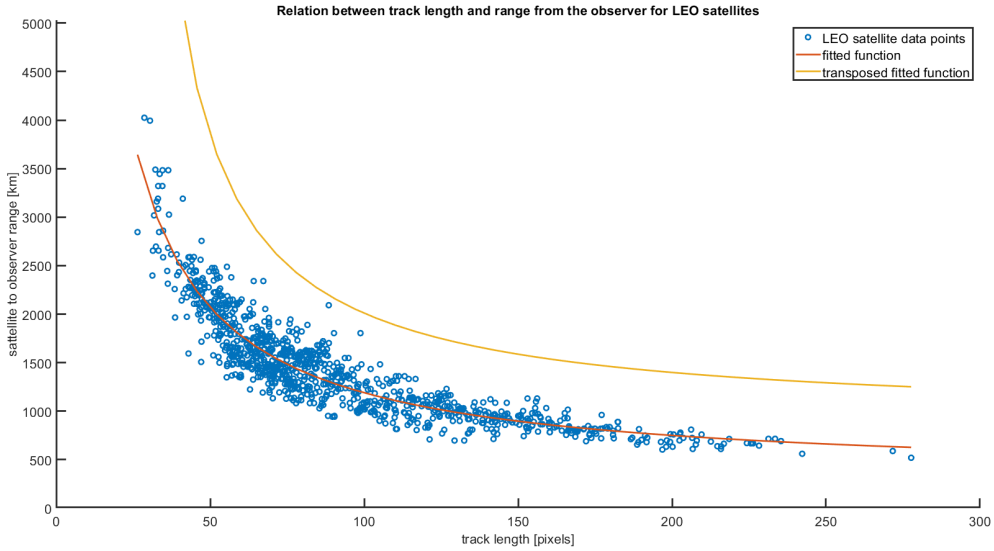

Figure 2.12: statistical relation between the track length in pixels and the range. The blue dots represent 1031 observed satellites in LEO. The red line is the fitted function through the data with relation y = a/x+b. The blue line is the transposed fitted function which is used as the maximum range constraint based on the pixel length of the track.

Semi-major axis

The semi-major axis can be used as a constraint for the admissible region, as developed by DeMars [10]. This constraint is obtained from his work and reproduced for this research. The specific orbital energy can be expressed as a function of the gravitational parameter of the planet and the semi-major axis, as can be seen in equation 2.51.

A given semi-major axis can be used to compute its corresponding specific orbital energy. Solving equation 2.43 with the specific orbital energy for the given semi-major axis will let you constrain the admissible region. Applying this constraint for a minimum and maximum semi-major axis constrain reduces the admissible region. A schematic representation of the semi-major axis constrained can be seen in figure 2.13 as the green lines.

$$\varepsilon = -\frac{\mu}{2a} \tag{2.51}$$

This research is focused on LEO satellites. The maximum semi-major axis for LEO satellites varies in the literature. For this research the maximum semi-major axis is set to 2000 km above the Earth surface [7]. The minimum semi-major axis is set to 250 km plus the Earth radius. At this distance satellites will de-orbit within

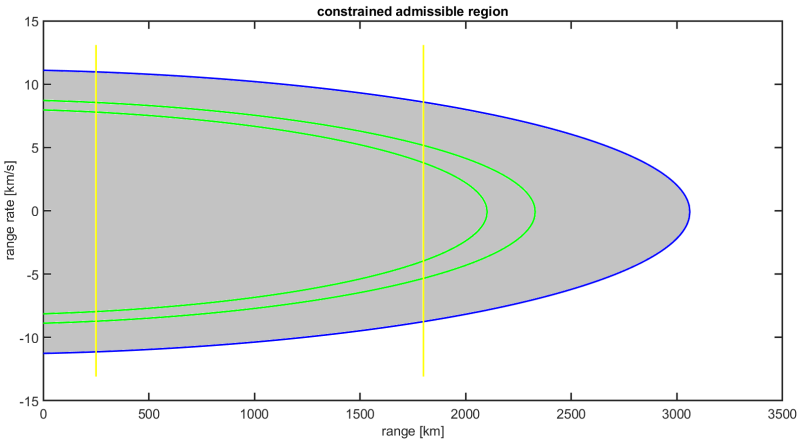

Figure 2.13: Schematic representation of the semi-major axis constraints (green lines) on the admissible region. Appendix B provide the data and graphs to reproduce this method.

a few days without active thrust. Resulting in a maximum semi-major axis of 8378 km and a minimum semi-major axis of 6628 km.

Eccentricity

The eccentricity can be used as another constraint for the admissible region, as developed by DeMars [11]. This constraint is obtained from his work and reproduced for this research. The eccentricity can be expressed as function of the specific orbital energy, specific angular momentum and the gravitational parameter, as can be seen in equation 2.52. To be able to use the eccentricity as a constraint the specific angular momentum needs to be expressed in terms of the known variables for an observation.

$$e = \sqrt{1 + \frac{2\epsilon||\mathbf{h}||^2}{\mu^2}} \tag{2.52}$$

where:

- e: eccentricity of the orbit
- h: specific angular momentum of the object

The specific angular momentum is defined as a function of the objects position and velocity, given by equation 2.53.

$$\mathbf{h} = \boldsymbol{r}_{obj} \times \mathbf{v}_{obj} \tag{2.53}$$

Defining the following vector parameters will enable the expression of the specific angular momentum in known variables.

$$\boldsymbol{h_1} = \boldsymbol{r}_{cam} \times \boldsymbol{u}_{\rho} \tag{2.54}$$

$$\boldsymbol{h_2} = \boldsymbol{u}_{\rho} \times (\dot{\alpha}\boldsymbol{u}_{\alpha} + \dot{\delta}\boldsymbol{u}\delta) \tag{2.55}$$

$$\boldsymbol{h_3} = \boldsymbol{u}_{\rho} \times \dot{\boldsymbol{v}}_{cam} + \boldsymbol{r}_{cam} \times (\dot{\alpha}\boldsymbol{u}_{\alpha} + \dot{\delta}\boldsymbol{u}_{\delta}) \tag{2.56}$$

$$\boldsymbol{h_4} = \boldsymbol{r}_{cam} \times \boldsymbol{v}_{cam} \tag{2.57}$$

Making use of the above vector parameters, the specific angular momentum can be rewritten to equation 2.58.

$$\boldsymbol{h} = \boldsymbol{h_1}\dot{\rho} + \boldsymbol{h_2}\rho^2 + \boldsymbol{h_3}\rho + \boldsymbol{h_4} \tag{2.58}$$

Defining the following parameters:

$$c_0 = \|\boldsymbol{h_1}\|^2 \tag{2.59}$$

$$c_1 = 2\boldsymbol{h_1} \cdot \boldsymbol{h_2} \tag{2.60}$$

$$c_2 = 2\boldsymbol{h_1} \cdot \boldsymbol{h_3} \tag{2.61}$$

$$c_3 = 2\boldsymbol{h_1} \cdot \boldsymbol{h_4} \tag{2.62}$$

$$c_4 = \|\boldsymbol{h_2}\|^2 \tag{2.63}$$

$$c_5 = 2\boldsymbol{h_2} \cdot \boldsymbol{h_3} \tag{2.64}$$

$$c_6 = 2\boldsymbol{h_2} \cdot \boldsymbol{h_4} + \|\boldsymbol{h_3}\|^2 \tag{2.65}$$

$$c_7 = 2\boldsymbol{h_3} \cdot \boldsymbol{h_4} \tag{2.66}$$

$$c_8 = \|\boldsymbol{h_4}\|^2 \tag{2.67}$$

By taking the square of the length of the specific angular momentum vector, from equation 2.58, equation 2.68 is found. This operation is required in order to be able to substitute this term in equation 2.52.

$$||\mathbf{h}||^2 = c_0\dot{\rho}^2 + P(\rho)\dot{\rho} + U(\rho) \tag{2.68}$$

where:

$$P(\rho) = c_1\rho^2 + c_2\rho + c_3 \tag{2.69}$$

$$U(\rho) = c_4\rho^4 + c_5\rho^3 + c_6\rho^2 + c_7\rho + c_8 \tag{2.70}$$

Substituting the expression for the specific angular momentum of equation 2.68 and the specific orbital energy of equation 2.41, rearranged, in equation 2.52 will result in a function where the range and range rate are the only two unknowns for a given eccentricity. Rearranging this relation will result in equation 2.71.

$$(\dot{\rho}^2 + w_1\dot{\rho} + f(\rho))(c_0\dot{\rho}^2 + p(\rho)\dot{\rho} + U(\rho)) = -\mu^2(1-e^2) \tag{2.71}$$

This expression can be re-written more clearly by defining the following scalar parameters:

$$a_4 = c_0 \tag{2.72}$$

$$a_3 = P(\rho) + c_0 w_1 \tag{2.73}$$

$$a_2 = U(\rho) + c_0 f(\rho) + w_1 P(\rho) \tag{2.74}$$

$$a_1 = f(\rho)P(\rho) + w_1 U(\rho) \tag{2.75}$$

$$a_0 = f(\rho)U(\rho) + \mu^2(1-e^2) \tag{2.76}$$

This results in equation 2.77.

$$a_4\dot{\rho}^4 + a_3\dot{\rho}^3 + a_2\dot{\rho} + a_1\dot{\rho} + a_0 = 0 \tag{2.77}$$

Solving this equation for a given eccentricity and range will result in four solutions for the range rate. The real solutions can then be used to add a constraint to the admissible region. A schematic representation of this constraint is shown in figure 2.14 with the red circle. The dark grey area in the middle is called the constrained admissible region which will be used to generate multiple hypotheses.

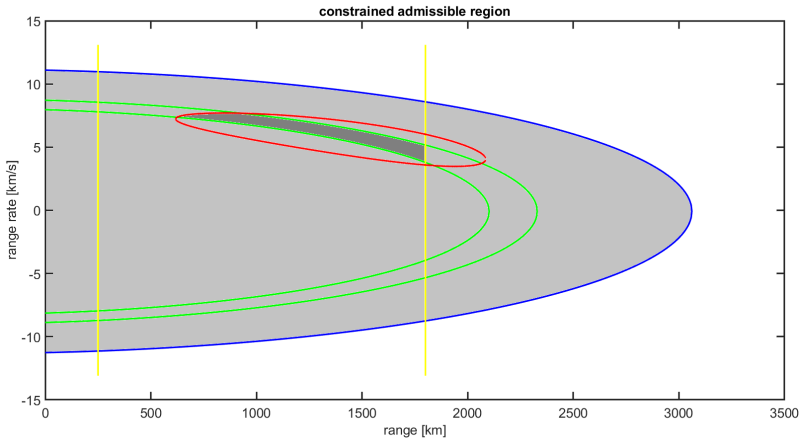

Figure 2.14: Schematic representation of the eccentricity constraint (red line) on the admissible region. The dark grey area represents the constrained admissible region, being constrained by the range, semi-major axis and eccentricity constrained. Appendix B provide the data and graphs to reproduce this method.

The eccentricity constraint will only be used to define a maximum eccentricity. This is due to the fact that there is no clear minimum eccentricity for LEO satellites. The TLE database is analysed with a tool written by Marco Langbroek called TLE extract[7] and from this analysis it is concluded that LEO satellites have an eccentricity ranging from 0 till 0.202. The constrained admissible region is constructed based on the measured angle values and approximated angle rate values, therefore a safety margin is used on the eccentricity constraint. The eccentricity constraint used in this work is set to 0.3 for LEO satellites.

2.4.3. Hypothesis selection

The constrained admissible region will be sampled by a grid overlay in order to define multiple hypotheses. These multitude will be filtered to determine the most accurate representation of the current state.

The sets of range and range rate values are determined by applying a grid over the admissible region where each grid point represents a range and range rate set. This in combination with the already known values from the observation result in a fully defined, hypothetical, state.

An example can be seen in figure 2.15, The blue dots in this image are the grid points. The grid is constructed between a minimum and maximum range limit, and a minimum and maximum range rate limit. The minimum range for the grid is determined by either the minimum range constraint or the smallest range value from the eccentricity constraint. Which of the two is the largest is used as the minimum grid value. The maximum grid range value is determined by either the maximum range constraint, maximum range value of the eccentricity constraint, or the maximum range value of the semi-major axis constraint. Which of the three is the smallest is used as the maximum range value of the grid. This can be seen in figure 2.15, where the lower range limit is determined by the eccentricity constraint and the upper range limit by the semi-major axis constraint.

The range rate limits are determined by the eccentricity constraint. The maximum range rate value of the eccentricity constraint is used for the maximum limit for the grid in the range rate axis. The minimum value

[7] `https://langbrom.home.xs4all.nl/software.html`, accessed at 13-03-2021

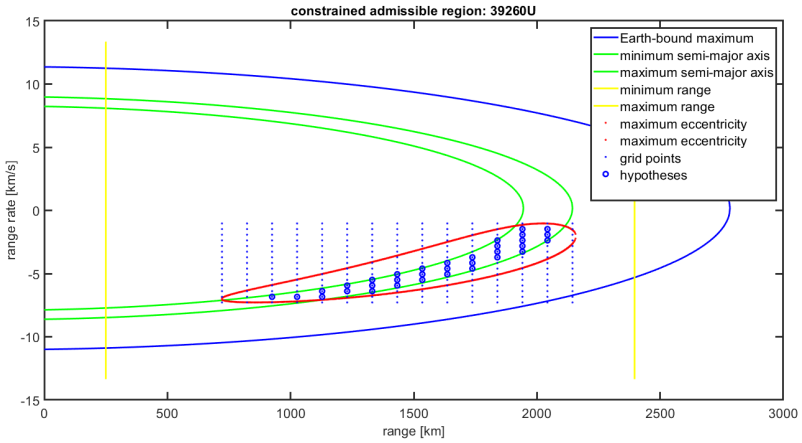

Figure 2.15: Illustration of the grid overlay of size 15 on the admissible region. the blue line is the admissible region, the yellow line represents the range constraints, the green line is the semi-major axis constraints and the red line is the eccentricity constraint. Th blue dots illustrate the grid points, where the circled blue dots are within the constrained admissible region and comply with all the given constraints. Appendix B provide the data and graphs to reproduce this method.

of the eccentricity constraint is used for the minimum limit for the grid in the range rate axis. With these four limits a grid overlay is created as seen in figure 2.15. The grid size in this example is set to a grid of 15 by 15. This example is an illustration to describe the process, appendix B shows six examples that can be reproduced.

Each grid point (blue point) that complies with the range, semi-major axis and eccentricity constraints will be flagged as a valid hypothesis and are represented with the blue dots that are circled with the blue circle. Each set of range and range rate, in combination with the angle and the angle rates, are converted to the J2000-inertial reference frame in Cartesian coordinates. Equation 2.39 and 2.40 are used to perform this transformation. This state makes it possible to calculate forces acting on the object when propagation is required.

The grid size is a tuning variable. The larger the grid size the more valid hypotheses will be obtained, and the closer the initial hypothesis can be to the correct solution. It will also increase the computational cost of both the CAR algorithm, but more importantly the MHF.

For this research a study was performed to find the optimal grid size. Four satellites were propagated for a single observation arc. It shows the number of hypotheses that where generated, the number of data points needed to convert to a single solution, the position and velocity error at the conversion point, the position and velocity error at the end of the observation arc, the computation time and the a bolean to show if the method converted to a single hypothesis at the end of the observation arc. This analysis is performed for a grid size of 5, 10, 15, 20 and 25 points. The data is shown in appendix A

The average values of the four satellites are given in table 2.3. This shows that there is a significant decrease in position and velocity error for both at the conversion point and at the and of the observation arc. The grid size between 10 and 25 do not show any significant decrease in these errors, but do show a steady increase in computation time. It is also remarkable that satellite 6257U, with only 28 data points is not able to converge to a single hypothesis for a grid size of 10 and larger. In the result section a closer look will taken at the applicability of the method, to determine the average number of data points in order to find a single solution out of the CAR-MHF method. As expected does the number of hypotheses increase for larger grid sizes. More hypotheses also mean an increase in number of observations is required to converge to a single solution.

Based on table 2.3, supported by appendix A, this research will be using a grid size of 10, because this gives the best accuracy over computation relation. Also there is no significant increase in accuracy for larger grid size. So even if computation time was not one of the trade-off variables, there would not be a significant reason to use larger grid sizes.

Table 2.3: Average values from the grid size analysis for grid sizes between 5 and 25, for four different satellites

Grid size	5	10	15	20	25
hypotheses	5.00	24.00	58.25	115.67	186.67
epochs to conversion	9.25	28.33	35.33	42.67	41.00
At conversion point					
Position error [km]	22.41	0.88	0.97	0.43	1.20
Velocity error [m/s]	52.89	3.84	2.61	0.81	1.80
At end of arc					
Position error [km]	7.27	0.82	0.77	0.46	1.18
Velocity error [m/s]	5.88	1.27	1.09	0.84	1.84
Time [second]	8.48	42.81	103.81	203.33	425.00

2.5. Multiple hypotheses filter

The multiple hypotheses filter starts with the valid hypotheses expressed in Cartesian coordinates in the J2000-inertial reference frame that resulted from the CAR algorithm. Each hypothesis is improved on by the Extended Kalman Filter (EKF), discussed in section 2.5.1. The worst performing hypotheses are eliminated until there is only one hypothesis remaining or multiple hypotheses converged to a single solution, which should be the best approximation of the true state of the object. The criterion used for the elimination are discussed in section 2.5.2. The last hypothesis remaining is considered the initial orbit determination solution. If after converging more data is available, the EKF acts as a Orbit Determination algorithm to improve the IOD solution with the extra data.

The multiple hypotheses filter is based on the work of DeMars [10], to be more specific, the constrained admissible region. Yet, the method differs more significantly for the multiple hypotheses filter. The main two differences are as follows. The data set is already known to belong to the same satellite and, consequential to the type of data set used, the elimination criterion is redefined for this application of the CAR-MHF [9]. The second difference is the use of the Extended Kalman Filter instead of the Unscented Kalman Filter (UKF) used by DeMars.

The CAR-MHF developed by DeMars [10] and tested by Kelecy [17] on simulated LEO objects, does not require all observations to belong to a single object. The Nearest Neighbour is used to determine the data correlation. When multiple measurements correlate to an object, the Probabilistic Data Association is used. This method weights the measurements with the probability that the measurement correlates to the object. This weighting factor is then used to update the Kalman filter for each of the measurements. This part of the algorithm is omitted, firstly, since the IPA already groups the measurements per object. Secondly, the focus of this research is the applicability of the CAR-MHF on real observations in order to access the stability and accuracy, therefore keeping other sources of uncertainty to a minimum.

The CAR-MHF for this research uses the EKF instead of the UKF, as proposed by DeMars [10]. A literature study, preceding this research showed that the EKF showed similar performance compared to the UKF, while having a lower computation cost [26].

2.5.1. Extended Kalman filter

The EKF will be set-up for each hypothesis following from the CAR. Each hypothesis is an initial state of the Kalman filter and will follow the steps of the EKF for each measurement until eliminated or a being the only hypothesis remaining. The initial state is given by a state vector, as can be seen in equation 2.78

$$\boldsymbol{X} = \begin{bmatrix} x \\ y \\ z \\ \dot{x} \\ \dot{y} \\ \dot{z} \end{bmatrix} \tag{2.78}$$

The EKF is an algorithm to improve a state by using weighted measurements. The weight of the measurement is based on the uncertainty of the measurement and the uncertainty of the initial state. When the measurements have a high uncertainty, the state will only be adjusted slightly, since the measurements are not reliable.

The Kalman filter starts with an initial state of an object and its uncertainty, the covariance matrix. In this research, the initial state of the satellite is expressed in position and velocity components expressed in Cartesian coordinates with an unknown uncertainty. The initial uncertainty is based on the initial hypotheses generated from the CAR. The set of hypotheses show a spread for each of the elements of the state vector. The maximum possible uncertainty of each element of the state vector is the maximum value minus the minimum value, found in the set of hypotheses. For example, all hypotheses have a value for the x-position. Taking the maximum and minimum value of this sub-set and subtracting hem from each other results in the maximum uncertainty. This will be used as the initial uncertainty for the x-position. This initial uncertainty matrix will be updated when measurements are processed to a more accurate value.

The Kalman filter moves from one epoch to another, where at each epoch the following two steps are performed: predicting the state and correcting the prediction based on the measurement at set epoch. The Kalman filter operates with respect to a reference orbit around which the dynamics are linearised. The Taylor series expansion is used for the linearisation.

The reference orbit is defined based on the initial state at the previous epoch, given as $\boldsymbol{X}_A$. This initial state is then integrated with the Runge-Kutta-Fehlberg 4(5) to the current epoch, given as $\boldsymbol{X}_B$. The given state vectors and the covariance matrices used in this research has a specific notation. In order to explain this notation the state vector, $X_{(a)|(b)}$, will be used as an example. The (a) represents the time indication, where $(i-1)$ refers to the state at the previous epoch, and (i) refers to the state at the current epoch. The (b) indicates if it the predicted state without correction, $(i-1)$, or the predicted state with correction based on observations (i). So $X_{(i)|(i-1)}$ is the predicted state vector at the current epoch before the state vector is corrected with the information from the observations.

The state input going into the Kalman filter is the state at the current epoch given as $\boldsymbol{X}_{(i-1)|(i-1)}$. The next step is the prediction step, given in 2.79. The state is predicted based on the current state, the time between the two epochs, and the orbital mechanics. The state is propagated with the RKF4(5) integrator, taking the spherical Earth, J2, J3, and J4 effects into account, as discussed in section 2.1.3. The RKF4(5) is a variable step size integrator, therefore the propagation can be performed in multiple time steps in order to minimise propagation errors, based on the given tolerances.

$$\boldsymbol{X}_{(i)|(i-1)} = f(\boldsymbol{X}_{(i-1)|(i-1)}, \Delta t) \tag{2.79}$$

The prediction step can also be performed by the use of a state transition matrix, given in equation 2.80. This matrix makes a linear approximation for the dynamics at an initial state. This makes it possible to approximate the next state at the next epoch for small time steps. Due to the linearization of the dynamics, the error will increase for larger time steps.

$$\phi(\boldsymbol{X}_{(i-1)|(i-1)}) = I(6x6) + F(\boldsymbol{X}_{(i-1)|(i-1)})\Delta t \tag{2.80}$$

where $F(\boldsymbol{X}_A)$ is the Jacobian of the time derivative of the state vector evaluated at the reference orbit at the previous epoch. The Jacobian is given by equation 2.81

$$F(\boldsymbol{X}_{(i-1)|(i-1)}) \approx \frac{\partial \dot{\boldsymbol{X}}}{\partial \boldsymbol{X}} = \begin{bmatrix} \frac{\partial \dot{x}}{\partial x} & \frac{\partial \dot{x}}{\partial y} & \frac{\partial \dot{x}}{\partial z} & \frac{\partial \dot{x}}{\partial \dot{x}} & \frac{\partial \dot{x}}{\partial \dot{y}} & \frac{\partial \dot{x}}{\partial \dot{z}} \\ \frac{\partial \dot{y}}{\partial x} & \ddots & & & & \vdots \\ \frac{\partial \dot{z}}{\partial x} & & \ddots & & & \vdots \\ \frac{\partial \ddot{x}}{\partial x} & & & \ddots & & \vdots \\ \frac{\partial \ddot{y}}{\partial x} & & & & \ddots & \vdots \\ \frac{\partial \ddot{z}}{\partial x} & \cdots & \cdots & \cdots & \cdots & \frac{\partial \ddot{z}}{\partial \dot{z}} \end{bmatrix} \tag{2.81}$$

where $\dot{x}, \dot{y}$, and $\dot{z}$ follow from the state vector, given in equation 2.78 and $\ddot{x}$, $\ddot{y}$, and $\ddot{z}$, are given in equations 2.18, 2.19, and 2.20, respectively. Due to the complex nature of the derivatives they are computed using a computer program and copied in to the code to prevent typing errors.

Due to the large time step between two observation arcs, the state transition matrix is not able to linearly propagate from one observation arc to the next observation arc. This would result in large linearisation errors since the time between observation arcs is in the magnitude of hours till days. The RKF4(5), with its variable step size integrator, should be able to propagate over these large times steps. This is due to the fact that this integrator splits these large time steps up in smaller time steps, preventing linearisation errors due to large time steps. For this reason the state propagation step, as seen in equation 2.79, is performed with the RKF4(5) integrator.

The state transition matrix is further on used to propagate the covariance matrix, in equation 2.89. The earlier described linearisation error would also apply when the covariance matrix is propagated with these large time steps and is an effect that will be discussed in detail in the validation, in section 3.3.2, the validation of the EKF.

A predicted measurement needs to be calculated next. The measurements angles, right ascension and declination need to be expressed in terms of elements of the state vector. These relations are shown in equation 2.82 and 2.83, respectively. In the program the *atan2* function of Matlab is used to correctly take the quadrants into account.

$$\alpha = \arctan(\frac{y}{x}) \tag{2.82}$$

$$\delta = \arcsin(\frac{z}{\sqrt{x^2+y^2+z^2}}) \tag{2.83}$$

With these expressions it is possible to calculate the Jacobian for the measurement, which is given by equation 2.84

$$H(\boldsymbol{X}_A) = \begin{bmatrix} \frac{\partial \alpha}{\partial x} & \frac{\partial \alpha}{\partial y} & \frac{\partial \alpha}{\partial z} & \frac{\partial \alpha}{\partial \dot{x}} & \frac{\partial \alpha}{\partial \dot{y}} & \frac{\partial \alpha}{\partial \dot{z}} \\ \frac{\partial \delta}{\partial x} & \frac{\partial \delta}{\partial y} & \frac{\partial \delta}{\partial z} & \frac{\partial \delta}{\partial \dot{x}} & \frac{\partial \delta}{\partial \dot{y}} & \frac{\partial \delta}{\partial \dot{z}} \end{bmatrix} \tag{2.84}$$

From equation 2.84 two derivations are expanded and shown in equation 2.85 and 2.86.

$$\frac{\partial \alpha}{\partial x} = -\frac{y}{x^2+y^2} \tag{2.85}$$

$$\frac{\partial \delta}{\partial x} = -\frac{xz}{\sqrt{\frac{x^2+y^2}{x^2+y^2+z^2}}(x^2+y^2+z^2)^{\frac{3}{2}}} \tag{2.86}$$

The Jacobian for the measurements are used in equation 2.87

$$\boldsymbol{Z}_{(i)|(i-1)} = H(\boldsymbol{X}_{(i)|(i-1)})\boldsymbol{X}_{(i)|(i-1)} \tag{2.87}$$

to determine the predicted (or expected) measurement, which can then be compared to the measurement which is observed. The equation for subtracting the observed and predicted measurement is given in equation 2.88, where $\boldsymbol{Z}_m$, is the measured right ascension and declination in vector form.

$$\Delta \boldsymbol{Y}(i) = \boldsymbol{Z}_m - \boldsymbol{Z}_{(i)|(i-1)} \tag{2.88}$$

The difference between the observed and predicted measurement is known, and now the weight at which the Kalman filter takes this in to account, the Kalman gain, needs to be determined. This is based on the uncertainty of the initial state and the uncertainty of the measurement.

The state covariance matrix is updated based on the state transition matrix, as shown in equation 2.89. This is also an intrinsic inaccuracy of this method. The state transition matrix uses linearised dynamics to be able to propagate a state from one epoch to another. This linearisation assumption is only valid for small time steps. This is also the reason why the state transition matrix is not used to propagate the state for this implementation of the EKF. But the state transition matrix is an intrinsic element of this method, and is necessary to propagate the covariance matrix. With increased time steps the propagation error for the covariance matrix will increase, which could lead to instabilities. This phenomena will be further elaborated on in the rest of the research.

$$P_{(i)|(i-1)} = \phi(\boldsymbol{X}_{(i-1)|(i-1)}) P_{(i-1)|(i-1)} \phi^T(\boldsymbol{X}_{(i-1)|(i-1)}) + Q \tag{2.89}$$

where Q represents the dynamical model uncertainty, since the dynamical model is not a perfect representation of the real world dynamics. $P_{(i-1)|(i-1)}$ is the state covariance matrix at the current epoch and $P_{(i)|(i-1)}$ is the propagated covariance matrix to the next epoch, yet before correcting with the observation at the next epoch.

Adding the dynamical model uncertainty prevents the state uncertainty to become so small that the Kalman filter does not respond to new input. The model uncertainty is based on the difference between the dynamical model used to the propagation, as given in equation 2.79, and the SGP4 orbits. Orbits based on the SGP4 theory are most accurate orbit data currently available for this research.

The dynamic model uncertainty varies for different time steps due to increased propagation errors over longer propagation periods. In order to access this behaviour four satellites are propagated for 13 different time step sizes. Between 6.4 seconds and 7.3 hours, where each different time, the step size is doubled. In order to have a accurate representation, each satellite is propagated from a random time, between the third of January 2020 00:00:00 and the ninth of January 2020 00:00:00 in order to have a wide range of different starting conditions. The Matlab 2018 uniform random number generator with seed 404 is used. A six day period is used because on average a TLE is updated once or twice per week[8]. Per time step, per satellite, 500 propagation are performed. For each propagation, the difference between the propagated state and the SGP4 is calculated. Four times 500 samples are sufficient data points to have an indication of the model uncertainty.

Four satellites, 6257U, 37347U, 38771U, and 10793U, are propagated with the latest known TLE at that time. with the RKF4(5) theory, the same integrator as used in the Kalman filter. These four satellite where selected due to their difference in eccentricity, semi-major axis and inclination, as can be seen in table 2.4. These satellites with these orbital elements are selected to analyse a wide range of different orbits.

Table 2.4: Input values for the RKF4(5) validation. Satellite 37347U, 10793U, 62557U and 38771U shown the initial state at the beginning of the propagation on 03-01-2020 00:00:00, general orbital parameters and the radar cross section.

Satellite	37347U	10793U	6257U	38771U
Inclination [deg]	50.3	28.2	81.3	98.7
semi-major axis [km]	8078	7618	7249	7198
Perigee [km]	299.1	575.0	836.2	826.1
Eccentricity	0.17	0.088	0.0058	0.00020
RCS [m^2]	3.8	9.4	6.6	15.5

[8] `http://celestrak.com/columns/v04n05/`, accessed at 28-04-2022

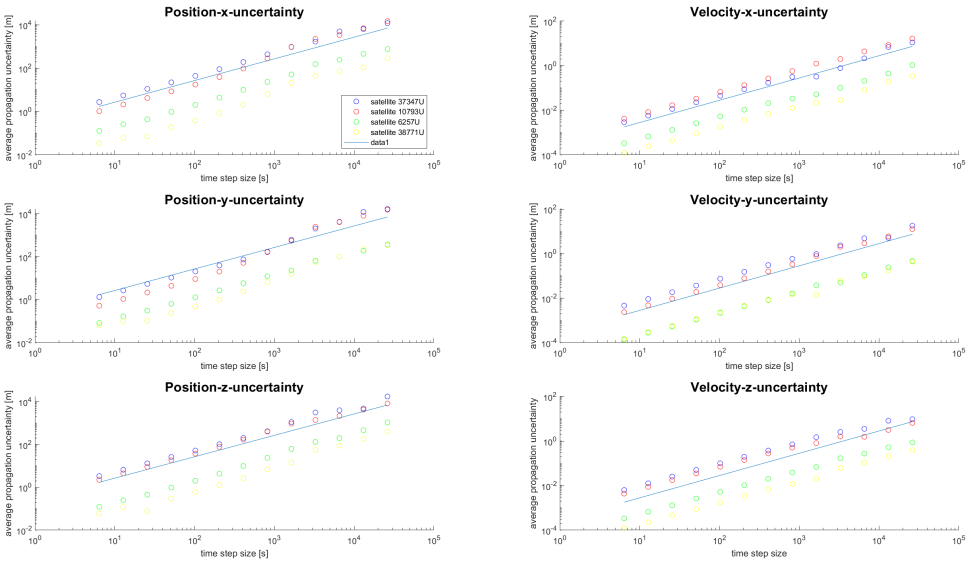

Figure 2.16: Model uncertainty shown for different time steps, based on the average error out of 500 random simulations, per satellite, per time step. The four different satellites are shown by the coloured circles. The blue line represents the rough trend of the resulting model uncertainty

The difference between the SGP4 orbit and the RKF4(5) orbit is calculated for different step sizes. Figure 2.16 shows that the difference increases linear with the time steps. Taking the average value of the four satellites, for each time step size, and fit a linear relation of the general form $y = a \cdot x$ though these values result in a estimated model uncertainty dependent on the propagation step size. The position and velocity model uncertainty is given in equation 2.90 and 2.91, respectively.

$$Q_{position} = 0.27 \cdot \Delta t \tag{2.90}$$

$$Q_{velocity} = 0.28 \cdot 10^{-3} \Delta t \tag{2.91}$$

The model uncertainty of satellite 37347U and 10793U are one to two orders of magnitude larger then the other two satellites. During the validation of the RKF4(5) method, discussed in section 3.3.1, a closer look will be given in the difference in order of magnitude.

The model uncertainty covariance is given by equation 2.92 and will be used to determine the Kalman gain. The model uncertainty takes both the uncertainty of the state (state covariance matrix) and the uncertainty of the measurement into account.

$$S(i) = H(\boldsymbol{X}_{(i)|(i-1)}) P_{(i)|(i-1)} H(\boldsymbol{X}_{(i)|(i-1)})^T + R \tag{2.92}$$

Where R is the measurement uncertainty, normally given by the uncertainty of the measurement device. In this research the measurement uncertainty is determined statistically when using the end of track points as observations. For the right ascension en declination the difference between the SGP4 solution and the end of track is taken. Both are given in the data format file resulting from the IPA algorithm. This analysis is performed all observation of the available LEO satellites. Based on the standard deviation for these angles, a fixed measurement uncertainty R is set for all applications.

22541 Measurements were analysed, where the SGP4 based sky-position was determined at the epoch of the each measurement. The difference between the SGP4 based sky position and the measured sky position is taken. From these 22541 measurements it was found that for both the right ascension and declination difference, the mean is less then 0.01 degree. Based on these same difference it was found that the standard

deviation for the right ascension is 0.15 degrees and the standard deviation for the declination is 0.05 degrees. These numbers indicate the accuracy for observations made using the optical based measurements in combination with the developed software to determine the sky position. The indication for the accuracy of the measurements is then used for all observation by applying these values as measurement uncertainty. These measurement uncertainty as applied in the EKF is given in equation 2.93.

$$R = \begin{bmatrix} 0.15^2 & 0 \\ 0 & 0.05^2 \end{bmatrix} \tag{2.93}$$

Where R stands for the measurement uncertainty matrix, with individual measurement uncertainties are given on the diagonal.

When the SGP4 based observations are used the measurement uncertainty is set to 10^{-8} degrees. In this case the observations are equal to the true solution, the SGP4 solution, and the uncertainty is zero. In order to preserve the behaviour of the EKF it was chosen to set the measurement uncertainty to a low value. This way the behaviour of the EKF can still be observed when analysing SGP4 measurements as input.

The Kalman gain weighs the uncertainty of the initial state (state covariance matrix) in combination with the model uncertainty. Equation 2.94 shows the relation for the Kalman gain.

$$K(i) = P_{(i)|(i-1)} H(\boldsymbol{X}_{(i)|(i-1)}) S(i)^{-1} \tag{2.94}$$

With the Kalman gain and the difference between the predicted and measured observation angles, given in equation 2.88 it is possible to correct the predicted state based on the measurement. The expression for this is given in equation 2.95

$$\boldsymbol{X}_{(i)|(i)} = \boldsymbol{X}_{(i)|(i-1)} + K(i)\Delta\boldsymbol{Y} \tag{2.95}$$

The corresponding state uncertainty also needs to be updated based on the new measurement. This is given in equation 2.96.

$$P_{(i)|(i)} = [I - K(i)H(\boldsymbol{X}_A)]P_{(i)|(i-1)} \tag{2.96}$$

Through these steps the Kalman filter is looped for each epoch. After each epoch the elimination criteria is checked to determine if a hypothesis needs to be eliminated. This will be discussed in the next section.

2.5.2. Elimination criterion

The elimination criterion determines when a hypothesis needs to be eliminated. In literature of DeMars et al. 2012, about the CAR-MHF, it is not clearly stated how the elimination criterion is defined. Therefore part of this research was to define and test and an elimination criterion. The design and testing of the elimination criterion is discussed in this section.

The elimination criterion is based on the residual of the hypothesis, the Mahalanobis distance. The relation for calculating the residual, $d^2(i)$, is given in equation 2.97. The residual is dependent on the measurement covariance and the difference between the predicted measurement and the true measurement.

$$d_i^2 = \Delta Y_i^T S_i^{-1} \Delta Y_i \tag{2.97}$$

The general concept of the developed elimination criterion is: if the residual of the hypothesis is larger then the mean residual value of all other hypotheses, then the hypothesis is eliminated.

Each observation used for the CAR-MHF has a measurement error. For this reason the elimination criterion can convert to the incorrect hypothesis if there is a large error in a single observation. To counter this an average residual will be used, whereby the average of the residuals of the last n epochs need to be larger then the average residual of all other hypotheses of the last n epochs. For a given hypothesis, i_a, the relation is shown in equation 2.98. The number of data points, n, for which this average will later be determined.

$$\frac{\sum_{j-n}^{j} d_{i_a,j}^2}{n} > \frac{\sum_{1}^{i}\sum_{j-n}^{j} d_{i,j}^2}{n(i-1)} for\ i \neq i_a \tag{2.98}$$

where:

- i: number of hypothesis
- i_a: The current hypothesis, a, that is being evaluated.
- j: Epoch number

The testing and validation of the elimination criteria will be discussed in the validation, in section 3.3.3.

2.5.3. Summary of the CAR-MHF

The CAR-MHF is an angle-only initial orbit determination algorithm. The algorithm starts with 3 consecutive observations from which the angle rates are determined by interpolation with a second order polynomial. With the observed angles and the angle rates at the second observation it is possible to construct the admissible region. This is a region in the range vs. range-rate domain and is constructed by the physical limitation that the observed satellite is orbiting the Earth, a maximum and minimum semi-major axis, and a maximum eccentricity, following the theory as described by DeMars et al. 2012[10]. These constraints are set for all satellites expected in the LEO regime. The minimum and maximum range are additional two constraints, introduced by myself, where the maximum range is based on the length of observed track, for which a statistical relation has been found in this research. The area in the range vs. range-rate domain that complies with all the constraints is called the admissible region. In this region a set of range and range-rate values are selected. For each set of range and range rate values, together with the already established angle and angle-rate values, a state vector can be constructed, which is called a hypothesis.

For each hypothesis an Extended Kalman Filter is constructed, which will start with an initial state, the hypothesis, at the second observation, the second epoch. The EKF will improve the state of each hypothesis with consecutive observations starting at the third epoch. In order to eliminate hypotheses, an elimination criterion is created. This elimination criterion eliminates a hypothesis when the residual of the hypothesis is larger then the residual of all other hypotheses. The set of EKF's will continue with propagating each state until a single hypothesis remains. This process is called the initial orbit determination for the CAR-MHF. After convergence to a single solution the method automatically continues as a orbit determination algorithm, where the state is improved with for each epoch where data available is.

2.6. Statistical analysis of the observed satellites

The statistical analysis of the observed satellites focuses on the observed satellite and the conditions under which they are observed. First, the radar cross section for the satellites is discussed. Secondly, the orbital elements, semi-major axis, eccentricity, and inclination for the observed satellites are discussed in section 2.6.3.

2.6.1. Analysis of RCS, brightness and phase angle

This section discusses the different parameters that can influence the apparent magnitude of a satellite. The parameters in this research contain the Radar Cross Section (RCS) and the phase angle. In this research it is investigated what the favourable combination of these parameters for the brightest observations of satellites. Hereby the RCS of the observed satellite is analyses, which will also result an indication of the size of satellites observed by a set-up used for this research. The phase-angle is determined to find out if there is relation between the phase angle and the brightness of the satellite. Finally, the method used to determine the apparent magnitude of the satellite track is discussed.

2.6.2. Radar cross section

The Radar Cross Section (RCS) is an indication for the surface area of a satellite. Currently CSpOC publishes the RCS for most tracked satellites in three categories, small, medium, and large. The categories are shown in table 2.5. This information is used to determine the size of satellites that are detected with the current set-up.

Table 2.5: The radar cross sections categories as published by CSpOC

RCS size range (m^2)	Categories
RCS <0.1	Small
0.1 <RCS <1.0	Medium
1.0 <RCS	Large

Up to May 24, 2017, the CSpOC did not use the categories indications for the radar cross sections, but used a determined radar cross section. Dr. M. Langbroek, a consultant for the FOTOS2 work group helped with finding this catalogues. This catalogues shows the NORAD satellite ID number, the mean radar cross section and the number of observations on which the mean radar cross section was determined [9]. Satellites which are observed and were already in orbit before May 24, 2017 can be used to perform a more detailed analysis of the RCS of the observed satellites.

Phase angle

The phase angle is the angle from the sun, to the satellite, to the camera. A schematic representation is given in figure 2.17. To determine the phase angle, it is assumed that angle b is approximately zero. This is due to the fact that the distance from the camera to the satellite is multiple magnitudes smaller the distance from the camera to the sun. Angle a can be calculated based on the TLE position of the satellite and the position of the sun can be obtained from an ephemeris. The phase angle can be calculated with equation 2.99, which is derived from basic geometry.

$$c_{phase-angle} = 180 - a \tag{2.99}$$

The phase angle is calculated in this research in order to find out if there is a desired phase angle at which satellite can be observed more favourable.

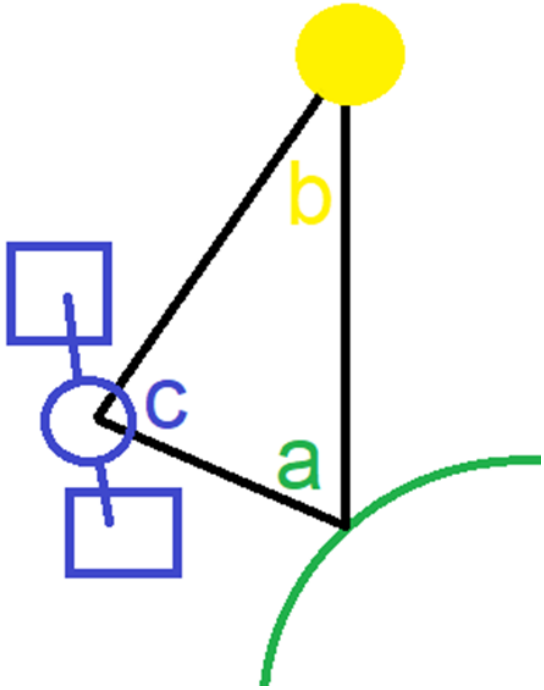

Figure 2.17: Schematic representation of the phase angle. The green circle represents %the camera position on Earth, where the angle satellite-camera-sun is angle a. The yellow dot represents the sun, where the angle satellite-sun-camera is angle b. The lines represent the satellite, where the angle camera-satellite-sun is angle c.

[9] `https://www.prismnet.com/~mmccants/catalogs/index.html`, *acceded at: 19-08-2020*

Apparent magnitude of the satellite track

The IPA algorithm also contains a function to approximate the apparent magnitude of the satellite track based on the stars in the image as a reference. The pixel values of the satellite track are added together to determine the absolute satellite flux. The average background pixel value times the number of pixels that make up the satellite track is subtracted from the absolute satellite flux. This will result in the relative satellite flux, which will then be expressed as a logarithmic value with a 10 base.

The apparent magnitude of the satellite track can be calculated with the reference values of the stars. The flux and apparent magnitude of the stars that can be seen in the same image are obtained from a star catalogue. The relation between the flux and the apparent magnitude for this research is given in equation 2.100.

$$m = -2.5 f_{flux} + b_{fit} \tag{2.100}$$

where:

- m: apparent magnitude
- f_{flux}: relative flux
- b_{fit}: curve fit tuning variable

The b_{fit} is obtained by fitting the flux and magnitude of the observed stars. With this equation and the flux of the satellite track, the apparent magnitude of the satellite track can be calculated.

2.6.3. Analysis of the orbital elements

Each camera used in this research has its own location and/or direction in which it is pointed. For this reason an analysis is performed of the type of orbits that are observed for the different cameras. The semi-major axis, eccentricity, and inclination will be analysed when distinguishing the differences in orbits. These orbital elements are most significant for the general characteristics and shape of the orbit. The other three orbital elements only describe the orientation of the orbit. These orbital elements will be obtained from the TLE of the observed satellite.

3

Algorithm and validation

The algorithm and validation chapter discusses the algorithms used in this research, based on the theory presented in the methodology, chapter 2. These algorithms needs to be validated in order to produce reliable results. The frame transformations are validated in section 3.1. The constrained admissible region algorithm is validated in section 3.2. Finally, the Multiple hypotheses filter is verified and validated in section 3.3.

3.1. Frame transformations

All inputs used during this research need to be in the same reference frame in order to be able to add and subtract state vectors from each other. The camera position, satellite observations, and the SGP4 reference all need to be in the J2000 reference frame. The required conversions will be discussed here, and then validated.

3.1.1. Camera Position

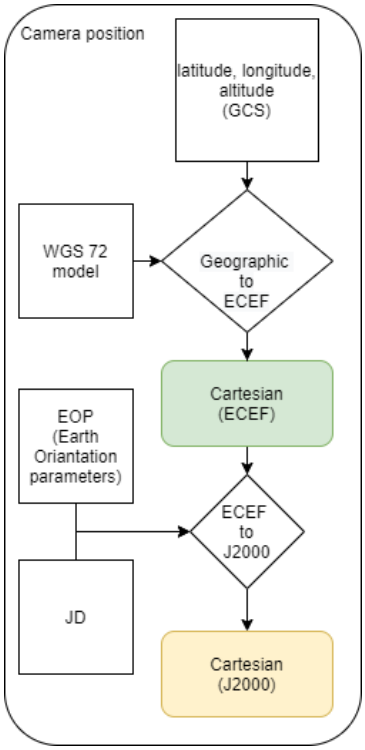

Figure 3.1: Camera position frame transformations, where the squares represents inputs, the diamonds represents operations, and the rounded squares represents outputs. Green is marked for the ECEF reference frame and yellow for the J2000 reference frame

The camera position is given in latitude, longitude and altitude, which is called the geographic coordinates in

the ECEF reference frame. First the geographic coordinates need to be transformed to Cartesian coordinates in the ECEF reference frame. Second, the ECEF reference frame is transformed to the J2000 reference frame. A schematic representation of this process is given in figure 3.1. The squares represents inputs, the diamonds represents operations, and the rounded squares represents outputs. Green is marked for the ECEF reference frame and yellow for the J2000 reference frame.

Geographic to Cartesian coordinate system validation

The transformation from the Geographic coordinate system to the ECEF reference frame is a single equation, shown in the methodology in equation 2.4. The validation is performed by testing generic scenarios. For this validation four scenario's were tested, given in table 3.1. The radius of the Earth is set to 6378,135.0 km and the Earth flattening is set to one over 298.26, according the WGS 72 Earth model.

Table 3.1: Geographic coordinate system to ECEF Cartesian coordinate system validation scenario's

Scenario	Latitude [degrees]	Longitude [degrees]	Altitude [km]
1	0	0	0
2	0	270	0
3	45	0	0
4	0	0	1000

Due to the use of the generic testing cases the expected answers can be deduced by logic. With a zero latitude, the Earth flattening factor has no effect on the outcome. Setting the Longitude and latitude both to zero would result in only a x-axis component in the ECEF reference frame. This is due to the fact that the zero longitude points towards the prime meridian, which is also the x-axis direction in the ECEF reference frame. A latitude of zero also means the point is on the equator, therefore it is in the x-y plane of the ECEF reference frame. For this reason the first scenario should result in only an x component and should be equal to the radius of the Earth.

Scenario 2 differs from scenario 1 by a rotation around the z-axis by 270 degrees. Due to this, the solution should still be in the x-y plane and therefore the z-component in the ECEF reference frame is expected to be zero. Due to the rotation of 270 degrees the x-component is expected to be zero and the y-component is expected to the minus the Earth radius.

Scenario 3 differs from scenario 1 by a rotation around the y-axis by 45 degrees. Due to this rotation the solution should be in the x-z plane, therefore the y-component of the ECEF coordinate system is expected to be zero. For a spherical Earth the x & y-component are equal to the Earth's radius divided by the square-root of two. However due to the flattening of the Earth, the radius towards the equator is expected to be larger then the radius towards the poles. Equation 2.4, with the flatting factor in the equation, was used to calculate by hand, to determine the validation values. The results from Matlab and the hand calculations are the same. Also as expected the x-component is larger then the z-component due to the flattening of the Earth.

Scenario 4 differs from scenario 1 by an additional altitude of 1000 km. Therefore the y & z component should still be zero and the x-component should be the radius of the Earth plus a 1000 km.

The expected results and the results from the algorithm are shown in table 3.2. The validation values are obtained by calculating the geometry by hand.

Table 3.2: Validation results for four generic situations for the geographic coordinate system to the Cartesian coordinate system for an ECEF reference frame. The validation values are the expected results and the algorithm values are the outcome from the algorithm used

	Validation values			Algorithm values		
Scenario	x [km]	y [km]	z [km]	x [km]	y [km]	z [km]
1	6378.135	0	0	6378.135	0	0
2	0	-6378.135	0	$-1\cdot10^{-12}$	-6378.135	0
3	4517.591	0	4487.348	4517.591	0	4487.348
4	7378.135	0	0	7378.135	0	0

The validation results show almost the same values for all expect the x-value for scenario 2. This error is assumed to be a truncation error and is small enough to neglect.

It is concluded that the coordinate transformation from geographic to Cartesian is working as intended and is therefore validated. As an extra check a full chain test for frame transformations, discussed in section 3.1.4, will be performed to also verify for non-generic scenarios.

ECEF to J2000 reference frame transformation

The ECEF to J2000 reference frame transformation is based on the time, given in Julian Days, at which the state vector is observed, and the Earth orientation at that time. The Earth Orientation Parameter [2] are published by the International Earth Rotation and Reference Systems Service for every Julian day.

The frame transformation will be validated with two test cases. The first test case consists of an example from the fundamentals of astrodynamics and applications by D.A. Vallado [30]. The second test case results from in-house software of the TU Delft, written by Ir R. Noomen, assistant professor at the TU Delft. Dr. Ir. E.J.O. Schrama provided me with the transformation matrix, generated from this software, in order to perform the validation step.

The first test case is given for April 6, 1994 07:51:28.788 for the position and velocity in the ECEF reference frame given in table 3.3. The validation values are obtained from example 1-6, from the fundamentals of astrodynamics and applications textbook, by D.A. Vallado [30]. The first edition of the textbook contains the incorrect values of the example, therefore the correct values for this test case have been obtained from the errata listing for First Edition, table 1-6 [31].

Table 3.3: Validation results for the ECEF to J200 reference frame transformation for the first test case

	Position			Velocity		
	x [km]	y [km]	z [km]	x [km/s]	y [km/s]	z [km/s]
ECEF Coordinates	-1120.36796	7894.51292	6374.08086	-3.18709	-2.90517	5.53765
J2000 Validation values [31]	5102.50960	6123.01152	6378.13630	-4.74321	0.79053	5.53375
J2000 Algorithm values	5102.37299	6123.12159	6378.13743	-4.74322	0.79043	5.53375
J2000 difference	0.13660	0.11007	0.00113	$8.28{\cdot}10^{-6}$	$1.03\cdot10^{-4}$	$1.20{\cdot}10^{-6}$

Table 3.3 shows a state vector in the ECEF reference frame and the transformed state vector in the J2000 reference frame for both the validation values and the algorithm values. The validation values result from erratav er1 [31] and the algorithm values result from the algorithm used in this research. The last row presents the difference between the last two mentioned rows.

The position error is smaller than a kilometre and the velocity difference is approximately 10 centimetre per second. The reason for the deviation is expected to be caused by the fact that, the example, which this first test case is build around, used mathematical models to estimate the precession, nutation and polar motion. For the software used in this research the measured position of the Earth is used, obtained from an EOP file, provided by the international Earth Rotation and Reference System Service. This is the assumed to cause the difference and for this reason a second case is tested to verify this presumption.

The second test case makes use of the in-house software at the TU Delft which uses the EOP data. For the first of December at 00:00:00.0 2020, the transformation matrix, based on the TU Delft software, is given. The transformation matrix, R, is given in equation 3.1. Looking at equation 3.2, the standard form for a z-axis frame transformation, the matrix in equation 3.1 has the appropriate form. The lower right value is close to one and the values above and to its left are close to zero.

$$R = \begin{bmatrix} 0.3478556790 & -0.9375480597 & 0.2495846884\cdot10^{-3} \\ 0.9375480875 & 0.3478556933 & 0.1503879482\cdot10^{-4} \\ -0.1009190477\cdot10^{-3} & 0.2287663171\cdot10^{-3} & 0.9999999687 \end{bmatrix} \tag{3.1}$$

$$R_z = \begin{bmatrix} \cos(\theta_z) & -\sin(\theta_z) & 0 \\ \sin(\theta_z) & \cos(\theta_z) & 0 \\ 0 & 0 & 1 \end{bmatrix} \tag{3.2}$$

Since only the transformation matrix is given, an expression needs to be derived to be able to calculate the velocity transformation. This expression is given in equation 3.3 [30].

$$V_{J2000} = R_{ECEF}(V_{ECEF} + (\omega_E \times P_{ECEF})) \tag{3.3}$$

where:

- V_{J2000}: Velocity vector in the J2000 reference frame
- V_{ECEF}: Velocity vector in the ECEF reference frame
- ω_E: Earth rotation rate, set at $7.29 \cdot 10^{-5} rad/s$
- P_{ECEF}: Position in the ECEF reference frame

Table 3.4 presents the results for the second test case. The difference between the result from the algorithm and the validation values are a lot less then the previous test case. With that it can be concluded that the difference in the previous test case does result from the difference in the source used to determine the Earth's position. With the results in table 3.4 it is also shown that the algorithm works as intended and is therefore verified.

Table 3.4: Validation results for the ECEF to J200 reference frame transformation for the second test case

	Position			Velocity		
	x [km]	y [km]	z [km]	x [km/s]	y [km/s]	z [km/s]
ECEF Coordinates	5906.05060	2149.62662	1100.81193	0	0	0
J2000 Validation values	39.34972	6284.98286	1100.70763	-0.45830	$2.84939 \cdot 10^{-3}$	$1.14343 \cdot 10^{-4}$
J2000 Algorithm values	39.34976	6284.98287	1100.70758	-0.45830	$2.84934 \cdot 10^{-3}$	$1.14640 \cdot 10^{-4}$
J2000 difference	$4.61881 \cdot 10^{-5}$	$7.85389 \cdot 10^{-6}$	$-4.57791 \cdot 10^{-5}$	$1.00278 \cdot 10^{-8}$	$-4.86486 \cdot 10^{-8}$	$2.97399 \cdot 10^{-7}$

3.1.2. Satellite observations

The observations are taken from the IPA which is developed during FOTOS. Each image is time stamped at the time it was taken. With this information and the found tracks in the image, it is possible to determine and observed right ascension and declination at the end of each track with their corresponding time. This is called an observation. These observations are presented in the Topocentric Equatorial Coordinate reference frame. A schematic representation of this process is shown in figure 3.2.

The IPA is used and described in the work of T.P.G. Wijnen et al.in 2019 [33]. The software is validated by checking if the end points of the track correspond within 10 pixels with a known satellite position. This known satellite position is obtained by using satellites from the CSpOC TLE database, propagated by means of the SGP4 theory, and then converted to pixel position in the image. For this research the track end points are sorted per satellite. When a track end point corresponds within 10 pixels of a satellite from the CSpOC database, this track end point is added to a list for that specific satellite. Therefore the data used for this research is sorted per satellite from which the observation probably originates. The fact that each observation used for this research corresponds within 10 pixels with a satellite, validates the IPA algorithm, and ensures the correct observations are used for this research.

3.1.3. SGP4 reference state

The reference state propagated with SGP4 is used to evaluate the quality of the obtained results from the CAR-MHF. The SGP4 is used to propagate the state of the satellite to a desired epoch. In order to do this, the TLE of the satellite needs to be known. For this research the TLE will only be used to calculate the earlier mentioned reference state, it is specifically not used for the CAR-MHF. The state vector resulting from the SGP4 propagator is given in a TEME reference frame. In order to be able to accurately evaluate the quality of the

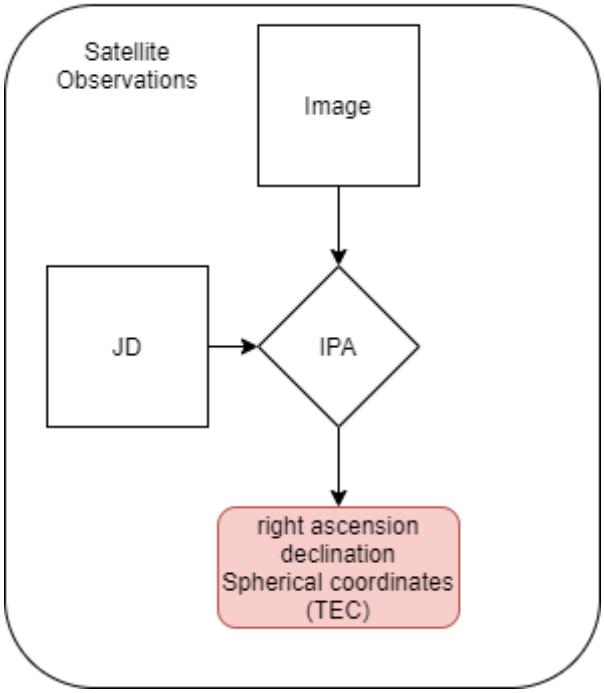

Figure 3.2: Schematic representation of the process of obtaining observations. The squares represent inputs, the diamond represents a process, and the rounded square is the output of the process.

result, the reference state needs to be expressed in the J2000 reference frame. The TEME to J2000 reference frame transformation requires the Julian day at the observation and the EOP data of the Earth rotation. A schematic representation of this process is shown in figure 3.3. The SGP4 (Version 7 Aug 2006) and TEME to J2000 (version 30 Oct 2017) reference frame transformation are both obtained from Celestrak Astrodynamics software library, based on the book Fundamentals of Astrodynamics and Applications [3].

SGP4 routine & TEME to J2000 reference frame transformation

The SGP4 routine and the TEME to J2000 reference frame transformation algorithms will be validated in one step. The algorithm will be validated by comparing the results with the in-house software of the TU Delft. This application is written and validated by Ir. Ron Noomen, assistant professor at the TU Delft. This software is used to read the TLE's and propagate them to the desired epoch in the J2000 reference frame. The TLE used for the validation is given in table 3.5 and both applications use the same TLE as input. The algorithm used for this research has split this transformation in two steps, with the two described algorithms. The TLE will be propagated to the correct epoch by applying the SGP4 routine. The position is then given in the TEME reference frame, then the position is transformed from TEME to the J2000 reference frame, making use of the TEME to J2000 reference frame transformation algorithm. At this stage the position of the satellite is in the same format and reference frame as the results from the in-house software of the TU Delft and the results can be compared.

Table 3.5: Two-line element used for the SGP4 & TEME to J2000 reference frame transformation algorithm validation. The TLE is published at April 30th 2020

	NORAD number	Security classification	ID number	Epoch	First time derivative	Second time derivative	Drag Term	Ephemeris type	Element set number	Check sum
TLE line 1	36508	U	10013A	20121.85356647	.00000075	00000-0	17791-4	0	999	8
	NORAD number	Inclination	R.A.A.N.	Eccentricity	Argument of Perigee	Mean Anomaly	Mean motion	revolution number		check sum
TLE line 2	36508	92.0283	96.1705	0008118	30.7720	329.3962	14.52175552	53334		2

The TLE is propagated to the first of May, at 16:00:00.0 in 2020. Then the state is transformed from the TEME to the J2000 reference frame, with the functions written by Vallado in Matlab[3], as applied in the algorithms written for this research. This date is selected since for this data validation data is available. Validation values are given in table 3.6. The second row presents the results from the SGP4 propagator in combination

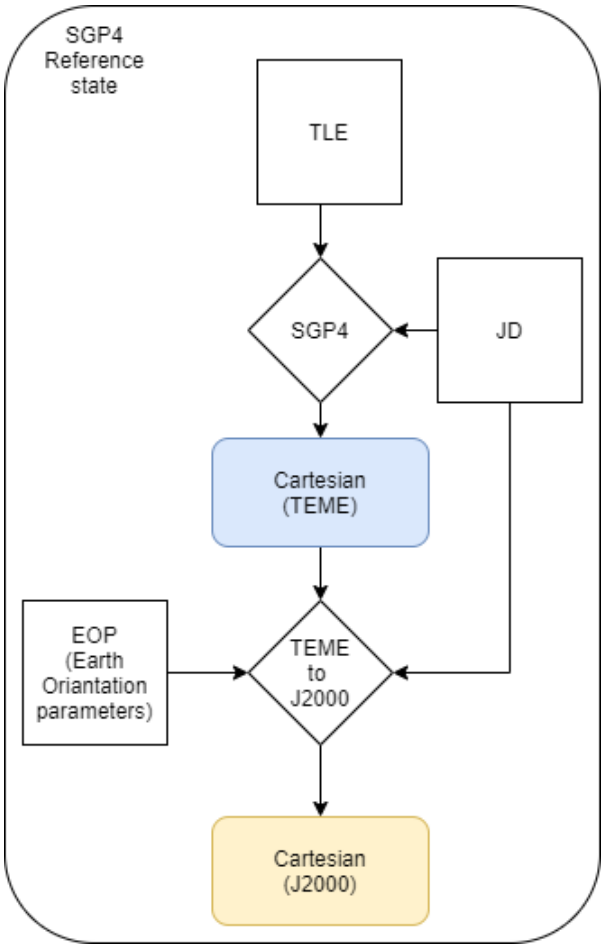

Figure 3.3: Schematic representation of the process of calculating a reference position in the J2000 reference frame, based on the TLE of the satellite. The squares represent inputs, the diamond represents a process, and the rounded squares are the output of the processes.

with the reference frame transformation algorithm as used in this research, and the last row shows the difference. Based on this result it can be concluded that the SGP4 propagator and the TEME to J2000 reference frame transformation works properly with negligible errors, and are hereby both the SGP4 and TEME to J2000 reference frame transformation algorithm is validated.

Table 3.6: Validation results for the SGP4 & TEME to J2000 reference frame transformation algorithm, as compared to the results from the in-house software of the TU Delft. For the TLE given in table 3.5 propagated to 16:00:00 on the first of May, 2020.

	Position			Velocity		
	x [km]	y[km]	z[km]	x [km/s]	y [km/s]	z [km/s]
J2000 validation values	-481.55789	2157.61624	-6752.41154	-0.70712	7.07639	2.31842
J2000 algorithm values	-481.55806	2157.61674	-6752.41152	-0.70712	7.07639	2.31842
J2000 difference	$-1.70\cdot10^{-4}$	$5.05\cdot10^{-4}$	$2.11\cdot10^{-5}$	$-2.84\cdot10^{-8}$	$-1.88\cdot10^{-7}$	$4.97\cdot10^{-7}$

3.1.4. Full chain validation

In previous sections the routines are discussed that transform the position of the object, camera, and SGP4 reference state to the desired reference frame. In this section the reference state will be used to check if the results are consistent.
In order to check if all routines work properly, the expected observations (α,δ) are calculated based on the position of the camera and the SGP4 reference state of a satellite at a time at which an observation of that satellite is available. All these calculations are performed by the Matlab scripts the author wrote himself.

The results from these scripts are compared to the SGP4 based sky positions, which are calculated by the the $PyEphem$ module, used in the IPA algorithm. If both script come up with similar values the code is validated.

The sky projection can be calculated by rewriting equation 2.26 into equation 3.4.

$$\boldsymbol{r}_{obj/cam} = \boldsymbol{r}_{obj} - \boldsymbol{r}_{cam} = \begin{bmatrix} x_{obj/cam} \\ y_{obj/cam} \\ z_{obj/cam} \end{bmatrix} \tag{3.4}$$

The right ascension and declination can be calculated with equation 3.5 and equation 3.6. In the code the $atan2$ function of Matlab is used in order to guarantee the correct quadrant solution.

$$\alpha = \arctan(\frac{y_{obj/cam}}{x_{obj/cam}}) \tag{3.5}$$

$$\delta = \arcsin \frac{z_{obj/cam}}{\sqrt{x^2_{obj/cam} + y^2_{obj/cam} + z^2_{obj/cam}}} \tag{3.6}$$

The difference between the SGP4-based sky positions and the calculated observations are shown in figure 3.4 for satellite 10793U. This analysis is repeated for the top five satellites with the most observations. The maximum error in right ascension and declination is given for each satellite. The great circle distance between the two points is calculated and based on this angle an approximate projected distance between the two observations are calculated based on the distance between the observer and the satellite.

Table 3.7 shows the validation result for these five satellites. Here it can be seen that the largest difference for the right ascension and declination are around the order of magnitude 0.01 degrees and smaller. The pixels in an image have a resolution of around 0.02 degrees, therefore this difference can be seen as sub-pixel level. Since the source data of the measurements are pixel based, this difference is smaller then the measurement uncertainty introduced by the source data. The difference presented can be caused by the following reasons:

- The Python and Matlab implementation may not be strictly identical.
- the TEME to J2000 reference frame transformation is different between the two programs.

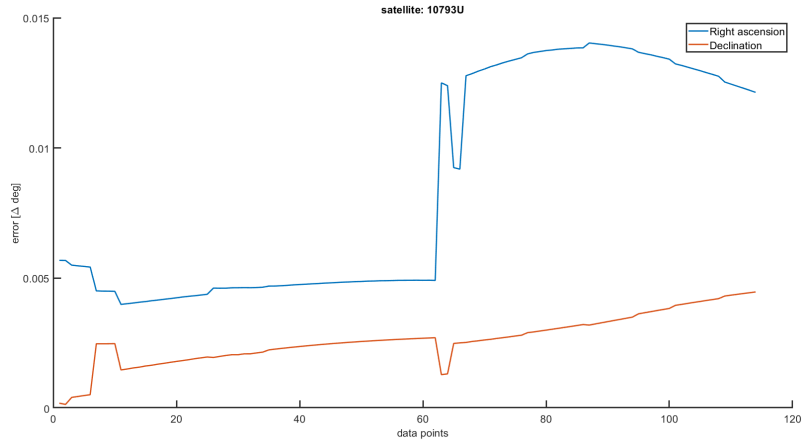

Figure 3.4: Result of the full chain validation for the frame transformations. The difference between the calculated and observed SGP4 observation angles is shown for all observations of satellite 10793U

The Python based program uses Pyephem to calculate the right ascension and declination based on a time and TLE, The fact that this research is performed in Matlab, the coding in Matlab and Python are not strictly identical, therefore small differences can occurs.

The TEME to J2000 reference frame transformation was not validated based on examples or test cases. So this transformation can be the reason for the error. The difference is sub-pixel level and also well within the SGP4 uncertainty, therefore the this will not cause significant errors and it is concluded that all reference frame transformations are considered validated.

Table 3.7: Full chain validation for the reference frame transformations. The results of the 5 satellites with the most observations available are used to validate the software. The maximum projected distance between the python based observation and the Matlab based observation for each satellite is presented, with the corresponding right ascension, declination, great circle distance, and distance between the observer and the satellite.

Satellite number	$\Delta\alpha$ [degrees]	$\Delta\delta$ [degrees]	Great circle distance [degrees]	Distance observer - satellite [km]	Projected distance [m]
10793U	0.012	0.0045	0.0063	2545.5	278.6
39260U	0.0048	0.0015	0.0022	1689.4	64.2
26083U	0.0039	0.0013	0.0018	2366.6	74.5
38771U	0.0046	0.0017	0.0023	1541.1	61.4
27601U	0.0059	0.0051	0.0057	910.7	90.3

3.2. Constrained asmissble region

The constrained admissible region is used to find valid hypotheses for the multiple hypotheses filter. The workflow of the process of establishing these hypotheses is presented in figure 3.5. The algorithm starts with three observations which are not further spread in time than 5 minutes, indicated with Epoch 1 till 3. At each epoch the right ascension, declination and the corresponding time is obtained. These are used in the angle interpolation algorithm in order to find the time rate of change of the right ascension and declination for the second epoch. With the observed angles, angle rates, and the position of the camera, it is possible to establish the admissible region. This region is expressed in the range versus range-rate domain.

The admissible region can then be constrained by applying the range, semi-major axis, and eccentricity constraints, resulting in the constrained admissible region. In this region, couples of range and range-rate values are selected. Each couple is then paired with the observed angle and angle-rates, to form a fully defined state vector in the Topographic equatorial coordinate reference framer. With the location of the camera in the J2000 reference frame in combination with the transformation from spherical coordinates to Cartesian coordinates it is possible to express the hypothesis in Cartesian Coordinates in the J2000 reference frame.

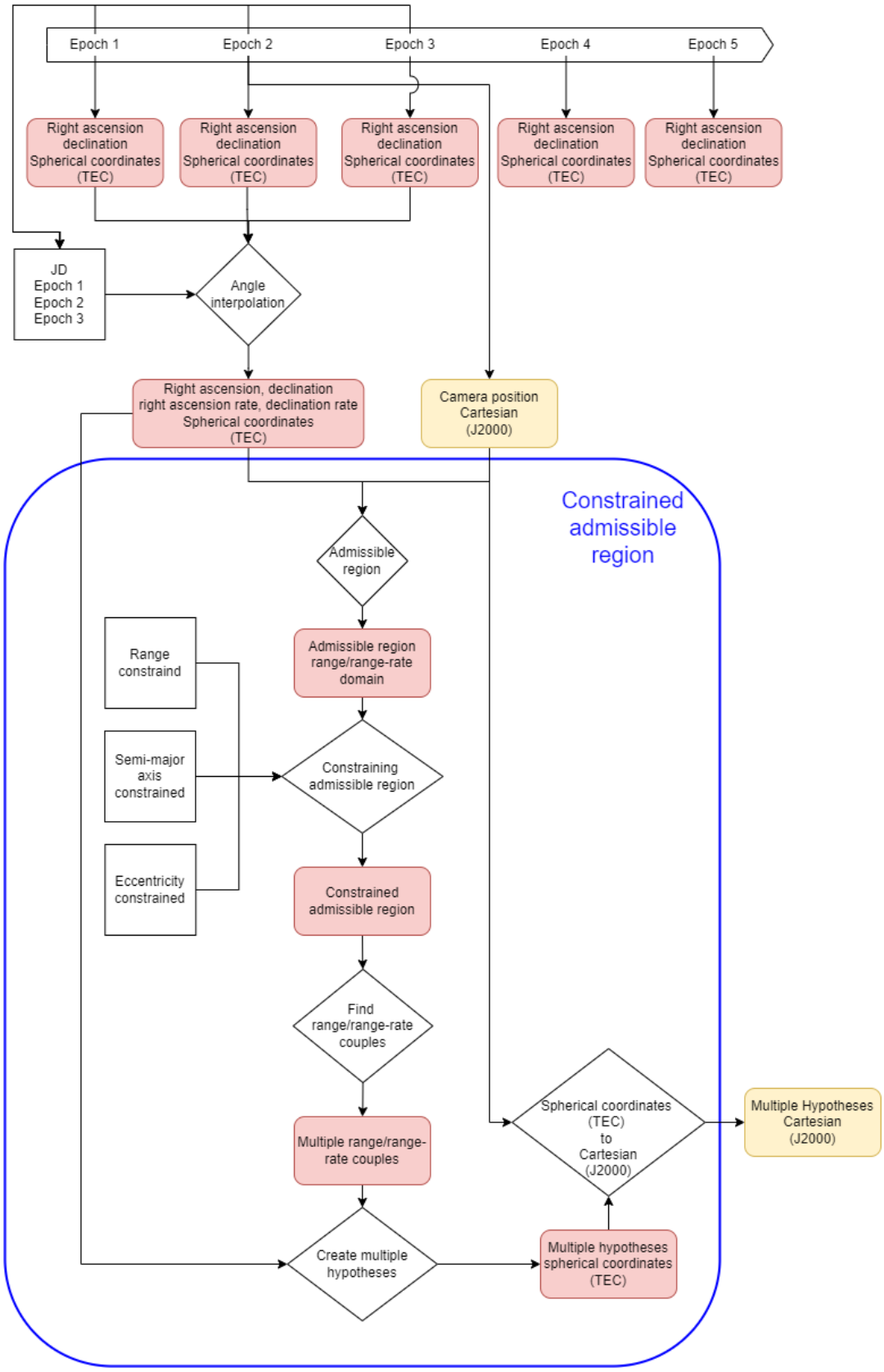

Figure 3.5: Workflow of the constrained admissible region algorithm. The squares are inputs, the diamonds are algorithms, and the rounded squares are outputs/inputs.

Table 3.8: Validation inputs for the constrained admissible region for satellite 37756U.

Satellite	39260U
Right ascension [deg]	338.33
Declination [deg]	-63.65
Right ascension rate [deg]	0.36
Declination rate [deg]	0.14
Camera latitude [deg]	-29.26
Camera longitude [deg]	-70.74
Camera altitude [m]	2369.40
Camera ID	LSS
Time [Julian day]	2458851.620937
Minimum range constrained [km]	250.00
Track length [pixels]	73.06
minimum semi-major axis [km]	250.00
maximum semi-major axis [km]	2000.00
maximum eccentricity [-]	0.30

3.2.1. Constrained admissible region validation

The constrained admissible region is validated by comparing the CAR with the SGP4 reference state. By computing the SGP4 reference state in the range-range rate domain. If the SPG4 reference state is within the CAR for multiple satellites, the CAR algorithm is validated.

The SGP4 reference state is calculated for the given satellite at the epoch at which the CAR is created. The state is then transformed into a topocentric reference frame by subtracting the position of the camera. Finally the Cartesian coordinates are transformed to spherical coordinates where the range and range-rate value is plotted in the CAR region. The test is performed for multiple camera from all the stations. By visual inspection it is checked if the SGP4 reference state is positioned within the constrains of the admissible region.

Figure 3.6 presents the CAR for satellite 37756U. The inputs used to generate the CAR are shown in table 3.8. In figure 3.6 it can be seen that the SGP4 reference state, represented with the red cross, is within the range, semi-major axis, and eccentricity constraint. The SGP4 reference state is relatively far from the initial hypotheses represented with the dots with the blue circle around them in the grey section. Increasing the sample density would increase the change of having an hypothesis close to the solution, but will result in more hypotheses that are within CAR. Therefore it would take more data points and computational power for the multiple hypotheses filter. For this validation a low sample density is used for the hypotheses grid, for a clear visual representation.

This analysis is repeated for another five satellite, and all the validation results can be found in appendix B. For all the six cases the SGP4 reference state is in the CAR. Based on these results it is concluded that the constrained admissible region algorithm is validated successfully.

3.2.2. Spherical coordinates in the TEC reference frame to Cartesian coordinates in J2000 reference frame transformation

The transformation from spherical coordinates in the TEC reference frame to Cartesian coordinates in the J2000 reference frame consist of two steps. The transformation from spherical coordinates to Cartesian, described by equation 2.28 and 2.29, and the transformation from TEC reference frame to the J2000 reference frame, where the centre of the reference frame is shifted from the observer to the centre of the Earth, described by equation 2.26 and 2.27.

The book orbital mechanics for engineering students, by Howard Curtis [8] described an example where this position frame transformation is given. This example will be used to validate the transformation. Table 3.9 shows the input values for the validation and originate from example 5.7 [8].

Table 3.10 shows the expected results, based on the example from Curtis, described as J2000 validation val-

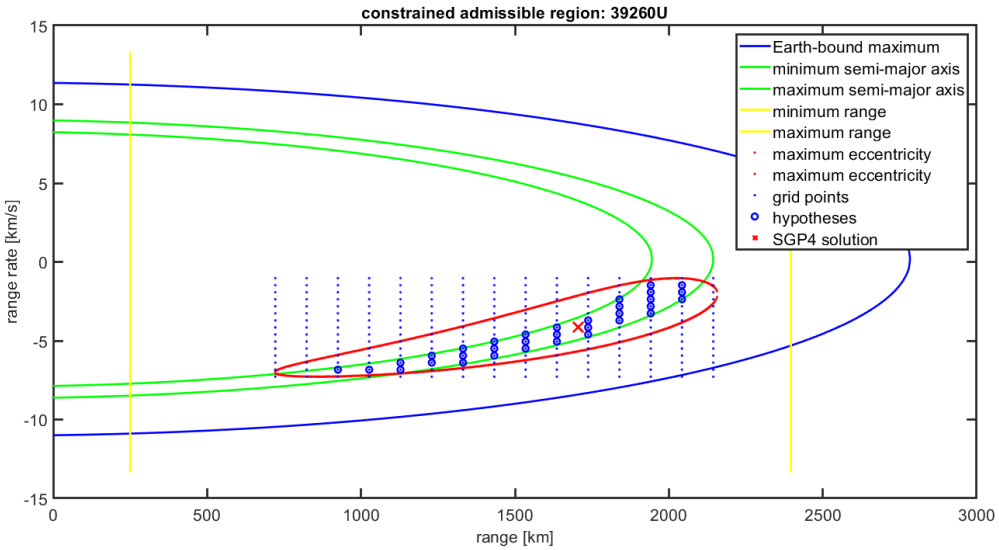

Figure 3.6: CAR validation data for satellite 37756U, where it is shown that the satellite state, represented with the red cross, is within the constrained admissible region, where constraints are represented with the green, yellow and red lines. The area with the blue circles around the blue dots represents the constrained admissible region.

Table 3.9: Validation input for coordinate frame transformation from polar coordinates in the TEC reference frame to the J2000 reference frame.

Right ascension [deg]	298.4
Declination [deg]	51.01
Distance object-observer [km]	1960
Station x-position [km]	-5955
Station y-position [km]	-699.5
Station z-position [km]	2168

ues, and the output from the algorithm, given in the row J2000 algorithm values. Since the example only gave round numbers as solution, the difference between the two can be explained as rounding errors. The velocity frame and coordinate transformation was not shown in the example and could therefore not be validated in a similar manner.

Table 3.10: Validation results for the transformation between spherical coordinates in the TEC reference frame to the Cartesian coordinates in the J2000 reference frame.

	Position		
	x [km]	y [km]	z [km]
J2000 Validation values	-5368	-1784	3691
J2000 Algorithm values	-5368.5	-1784.3	3691.4
J2000 difference	0.5	0.3	0.4

The position frame and coordinate transformation is validated by the example. This shows the method to be reliable. The algorithm to transform the spherical coordinates TEC reference frame to Cartesian coordinates J2000 reference frame was obtained from DeMars [10], which also described the velocity transformation. Based on this example the method is seen as correct. The velocity frame and coordinate transformation by double checking for typo in the algorithm, which was not the case. Also a sanity check was performed where the hypotheses generated by the algorithm in Cartesian coordinates showed values within the expected range. All this ensured the author from the correct implementation of these four equations and is deemed valid.

3.3. Multiple hypothesis filter

Figure 3.7 shows a schematic representation of the MHF where a time line is shown on top, with the different epochs. An overview of the constrained admissible region is given. The process of the multiple hypotheses filter is shown for a single hypothesis but happens for all hypotheses in a loop. The result from the other hypotheses is represented by the square boxes: *Residual other hypotheses* and *state vector other hypotheses*. These inputs are needed from all hypotheses in order to establish the elimination criterion.

The multiple hypotheses filter moves from epoch to epoch until only one hypothesis remains. The MHF starts with a state vector for each hypothesis, the hypothesis itself, and and initial state covariance matrix. The measurement uncertainty and process noise are inputs. At each epoch the camera position and the observed angles with their corresponding time is required as input. The EKF starts with propagating, i.e. predicting, the state at the epoch from the earlier epoch. This is done with the Runge-Kutta Felberg 4(5) integrator. Next the EKF will weigh the predicted state with the measured state, based on their corresponding uncertainties. Resulting in the state at set epoch, the covariance, and the residual.

This process is repeated for all initial hypotheses and based on the residual of a hypothesis compared to the residual of all other hypotheses, it is determined if the hypothesis is eliminated. After which it is checked if the hypothesis is the last one remaining. If this is not the case, then the multiple hypotheses filter continues to the next epoch for all remaining hypotheses. If it is the last hypothesis remaining, it is considered the initial orbit determination solution for the multiple hypotheses filter. The EKF can still continue after this point to improve the state, but at that point, it is no longer a multiple hypotheses filter.

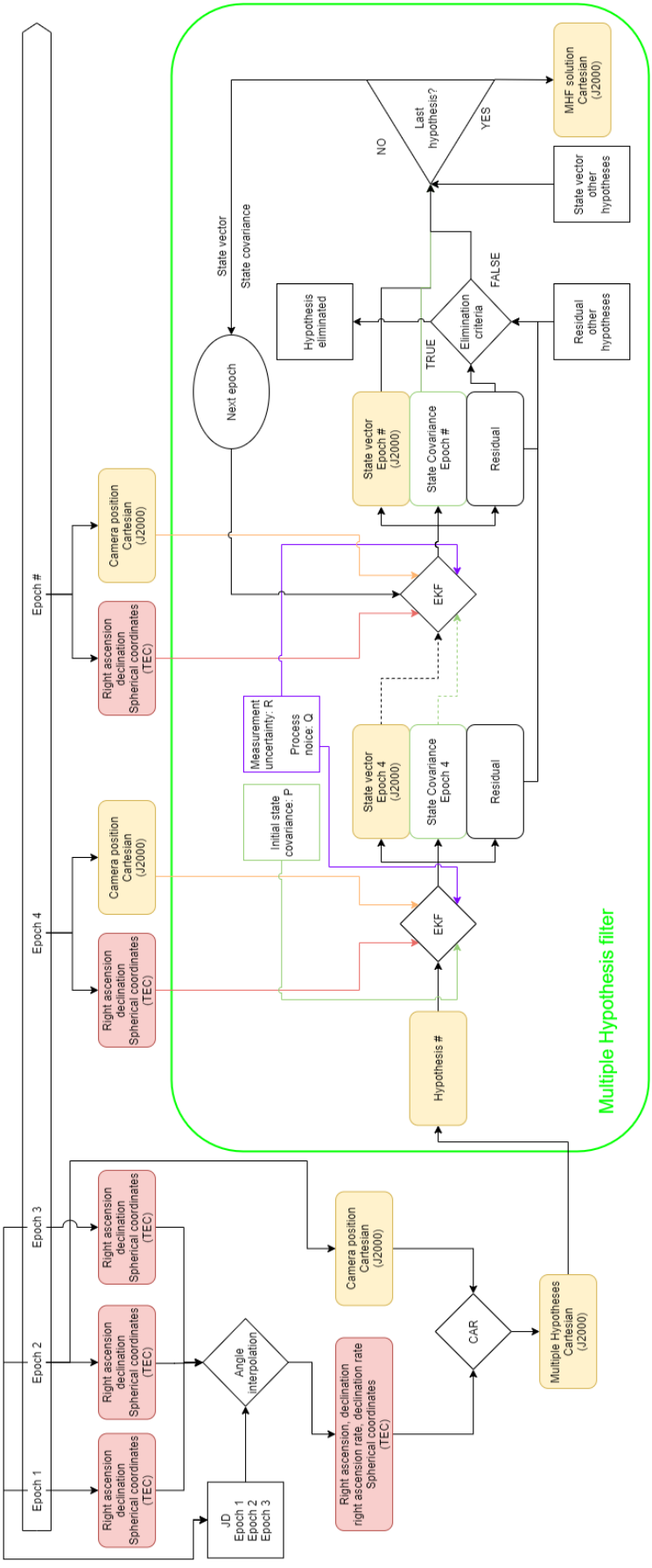

Figure 3.7: schematic representation of the multiple hypotheses filter. The squares represents inputs, the diamonds represents algorithms, and the rounded square are outputs/inputs. The dotted lines are one-time initial inputs. The green box circles the algorithms, as part of the multiple hypotheses filter.

The Runge-Kutta Felber 4(5), will be validated to ensure no large prediction errors occur. The extended Kalman filter is tested to ensure it converges on measurements. Finally the elimination criterion is tested to ensure the best solution remains.

3.3.1. Runge-Kutta Felberg 4(5)

The Runge-Kutta Felberg 4(5) method is tested for the five LEO satellites with the most observations. The epochs of the observations will be used to give a comparable test case for which the algorithm will be applied in this research. The test starts with the exact initial state as determined by the SGP4 reference state. The integrator then propagates from epoch to epoch without knowledge of the SGP4 reference. The error is the difference between the SGP4 orbit, compared to the propagated orbit.

Four satellites, 37347U, 10793U, 6257U and 38771U are propagated for five consecutive orbits, starting from the third of January 2020, 00:00:00. The last known TLE at that time will be used to determine the initial state and to determine the SGP4 reference state. So the TLE's as published on January the Third, 2020 are used. The dynamical model include the point mass gravity and the J2, J3, and J4 effect, as described in the method. The initial starting conditions are shown in table 3.11, including general orbital characteristics and the radar cross section. The tolerance of the RKF4(5) is set to 10^{-12}. Three different time steps are used, 6.4 seconds, 204.8 seconds (approximately 3.5 minutes), 3276.8 seconds (approximately 1 hour).

These four satellites are selected due to their difference in eccentricity, inclination and semi-major axis. All satellites have a widely different orbit, therefore getting a good representation of all different orbits that can occur.

Table 3.11: Input values for the RKF4(5) validation. Satellite 37347U, 10793U, 62557U and 38771 shown the initial state at the beginning of the propagation on 03-01-2020 00:00:00, general orbital parameters and the radar cross section.

Satellite	37347U	10793U	6257U	38771U
Initial state - Px [km]	5705.1	-7789.9	-1922.4	1728.9
Initial state - Py [km]	159.2	1800.5	-478.4	5260.8
Initial state - Pz [km]	6109.2	-1884.6	-7013.2	-4611.3
Initial state - Vx [km/s]	-2.74	-1.7	6.70	2.86
Initial state - Vy [km/s]	6.21	-5.8	-2.60	3.96
Initial state - Vz [km/s]	0.69	2.8	-1.63	5.60
Inclination [deg]	50.3	28.2	81.3	98.7
semi-major axis [km]	8078	7618	7249	7198
Eccentricity	0.17	0.088	0.0058	0.00020
Perigee [km]	299.1	575.0	836.2	826.1
RCS [m^2]	3.8	9.4	6.6	15.5

RKF4(5) analysis 6.4 seconds time step

First the RKF4(5) will be tested for a step size of 6.4 seconds. The error is defined as the difference between the SGP4 reference orbit and the RKF4(5) model. The maximum error is the moment where in the 5 orbits the error is the largest. The mean error is the average increase in error per time step. So the average error that is introduced when propagating 6.4 seconds.

The resulting errors are shown in table 3.12. Here it can be seen that the satellites have different error behaviours. Where the error for satellite 37347U can be explained by atmospheric dray, since it has a low perigee of 299 km. The other satellites have a perigee larger then 500 km, so looking at figure 2.4, the atmospheric drag is not a significant perturbing force, when comparing it to other perturbing forces.

The atmospheric drag of satellite 37347U can be shown by plotting the apogee of the orbit over time. When the satellite decelerate due to atmospheric drag at perigee, the apogee decreases. This is tested with the TLE of the satellite, given on the third of January, 2020. With this TLE, and the SGP4 theory, the position of the satellite is calculated for each day, for the next three years, starting on the third of January 2020.

Table 3.12: Maximum and mean state error for satellite 37347U, 10793U, 6257U, and 38771U. The error is defined as the difference between the SGP4 reference and the RKF45 solution, propagated for 5 orbits. The maximum error is the error at the largest offset, the mean error is the average error increase per time step of 6.4 seconds.

Satellite	37347U	10793U	6257U	38771U
Maximum position error [m]	5455.6	36138.5	4659.9	504.6
Maximum velocity error [m/s]	5.8	37.6	4.7	0.5
Mean position error [m]	5.88	8.1	0.98	0.5
Mean velocity error [m/s]	0.007	0.01	0.001	0.0005

Figure 3.8 shows the decrease in apogee over a period of three years. This confirms the presumption that atmospheric drag is experienced. Secondly small interval fluctuations are observed. These are probably caused by third body perturbations. This also shows that for small time scales the third body perturbations have a more significant effect of the orbit then the atmospheric drag.

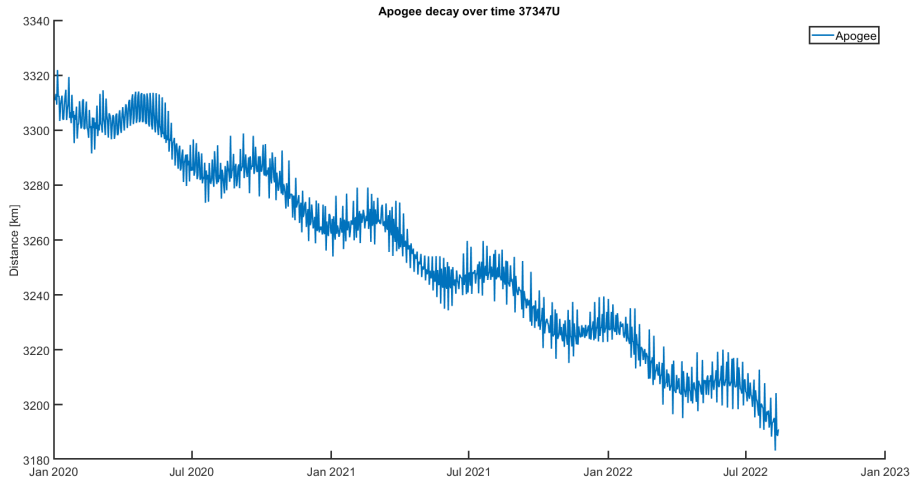

Figure 3.8: Apogee calculations based on the given TLE of the third of January 2020 and the SGP4 theory. Here it can be seen that apogee decreases, due to atmospheric drag. Also small period fluctuations are visible.

Satellite 10793U shows a significant larger error then satellite 38771U, where the inclination and eccentricity are the major difference between these satellites. The eccentricity, will primarily influence the perigee, and since it was already proven that a perigee of altitude of 500 km does not show significant atmospheric drag, the difference is expected to be caused by the inclination. In order to investigate this, four more satellites are analysed to determine if this is a trend of coincidence.

Table 3.13 shows the important orbital elements of the satellites that are used to analyse the propagation error depending on the inclination. The RKF45 method and the SGP4 method is used to propagate the satellite for 100 days, with a step size of 24 hours. A larger time scale is selected to make the effects more apparent. The solutions are transformed to Kepler elements and the difference between the two are taken.

Appendix G shows the results for all six satellites. All three low inclined satellites show similar behaviour, compared to each other. Similar can be said about the high inclined satellites. With this it can be said that it is no coincidence that the satellites do behave differently and have therefore different errors.

Figure 3.9 shows the difference in Kepler elements between the SGP4 and RKF4(5) orbit, as an example for the low inclined satellites. Here it can be seen that the true anomaly shifts linearly over time. The error in the semi-major axis is around the order of magnitude of kilo meters. The error in all other orbital elements are small.

Table 3.13: Orbital elements of satellite 38771U, 29499U, 23851U, 10793U, 10954U, and 25510U to indicate the important differences between the satellites.

Satellite	38771U	29499U	23851U	10793U	10954U	25510U
Inclination [deg]	98.7	98.1	98.9	28.2	28.4	31.4
semi-major axis [km]	7198	7048	7278	7618	7446	7143
Eccentricity	0.0002	0.02	0.0008	0.009	0.07	0.03
Perigee [km]	826.0	537.0	902.0	574.9	555.7	539.8

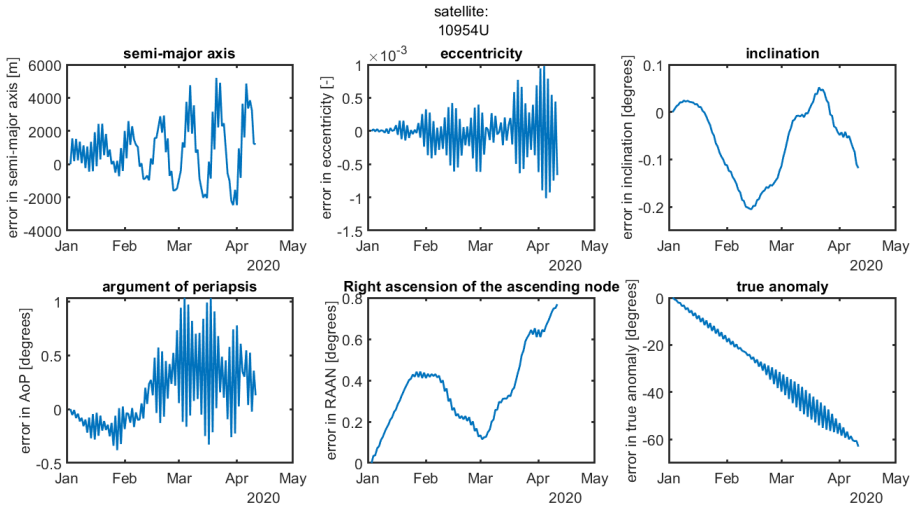

Figure 3.9: Propagation difference in Kepler elements between the SGP4 orbit and the RKF4(5) method. Analysed from the start of January 2020, for three months. Here it shows a satellite with a low inclined orbit.

Figure 3.10 shows the difference in Kepler elements between the SGP4 and RKF4(5) orbit, as an example for the high inclined satellites. Here it can be seen that the right ascension of the ascending node shows a linear error with respect to time. Also the inclination error shows a smooth trend, but is small. The error in the semi-major axis is one order of magnitude smaller compared to the low inclined satellites. Most importantly, the difference in the true anomaly does not shift in time.

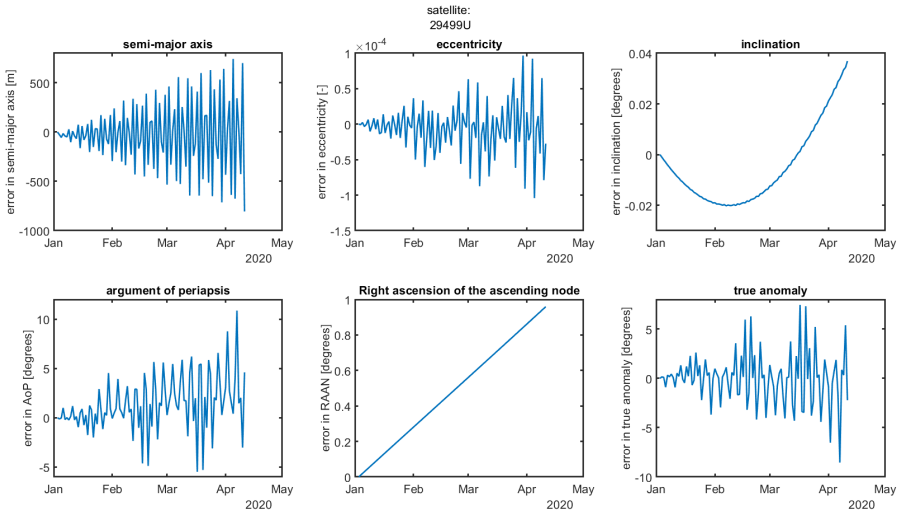

Figure 3.10: Propagation difference in Kepler elements between the SGP4 orbit and the RKF4(5) method. Analysed from the start of January 2020, for three months. Here it shows a satellite with a high inclined orbit.

The difference in error between the low and high inclined orbits, as seen in table 3.12, is caused by the shift in true anomaly for the low inclined orbits. Literature research did not provide information to explain why this difference occurred. Therefore a hypothesis was developed why this difference occurs. The error is caused by either the Earth gravity field model, third body perturbations of the Sun and Moon, or Solar radiation, or a combination of theses. Since these effects are taken into account for the SGP4 theory and not in the dynamics of the RKF4(5).

The third body perturbations, and solar radiation pressure all occur in the orbital plane of the solar system, therefore for low inclined satellites, the perturbing forces are applied in the orbital plane of the satellite. Adding each orbit a bit of perturbation, resulting in a cumulative error, causing the true anomaly to shift, causes the errors as seen. For the high inclined satellites, these perturbing forces act perpendicular to the orbital plane of the satellite. With the orbital motion it results in a more osculating error compared to the cumulative error, due to this reason the error is smaller for high inclined satellites.

RKF4(5) analysis for 6.4 seconds, 3.4 minutes, and 0.9 hours time step

Table 3.14 shows the maximum and mean position and velocity error for the four earlier mentioned satellites for three different time steps. The error is defined as the difference between the SGP4-based orbit and the RKF4(5)-based orbit. The maximum error is the error is the largest error over the time span. The mean error is the average increase in error per time step.

Appendix E shows the error behaviour over time for each satellite. It shows the total error per epoch, but also the error increase per epoch.

It can be seen that the maximum error does not differ significant for different time steps. This is due to the fact that a variable time step propagator is used. This propagator selects the optimal intermediate step size, based on the tolerance. For this reason the error does not increase significant for different time steps. The Mean error does increase for increased step sizes. This is due to the fact that the measurement point is later in time for larger step sizes, so the cumulative propagation error is increased.

The error per time step for low time intervals between zero and five minutes can be acceptable but for larger time steps the propagation error increases. This can be countered by adding third body perturbations, atmospheric drag, better Earth gravity model, and solar radiation pressure to the dynamical model. Adding dynamics is the balance between performance and accuracy, and first needs to be looked at if the extra accuracy is needed for the EKF for which the RKF4(5) will be used. The discussion if extra dynamics needs to be added to the model will be continued after the validation of the EKF.

Table 3.14: The maximum and mean error for the RKF4(5) over a period of 5 orbits, for four different satellites.

Time step [s]	Satellite	37347U	10793U	6257U	38771U
6.4	Maximum position error [m]	5455.6	36138.5	4659.9	504.6
	Maximum velocity error [m/s]	5.8	37.6	4.7	0.5
	Mean position error [m]	5.88	8.1	0.98	0.5
	Mean velocity error [m/s]	0.007	0.01	0.001	0.0005
204.8	Maximum position error [m]	5293.5	35955.7	4835.2	435.5
	Maximum velocity error [m/s]	5.6	37.4	4.9	0.5
	Mean position error [m]	184.5	256.1	32.3	24.0
	Mean velocity error [m/s]	0.2	0.4	0.03	0.02
3276.8	Maximum position error [m]	5840.9	43740.6	5059.4	435.6
	Maximum velocity error [m/s]	5.3	45.8	5.3	0.5
	Mean position error [m]	652.6	4002.4	259.9	34.7
	Mean velocity error [m/s]	1.5	6.4	0.5	0.05

3.3.2. Extended Kalman filter

The Jacobian matrix of the time derivative of the state vector, as shown in equation 2.81 as part of the EKF will be validated first. The EKF will then be validated on a single observation arc. Next the EKF will be validated for multiple observation arcs.

State transition matrix & Jacobian matrix validation

The Jacobian matrix, a matrix used to construct the state transition matrix, consists of complex partial derivatives, therefore this matrix will be validated in order to ensure no typing, or other errors were introduced. Equation 2.80 shows the relation between the Jacobian matrix and the state transition matrix. The validation strategy is suggested by Dr. E.J.O. Schrama, Associate Professor at the Faculty of Aerospace engineering at the Tu Delft. The main idea of the validation strategy is that propagating the offset between two states should result in the same result as difference between the two propagated states.
The validation strategy will be explained in formulas know to make it more clear. Equation 3.7 describes the relation between state a and state b, where $\Delta X_{(i-1)}$ can be any arbitrary value.

$$\boldsymbol{X}_{(i-1)_b} = \boldsymbol{X}_{(i-1)_a} + \Delta X_{(i-1)} \tag{3.7}$$

Both state a and state b are propagated, by using the state transition matrix, constructed by the state a. The propagation of state a is shown in equation 3.8.

$$\boldsymbol{X}_{(i)_a} = \phi(\boldsymbol{X}_{(i-1)_a})\boldsymbol{X}_{(i-1)_a} \tag{3.8}$$

The propagation of state b is shown in equation 3.9.

$$\boldsymbol{X}_{(i)_b} = \phi(\boldsymbol{X}_{(i-1)_a})\boldsymbol{X}_{(i-1)_b} \tag{3.9}$$

The difference between the two states at epoch i can be calculated in two different manners, both shown in equation 3.10. When the Jacobian matrix and the state transition matrix are correctly formulated, both equations should result in the same value.

$$\begin{aligned} \Delta X_{(i)} &= \phi(\boldsymbol{X}_{(i-1)_a})\Delta X_{(i-1)} \\ &\quad or: \\ \Delta X_{(i)} &= \boldsymbol{X}_{(i)_b} - \boldsymbol{X}_{(i)_a} \end{aligned} \tag{3.10}$$

This validation is performed for three different satellites, for a period of 5 consecutive orbits with at least 4800 propagation steps. The input data for this validation is given in table 3.15. These three satellites are selected

Table 3.15: Input values for the validation of the Jacobian matrix and the state transition matrix for the satellite 6257U, 37347U, and 10793U on the third of January 2020.

Satellite	6257U	37347U	10793U
Time Step [s]	6.4	6.4	6.4
Number of Orbits	5	5	5
TLE	Table 3.17	Table 3.16	Table 3.18
Number of epochs	4801	5756	5175
Dynamical model	J2, J3 & J4	J2, J3 & J4	J2, J3 & J4
initial date/time	03-01-2020 00:00:00	03-01-2020 00:00:00	03-01-2020 00:00:00
offset	1 km & 10 m/s	1 km & 10 m/s	1 km & 10 m/s

Table 3.16: Two-line element of the satellite 37347U, used for the validation of the Jacobian matrix and the state transition matrix.

TLE line 1	NORAD number	Security classification	ID number	Epoch	First time derivative
	37347	U	11001D	19365.33745486	0.00005087
	Second time derivative	Drag Term	Ephemeris type	Element set number	Check sum
	42285-5	23791-3	0	999	2
TLE line 2	NORAD number	Inclination	R.A.A.N.	Eccentricity	Argument of Perigee
	37347	50.3482	306.4462	0.1844775	173.3273
	Mean Anomaly	Mean motion	revolution number		check sum
	189.6266	11.73027881	36661		3

Table 3.17: Two-line element of the satellite 6257U, used for the validation of the Jacobian matrix and the state transition matrix.

TLE line 1	NORAD number	Security classification	ID number	Epoch	First time derivative
	6257	U	72085B	20001.45528146	$2.0 \cdot 10^{-8}$
	Second time derivative	Drag Term	Ephemeris type	Element set number	Check sum
	0000-0	-0.65588-5	0	999	0
TLE line 2	NORAD number	Inclination	R.A.A.N.	Eccentricity	Argument of Perigee
	37347	81.2586	342.5511	0.0057941	38.35
	Mean Anomaly	Mean motion	revolution number		check sum
	322.1766	14.06440293	41996		7

Table 3.18: Two-line element of the satellite 10793U, used for the validation of the Jacobian matrix and the state transition matrix.

TLE line 1	NORAD number	Security classification	ID number	Epoch	First time derivative
	10793	U	78039B	200002.77766383	$1.61 \cdot 10^{-6}$
	Second time derivative	Drag Term	Ephemeris type	Element set number	Check sum
	0000-0	29074-4	0	999	2
TLE line 2	NORAD number	Inclination	R.A.A.N.	Eccentricity	Argument of Perigee
	10793	28.2246	194.5992	0.0883429	123.4733
	Mean Anomaly	Mean motion	revolution number		check sum
	245.3400	13.0538681998	98540		0

due to their difference in key orbital elements; the semi-major axis, inclination, and eccentricity. Due to the difference in orbits, reliable conclusions can be constructed, based on the given data.
Both of the offsets, as calculated in equation 3.10, are determined. For each epoch during the 5 orbits, where each epoch is 6.4 seconds apart. The difference between the two offsets is shown in figure 3.11 for satellite 37347U, figure 3.12 for satellite 6257U and figure 3.13 for satellite 10793U. The difference between the two offsets are significant small, where the position difference is of the order of magnitude $10 \cdot 10^{-6}$ till $10 \cdot 10^{-8}$ meters, and the velocity $10 \cdot 10^{-11}$ meters per second. The relative difference, with respect to the state vector of state a, is shown in figure 3.14, 3.15, and 3.16 for satellite 37347U, 6257U, and 10793U, respectively. This shows a relative difference on the order of magnitude between 10^{-15} and 10^{-16}. It is also seen that the graph is not smooth. This phenomena is often seen when the truncation error is the leading cause. Due to the small difference and having and showing the behaviour belonging to truncation error, it is concluded that difference is caused by the truncation error. Hereby the first step of validating these matrices is achieved.

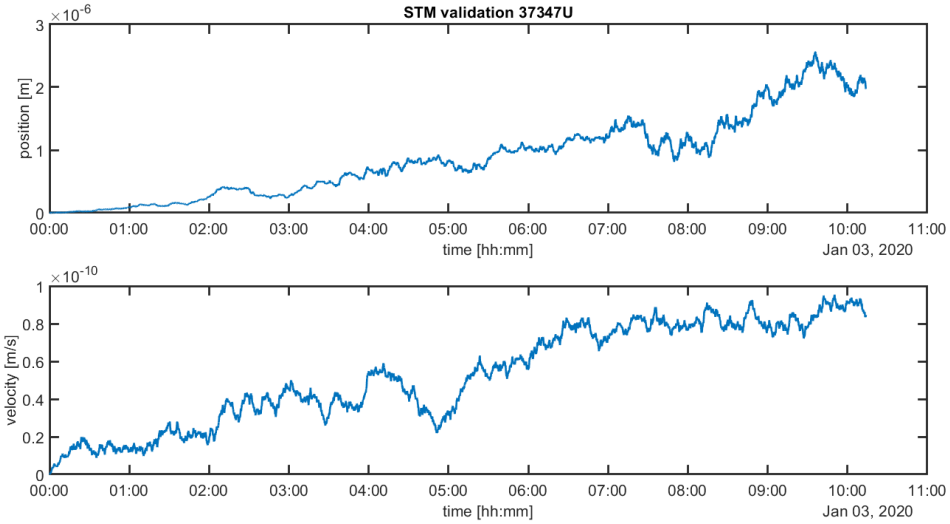

Figure 3.11: The difference between the propagated offset and the difference between two propagated states with an initial offset as described in equation 3.10 for satellite 37347U starting at 03-02-2020 00:00:00 for 5 orbits.

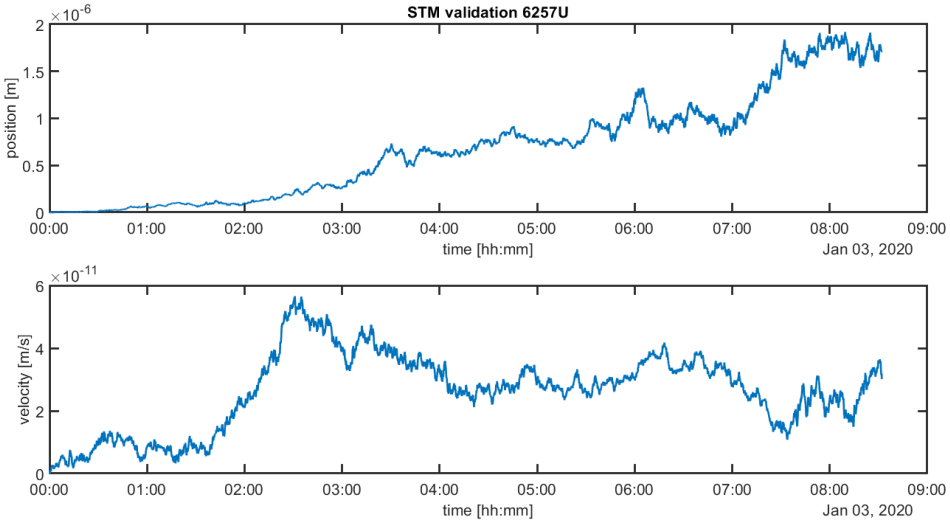

Figure 3.12: The difference between the propagated offset and the difference between two propagated states with an initial offset as described in equation 3.10 for satellite 6257U starting at 03-02-2020 00:00:00 for 5 orbits.

The second step to validate the State transition matrix is to compare the propagation from the state transition

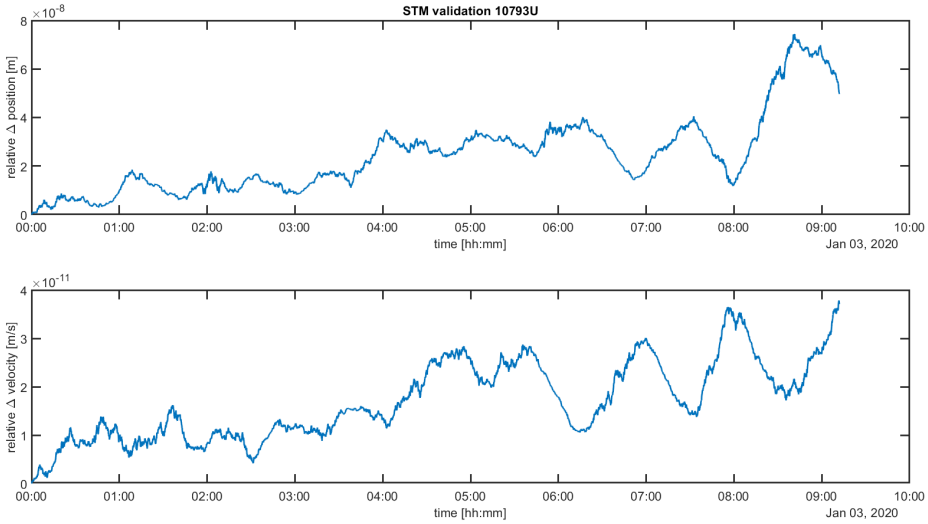

Figure 3.13: The difference between the propagated offset and the difference between two propagated states with an initial offset as described in equation 3.10 for satellite 10793U starting at 03-02-2020 00:00:00 for 5 orbits.

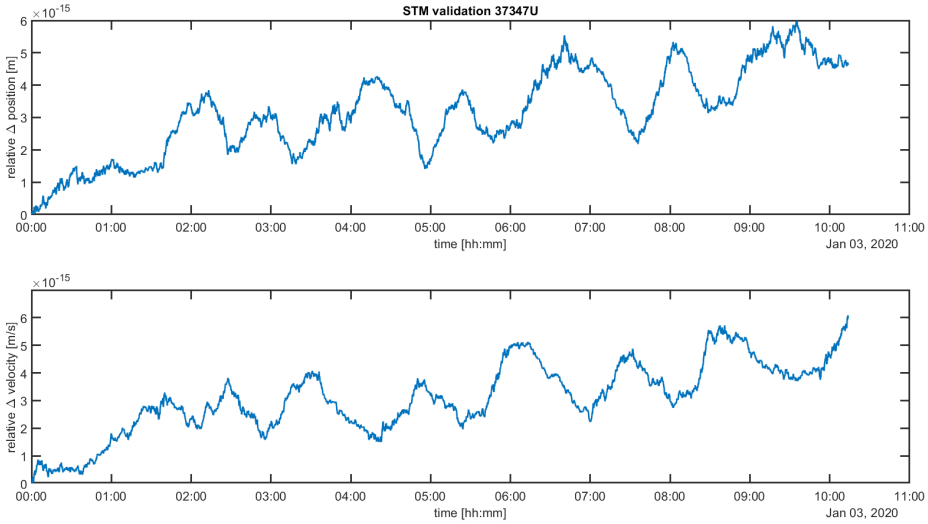

Figure 3.14: The relative difference between the propagated offset and the difference between two propagated states with an initial offset as described in equation 3.10, with respect to the state a, for satellite 37347U starting at 03-02-2020 00:00:00 for 5 orbits.

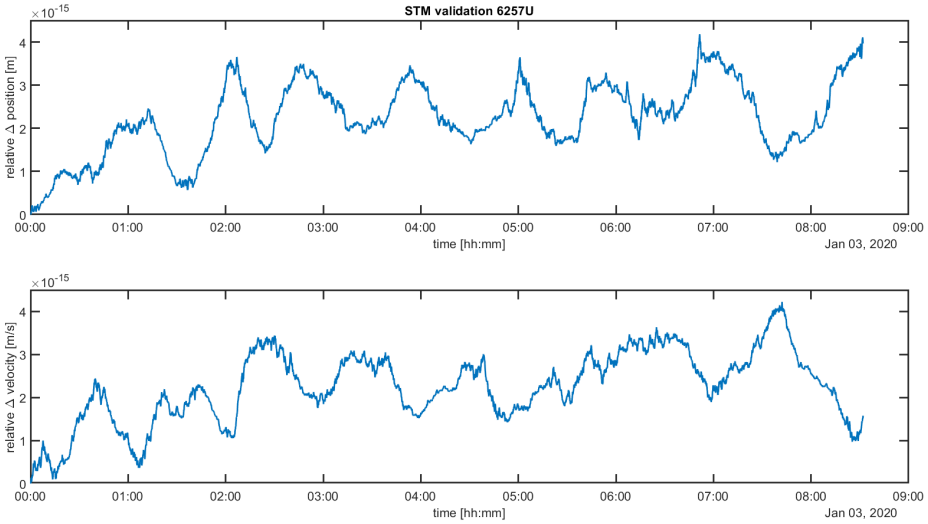

Figure 3.15: The relative difference between the propagated offset and the difference between two propagated states with an initial offset as described in equation 3.10, with respect to the state a, for satellite 6257U starting at 03-02-2020 00:00:00 for 5 orbits.

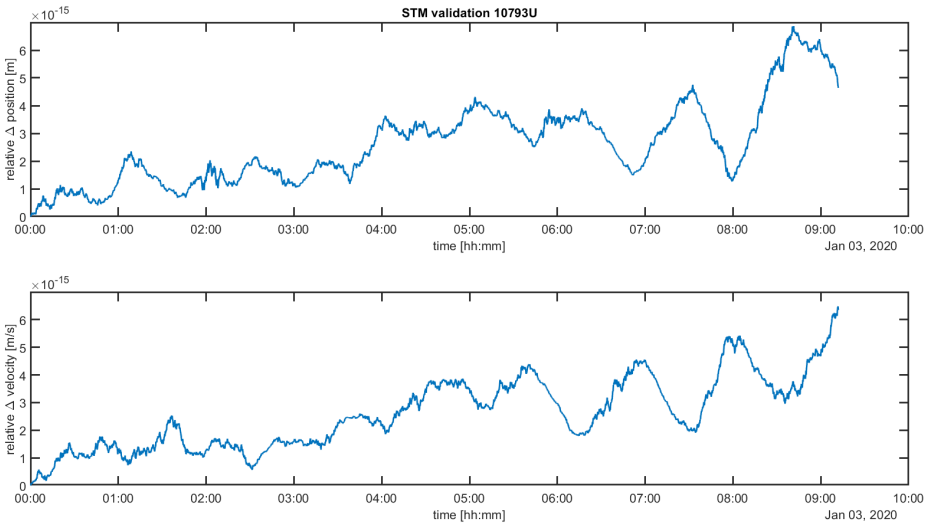

Figure 3.16: The relative difference between the propagated offset and the difference between two propagated states with an initial offset as described in equation 3.10, with respect to the state a, for satellite 10793U starting at 03-02-2020 00:00:00 for 5 orbits.

matrix with a propagated based on the dynamics. The propagation based on the state transition matrix is not used in the EKF to propagate the state, but is used to propagate the covariance matrix. But in order to validate the state transition matrix, propagation is required.

The state transition matrix propagation is given in equation 3.11. Equation 2.80 described how the state transition matrix is calculated. As can be seen in equation 2.81, this propagation is based on a linearization, based on a partial derivative.

$$\boldsymbol{X}_{(i)} = \phi(\boldsymbol{X}_{(i-1)})\boldsymbol{X}_{(i-1)} \tag{3.11}$$

The propagation based directly on the dynamics is shown in equation 3.12, where the dynamics, $\dot{\boldsymbol{X}}_{(i-1)}$, are given in equations 2.18, 2.19, and 2.20.

$$\boldsymbol{X}_{(i)} = \boldsymbol{X}_{(i-1)} + \dot{\boldsymbol{X}}_{(i-1)}\Delta t \tag{3.12}$$

Both methods are used to propagate satellite 37347U, 6257U, and 10793U for 5 orbits, similar to the previous validation step. The difference between the two methods, for each state vector element, is plotted in figure 3.17, 3.18, and 3.19 for satellite 37347U, 6257U, and 10793U, respectively.

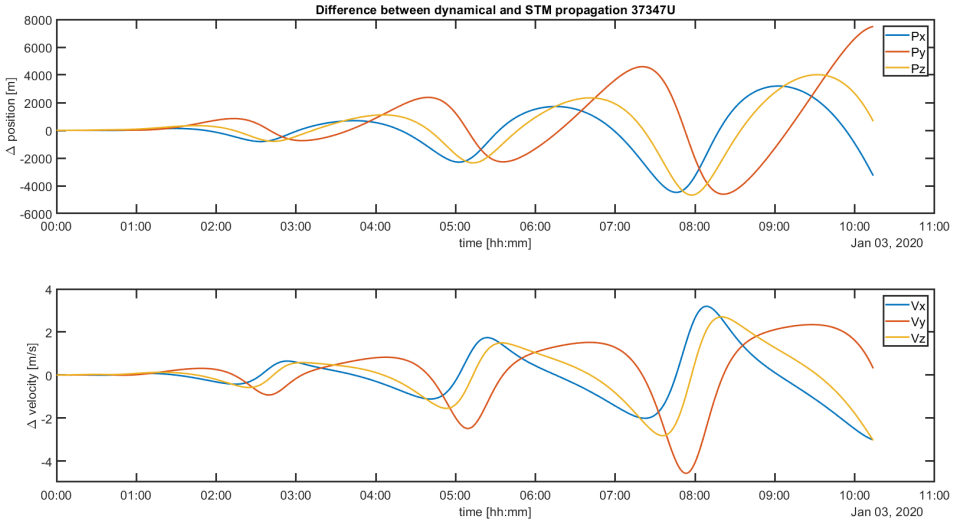

Figure 3.17: The difference between the dynamical propagation and the state transition matrix propagation plotted for the individual state vector variables. Analysis performed for satellite 37347U starting at 03-02-2020 00:00:00 for 5 orbits.

The error increases over time, due to the linearization by partial derivatives. The second term of equation 2.20 drops out by this partial derivative, since this term is not dependent on the state vector element $\boldsymbol{z}$. This results in a linearisation error, and it can be seen in table 3.19. This table shows the second term in equation 3.12, the change in velocity for a single propagation step. For equation 3.11 it is more complicated to show, since it is a matrix operation. These terms are calculated by multiplying the partial derivatives from the bottom left quadrant by the first tree values from the state vector, times the time step. For example, the added velocity term for the y-axis for the state transition matrix is calculate by multiplying $\frac{\partial \ddot{\mathbf{y}}}{\partial \mathbf{y}}$ by the y value from the state vector and the time step of 6.4 seconds.

$$\mathbf{x}\phi(\boldsymbol{X}_{(i-1)}) = \begin{bmatrix} 1 & 0 & 0 & \Delta t & 0 & 0 \\ 0 & 1 & 0 & 0 & \Delta t & 0 \\ 0 & 0 & 1 & 0 & 0 & \Delta t \\ \frac{\partial \ddot{\mathbf{x}}}{\partial \mathbf{x}} & 0 & 0 & 1 & 0 & 0 \\ 0 & \frac{\partial \ddot{\mathbf{y}}}{\partial \mathbf{y}} & 0 & 0 & 1 & 0 \\ 0 & 0 & \frac{\partial \ddot{\mathbf{z}}}{\partial \mathbf{z}} & 0 & 0 & 1 \end{bmatrix} \tag{3.13}$$

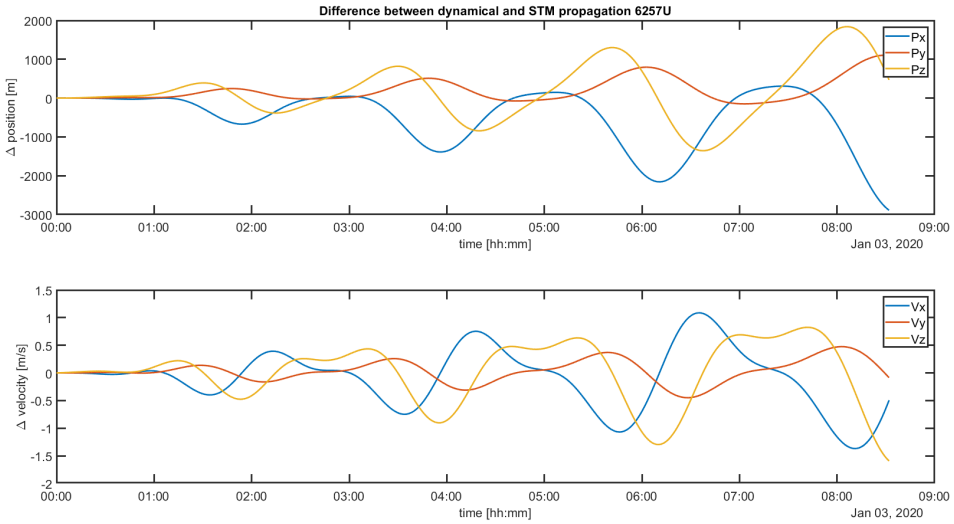

Figure 3.18: The difference between the dynamical propagation and the state transition matrix propagation plotted for the individual state vector variables. Analysis performed for satellite 6257U starting at 03-02-2020 00:00:00 for 5 orbits.

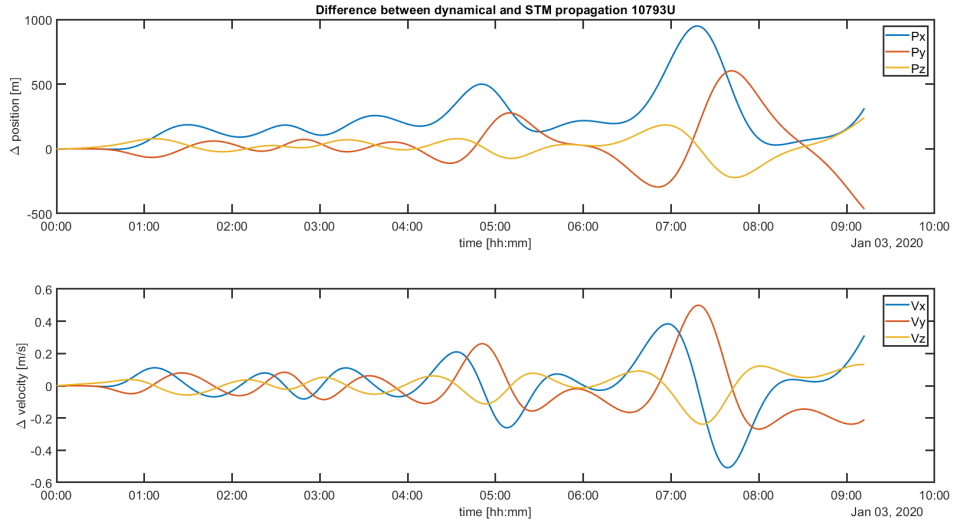

Figure 3.19: The difference between the dynamical propagation and the state transition matrix propagation plotted for the individual state vector variables. Analysis performed for satellite 10793U starting at 03-02-2020 00:00:00 for 5 orbits.

Table 3.19 shows the change in velocity when propagating from the first to the second epoch for satellites 37347U, 6257U, and 10793U, for two different propagation methods. It shows a significant larger difference in the z-term compared to the x & y term.

Table 3.19: The change in velocity for satellites 37347U, 6257U, and 10793U, propagated from 03-01-2020 00:00:00, for a time step of 6.4 seconds. The change in velocity is calculated by propagating the dynamics by use of the Euler method and the state transition matrix. The difference is for each axis is shown.

	Satellite	37347U	6257U	10793U
Velocity - Vx [m/s]	STM	-24.9	12.6	35.9
	Euler method	-24.9	12.6	35.9
	difference	$3.5{\cdot}10^{-15}$	$1.8{\cdot}10^{-15}$	$7.1{\cdot}10^{-15}$
Velocity - Vy [m/s]	STM	-0.7	3.1	-8.3
	Euler method	-0.7	3.1	-8.3
	difference	0	$4.4{\cdot}10^{-16}$	$1.8{\cdot}10^{-15}$
Velocity - Vz [m/s]	STM	-26.7	46.1	8.7
	Euler method	-26.7	46.1	8.7
	difference	$6.2{\cdot}10^{-5}$	$1.2{\cdot}10^{-4}$	$6.7{\cdot}10^{-5}$

The error introduced by the partial derivative for the z-term in inevitable and inherent to the method used to construct Jacobian matrix, and consequently state transition matrix. There are other methods to construct a state transition matrix, two methods are described by Ana Paula Chiaradia [6]. These methods have an analytical approach to construct the state transition matrix. These methods can be explored for further improvements.

The state transition matrix is not used to propagate the state, but only the covariance matrix. Secondly, the EKF will improve the state, based on the given date, reducing the error. What this validation showed is as following: the Jacobian and state transition matrix is correctly implemented since the difference is small, and the only significant difference can be explained, based on the method.

Both validation strategies show have shown that the state transition matrix is correctly implemented for the EKF.

Single arc observation

The extended Kalman filter will be tested with SGP4-based right ascension and declination obtained from the observed data for the following five satellites:

- Satellite 4794U, station LS, 03-01-2020, 58 data points, 05:38 minutes time span, Perigee distance 1429 km, inclination 101.5 degrees.
- Satellite 6257U, station LSE, 03-01-2020, 25 data points, 02:52 minutes time span, Perigee distance 836 km, inclination 81.3 degrees.
- Satellite 22284U, station SAE, 03-01-2020, 30 data points, 03:05 minutes time span, Perigee distance 841 km, inclination 71.0 degrees.
- Satellite 23404U, station AUE, 03-01-2020, 26 data points, 02:52 minutes time span, Perigee distance 841 km, inclination 101.9 degrees.
- Satellite 10793U, station LSN, 03-01-2020, 48 data points, 05:38 minutes time span, Perigee distance 575 km, inclination 28.2 degrees.

These satellites where selected due to their difference in data points, duration of the observation arc and different ground stations. .

The measurements of that satellite taken by a single station will be used and when the time step is larger then 30 minutes, the program is ended. This is done in order to let the program stop before it continues on to

the next observation arc. The initial state will be determined by the CAR algorithm, resulting in multiple hypotheses. These hypotheses will not be eliminated because the elimination step will be validated separately in the next section. The EKF settings as described in the method section will be used for this research.

Table 3.20 shows the position and velocity error at the end of the observation arc for the best hypotheses. The error is defined as the difference between the SGP4 orbit and the results from the EKF. Here it can be seen that for all satellites the error is around the order of magnitude of a kilometres or smaller.

Table 3.20: The position and velocity error for the EKF, after a single observation arc for satellites 4794U, 6257U, 22284U and 23404U, and 10793U for the best hypothesis.

Satellite		4794U	6257U	22284U	23404U	10793U
Position error	x-axis [m]	186.9	4.5	176.1	277.3	1442.5
	y-axis [m]	978.8	219.0	92.3	112.4	219.0
	z-axis [m]	97.1	255.1	3.8	129.8	43.7
Velocity error	x-axis [m/s]	1.5	0.7	0.5	1.2	1.2
	y-axis [m/s]	1.8	0.09	0.01	0.2	2.3
	z-axis [m/s]	4.1	0.3	0.7	0.4	0.3

Figure 3.20 shows the position and velocity for satellite 6257U for the EKF for the different hypotheses over the period of a single observation arc. The dark blue line, which is barely visible, is the SGP4-based reference solution. Figure 3.21 shows the singled out best performing hypothesis. These figures show that the EKF is able to converge continuously with increasing accuracy to the SGP4-based reference state.

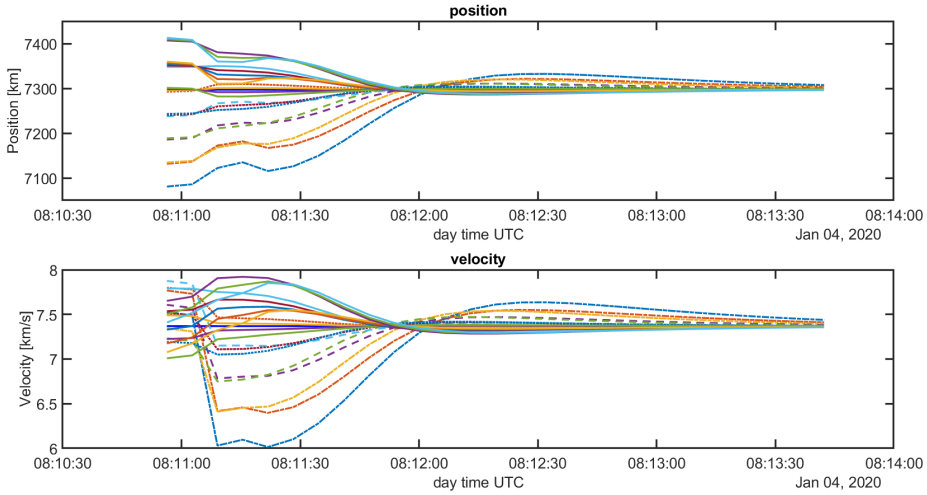

Figure 3.20: The hypotheses generated for satellite 6257U propagated and corrected with the EKF with SPG4-based observations. The EKF is applied on a single observation arc.

The final differences can be seen in table 3.20. The remaining difference can partially be explained by earlier discussed SGP4 implementations of Python and Matlab, discussed in the full chain validation, in section 3.1.4. The SGP4-based observations are obtained from the data file, generated by the Python script as part of Image Processing Algorithm. The SGP4 reference used in this validation is based on the Matlab implementation of the SGP4 theory. These implementations will not be fully identical and therefore result in small differences. The errors described in section 3.1.4, the full chain validation, are around the magnitudes of 100 meters.

Secondly, due to the progressively increase of accuracy for each epoch, the accuracy would increase even further in more data points where available. Therefore the limitations of the available data also tributes to the remaining error.

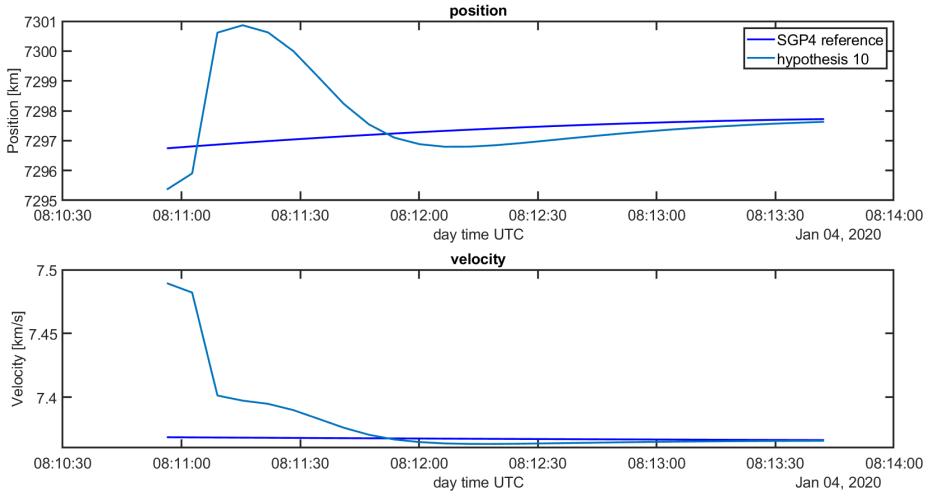

Figure 3.21: The best hypothesis generated for satellite 6257U propagated and corrected with the EKF with SPG4-based observations. The EKF is applied on a single observation arc.

Thirdly, the model errors, as discussed in the validation of the RKF4(5), in section 3.3.1, does also contribute to the remaining error. Despite these model errors the EKF is able to converge to the correct solution and therefore does not result in stability issues for single arc observations. The model errors where most apparent in low inclined satellites like the 10793U. The results of the EKF over time can be seen in figure 3.22 and 3.23

The divergence at the end of the observation arc can be caused by the model errors, which this satellite was more vulnerable to, but is can also be the Kalman filter that is still settling to the correct solutions.

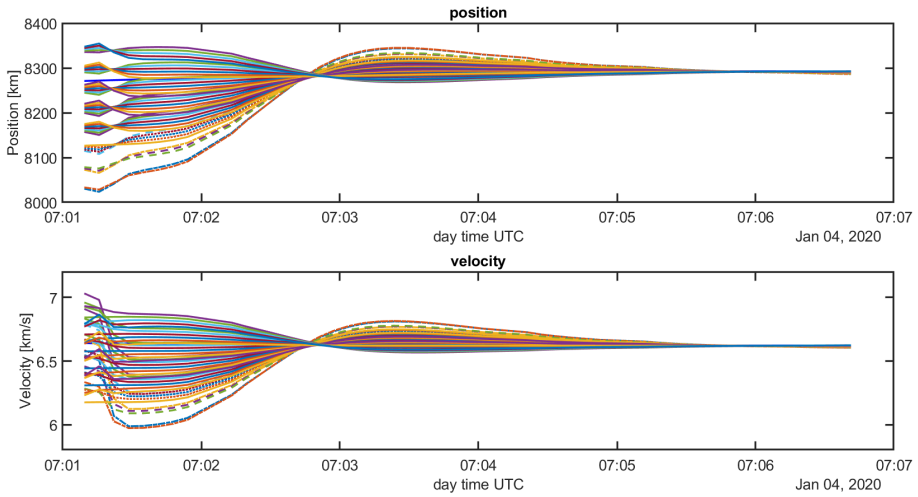

Figure 3.22: The hypotheses generated for satellite 10793U propagated and corrected with the EKF with SPG4-based observations. The EKF is applied on a single observation arc.

The remaining errors, as discussed in this section, are not significantly large to warrant any further investigation. When analysing observed data the observed position is based on a pixel. The pixel represents around a 0.02 degree angle of night sky. And the observations can also be off by one or two pixels. for a normal observation distance of 2000 km, this can result in divergences of around 2 km. Therefore the error in the EKF is small enough to be accepted.

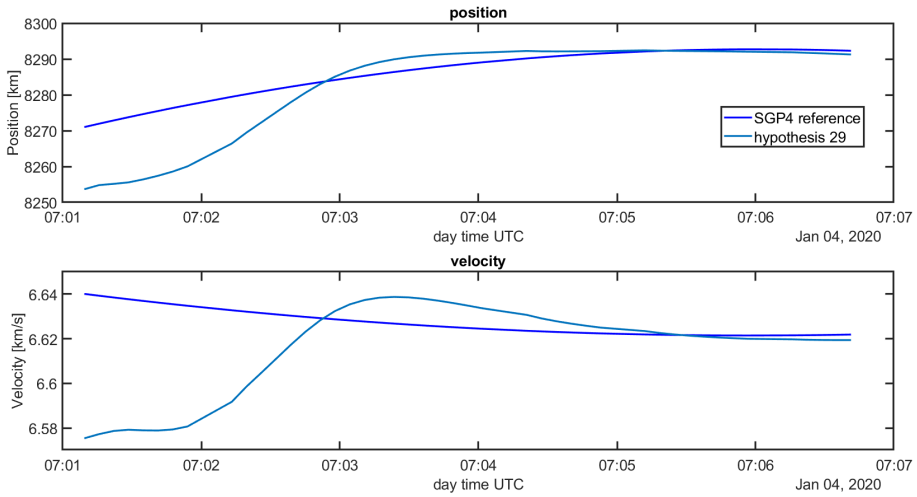

Figure 3.23: The best hypothesis generated for satellite 10793U propagated and corrected with the EKF with SPG4-based observations. The EKF is applied on a single observation arc.

Model error may become larger between observation arcs because the there is no data to correct the state. Therefore next, an analysis of the EKF for multiple arc observations will be performed in the next section.

Multiple-arc observations

The previous section has shown that the EKF works for a single observation arc. Now the EKF will be tested for multiple observation arcs. In order to validate this, a separate model was created, so that one is not dependent on the observed data from the telescopes.

The program propagated the state of the satellite with the EKF and uses generated observations. Here the number of observations in single observation arc and the duration of the gab can be manually selected in increments of 6.4 seconds, since this is the standard time between observations.

The program uses the TLE available at the third of January 2020 for each satellite as input. Satellite 38771U, 6257U, and 10793U are used. Table 3.21 described the Key orbital elements of these satellites. These satellites where selected due to their spread in orbital elements, especially inclination, resulting in representative sample.

Table 3.21: Key orbital elements for satellites used for the multi-arc EKF validation. The wide range in orbital elements like eccentricity, perigee, inclination, and semi-major axis is used to have a repressive sample

Satellite	38771U	6257U	10793U
Inclination [deg]	98.7	81.3	28.2
semi-major axis [km]	7198	7249	7618
Eccentricity	0.0002	0.005	0.09
Perigee [km]	826.0	836.2	574.9

The SGP4 algorithm calculates the reference state for the modelled period. The initial state at the first epoch plus an offset will be used as initial conditions for the EKF. The offset is determined, based on the initial offsets that where observed in the previous section, for the single arc EKF validation. These offsets are given in table 3.22 for satellites 4794U, 6257U, 222884U, and 23404U. The average offset between these satellites and the order of magnitude of these averages are used as initial offsets in the model. This means that the initial position offset is 10 km and the initial velocity offset is 100 m/s per axis.

The duration of the observation arc is set to 90 observations and approximately 10 minutes. This is based on the period that a LEO satellite is visible, under perfect conditions, from a stationary position on Earth. As an indication, at the time of writing, satellite 10793U has an observation duration of approximately 11.5

minutes, satellite 6257U approximately 10 minutes, and satellite 38771U 9.5 minutes, as found on `https://www.n2yo.com/`. This is only used as an indication. DeMars used in his study *Initial Orbit Determination using Short-Arc Angle and Angle Rate Data* [10] an observation period of 10 minutes and no obstructions. The starting date for each simulation is 03-01-2020 00:00:00.

The period between observation arcs is set to approximately two hours. This is around the order of magnitude of a orbital period of a LEO satellite. For this validation 4 observation arcs will be simulated. The goal is to see if the EKF is able to provide accurate and stable orbital predictions. The EKF will be initialised with the standard settings as described in the method section.

Table 3.22: Difference between the initial state and the reference state for the best solutions used for the validation of the EKF for the single observation arc. Used as input for initial offset for the validation model of the EKF for multiple observation arcs.

	Satellite	4794U	6257U	22284U	23404U	Average
Position difference [km]	x	9.4912	1.8434	6.5972	2.4835	5.103825
	y	9.0534	0.736	6.5719	8.8112	6.293125
	z	41.0483	0.1303	61.6515	56.3521	39.79555
Velocity difference [m/s]	x	5.1	264.2	103.2	164.9	134.35
	y	139.7	73.8	120.1	35.3	92.225
	z	191.8	57.7	365.3	362.1	244.225

Table 3.23 shows the position and velocity error at the beginning of an observation arc, and at the end of the observation arc, for four consecutive observation arcs. The error is defined as the difference between the SGP4 reference orbit and the EKF solution.

Table 3.23: The position and velocity error at the beginning and the end of an observation arc for satellites 38771U, 6257U, and 10793U. The observation arc contains 90 observations over a period of approximately 10 minutes. The gab is approximately 2 hours long.

Satellite		38771U				6257U				10793U			
observation arc		1	2	4	4	1	2	3	4	1	2	3	4
Position error	Initial error [km]	17.3	0.009	0.5	1.0	17.3	28.9	76.9	4237.9	17.3	4.9	1.6	33.0
	Final error [km]	0.008	0.07	0.6	1.4	1.0	14.8	349.8	5421.3	0.3	4.3	74.9	1162.8
Velocity error	Initial error [m/s]	173.2	0.1	4.5	5.4	173.2	29.4	431.5	3253.7	173.2	10.6	137.7	647.2
	Final error [m/s]	0.006	0.1	2.5	3.8	1.3	32.4	598.4	7688.8	0.8	3.1	170.4	2014.0

It can be seen that for all satellites the error at the end of the first observation arc is much smaller then the initial error. This is expected and is similar to the single observation arc validation. It can also be seen that when comparing the errors at the end of the first observation arc with the error at the beginning of the second observation arc that the the propagation error for satellite 38771U is small.

For all satellites it can be seen that the errors increase per observation arc. This is an unstable behaviour. This can be seen more clearly when looking at behaviour of the satellite during the different observation arcs, as figures 3.24, 3.25, 3.26, and 3.27 show the difference between the SGP4-based reference and the EKF solution for the first, second, third, and fourth observation arc, respectively. (other satellites are shown in appendix F.2). Here it can be seen that the for the first observation arc the behaves as expected, where the first few observations are needed to settle, and then converge to the correct solution. The next the observation arcs show different behaviour where the mostly diverge first after some started to converge a bit. Resulting in larger errors at the final epoch of the observation arc, compared to the first epoch of the observation arc.

It is thought that this behaviour is caused an inaccurate estimation of the covariance matrix when propagating from one observation arc to another. As can be seen in equation 2.89, the covariance matrix is updated in time by the state transition matrix, and the state transition matrix is not able to propagate large time steps due to the linearization used. In order to test this, the analysis is repeated, where the covariance matrix is reset to its default value at the beginning of each observation arc. By applying this test, the probably error is removed from the equation.

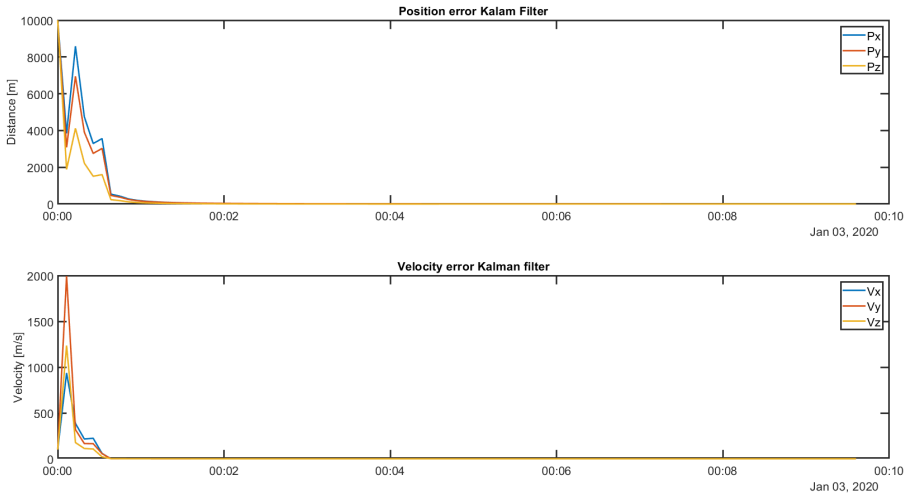

Figure 3.24: First observation arc for satellite 38711U, where the position and velocity difference between the SGP4-based reference state and EKF solution per epoch is visualised, for each separate element.

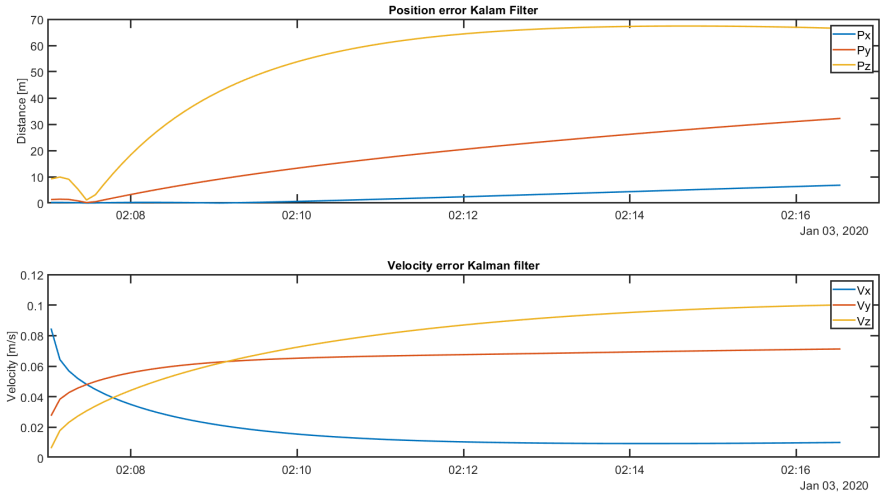

Figure 3.25: Second observation arc for satellite 38711U, where the position and velocity difference between the SGP4-based reference state and EKF solution per epoch is visualised, for each separate element.

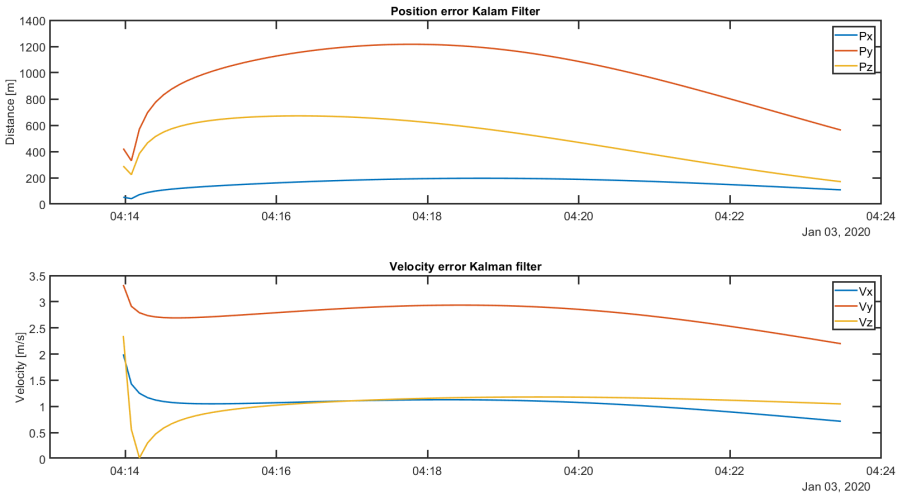

Figure 3.26: Third observation arc for satellite 38711U, where the position and velocity difference between the SGP4-based reference state and EKF solution per epoch is visualised, for each separate element.

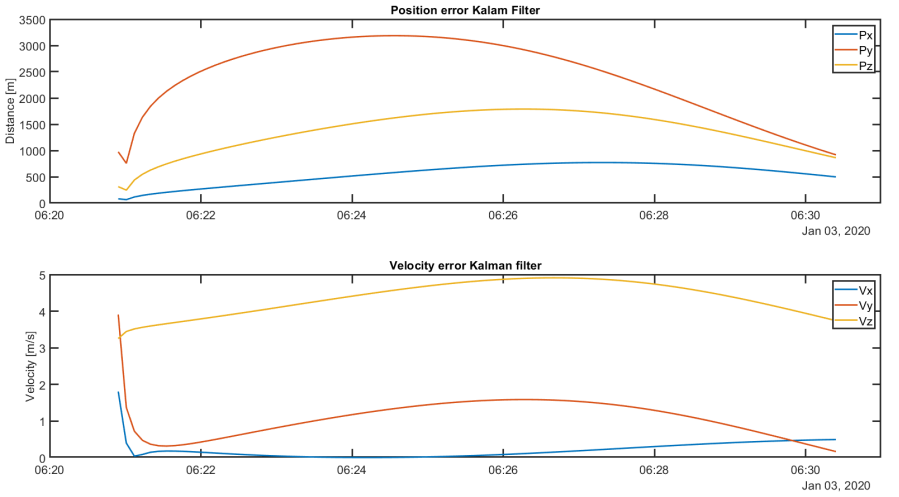

Figure 3.27: Fourth observation arc for satellite 38711U, where the position and velocity difference between the SGP4-based reference state and EKF solution per epoch is visualised, for each separate element.

Table 3.24 show the results of the earlier mentioned analysis. Here it can be seen that the error stays small for each observation arc for satellites 38771U and 6257U. Also the propagation errors are small. This is due to the earlier discovered fact the the propagation error resulting from the selected dynamical model, results in larger errors for satellites with a low inclination.

Here it can also be seen that the errors are smaller then the errors in the single observation arc validation. This is due to the different approaches. The single observation arc validation used observations calculated by the SGP4 method. For the multiple arc EKF validation new observations where generated for a given orbit in Matlab. Therefore the SGP4-based reference and the observations resulted from the same SGP4 model and therefore the errors can be smaller. Due to multiple observation arcs, more data is available, making it possible to closer converge to the correct solution.

Table 3.24: The position and velocity error at the beginning and the end of an observation arc for satellites 38771U, 6257U, and 10793U. The observation arc contains 90 observations over a period of approximately 10 minutes. The gab is approximately 2 hours long. In the beginning of each observation arc the covariance matrix is reset to its original values.

Satellite		38771U				6257U				10793U			
observation arc		1	2	4	4	1	2	3	4	1	2	3	4
Position error	Initial error [km]	17.3	0.01	0.04	0.2	17.3	5.8	0.1	0.2	17.3	1.0	1608.4	7846.4
	Final error [km]	0.008	0.04	0.004	0.02	1.0	0.05	0.04	0.01	0.3	247.4	496.9	$4.0 \cdot 10^8$
Velocity error	Initial error [m/s]	173.2	0.09	0.1	0.5	173.2	36.5	0.5	0.3	173.2	6.0	8860.7	15787.1
	Final error [m/s]	0.006	0.09	0.03	0.02	1.3	0.06	0.02	0.04	0.8	156.5	2120.5	$7.2 \cdot 10^8$

Figures 3.28, 3.29, 3.30, and 3.31 show satellite 38711U for the four different observation arcs where the covariance matrix is reset at the beginning of each observation arc. Here is can clearly be seen that each observation arc behaves as a single observation arc validation. It takes a few observation to settle in and then the solution converges to the reference solution.

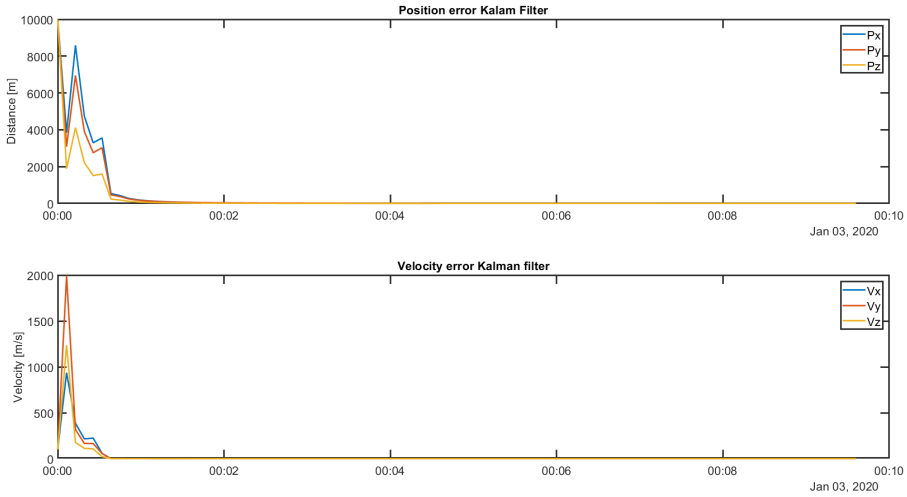

Figure 3.28: First observation arc for satellite 38711U, where the position and velocity difference between the SGP4-based reference state and EKF solution per epoch is visualised, for each separate element. Starting with an initialise covariance matrix.

On the basis of this last validation it can be shown that the EKF works correctly for each observation arc, but the translation of the covariance matrix from one observation arc to another causing problems. Since this is the only change that was made compared to the previous one.

As can be determined from the theory, the propagation of the covariance matrix with the state transition matrix is incorrect for large time steps, and therefore results in an incorrect covariance matrix at the beginning of the second observation arc. This causes the EKF to be less sensitive for the new observations, and thus puts too much confidence in the propagated solutions. Therefore the state is not improved on quickly and errors

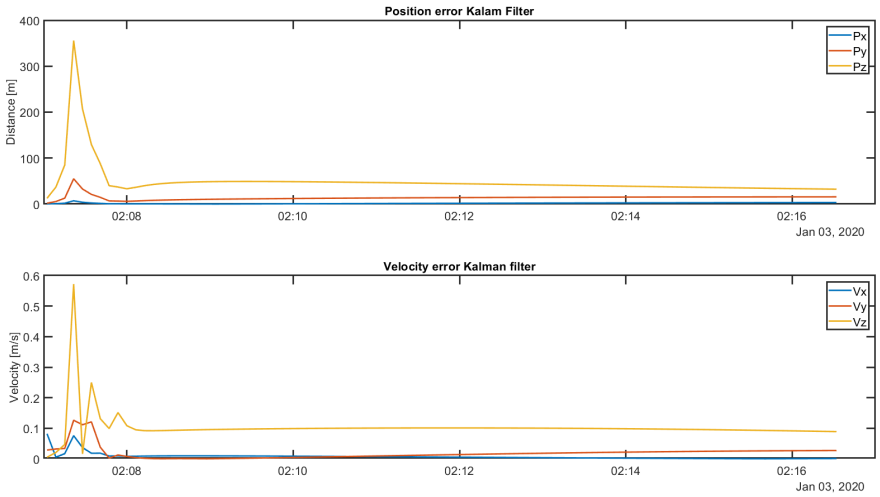

Figure 3.29: Second observation arc for satellite 38711U, where the position and velocity difference between the SGP4-based reference state and EKF solution per epoch is visualised, for each separate element. Starting with an initialise covariance matrix.

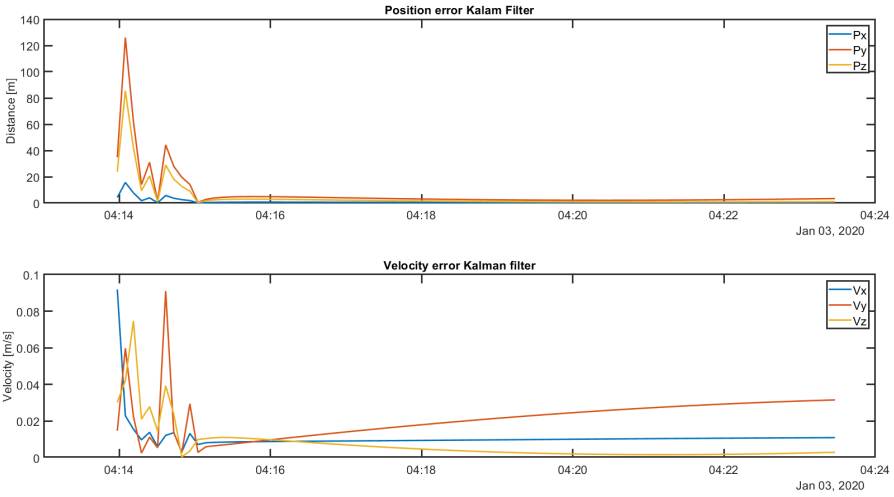

Figure 3.30: Third observation arc for satellite 38711U, where the position and velocity difference between the SGP4-based reference state and EKF solution per epoch is visualised, for each separate element. Starting with an initialise covariance matrix.

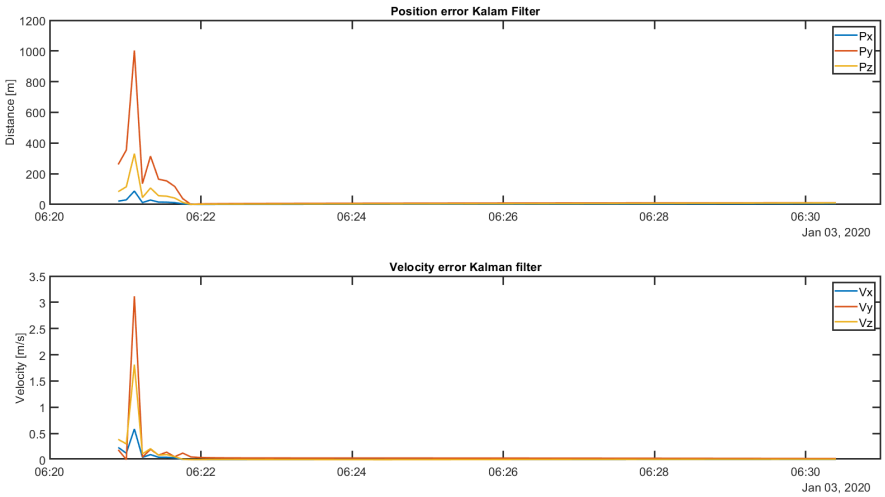

Figure 3.31: Fourth observation arc for satellite 38711U, where the position and velocity difference between the SGP4-based reference state and EKF solution per epoch is visualised, for each separate element. Starting with an initialise covariance matrix.

only starting to rise.

This is therefore probably the reason DeMars ([10], [11], [9] used an Unscented Kalman Filter for his application of the CAR-MHF. The UKF does not suffer from the problem that the EKF does have. The UKF does not propagate the covariance matrix but determines the covariance matrix based on propagated states, based on sigma points, and the spread of these different states determines the covariance matrix at each epoch. This only requires the method to propagate state. And as already shown in their research, this can be done with acceptable accuracy.

As could be seen for satellite 10793U, from the last analysis it would also be advised to add more perturbations to ensure stability when propagating from one observation arc to another. Especially since for this analysis an optimistic time between observations is used. In reality, with bad weather and limited ground stations, the time between observation arcs can be larger. Looking at figure 2.4 it would be advised to at the J5 effect, Lunar and solar gravity. Depending on the average perigee of LEO satellite atmospheric drag could also be added. For example for satellite 37347U with a perigee of 299.1 km, it could improve lightly but the change in apogee, as seen in figure 3.8, is 120 km over a period of three years. Also it can be seen that there are short period fluctuations, these are due to other perturbing forces like the J5 gravity term, lunar and solar gravity, which are equal or more potent at an altitude of 300 km, as can be seen in figure 2.4.

Therefore to improve the performance of the RKF4(5) to better ensure stable behaviour between observation arcs the dynamical model needs significant improvements by adding the J5 effect, lunar and solar gravity and drag. The principal error of the EKF, when propagating the covariance matrix over large time steps, is still not solved when adding these perturbing forces to the dynamics of the RKF4(5).

Following these recommendations a though experiment was performed in the possible mathematical ambiguity when atmospheric drag is added to a short arc application of the EKF. The thought experiment looked at the possibility for having multiple solution when atmospheric drag is one of the estimating parameters of the EKF, when the range is not directly measured. Since the atmospheric drag is not added in this research, it is not part of the research. For the interested reader, the thought experiment is presented in appendix H.

The scope of this research is to use the EKF as part of the CAR-MHF. Also the cause of the shortcomings of the EKF was found in a late stadium of this research, with a large amount of time invested in it. Therefore it is not feasible anymore to change the Kalman filter to a Unscented Kalman filter. This will be a recommendation for future research. Together with this recommendation is to add the earlier described perturbing forces, to improve stable behaviour between observation arcs. This research will stay within its scope of the EKF, and

will therefore only analyse the IOD for single observation arcs. If it is not possible to find an IOD within a single observation arc, then these results can not be analysed.

3.3.3. Elimination criterion

For the self-developed elimination criteria it is extra important to verify that the algorithm works as intended, and validate the correct values and solutions are found. The elimination criteria will be tested for multiple satellites for a single observation arc for SGP4-based observations. These observations have, in theory, no measurement errors and should therefore show stable performance. This is called the verification step. The next step is to validate the performance of the elimination criteria for the image based observations to validate the performance. The best performance can be tuned with the average value, n as described in equation 2.98, to find out over how many observations the elimination criteria needs to average over, in order to not be susceptible to the measurement uncertainty. This will be the validation step of the algorithm

Verification of the elimination criteria

For the verification satellites with SGP4-based observations (similated data points) are used for a single observation arc, going through the full process of the CAR-MHF. The default settings for the CAR-MHF, as described in the methodology, are used. The following five satellites are selected for this verification.
For the verification of the elimination criteria the following 5 satellites are selected:

- Satellite 4794U, station LS, 03-01-2020, 58 data points, 05:38 minute time span.
- Satellite 6257U, station LSE, 03-01-2020, 25 data points, 02:52 minute time span.
- Satellite 10793U, station LSN, 03-01-2020, 48 data points, 05:38 minute time span.
- Satellite 22284U, station SAE, 03-01-2020, 30 data points, 03:05 minute time span.
- Satellite 23404U, station AUE, 03-01-2020, 26 data points, 02:52 minute time span.

These where selected due to their difference in orbital elements, number of data points, different ground stations, and duration of the observation arc.

Figure 3.32 shows an example of the CAR-MHF for the observations made for satellite 10793U. It illustrates that when the residual increases the line stops due to the fact that the hypothesis is eliminated. Around 07:01:45 the penultimate hypothesis is eliminated and one hypothesis remains.

In order to assess the quality of the elimination criterion it is checked if the hypothesis that remains is also the best representation of the state. Figure 3.33 shows for each hypothesis the root sum square of the position and the velocity vector following from the CAR-MHF. In this figure the blue line that looks straight is the SGP4-based solution, which is used as a reference state of the satellite. In the figures it can be seen that the hypotheses furthest away are eliminated first until all hypotheses except one are eliminated according to the elimination criterion. The last remaining hypothesis is also the state closest to the reference line.

Finally the constrained admissible region is looked at. Figure 3.34 shows the constrained admissible region, where the red cross represents the SGP4-based state, and the blue dot with the red circle is the hypothesis that was selected through the MHF. Here it can clearly be seen that the selected hypothesis is close to the SGP4-based state.

These verification steps are performed for all five satellite, from different ground stations. This to ensure that the method works reliably and for the different ground stations. The results can be seen in appendix C. All five satellites show similar results, therefore the method is working as intended, and is therefore verified.

Validation of the elimination criteria.

When analysing real measurements, measurement errors are introduced. When one observation has a large measurement error at one point, then an hypothesis can be eliminated incorrectly. To counter this, the average residual of the last n (see equation 2.98), observations is used to determine if a hypothesis needs to be

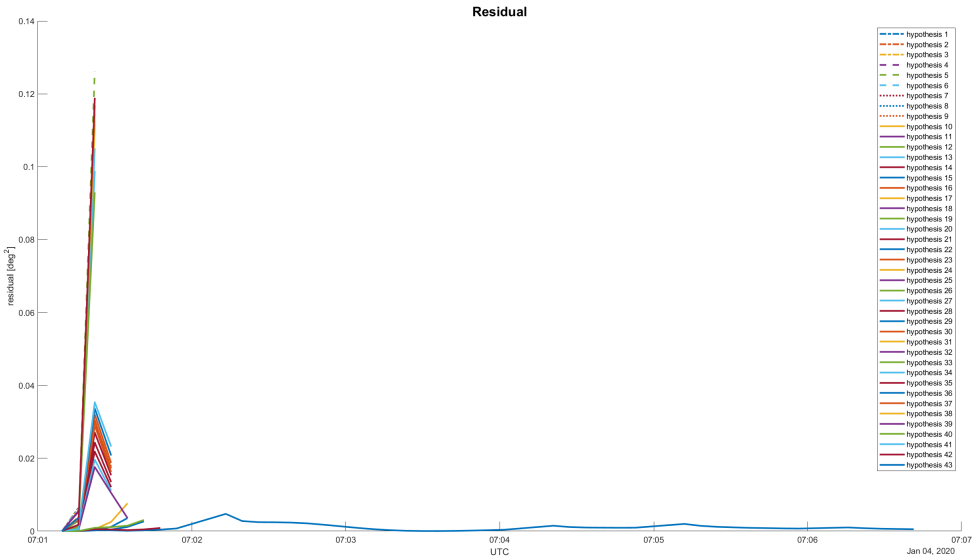

Figure 3.32: Satellite 10793U residual during the first observation arc. The residual line stops when a hypothesis is eliminated.

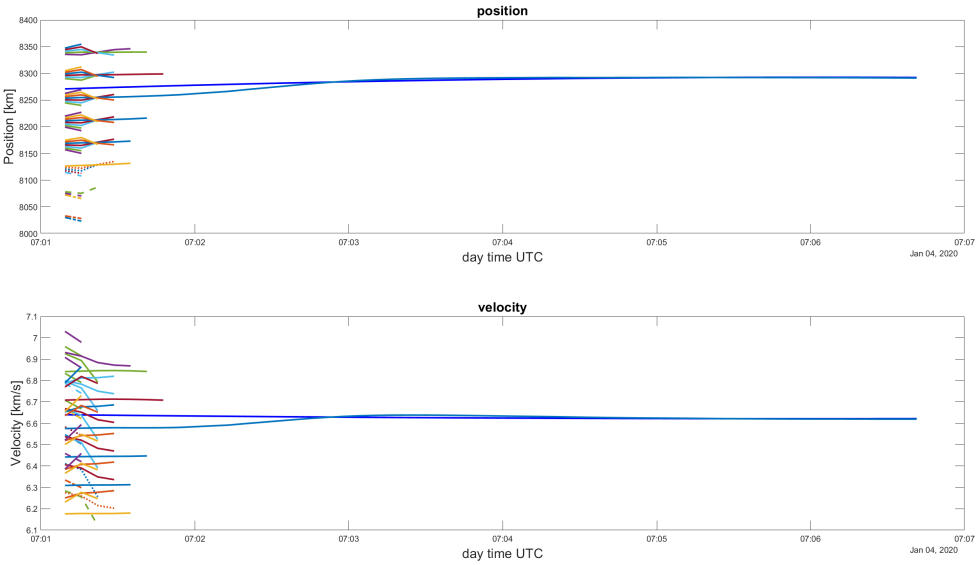

Figure 3.33: Satellite 10793U resulting position and velocity at each epoch for each hypothesis selected from the CAR over the duration of an observation arc. The blue line is the SGP4 state of the satellite, the expected solution. Hypothesis line stop when the hypothesis is eliminated.

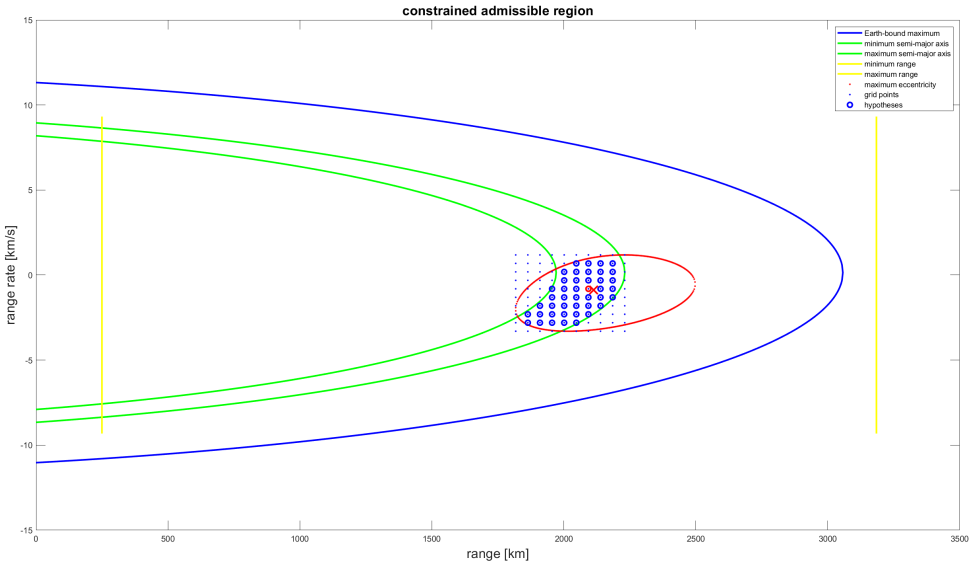

Figure 3.34: Satellite 10793U, constrained admissible region with the range, semi-major axis and eccentricity constraint. The blue dots represents the grid, and the blue circled dots represents the selected hypotheses. The red dot is the resulting hypotheses after the CAR-MHF with the described elimination criteria, and the red cross represents the SGP4-based correct state.

eliminated.

To determine the best value for n, four satellites are tested for values of n between one and nine, in steps of two. nine is selected as upper bound, since the larger the value for n, the more data points are needed to converge to a single solution, most probably. Therefore having higher values for n will make it so that the method is not applicable anymore for the short observation arcs used in this research.

The following satellites are used for this validation:

- Satellite 10793U, station LSN, 03-01-2020
- Satellite 23404U, station AUE, 03-01-2020
- Satellite 36095U, station LS, 03-01-2020
- Satellite 40113U, station LS, 03-01-2020

The results can be found in appendix D, where the state error at the convergence point and the state error at the end of the observation arc are shown. Also the number of observation to converge to a single solution and the computation time are given. Secondly for each value of n, for each satellite, the position and velocity scalars are plot for each epoch. This will show the development of the different hypotheses during the propagation of the EKF.

Table 3.25 shows the average state error for all satellite at the convergence point, and at the end of the observation arc. Here it can be seen that when the value for n increases the computation time increases and the number of observations required to converge increase. It can be seen that the error at the convergence point decrease for higher values of n. The error at the end of the observation arc stays relative constant.

The position and velocity errors are significant larger compared to the previous section. This is due to the use of measurements with measurement uncertainties. The performance of the algorithm in combination with the measurements will be looked at in dept in the next chapters of this report. Therefore in this section no further comments will be placed on the magnitude of the values. The error at the convergence point decreases for increased value on n, this is expected since more data points are required for larger numbers of n

Table 3.25: Validation for the elimination criteria for different values for, n, the number over which the average is taken.

n	1	3	5	7	9
hypotheses	22.75	22.75	22.75	22.75	22.75
epochs to conversion	5.50	10.25	12.75	25.00	23.75
At convergence point					
Position error [km]	132.40	78.25	89.90	42.48	24.18
Velocity error [m/s]	464.40	525.63	392.85	222.68	143.33
At the end of the arc					
Position error [km]	12.10	21.80	18.51	13.88	12.95
Velocity error [m/s]	67.91	56.23	78.65	50.21	59.43
Time [second]	12.23	18.40	24.92	33.19	38.12

to converge, therefore more data is available, and therefore the error becomes smaller.

The error at the end of the observation arc does not show a trend, therefore the performance is independent of the value of n. Figures 3.35, 3.36, 3.37, and 3.38 show the final hypothesis for each value of n fur the duration of the observation arc, for satellites 10793U, 23404U, 36095U, and 40113U, respectively. Appendix D shows for each separate case the hypotheses elimination over time. Here it can be seen that each hypothesis that is selected by this method is able to converge to the correct solution. Despite the fact that the MHF does not always select the closest hypothesis to the SGP4-based solution, non of the hypotheses that are selected by the MHF, for any value on n diverges. This also explains why the average error at the end of the observation arc is independent of n. Figure 3.38 shows only three lines, this is due to the fact that the CAR-MHF selected the same hypothesis for the n value of 1, 7, and 9, therefore these lines are stacked on top of each other and it looks like a single line.

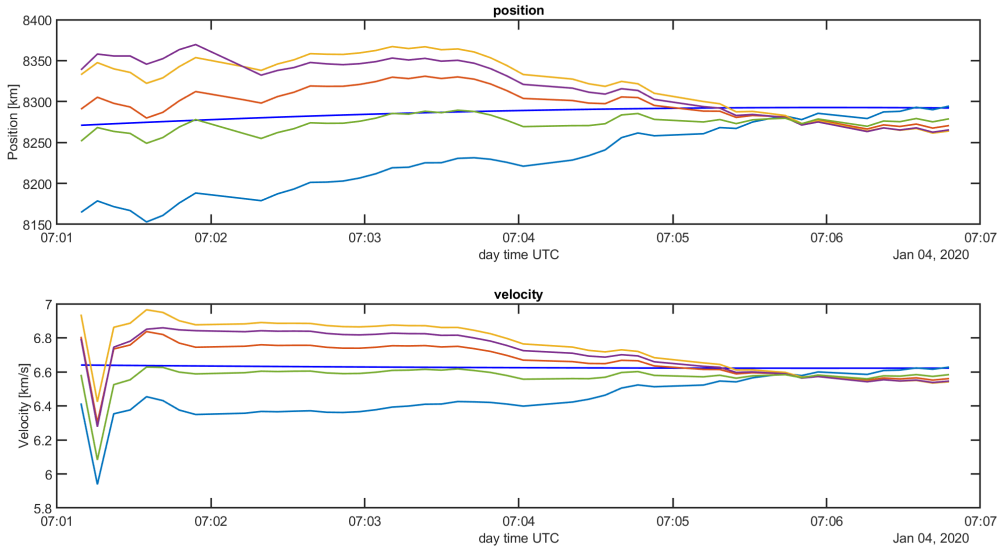

Figure 3.35: Satellite 10793U resulting position and velocity at each epoch for the final remaining hypothesis from the CAR-MHF. The blue line is the SGP4 state of the satellite, the expected solution. The other lines represents the 5 different solutions for the 5 different values of n.

All the satellites, for each value of n is able to converge to the solution, the MHF and its elimination criteria works as intended. The data set used for this research will not have huge outliers since a measurement is only linked to a specific satellite when it is within 10 pixels of the expected satellite in the image. Therefore limiting the maximum error to 0.2 degrees, and no large spike errors can occur. For this research we will use a value of n equals to one, and therefore no weighted average is applied. When there could be single outlier events in the data, it would be recommended to uses an average to limit the impact of outliers.

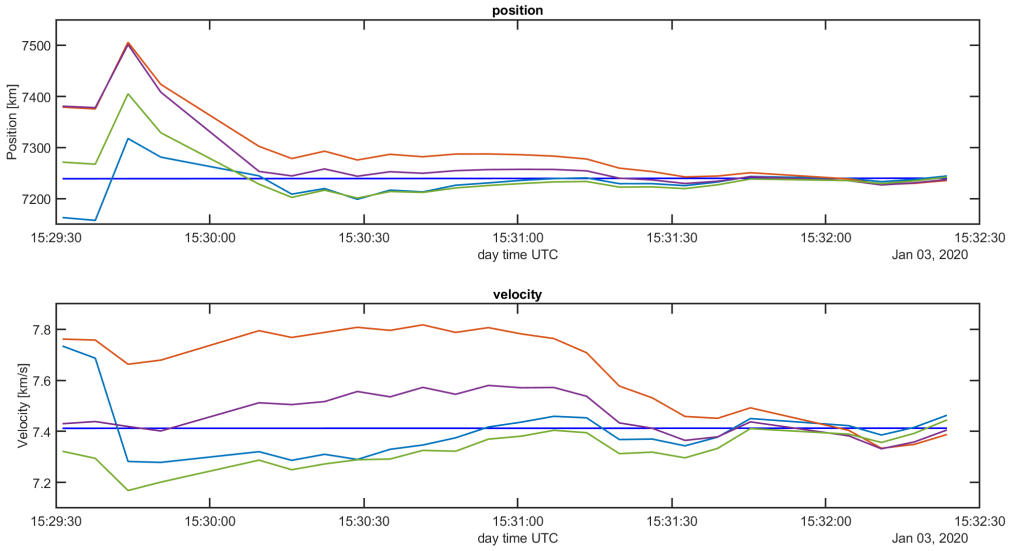

Figure 3.36: Satellite 23404U resulting position and velocity at each epoch for the final remaining hypothesis from the CAR-MHF. The blue line is the SGP4 state of the satellite, the expected solution. The other lines represents the 5 different solutions for the 5 different values of n.

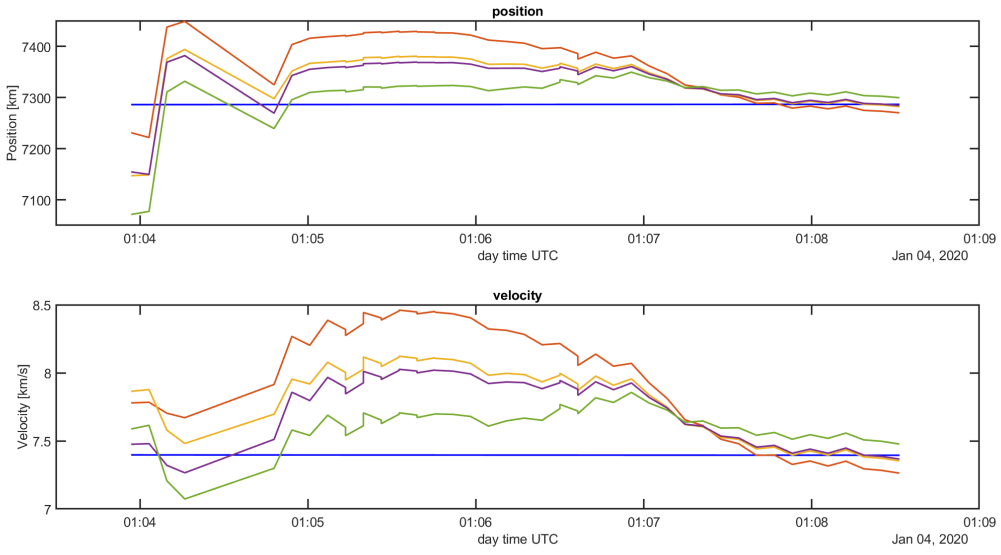

Figure 3.37: Satellite 36095U resulting position and velocity at each epoch for the final remaining hypothesis from the CAR-MHF. The blue line is the SGP4 state of the satellite, the expected solution. The other lines represents the 5 different solutions for the 5 different values of n.

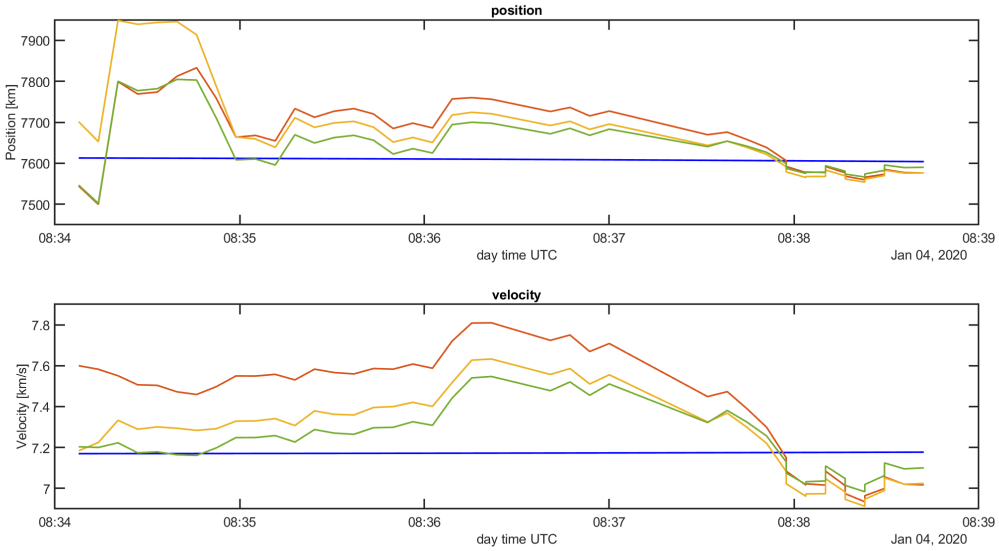

Figure 3.38: Satellite 40113U resulting position and velocity at each epoch for the final remaining hypothesis from the CAR-MHF. The blue line is the SGP4 state of the satellite, the expected solution. The other lines represents the 5 different solutions for the 5 different values of n.

4

Results

This chapter discusses the results. Section 4.1 discusses the performance of the CAR-MHF for 10 satellites which had the most observations in a single observation arc available. This analysis is performed to obtain detail insight and knowledge of dynamics of the problem. This detailed level of analysis is not possible for all 242 satellites, therefore the best 10 candidates are analysed first. With this knowledge the results of the overall performance of the CAR-MHF for all 242 satellites for which the CAR-MHF found a solution within a single observation arc is analysed. This can be seen in section 4.2. Section 4.3 presents a comparison between Gauss' method and the CAR-MHF for initial orbit determination. Finally, section 4.4 discusses the characteristics like radar cross section. but also the orbital elements: semi-major axis, eccentricity and inclination of the observed satellites.

4.1. CAR-MHF: performance analysis

The CAR-MHF is applied to single arc observations, as discussed at the end of the validation. The observation, as determined by the IPA, will be used as measurement. Using these observations enable the analysis of the performance of the algorithm, without having previous knowledge of the satellite. As reference the SGP4 theory will be used to determine the accuracy of the solutions.

The SGP4 based orbital elements discussed in this section are determined at each epoch. The reference orbital elements can not be directly obtained from the TLE, the TLE's describes mean orbital elements. For this reason each TLE is propagated to the epoch of interest and converted to Kepler elements. For this reason, when comparing results, the osculating orbital elements are presented, and can correctly be compared to the solutions from the CAR-MHF.

For the analysis a single ground station is used, and the data is stopped if the time between observations is larger then 20 minutes. Since contact time between a LEO satellite and a stationary ground station withing a single overpass can not realistically be larger. This to ensure the shortcomings of the EKF for large time step propagation will be limited to a minimum. Ten different satellites are used for this analysis with different orbital characteristics, contact time, number of observations and ground stations. The LEO satellites which had a large number of observations where selected to ensure a proper analysis. The satellites used for this analysis are shown in table 4.1. The default settings, as described in the methodology chapter, for the CAR-MHF.

Table 4.1: Characteristics of the 10 satellites used to analyse the performance of the CAR-MHF for track-based observations. Differentiating the satellites for inclination, semi-major axis, eccentricity, number of observations, observation duration, and ground station.

Satellite	23404U	38771U	10793U	10954U	25510U	29499U	4794U	25885U	22284U	39260U
Inclination [deg]	71.1	98.8	28.2	28.3	31.4	98.6	101.7	51.9	71.1	98.7
semi-major axis [km]	7225.9	7199.5	7623.1	7450.2	7148.3	7201.8	7831.7	8342.5	7226.4	7218.4
Eccentricity	0.0021	0.0011	0.0878	0.0696	0.0324	0.0008	0.0030	0.0006	0.0021	0.0007
number of observations	26	24	52	74	44	34	28	46	30	30
observation arc [mm:ss]	02:52	02:14	05:38	08:24	02:26	04:08	02:39	04:59	03:05	02:52
Ground station	AUE	AUE	LS	LS	LS	LS	LSC	LSE	SAE	SAE

For each satellite the SGP4 reference and the CAR-MHF solution is expressed in Kepler coordinates. For each satellite the development of the EKF solution over the period of the observation arc is calculated. For example, 4.1, shows the solution of the CAR-MHF for a single observation arc on the third of January, from the ground-station of La Silla.

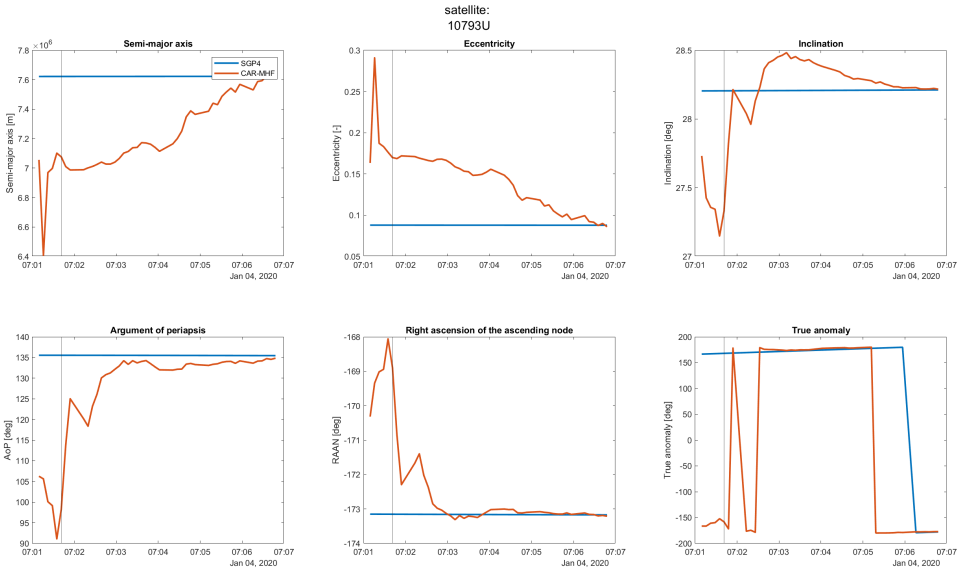

Figure 4.1: The solution of the CAR-MHF for a single observation arc for satellite 10793U on the third of January over ground station La Silla. The track-based observations are the measurements used for the EKF. Here the blue line is the SGP4-based reference and the orange line is the CAR-MHF solution. The grey line is the convergence point of the CAR-MHF filter.

In this graph it can clearly be seen that that the solution improves over time, since the orange line comes closer and closer to the SGP4-based reference line, as more data points are added. The solution of the CAR-MHF is not shown as a smooth line. This is due to the fact that the observations are not fully correct due to observation errors. Similar graphs for each satellite are available in appendix I. The vertical grey line indicated the moment where the CAR-MHF eliminated all but one hypothesis. Almost all show that the CAR-MHF solution still improves significantly over the duration of the observation arc. For the CAR-MHF, within a single observation arc, there is no reason not to use the remaining observations available in the observation arc to improve the solution. None of the 10 solutions of the satellites in this analysis of the CAR-MHF show unstable, divergent, behaviour, therefore the early and inaccurate IOD solution after convergence is not an issue.

4.1.1. Eccentricity

For each satellite an error is determined. This error is determined at the last available data point and is the difference between the CAR-MHF and the SGP4-based reference, expressed in Kepler elements. The difference can then also be expressed as a percentage difference. This is defined as the error divided by the SGP4-based Kepler element value, times 100%.

This percentage error is calculated for each satellite and presented in the box plot in figure 4.2. Here it can be seen that the eccentricity error is by far the largest error. This can also be seen when looking at the individual satellites in appendix I. This is an expected result, since the observation arcs only views a small section of the full orbit. This phenomena will be discussed in more detail later in this section.

4.1.2. Argument of periapsis and True anomaly

Another box plot of the percentage error is shown, but now without the eccentricity in order to observe the percentage error for the other Kepler elements. Figure 4.3 shows this box plot. Here it can be seen that the

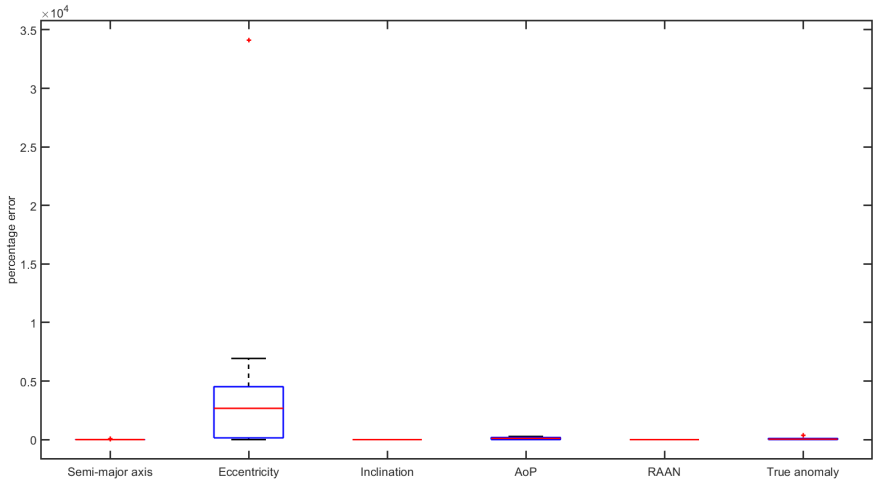

Figure 4.2: Box plot of the percentage error of the Kepler elements at the end of each observation arc of the 10 analysed satellites. The percentage error is the percentage of the error compared to the SGP4-based orbital element of the satellite.

Argument of periapsis and the True anomaly show the largest error. The Argument of periapsis points at the perigee of the orbit. When the eccentricity can not correctly be determined due tot the small observation arc, it follows than that the Perigee can also be harder to determine accurately. The angle-only observations do make it possible to determine the projected position of the satellite. So a shifted Argument of periapsis will result in a shift in True anomaly. Figure 4.4, for satellite 10954U shows this effect neatly.

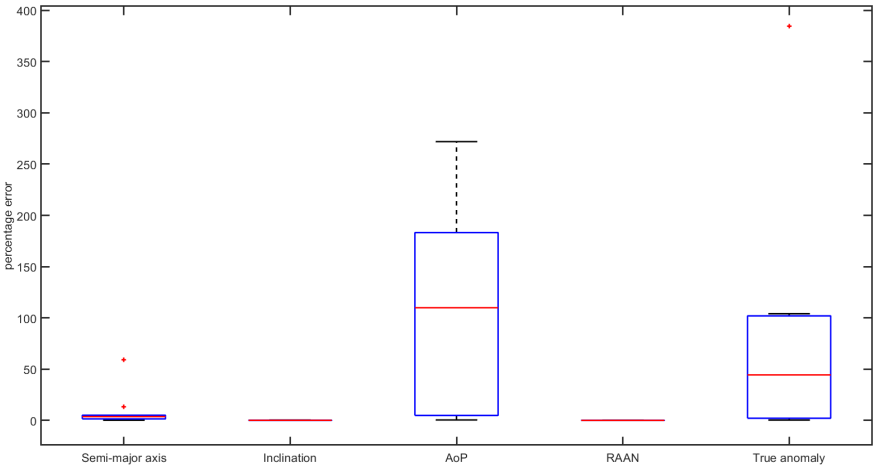

Figure 4.3: Box plot of the percentage error of the Kepler elements at the end of each observation arc of the 10 analysed satellites. The percentage error is the percentage of the error compared to the SGP4-based orbital element of the satellite. The eccentricity error is excluded in this box plot.

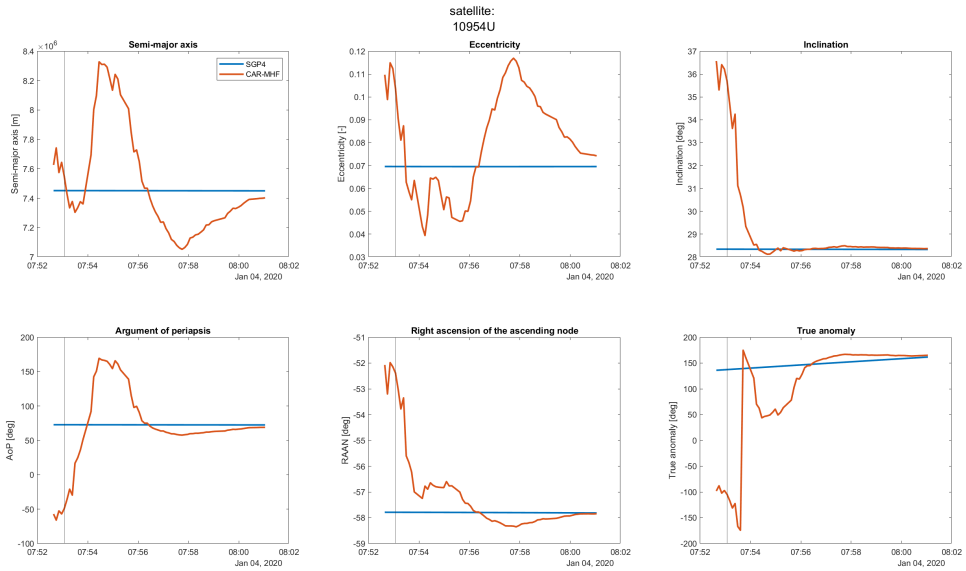

Figure 4.4: The solution of the CAR-MHF for a single observation arc for satellite 10954U on the third of January over ground station La Silla. The track-based observations are the measurements used for the EKF. Here the blue line is the SGP4-based reference and the orange line is the CAR-MHF solution. The grey line is the convergence point of the CAR-MHF filter.

Following this line of reasoning, adding the error of the Argument of periapsis and the True anomaly would cancel this effect. The addition of the Argument of periapsis and True anomaly over the period of a short observation arc, for satellite 23404U, is shown in figure 4.5. For all other satellites, these graphs are shown in appendix I.

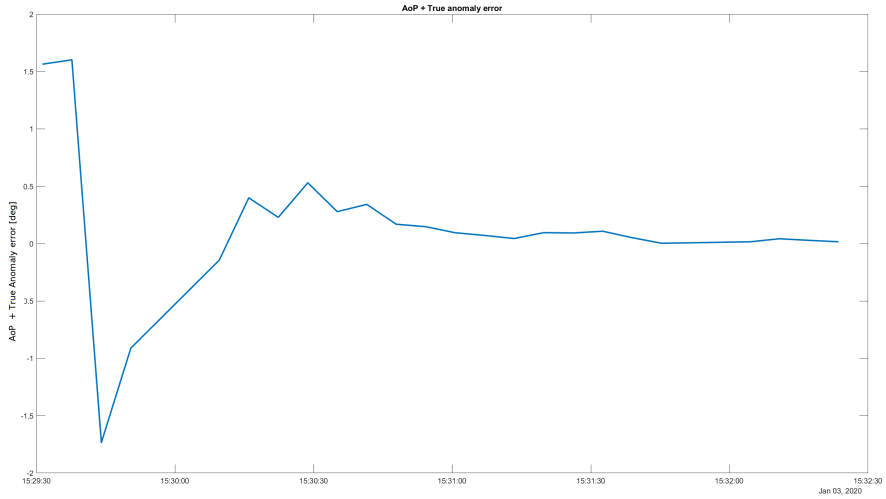

Figure 4.5: The addition of the Argument of periapsis and the True anomaly errors over the short arc observation of satellite 23404U, on the night of the third of January, by the ground station in Australia.

It can be seen that the addition of these two orbital elements show a relative small error. This confirms that the position in the orbit is accessed with a fair accuracy, but the orbit itself is not accurately determined. Figure 4.6 shows a box plot of the error of the argument of periapsis added to the error of the True anomaly for all 10 satellites, at the end of each observation arc, in degrees. Here is can be seen that with a median of around 0.05 degrees the error is small.

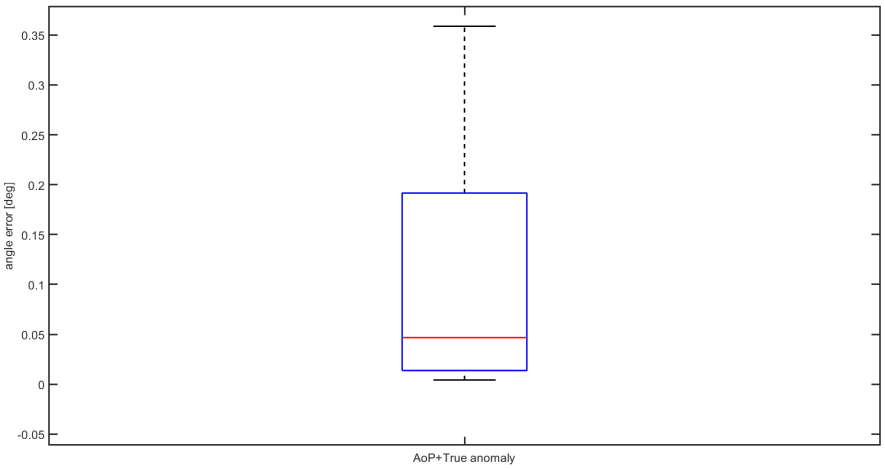

Figure 4.6: Box plot showing the addition of the error of the Argument of periapsis and the True anomaly for all 10 satellites at the end of the observation arc.

4.1.3. Semi-major axis

Now only showing the box plot for the percentage error of the semi-major axis, inclination, and Right Ascension of the Ascending node (RAAN). This is shown in figure 4.7. Here it can be seen that the semi-major axes has the next largest percentage error, with two outliers, satellite 38771U and 4794U. These outliers require an extra look.

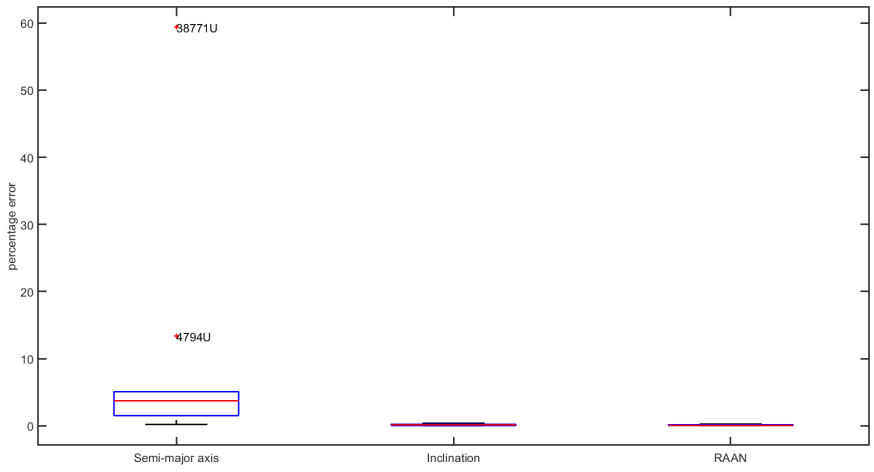

Figure 4.7: Box plot of the percentage error of the Kepler elements at the end of each observation arc of the 10 analysed satellites. The percentage error is the percentage of the error compared to the SGP4-based orbital element of the satellite. The eccentricity, Argument of periapsis, and True anomaly error is excluded in this box plot.

Satellite: 38771U

The CAR-MHF solution of for satellite 38771U is shown in figure 4.8. Here it can be seen that the CAR-MHF found another semi-stable solution for these observations. This can be seen at the CAR-MHF lines being steady away from the SGP4 reference, without clear signs of closing the gab. The semi-major axis and eccentricity show a large off-set, and the orbital elements are looked closer at to determine what semi-stable solution was found.

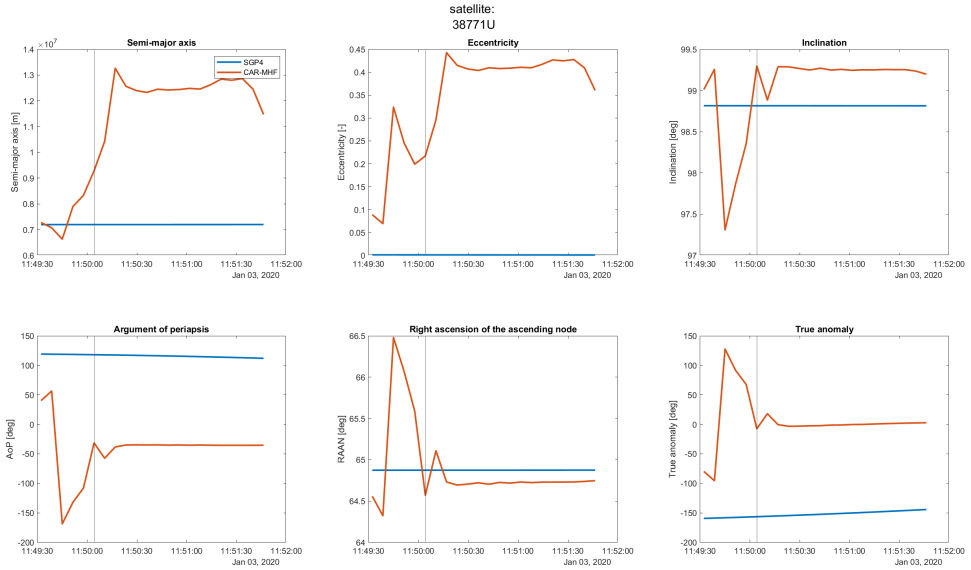

Figure 4.8: The solution of the CAR-MHF for a single observation arc for satellite 38771U on the third of January over ground station Australia. The track-based observations are the measurements used for the EKF. Here the blue line is the SGP4-based reference and the orange line is the CAR-MHF solution.

Figure 4.9 shows a schematic representation of the SGP4 reference orbit, a near circular orbit, presented in blue. In green, the semi-stable CAR-MHF solution is drawn. The short red line represents the observation arc. Here it shows that for the short observation arc, both orbits can be fitted with reasonable good results. With another observation arc, somewhere else in the orbit would have been available and would have been used, the EKF, as part of the CAR-MHF, would have noticed the difference in orbits, and therefore would have corrected itself. Therefore the CAR-MHF solution was described as a semi-stable solution, since when the observation arc would be longer, or a second observation arc would be added, the found solution would collapse to the true orbit. The dip at the last two observation could indicate that at the end of the observation arc, it started to correct itself.

Due to the limitations of the current method, a second observation arc can not be added, without introducing large, fundamental errors, resulting in unstable behaviour. This example illustrated the short comings of using short arc-angle only observations.

Satellite: 4794U

Similar to satellite 38771U, in the previous section, satellite 4794U shows a similar semi-stable solution. This can be seen in figure 4.11. Here the semi-major axis is smaller then the SGP4-based reference orbit. The solution found by the CAR-MHF fitted the observation arc through the apogee of the semi-stable solution.

Figure 4.11 shows the SGP4-based reference orbit, CAR-MHF solution in green, and the short red line represents the observation arc. This also visualises how both orbits could be feasible when only short arc angle observations are available. The inclination and RAAN do not play a part in this phenomena, since these determine the orbital plane.

4.1.4. Inclination and Right ascension of the ascending node

The box plot of the inclination and RAAN both show small percentage errors, as shown in figure 4.12. When looking at figure 4.1 it can be seen that the initial error for the inclination and RAAN are small. The hypotheses generated by the CAR-part of the algorithm are based on three sets of angle observations, resulting in an

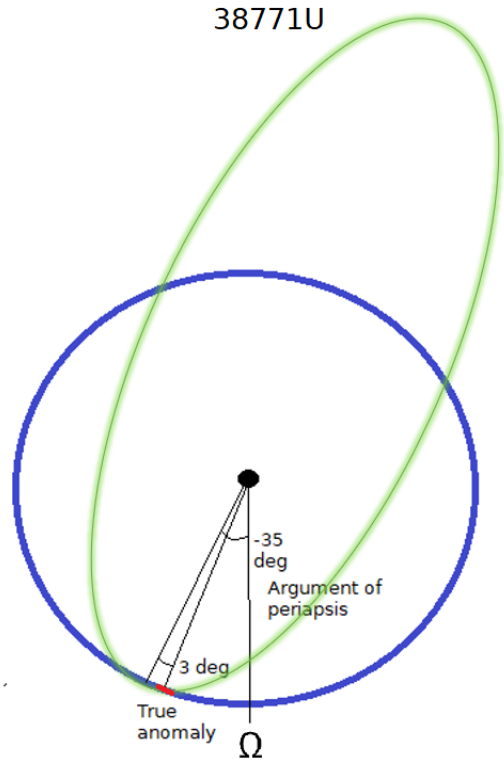

Figure 4.9: Schematic representation of the SGP4 orbit (Blue line) and the semi-stable solution found by the CAR-MHF (green line) for satellite 38771U. The short red line indicated that observation arc.

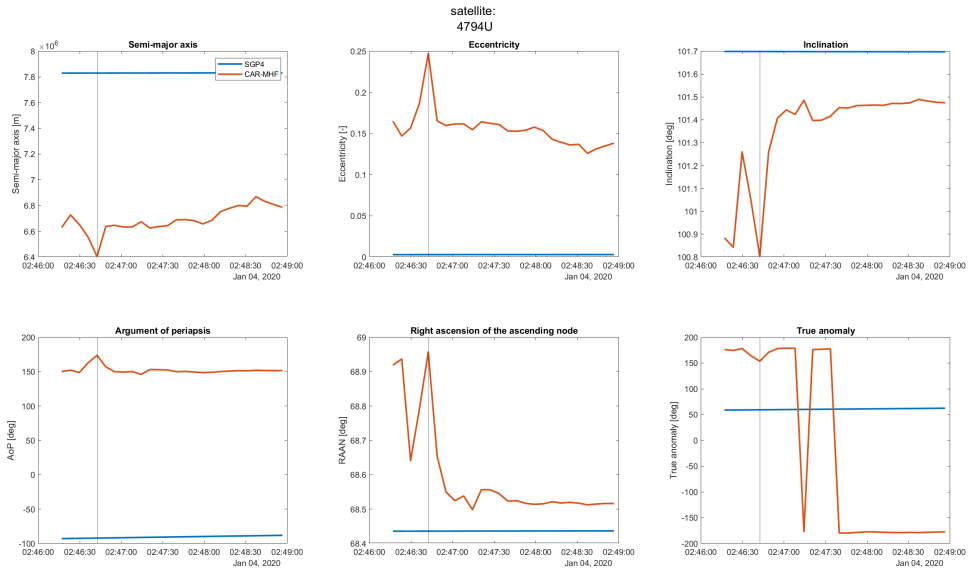

Figure 4.10: The solution of the CAR-MHF for a single observation arc for satellite 4794U on the third of January over ground station La Silla„ central camera. The track-based observations are the measurements used for the EKF. Here the blue line is the SGP4-based reference and the orange line is the CAR-MHF solution.

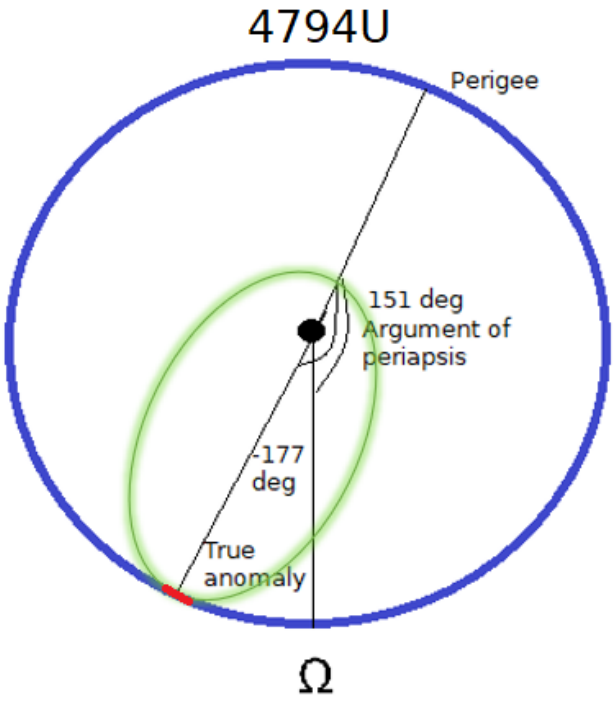

Figure 4.11: Schematic representation of the SGP4 orbit (Blue line) and the semi-stable solution found by the CAR-MHF (green line) for satellite 38771U. The short red line indicated that observation arc.

reasonable fit of the orbital plane, depending on the measurement errors. Over the period of the observation arc, these measurement errors are averaged out by the EKF, as part of the MHF, resulting in even better approximations of these two orbital elements.

General CAR-MHF short arc characteristics

Figure 4.13 shows a box plot of general arc and CAR-MHF performance characteristics for the analysed 10 satellites. The number of observations required for the CAR-MHF to converge to a single solution is between 5 and 7, with its median on 6. This is a relative small number of observations, making it possible to apply the method for observation arcs with a small number of observations. The quality of these results are then expected to be poor. Propagating inaccurate states over larger periods of time, without observations to counter propagation errors, will most probably result in unstable behaviour, but is not part of this research. The time between the first observation and the observation at which the CAR-MHF solution converged is with a median of 32 seconds relative short.

The duration of the observation arcs for all 10 satellites is between around two and nine minutes, with its median around three minutes. This visualises the duration and spread of the observation arcs. DeMars Et. Al [10] used for its simulation the assumption of no obstructions and a full 10 minute observation arc. The box plot shows that is is an overoptimistic value. These 10 satellites where partly selected due to their large number of observations, even these numbers are on the up-side of the available observations per observation arc.

On the bottom right of figure 4.13 it shows the percentage of time of the observation arc, compared to the orbital period of the satellite. Here it can be seen that this is 5% or less, with the exception of satellite 10954U. In table 4.1 it can be seen that this observation arc also had 74 observations. This is significant more then the other satellites. The La Silla station, with 5 cameras does make it more likely to capture larger observations arc, because one can link the observations from multiple cameras to a single observation arc. This number of observations per observation arc are unfortunately the exception.

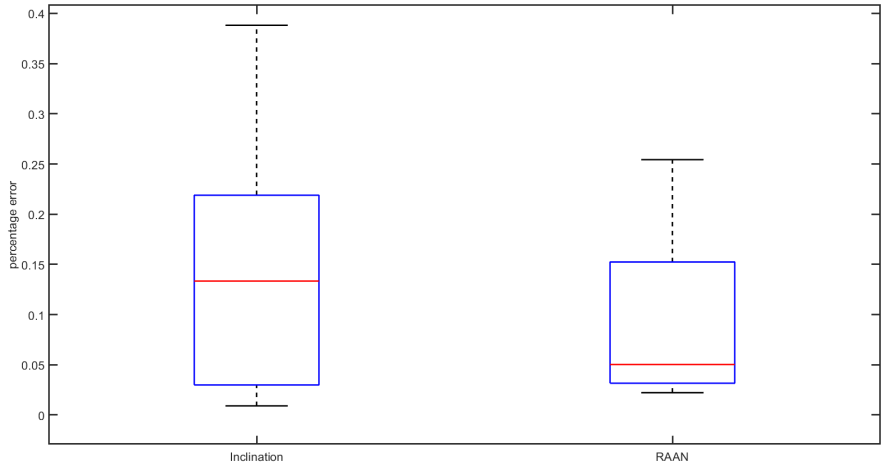

Figure 4.12: Box plot of the percentage error of the Kepler elements at the end of each observation arc of the 10 analysed satellites. The percentage error is the percentage of the error compared to the SGP4-based orbital element of the satellite. Only showing the inclination and RAAN.

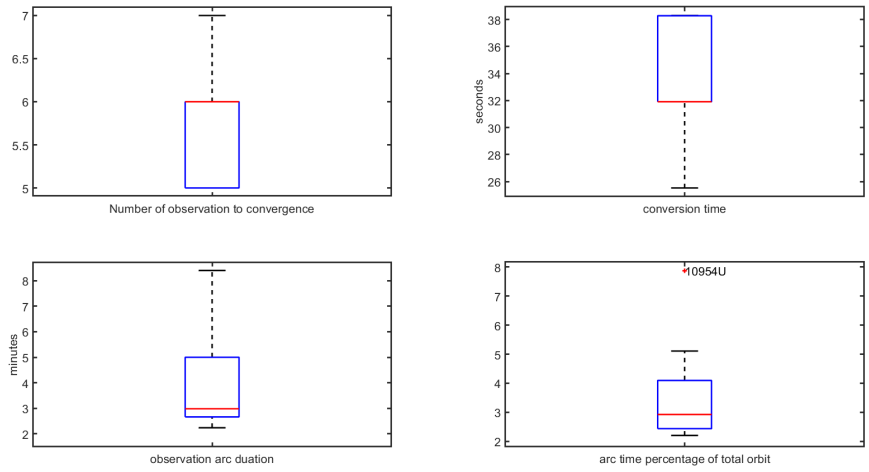

Figure 4.13: General characteristics of the short arc CAR-MHF method for the 10 analysed satellites. Top left shows the distribution of the number of observations required for the CAR-MHF to converge to a single solution. Top right shows the time in seconds between the first observation till the moment the CAR-MHF converged to a single solution. Bottom left shows the time in minutes between the first and last observation of the observation arc. Bottom right shows the percentage of time the satellite is observed compared to its orbital period.

4.1.5. Mahalanobis distance

The Mahalanobis distance is a unit-less distance between a point and the distribution the data point belongs to. It is an measurement of how many standard deviations the point is from the mean of the distributions. The Mahalanobis distance is given by equation 4.1.

$$d^2 = \Delta Y^T P^{-1} \Delta Y \tag{4.1}$$

where:

- d^2 is the Mahalanobis distance
- ΔY is the difference between the state vector solution from the CAR-MHF solution and the SGP4-based reference solution.
- P is the covariance matrix of the state vector as calculated by the EKF, as part of the CAR-MHF.

The Mahalanobis distance calculated for the 10 different satellites, over the duration of the observation arc. Here two different behaviours are observed. These two behaviours are sketch in figure 4.14 and figure 4.15. Each satellite its individual trend is shown in appendix I.

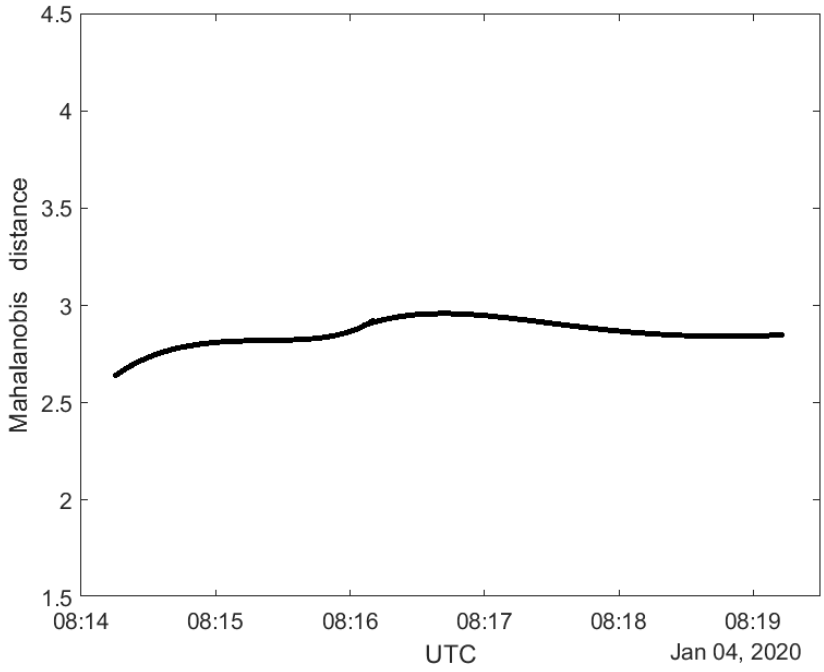

Figure 4.14: On of the two behaviour of Mahalanobis distance as seen for the satellite 39260U, 25885U, and 23404U

The Mahalanobis distance for satellite 25885U, for example, shows a relative steady value over the period of the observation arc. This is seen in figure 4.16. It can be seen that the Mahalanobis distance does not decrease over time.

The Mahalanobis distance for satellite 29499U, for example, shows the other trend, where the Mahalanobis distance increases over the duration of the observation arc. This can be seen in figure 4.17. Non of the satellites show a significant decrease in the Mahalanobis distance.

In order to investigate the increase for the Mahalanobis distance, the covariance and state are shown separately. Figure 4.18 shows the added value of the covariance elements of the covariance matrix. The general trend observed here is that the covariance decreases.

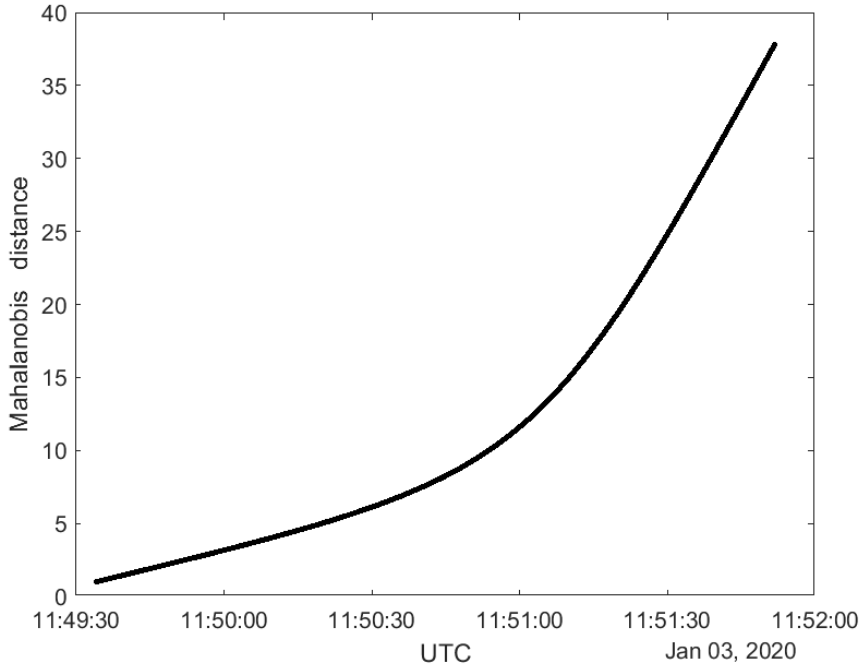

Figure 4.15: On of the two behaviour of Mahalanobis distance as seen for the satellite 38771U, 10793U, 10954U, 25510U, 29499U, 4794U, and 22284U

The difference between the SPG4-based reference and CAR-MHF solution also decreases over time, as can be seen in figure 4.19. So either the covariance matrix decreases faster then the difference in state vector, or vise versa. Since a larger Mahalanobis distance means that the state is more standard deviations away.

The Mahalanobis distance is expected to decrease when more data is available. The Kalman filter calculated covariance matrix has the tendency to stabilise after sufficient data points, while still expecting an improvement of the state for large enough continues data sets. The short observation arcs that are analysed are not large enough to reach this point. Thus the Mahalanobis indicated that the Kalman filter has insufficient data points to reach a stable solution.

4.1.6. Propagation predictions

The current implementation of the CAR-MHF limits only to single observation arcs due to mathematical shortcomings. But in order to assess the quality of the solutions at the end of the observation arc, the solutions will be propagated for a larger period of time.

The average time gap between observation arcs for all LEO satellites available is calculated and was found to be 16 hours. For each of the satellites the solution at the end of the observation arc will be propagated with the RKF4(5) method with the described dynamics. Satellite 38771U and 4794U will be excluded from this analysis. It was already determined that these satellite found a different semi-stable solution, and thus propagating these satellites will only result in larger errors.

Table 4.2 shows the average propagation error for the ten satellites, excluding 38771U and 4794U. Here it can be seen that the inclination and RAAN errors are still small. All other orbital elements show a significant error, putting a question mark if a sequential OD method stable enough for this problem.

4.2. General performance analysis

The performance analysis looks at general statistics for the CAR-MHF and looks at the elements which influence the performance of the CAR-MHF. Different elements like; the number of observations, and time span of observation arc are investigated, position in the orbit, eccentricity of the orbit,

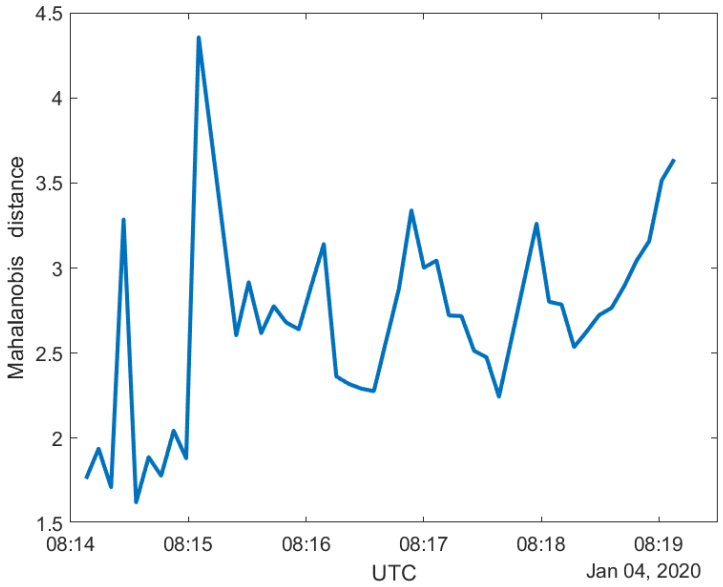

Figure 4.16: The Mahalanobis distance for satellite 25885U, on the night of the third of January, by the ground station in Australia.

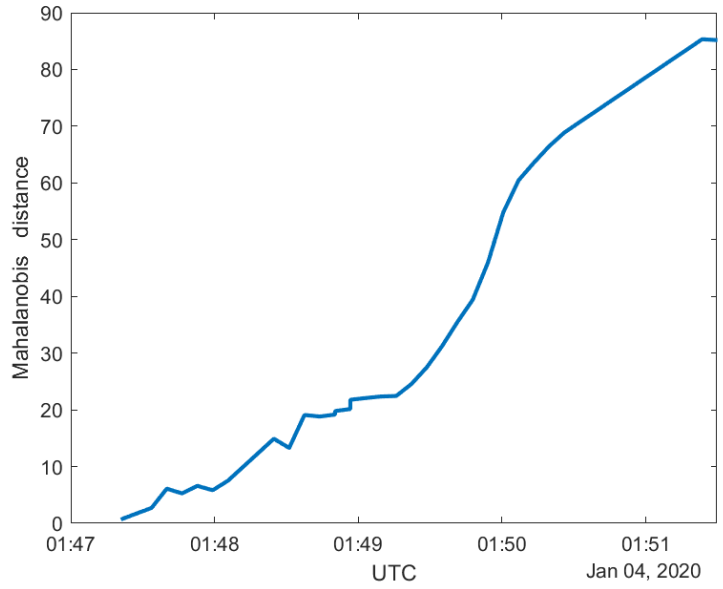

Figure 4.17: The Mahalanobis distance for satellite 29499U, on the night of the third of January, by the ground station in Australia.

Table 4.2: The average propagation error of the solution at the end of the observation arc of eight satellites propagated for 16 hours.

	Average error
Semi-major axis [km]	20.7
Eccentricity	0.03
Inclination [deg]	0.06
Argument of periapsis [deg]	85.6
RAAN [deg]	1.9
True anomaly [deg]	175.1

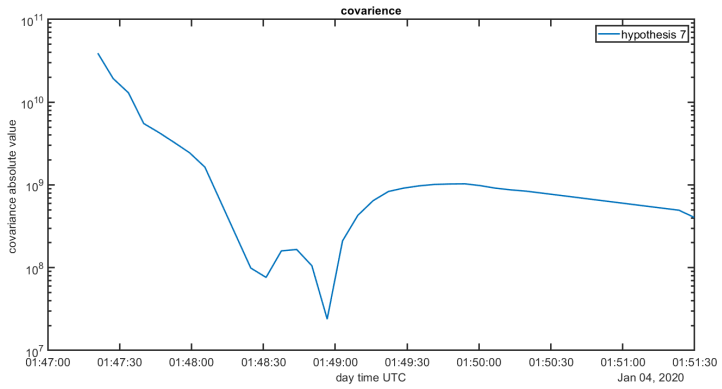

Figure 4.18: The added value of the elements of the covariance matrix for satellite 29499U, on the night of the third of January, by the ground station in Australia.

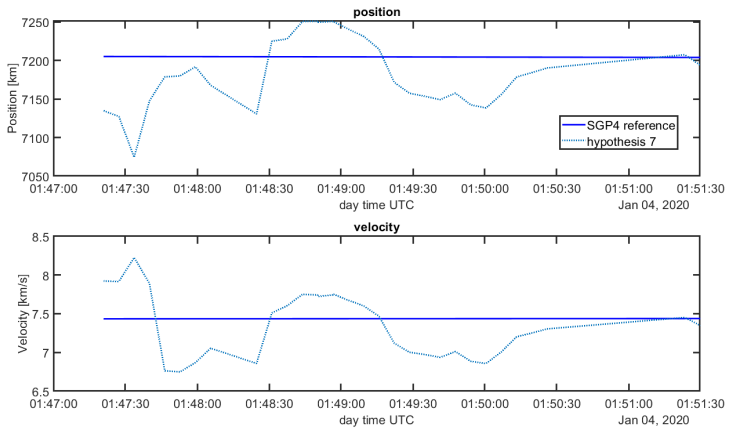

Figure 4.19: The SGP4-based reference and CAR-MHF solution for satellite 29499U, on the night of the third of January, by the ground station in Australia.

The position in the orbit can have influence on the accuracy, since at the perigee of a highly eccentric orbit the change in curvature is more apparent then for a true anomaly of 90 degrees where the curvature is less. Therefore also expecting better results for more eccentric orbits. When more observations are available, the EKF, as part of the CAR-MHF, is able to find a better estimation, therefore expecting better results. When longer observation arcs are available, a larger part of the orbit is observed. It is expected that this will increase the performance of the CAR-MHF.

In order to be able to confidently draw conclusions a larger data set then 10 satellites is required. Therefore the CAR-MHF if applied to all observed LEO satellites for which data was available.

4.2.1. General statistics

The CAR-MHF was able to construct hypotheses for 399 satellites out of the total 860 observed LEO satellites. From these 860 satellites, 278 only had two observations, not sufficient enough to construct the constrained admissible region, which requires a minimum of 3 observations. For 399, out of the 582 satellites, the CAR-MHF filter was able to generate hypotheses. The reason that for 183 satellites it was not possible to generate these hypotheses is due to the fact that there was no single observation arc with at least 3 observations.

The CAR-MHF was able to find a single solution (eliminating all but one hypothesis) for 276 out of the 399 satellites. For these satellites it takes an average of 4.4 observations to find this single solution. But the next step is to know the quality of these solutions.

These solutions are defined as the state at then end of the first observation arc. The solution of these 286 satellites were then checked if the solution were realistic by checking of the eccentricity is smaller then 1, and the perigee distance is larger then the Earth radius, With these limitations, 242 satellites with a valid solution remain. These satellites are used for the performance analysis.

4.2.2. Number of observations

The number of observations per satellite is first looked at. Figure 4.20 shows the number of satellites per observation group of 10 observations each. So there are 91 satellites which have between 1 and 10 observations.

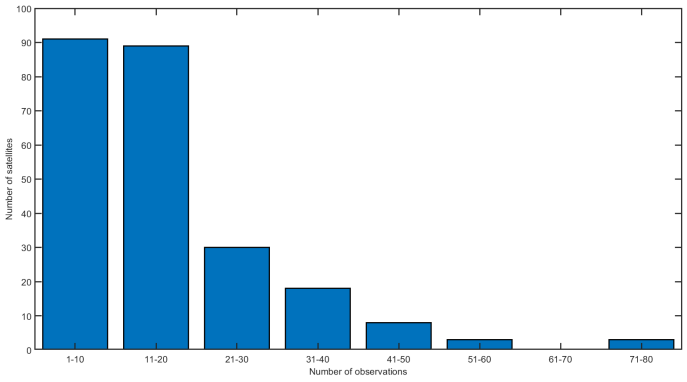

Figure 4.20: The 180 satellites for which a valid CAR-MHF solution is found presented in a bar-chart showing the number of observation per satellite, where the observations are grouped in sets of ten.

Figure 4.21 shows the average duration of the observation arc for the different observation groups. This graph is shown to obtain a general feeling of the length of the observation arcs. As was seen in section 4.1, the results from the 10 satellites, the solution at the convergence point, can still be very poor. Therefore satellites with short observation arcs, like 10 or less, are expected to have significant errors.

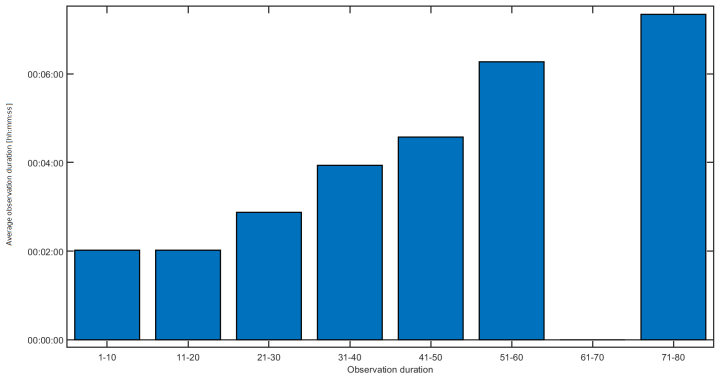

Figure 4.21: The average duration of an observation arc in minutes, per group of number of observations.

4.2.3. Kepler performance

Figure 4.22 shows the average error for each Kepler element per observation group. The error is defined as the difference between the CAR-MHF solution and the SGP4-based reference. The average is taken over all the satellites in a observation group, per observation group.

This graph confirms the conclusion from the previous section, that the CAR-MHF is able to determine, on average, the orbital plane (as based on the inclination and RAAN errors) with less then one and a half degree accuracy, independent on the number of the number of observations. For all orbital elements expect the argument of periapsis and true anomaly show an increase in accuracy with increased number of observations. Where the observation group 71-80 does not follow this trend. Since this group has only three satellites this can easily be caused by an outlier.

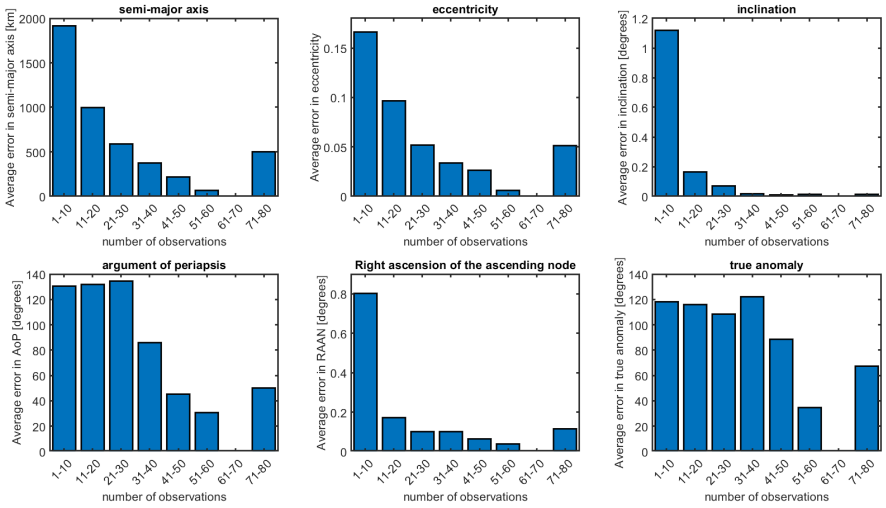

Figure 4.22: Bar graph of the average Kepler error, per observation groups. The error is defined as the difference between the SGP4-based reference and the CAR-MHF solution, determined at the end of the observation arc. Showing the results for all 242 satellites for which a CAR-MHF solution is found.

In order to further investigate the error behaviour for different Kepler elements, a scatter plot per Kepler element is shown for the number of observations. Figure 4.23 shows the scatter plot, and it shows, especially for the eccentricity error the outlier that explains the increase in average error for the observation group 71-80 observations. The outlier is satellite: 25885U.

The solution of the CAR-MHF over the duration of the observation arc is shown in figure 4.24. Here the blue

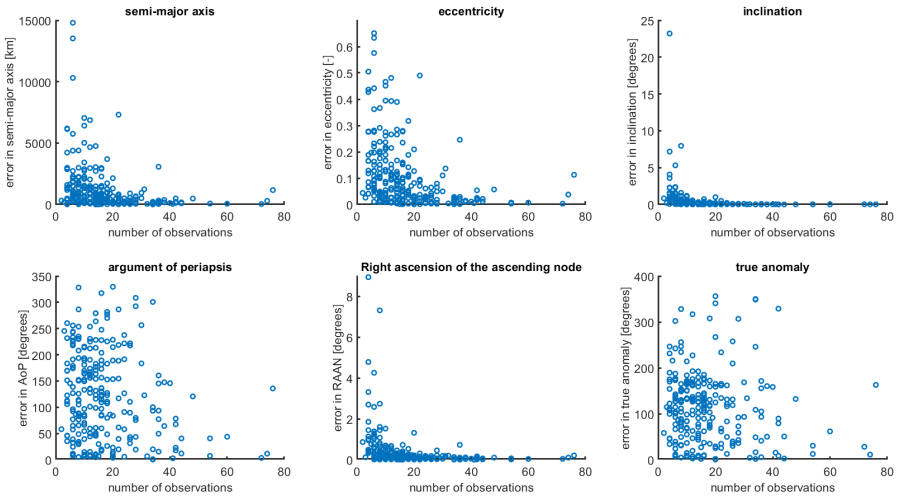

Figure 4.23: Scatter plot of the error in the Kepler elements for the 242 satellites with a realistic solution plotted against the number of observations in the observation arc. The error is defined as the difference between the SGP4-based reference state and the CAR-MHF solution at the end of the observation arc.

line represents the SGP4 reference and the orange line the CAR-MHF solution. Figure 4.25 shows the observation angle error for the right ascension and declination of the duration of the observation arc. The error is defined as the difference between the observation as determined by the IPA algorithm, and the SGP4-based observation angle. In the beginning of the observation arc sharp spikes in the CAR-MHF solution and the observation angle errors are observed. At around 08:09:30 a relative large observation error is introduced. Also the second and third observation are relative far away from each other, with a approximately time of 1.25 minutes. This occurs once again around 08:12:00, here with a time gab of around 2 minutes.

As discusses earlier the linear propagation error of the covariance matrix, by using the State transition matrix, increases for larger time steps. Thus introducing unreliably covariance values. Also, the observation error after this large time step is also significant larger then the average observation error. This makes it that the EKF, as part of the CAR-MHF performs less then expected for this large number of observations in a single observation arc.

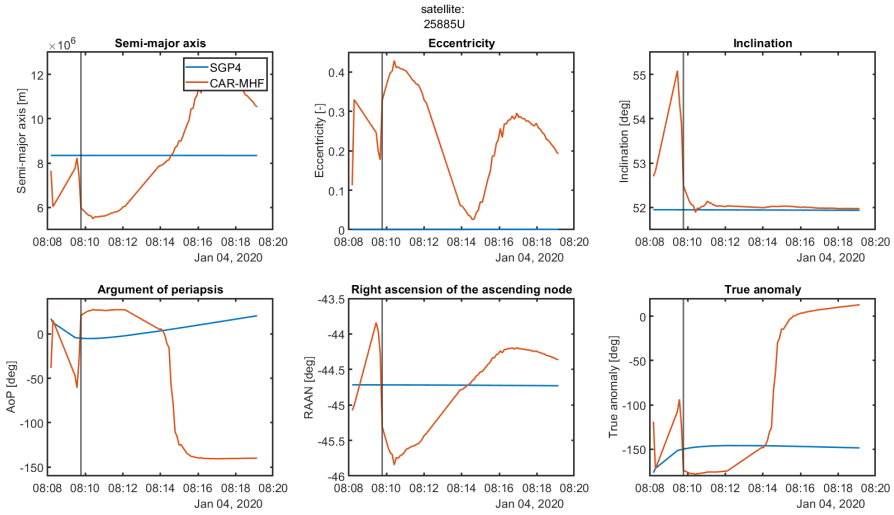

Figure 4.24: The CAR-MHF over the duration of a single observation arc, shown in orange. The blue line is the SGP4-based reference. The vertical black line is the convergence point, where only a single hypothesis remained.

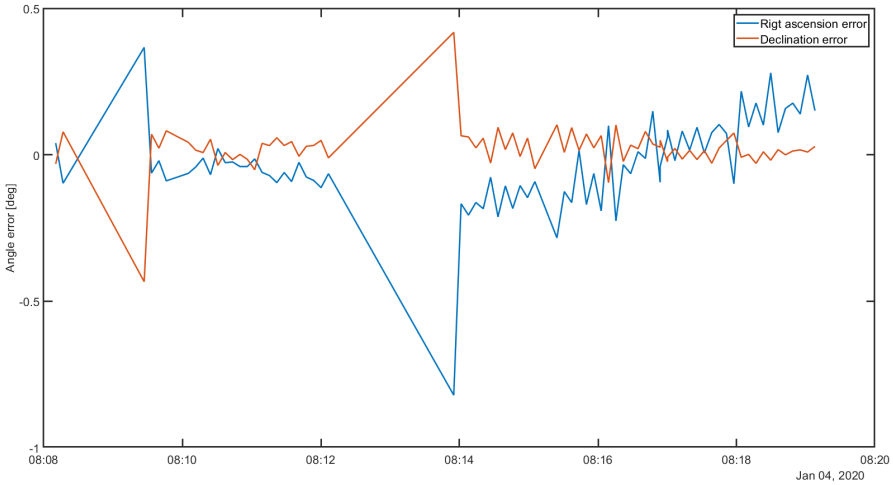

Figure 4.25: The right ascension and declination error, as defined as the difference between the observed and the SGP4-based angle, is shown for the observation arc of satellite 25885U.

The Argument of Periapsis and True anomaly does not follow the trend of increased performance for more observations. But as also was found in section 4.1, the analysis of the 10 satellites, it was found that the error between the SGP4-based reference and the CAR-MHF solution is expected to be small when adding the AoP and the True anomaly together. The average error of the combination of the two orbital elements, per observation group, is shown in figure 4.26.

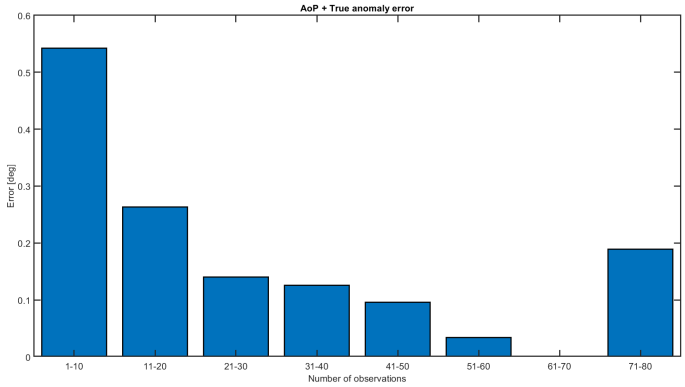

Figure 4.26: The average error of the added values of the Argument of periapsis and True anomaly, of the CAR-MHF, compared to the SGP4-based reference. Grouped together per observation group of 10 observations.

Here once again it is seen that the orientation within the orbital plane can be determined with and accuracy of 0.6 degrees or less, independent of the number of observations. The trend of increased performance with increased number of observations is also visible here. Where the last observation group, 71-80 observation, again deviates due to the earlier discussed outlier.

From these observations it can be concluded that the orbital plane and the orientation of the satellite w.r.t. the orbital plane can, on average, be determined with less then one degree accuracy for 10 observations or more. The eccentricity and semi-major axis solution could still use an improvement. Since the observations are angle observations, the range of the satellite can not directly be observed. The range can be determined indirectly by observing the movement of satellites. The eccentricity finds similar problems, and for the short arcs observations, multiple solutions of combinations of semi-major axis could be found. How this could be improved will be discussed in the discussion.

4.2.4. Observation arc duration

In order to assess the performance of the CAR-MHF a scatter plot is generated where the error for each Kepler element is shown w.r.t. the observation duration. The error is defined as the difference between the SGP4-based reference and the CAR-MHF solution at the end of the observation arc. The results are shown for all 242 satellites for which a realistic solution is found.

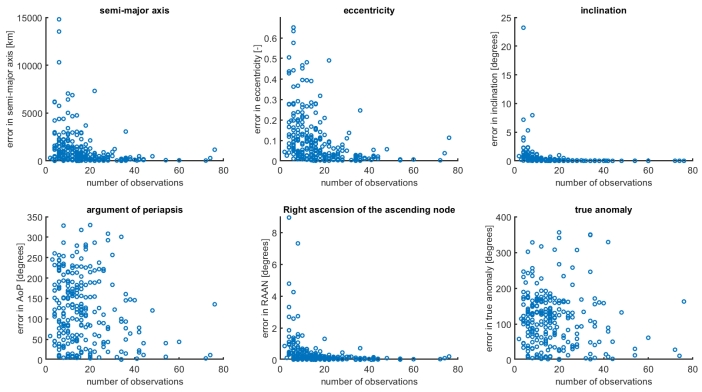

Figure 4.27: Scatter plot of the error in the Kepler elements for the 242 satellites with a realistic solution plotted against the number of observations in the observation arc. The error is defined as the difference between the SGP4-based reference state and the CAR-MHF solution at the end of the observation arc.

The results can be seen in figure 4.27. This graph shows similar results as figure 4.23, where the Kepler error is plotted against the number of observations. From this, it can be concluded that for this data set, the number of observation and the observation duration can be used interchangeable.

4.2.5. Eccentricity dependency

This section analyses the hypothesis if more eccentric orbits result in more accurate CAR-MHF solutions. More eccentric orbits have a more clear curvature in the orbit. But the question is, if this curvature is visible in the short observation arcs.

In order order to test this, the position and velocity errors are plotted for the SGP4-based eccentricity of the orbit. The error is defined as the difference between the SGP4-based reference and the CAR-MHF solution at the end of the observation arc. Then the root sum square of the position and velocity components are applied. These errors are calculated for all 242 satellites for which the CAR-MHF found a solution.

The results can be seen in figure 4.28, where it can be seen that a large group of satellites is located in the lower left corner. From this figure, no clear trend can be seen to support the hypothesis.

4.2.6. True anomaly dependency

Another possibility is that the location of the observation, with respect to the perigee, can influence the performance of the CAR-MHF. A similar set-up as the Eccentricity dependency is used for this analysis. The position and velocity error of the 242 satellites, determined at the end of the observation arc is calculated and plotted w.r.t the SGP4-based true anomaly.

Figure 4.29 shows the results, and here it can also be seen that there is no clear correlation between true anomaly and the magnitude of the error. Therefore no trend is found that observing specific parts of the orbit results in better results.

The dependency analysis of the eccentricity and true anomaly both showed that the their values do not significantly influence the quality of the solution. Where the Kepler performance had a clear increase in performance for more data points, c.q. longer observation arcs. With longer observation arcs, the general shape of

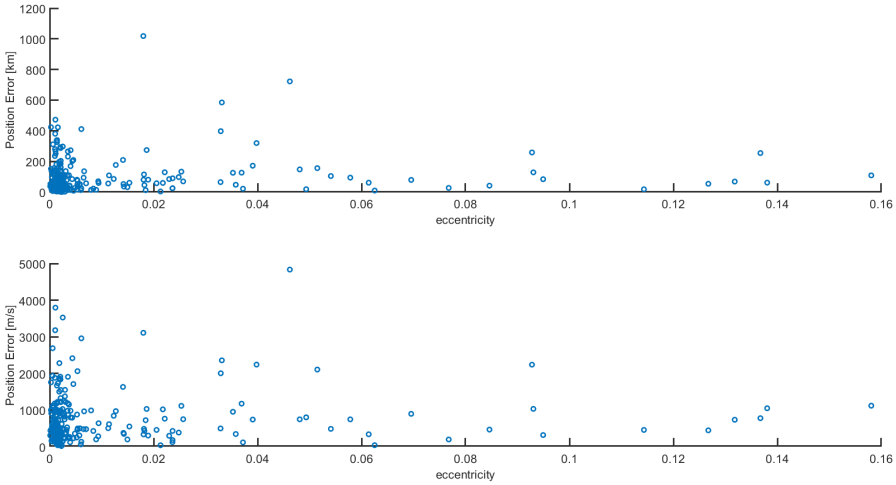

Figure 4.28: The position and velocity error at the end of the observation arc shown w.r.t. the SGP4-based eccentricity for the 242 satellites for which the CAR-MHF found a solution.

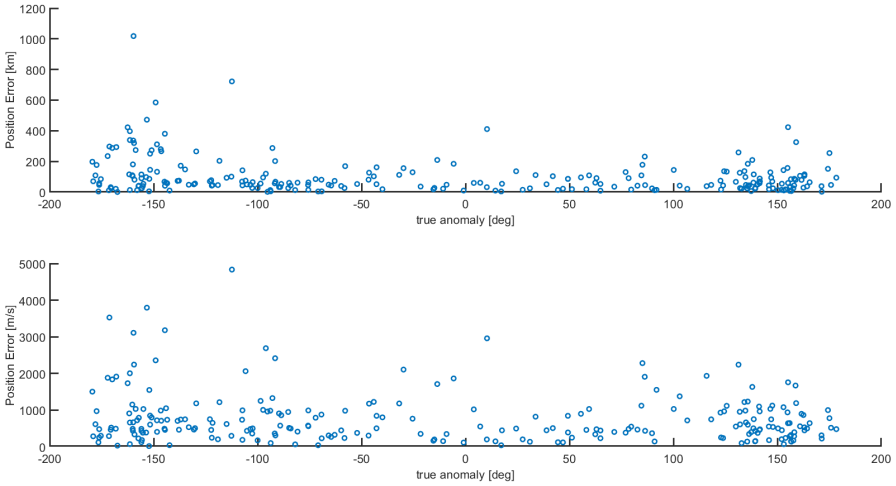

Figure 4.29: The position and velocity error at the end of the observation arc shown w.r.t. the SGP4-based true anomaly for the 242 satellites for which the CAR-MHF found a solution.

the orbit can be more accurately identified, resulting to better results. But it does not show that the eccentricity of the orbit, or the position of the observation arcs has a significant performance impact.

4.3. Gauss' method versus CAR-MHF

Gauss' method was used during the FOTOS study, preceding this research. This IOD algorithm will be compared to the CAR-MHF in this section. First the performance of Gauss' method will be discussed, after which the performance of the CAR-MHF will be discussed. In the last section the two will be compared to each other. The track-based observations will be used for this analysis.

Both methods will be applied to the 860 detected LEO satellites, on the first observation arc. For both methods to be able to be initialised, it requires at least three observations on a single observation arc. Therefor the methods can only be applied to 582 satellites.

4.3.1. Gauss' Method

Gauss' method has been applied on the 582 observed LEO satellites. The first, mid, and last observation of the observation arc is used. This way Gauss' method makes use of the whole observation arc, similar to the CAR-MHF.

The solution is considered valid when the perigee of the orbit is larger then the Earth radius and the eccentricity is smaller then one, and no invalid values (e.q. NaN). 399 Satellites have three or more observations. For 204 of those satellites a valid solution is found with Gauss' method.

To assess the quality of the solutions, the solution from Gauss' method is transformed to Kepler elements for comparison. The TLE of the satellite is propagated to the epoch for which Gauss' solution is found with the SGP4 theory. The SGP4-based state is then also transformed from Cartesian elements to Kepler elements. This way the orbital elements of the satellite is known at the requested epoch. These orbital elements are the osculating orbital elements, where the orbital elements in the TLE are the mean orbital elements. The orbital elements of the state vector found by Gauss' method is compared to the osculating orbital elements from the SGP4 theory. The absolute value of this difference is shown in figure 4.30. The absolute values are used to assess the magnitude of the error.

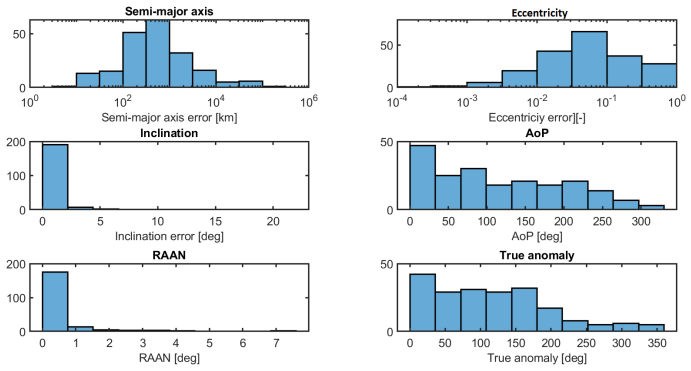

Figure 4.30: The Kepler element errors for the 204 satellites for which Gauss' method found a valid solution. Gauss' method is applied on the first observation arc available for each satellite. Gauss' solution is determined at the middle point of the observation arc.

Figure 4.30 shows that the inclination and RAAN errors are smaller then 5 degrees. Similar to the CAR-MHF it is found that the orbital plane can accurately be estimated with IOD algorithms. The AoP and true anomaly show a wide spread in results. Due to only using a single arc observations, the eccentricity is difficult to estimate, especially since measurement errors are introduced. As a consequence, the AoP and true anomaly show a wide spread in errors. Similar to previous analysis, the AoP and true anomaly are added, for the SGP4-based reference and the Gauss' method, then subtracted from each other to determine the error. The

resulting histogram is shown in figure 4.31. Here it can be seen that also for Gauss' method the position in the orbit can be calculated with an error smaller then 5 degrees, but mostly centred between the 0 and 0.3 degrees.

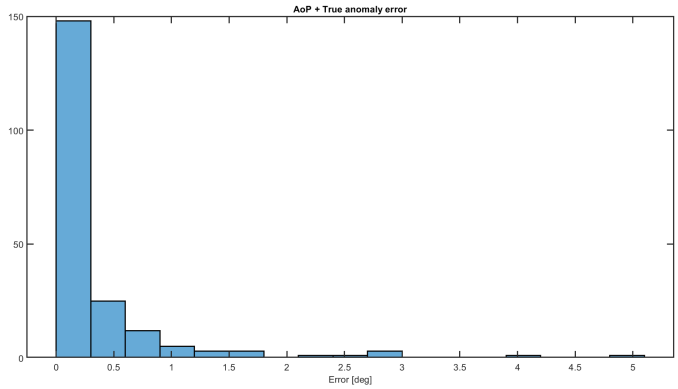

Figure 4.31: The error of the sum of the AoP and true anomaly, shown in a bar graph. The error is defined as the difference between the SGP4-based reference and Gauss' solution for the 204 satellite for which Gauss' method found a valid solution.

The semi-major axis and eccentricity errors are shown on a logarithmic scale. The median of the semi-major axis error is around the 400 km. The median error in the eccentricity is around 0.03.

From the results presented in this section it is concluded that Gauss' method approaches is able to determine the orbital plane of the satellite and the position in the orbital plane. But the semi-major axis and eccentricity show significant errors.

4.3.2. CAR-MHF

The CAR-MHF was able to find a feasible solution for 242 satellites. The solution presented in this section for these satellites are determined at the last epoch of the observation arc. These solutions are then compared to the osculating orbital elements at the last epoch of the observation arc to determine the error.

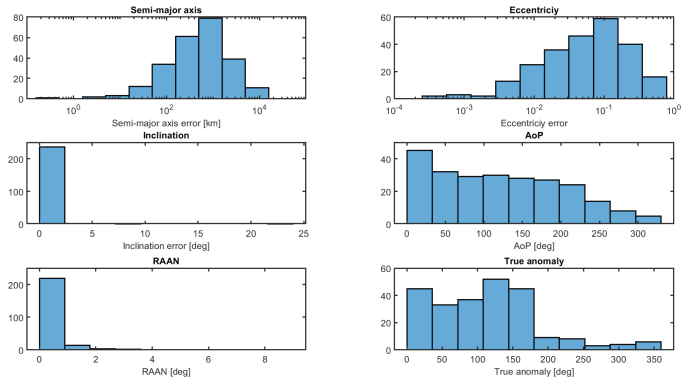

Figure 4.32: The error in Kepler elements for the 242 satellites for which the CAR-MHF found a valid solution. The error is defined as the difference between the SGP4-based reference and CAR-MHF solution, at the last epoch of the first observation arc.

Figure 4.32 shows the error in the orbital elements. This shows similar results as discussed in section 4.2.3, Kepler analysis of the CAR-MHF solution. The error for the AoP plus true anomaly is shown in figure 4.33.

Gauss' method and the CAR-MHF show no large difference when comparing figure 4.30 and 4.32. Therefore a more detailed comparison will be presented in the next section.

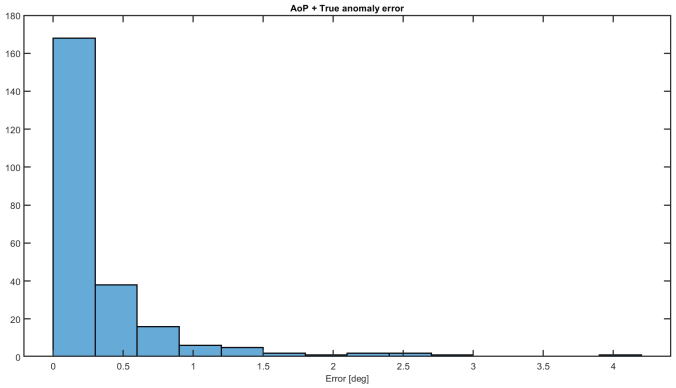

Figure 4.33: The error of the sum of the AoP and true anomaly, shown in a bar graph. The error is defined as the difference between the SGP4-based reference and the CAR-MHF solution for the 242 satellite for which the CAR-MHF found a valid solution.

4.3.3. Gauss' method versus CAR-MHF

In order to compare the performance of the CAR-MHF with Gauss' method, satellites are selected for which both method produced a valid solution. For all 204 satellites for which Gauss' method found a solution, the CAR-MHF also found a solution. These 204 satellites will thus be used to analyse the performance. The difference between the osculating orbital elements and the IOD methods, expressed in Kepler elements, for each satellite, is calculated. The CAR-MHF solution is located at the last epoch of the observation arc, and Gauss' method calculates the IOD solution at the middle point of the observation arc. These differences are shown in figure 4.34.

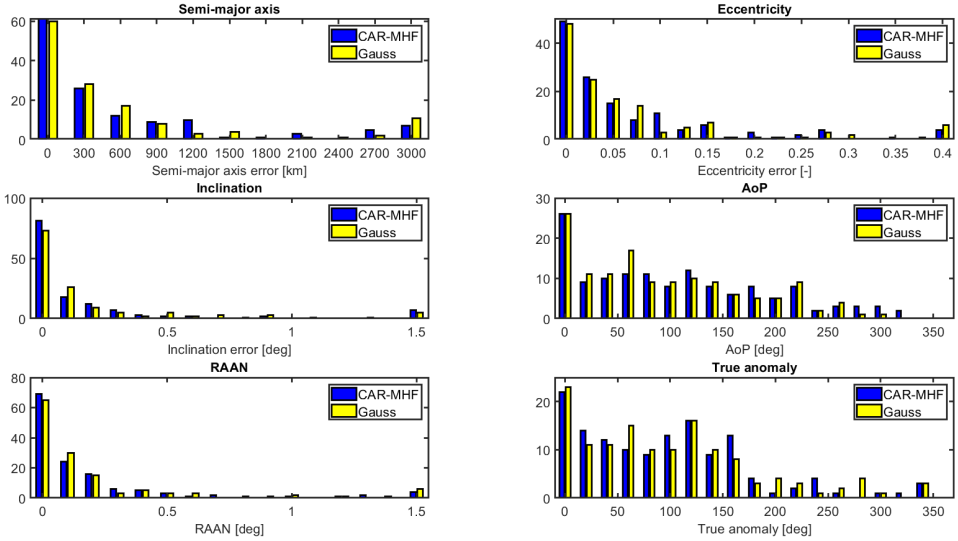

Figure 4.34: Error in the Kepler elements for the 204 satellites for which both the CAR-MHF and Gauss' method found a valid solution. The error is defined as the difference between the SGP4-based reference and the IOD solution. For the CAR-MHF the solution is located at the last epoch of the observation arc, and Gauss' method calculates the IOD solution at the middle point of the observation arc.

Figure 4.34 shows no clear performance difference between the two methods. In order to put values to the difference between the methods, the average error and the standard deviation is calculated for both methods, for each Kepler element, included the AoP and True anomaly added together. The error is defined as the difference between the SGP4-based reference and the CAR-MHF or Gauss' solution. The CAR-MHF solution is defined at the end of the observation arc. Gauss' solution is defined at the middle observation point. The results can be found in table 4.3. Here it can be seen that the CAR-MHF performs better then Gauss's method

for the semi-major axis. The CAR-MHF has an average error of 1282 km versus Gauss's method of 2192 km. For all other orbital elements the error is comparable between the two methods.

Table 4.3: The mean and standard deviation of the errors for the CAR-MHF and Gauss' method for the 204 satellites for which both satellites found a valid solution. The error is defined as the difference between the SGP4-based reference and the solution from the IOD algorithm. The CAR-MHF finds its solution at the end of the observation arc. Gauss' method finds its solution at the middle point of the observation arc.

Error	CAR-MHF		Gauss' method	
	mean	standard deviation	mean	standard deviation
Semi-major axis [km]	1282.41	2311.14	2192.57	6390.68
Eccentricity	0.11	0.13	0.12	0.17
Inclination [deg]	0.65	2.61	0.58	1.64
Argument of periapsis [deg]	125.35	88.36	110.60	78.73
RAAN [deg]	0.50	1.31	0.44	0.97
True anomaly [deg]	113.69	80.78	117.00	84.15
RAAN + True anomaly [deg]	0.22	0.58	0.34	0.65

Since the CAR-MHF uses the EKF to improve the state, where more observations result in increased accuracy, as seen in section 4.2.3. Therefore the hypothesis arises that the CAR-MHF could perform better for the "long" short arc observations. This hypothesis will be tested to get a better insight in possible differences

Based on figure 4.22, the extra short arc observation are defined between 0 and 20 observations. The long observation arc uses more than 30 observations. The long observation arc is not set even larger, because otherwise the number of satellites becomes small even smaller.

The error for the 88 satellites with 20 observations or less are shown in figure 4.35. Here it can be seen that the performance still does not show significant differences.

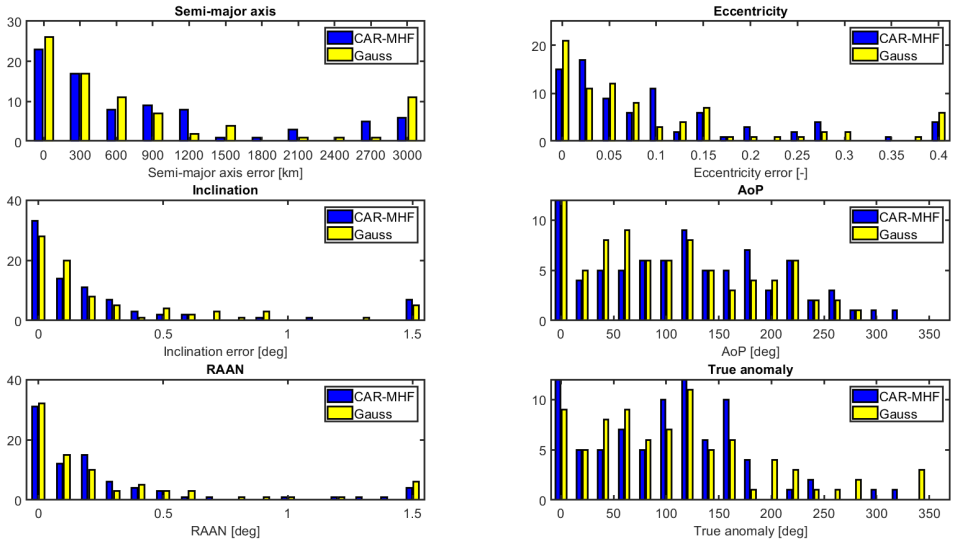

Figure 4.35: Error in the Kepler elements for the 88 satellites for which both the CAR-MHF and Gauss' method found a valid solution for observation arcs with less then 20 observations. The error is defined as the difference between the SGP4-based reference and the IOD solution. For the CAR-MHF the solution is located at the last epoch of the observation arc, and Gauss' method calculates the IOD solution at the middle point of the observation arc.

The error for the 25 satellites with more then 30 observations is shown in figure 4.36. This again does not show significant difference between the two methods. Based on this data it can be concluded that both methods

experience the same benefits of longer observation arcs.

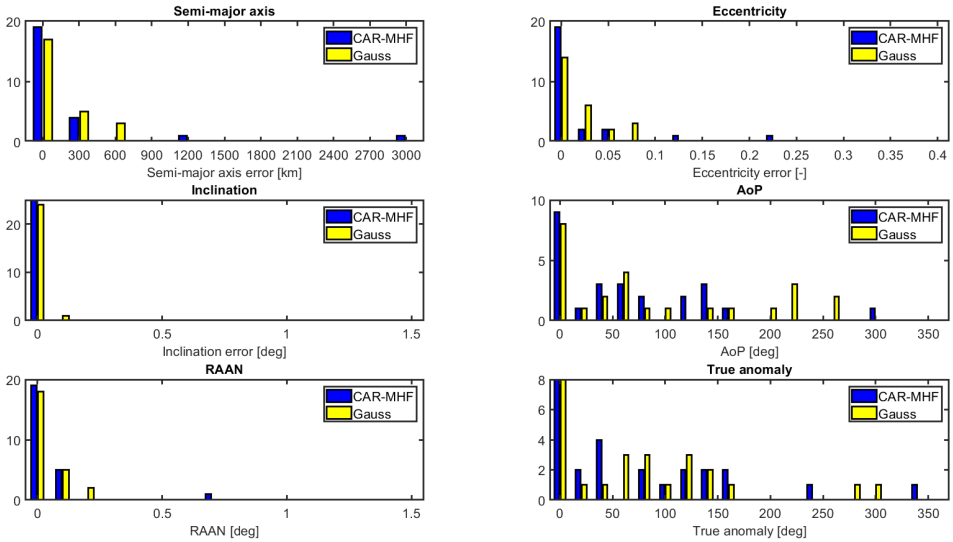

Figure 4.36: Error in the Kepler elements for the 25 satellites for which both the CAR-MHF and Gauss' method found a valid solution for observation arcs with less more then 30 observations. The error is defined as the difference between the SGP4-based reference and the IOD solution. For the CAR-MHF the solution is located at the last epoch of the observation arc, and Gauss' method calculates the IOD solution at the middle point of the observation arc.

To investigate if the difference between the 204 solutions from Gauss' method and the 242 solutions from the CAR-MHF filter, the duration of the time intervals are looked at. Gauss' solution show an average observation arc duration of 2:25 minutes, where the average observation arc duration for the MHF solutions is 2:04. Looking at the sample size of the MHF solutions for which the CAR-MHF was able to find a solution, and Gauss's method not, it shows an an average observation arc duration of 1:38 seconds. From this it can be concluded that the CAR-MHF is less sensitive for shorter observation arcs, than Gauss' method is, explaining the difference between the two methods.

4.4. Analysis of the observed satellites

The data available for this research can also be analysed to obtain an insight in the satellites which are observed. The Radar cross section and the apparent magnitude of the observed satellites will be analysed. Next the orbit regimes and their orbital elements will be presented to determine if there is possible a trend in satellites that are observed. All analysis is performed with the CSpOC data base as of available for the second, third, and fourth on January, 2020.

4.4.1. Radar cross section

The satellites for which the RCS values are known are analysed to obtain a rough indication of the size of the satellite in order to be able to be detected by the current set-up of cameras. Figure 4.37 shows the observed LEO satellites in comparison to all non-debris LEO satellites. On the left y-axis the number of satellites is given, corresponding to the bar heights. The right y-axis correspond to the yellow line, which shows the percentage of observed satellite for each bar in the histogram. Despite being observed by all three camera stations the International Space Station (ISS) is left out of RCS analysis. the ISS is a uniquely large object which would would skew the graph unnecessary, making it less insightful.

Figure 4.37 shows a clear drop of around the 1 square meter radar cross section. The RCS of 10 square meters and higher show around a 50% detection raid, but has also a relative small data set with less then 60 satellites. New insights obtained during this research resulted in a more thorough analysis of the RCS. These improvements will be discussed below.

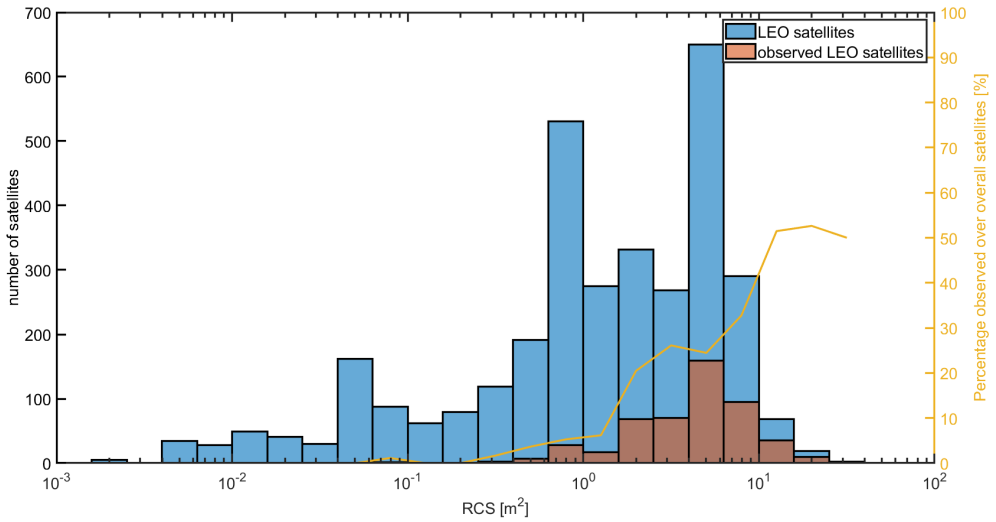

Figure 4.37: A histogram of the observed LEO satellites (orange) in comparison with all non debris LEO satellites (blue), for a given radar cross section. The yellow line represents the percentage of observed satellites with its scale to the left.

Only comparing the observed satellites with respect to the satellites that passed the Field of View (Fov) of any of the cameras during the observation periods, is more realistic. Since satellites that did not pass the FoV of the satellite are impossible to observe. The results are shown in figure 4.38. This already makes an improvement where around 70% of the satellites with a RCS of 10 square meters is observed.

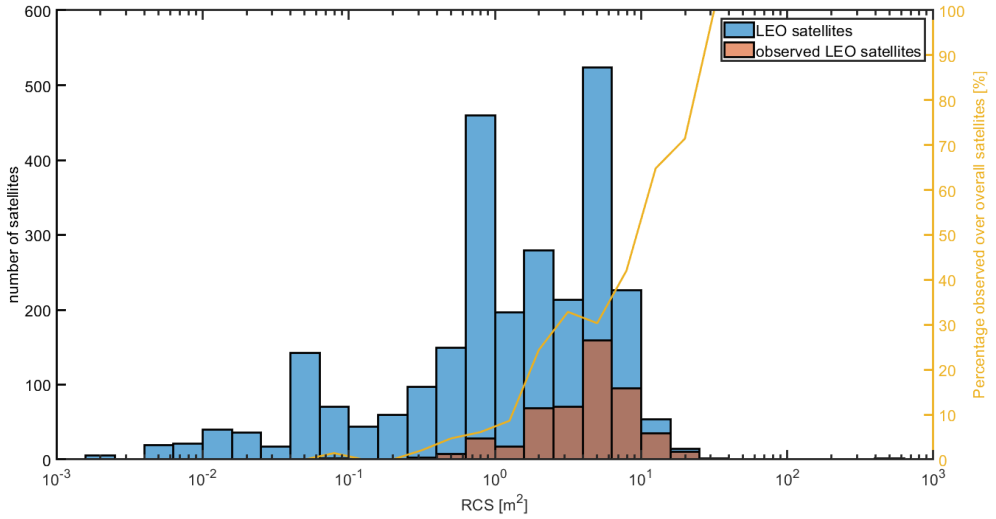

Figure 4.38: A histogram of the observed LEO satellites (orange) in comparison with all non debris LEO satellites that were within the field of view of the satellite during the observation period (blue), for a given radar cross section. The yellow line represents the percentage of observed satellites with its scale to the left.

The research of Thomas Wijnen et. al. [33] presented that most satellites are detected during twilight. This could be one of the reasons why not all large surface area satellites were observed. In order to test the conclusion of Thomas Wijnen, the number of observations per time is plotted for all observations in a bar chart. The time zones of the different stations are taken into account and therefore normalised. So an observation in La Silla at 12:00 local time is plotted at the same time at an observation in South Africa, local time, or Australia 12:00 local time. This is due to the fact that the twilight period is dependent on the local time. Local

observation time is based on the Julian day plus or minus the time zone of the observation station, as shown below.

- La Silla: Time zone GMT minus 6:00 hours.
- South Africa: Time zone GMT plus 2:00 hours.
- Australia: Time zone GMT plus 10:00 hours.

Figure 4.39 shows the number of observations with respect to the local time. Here it can be seen that the last night the least observations were taken. This is due to the fact that the La Silla station only had data for the second and third of January 2020. It can also be seen that at the start and end of the night, during twilight, the expected spikes are visible. Therefore confirming the expectation that most observations are taken during twilight.

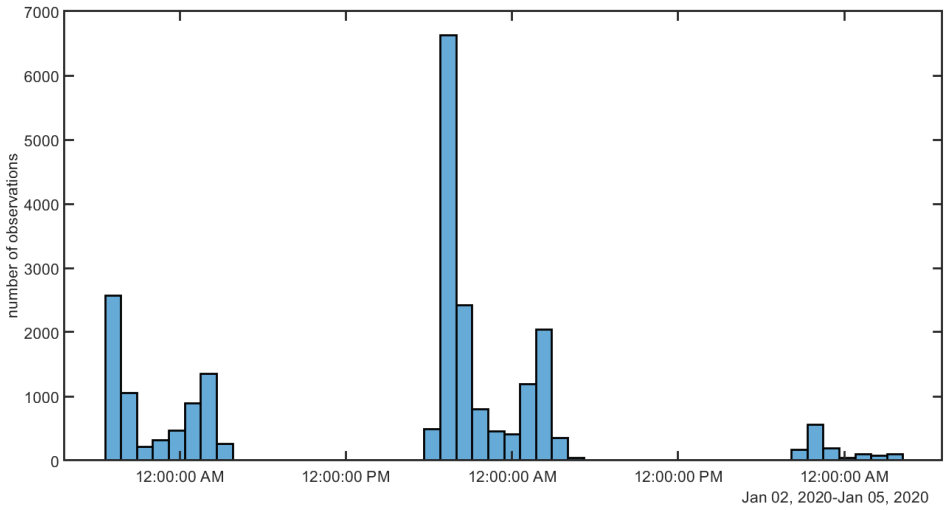

Figure 4.39: The number observations plotted for all observation stations for all the three nights together. The observation times are normalised to the local time of the station made the observation.

Now using this information the RCS analysis can be further improved by only analysing the satellites that passed the FoV of the Camera during twilight. Based on the spikes as seen in figure 4.39, the twilight is defined as between 18:00:00 - 21:00:00 and between 01:00:00 - 03:00:00 hours.

Figure 4.40 shows the observed satellites versus all satellites that passe the field of view of the cameras during twilight. Here it can be seen that from satellites with a RCS of three square meters and up have around a 80% change to be observed.

The attitude of the satellite is also effecting the probability of the detection of the satellite. When the satellites largest surface area is positioned in such a way that the light will not reflect to the observation stations, the satellite can not be observed, despite having a large surface area. To model each satellite independent to verify this statement is outside of the scope of this research but is a physical realistic reason why not all satellites with large RCS, thus assuming large surface area, are detected.

4.4.2. Magnitude of the satellites

A hypothesis is formed that the brightness of a satellite could depend on the size of the radar cross section. In order to test this observations available for this researches were taken. A selection of satellite with observations were selected that both had registered a magnitude and the RCS was known. This is shown in figure 4.41.

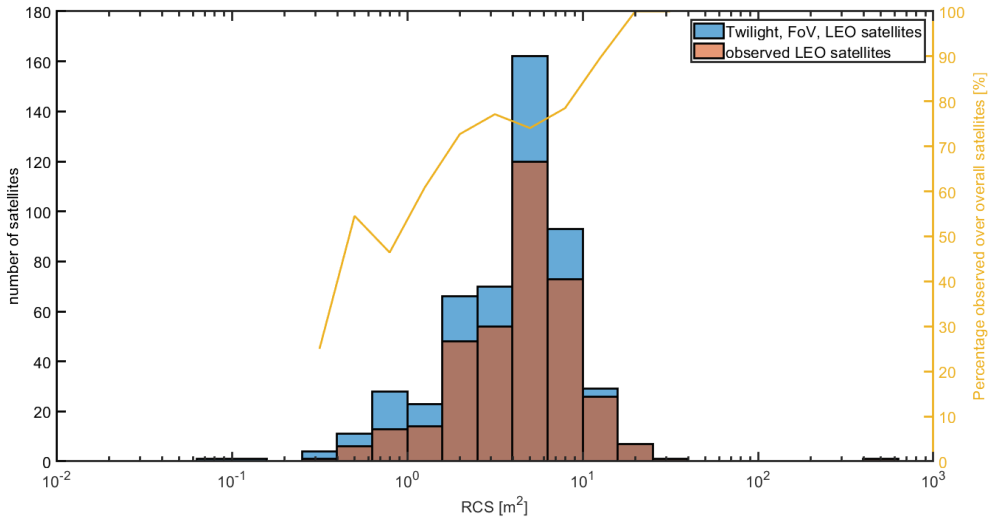

Figure 4.40: A histogram of the observed LEO satellites (orange) in comparison with all non debris LEO satellites that were within the field of view of the satellite during twilight (blue), for a given radar cross section. The yellow line represents the percentage of observed satellites with its scale to the left.

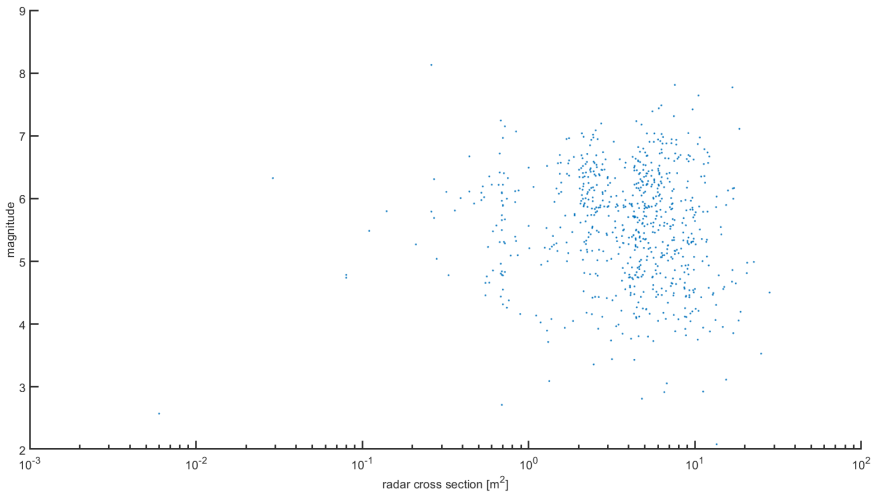

Figure 4.41: Scatter plot of the brightness of the satellite plotted against the radar cross section for all LEO observations that contained a brightness value

From this graph no clear relation was seen. This can be explained by other parameters that effect this relation like Albedo and phase angle.

Phase angle

Figure 4.42 shows a scatter plot of the phase angle compared to the magnitude. Here it can be seen that the phase angle can occur in a wide range. Yet not correlation between magnitude and phase angle can be seen.

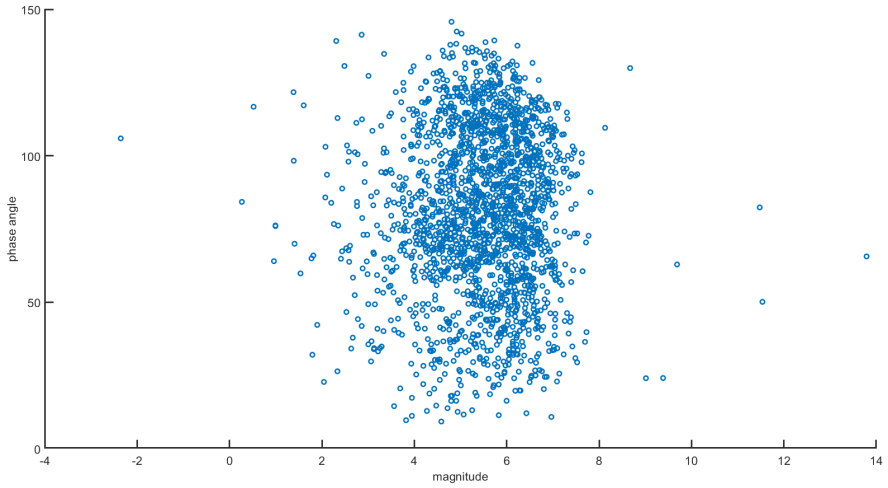

Figure 4.42: A scatter plot the the phase angle compared to the magnitude of the observation available over a period of three days.

When plotting the phase angle over the the duration of an observation night, for a single camera an effect can be observed. Figure 4.43 plots the phase angles for satellites observed on the third of January by camera LSE. Here it can be seen that the phase angle increases of the duration of the night. This is probably due to the rotation of the Earth.

4.4.3. Orbital elements of the satellites

The observed satellites are now analysed for their orbit regimes. Next, the semi-major axis, eccentricity, and inclination of the observed satellites are analysed to determine if there are satellites orbits which have a larger detection probability.

Orbit regimes

The IPA algorithm has detected over a 1000 satellites, for which most are LEO satellites. This is an expected result since the algorithm was developed for LEO satellites and LEO satellites are closed to the observed, making it easier to spot. The three day data set was able to detect 860 LEO satellites, from which 809 are non debris. This means that 17.2 % of all non-debris LEO satellites are observed.

The IPA has also detected Medium Eart Orbit (MEO) and Geosynchronous Equatorial Orbit (GEO) satellites. There were 55 MEO satellites observed, which is 17.6 % of all MEO satellites. The MEO satellites need further investigations in order to determine if it was a coincidence of that the software was able to correctly detect these satellites. These satellite orbit with an altitude of 20.000 km above the Earth surface, are highly unlikely to have observed tracks. In order to verify this, a observation of two satellites are analysed. This is to determine the quality of the recognised track. This analysis is performed for satellite 20026U and 20619U. A observation of per satellite is shown in figure 4.44 and 4.45, respectively. Here it can be seen that no clear track was detected and that the most probable is caused by noise in the pixels.

The IPA has also detected 114 GEO satellites, 10.7 % of all GEO satellites. Figure 4.46 and 4.47 show examples of detected GEO satellites in the images, where the diamonds are the determined end points of the line. In these images no clear line can be seen and it only shows noise. The GEO satellites are also not expected to be

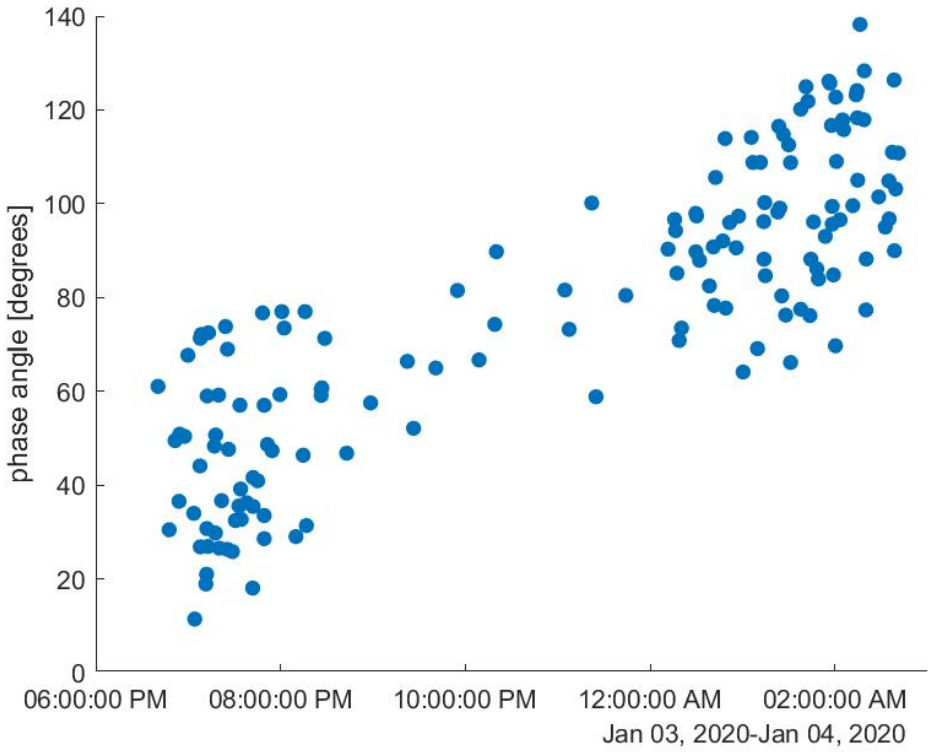

Figure 4.43: phase angle plotted over the duration of a observation night for station LSE, on the third of January.

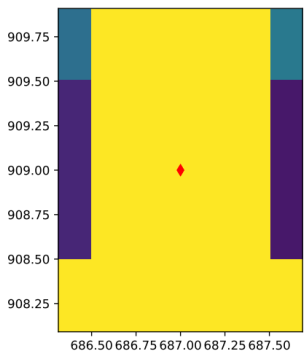

Figure 4.44: MEO satellite 20026U, detected by the IPA algorithm, where the diamonds represent the track end points

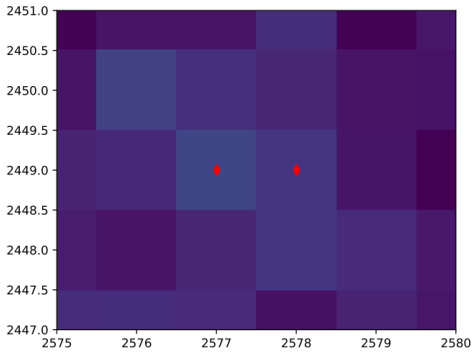

Figure 4.45: MEO satellite 20619U, detected by the IPA algorithm, where the diamonds represent the track end points

visible in the current set-up of cameras. GEO satellites are not expected to be bright enough to be detected. For these reasons it is concluded that the observed GEO satellites are a result of noise in data which had a GEO satellite within 10 pixels of the perceived line.

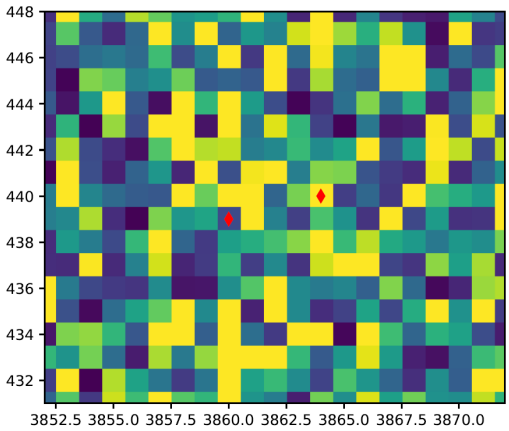

Figure 4.46: GEO satellite 28702U, detected by the IPA algorithm, where the diamonds represent the track end points

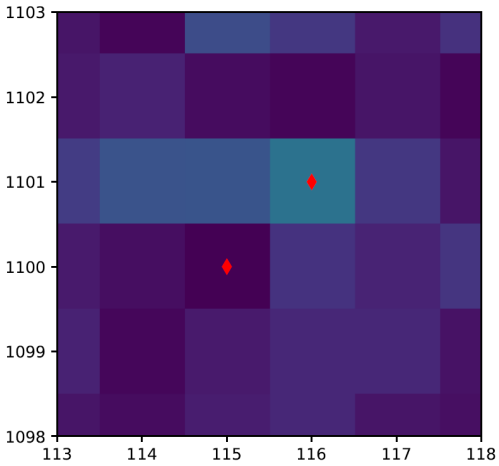

Figure 4.47: GEO satellite 40663U, detected by the IPA algorithm, where the diamonds represent the track end points

Eccentricity

The observed LEO satellites are compared to the LEO satellites that were in the field of view of the cameras. The observed satellites sorted by their eccentricity. The analysis is shown in figure 4.48, where the blue bars represent all the satellites in the cameras fields of view, the orange bar show the number of observed satellites. The yellow line is the percentage of the observed satellites for each bar, where the percentages are shown on the right y-axis. The horizontal red line shows the percentage of detected LEO satellites with respect to the LEO satellites in the field of view of the satellite for the whole data set. The x-axis shows the eccentricity.

It can be seen that most satellite in LEO, which passed the field of view of the cameras have an eccentricity close to zero. Therefore having less data points for high eccentric satellites. This makes the percentage of observed satellites spiky. The low number of satellites makes it statistically impossible to observe a trend.

Since most satellites are grouped up in the lower left corner, a zoomed in version of the previous figure is shown in figure 4.49. Also here no clear trend is observed.

Based on the orbital mechanics and the physics behind the observation window no clear trend is expected and non is showing in the data. Therefore it is concluded that there is no trend observed linking the percentage of observed satellites to their eccentricity.

Semi-major axis

The analysis of the previous section is performed in a similar fashion, but now as a function of the semi-major axis. The observed LEO satellites are compared to the LEO satellites that were in the field of view of the cameras. The observed satellites sorted by their semi-major axis. The analysis is shown in figure 4.50, where the blue bars represent all the satellites in the cameras fields of view, the orange bar show the number of observed satellites. The yellow line is the percentage of the observed satellites for each bar, where the percentages are shown on the right y-axis. The horizontal red line shows the percentage of detected LEO satellites with respect to the LEO satellites in the field of view of the satellite for the whole data set. The x-axis shows the altitude, the semi-major axis minus the Earth radius, assuming a circular orbit.

Figure 4.50 shows a slightly increasing trend for incrasing semi-major axis. This can on the one hand be ex-

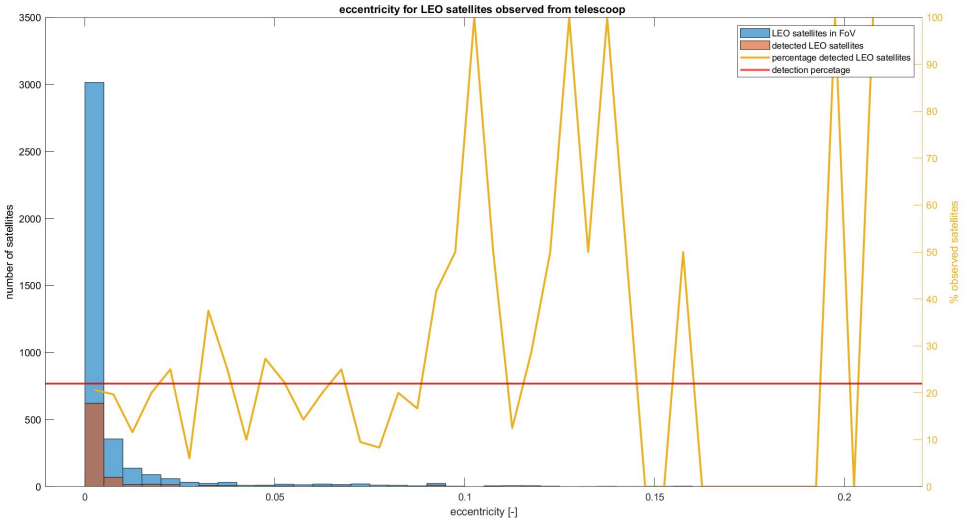

Figure 4.48: Eccentricity of the observed satellites compared to all satellites which where in the camera's field of view. The yellow line indicated the observed percentage and the red line is the average observed percentage of satellites

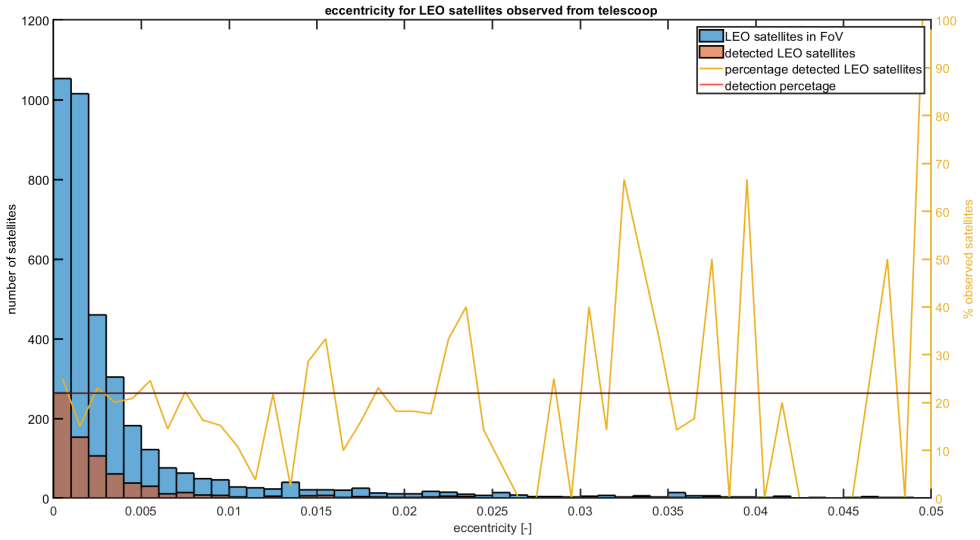

Figure 4.49: Eccentricity of the observed satellites compared to all satellites which where in the camera's field of view. The yellow line indicated the observed percentage and the red line is the average observed percentage of satellites. The x-axis is limited between 0 and 0.05.

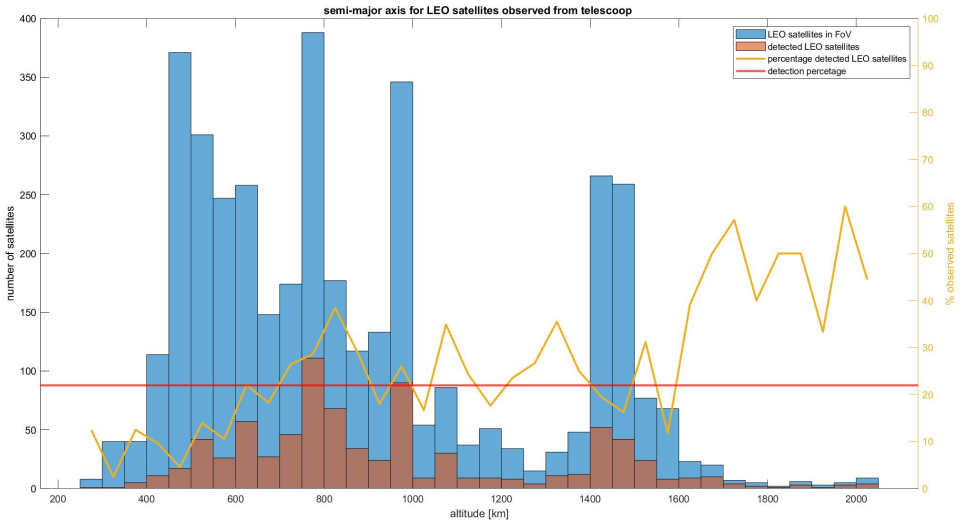

Figure 4.50: Semi-major axis of the observed satellites compared to all satellites which where in the camera's field of view. The yellow line indicated the observed percentage and the red line is the average observed percentage of satellites

pected since the observation window becomes larger for two reasons. The larger the semi-major axis the lower the orbital velocity. Secondly, the period at which the camera is not, and the satellite is in field of view of the sun becomes longer for satellites with an larger semi-major axis. On the other hand, if the semi-major axis increases, the satellite is further away, so the reflective light is spread over a larger area, making the light intensity experiences on the ground less intense. This decreases the observation probability.

In this case it is a statistical misinterpretation. From 1600 km and up has only a few satellites. Therefore not having enough data points to confidently identity this as a trend. Therefore no significant trend is found for the semi-major axis.

Inclination

Similar to the previous two sections, the inclination is analysed for possible trends in the observed satellites. The results are shown in figure 4.51. It can be seen that low inclinations up till about 32 degrees have a significant larger percentage of observed satellites compared to higher inclined satellites.

This can be explained by the fact that all three observation stations are located between -29.3 and -32.4 degrees latitude and that there are four cameras looking in the East/West direction and only two cameras looking in the North/South direction. The ground track of a 28 degrees inclined satellite and a satellite with a 83 degrees inclination are shown in figure 4.52[1]. Here it can be seen that an East/West looking camera around the -30 degrees latitude, can observe a much larger part of the low inclined orbit in comparison to the high inclined obit. Increasing the length of the orbit that can be seen increases the chance that the conditions are met for optical observations of satellites.

The probable cause of the high percentage of observed LEO satellite in the low inclination regime cannot be verified based on this data. A statistical small number of satellites is available for the low inclination regime. Therefore a trend can not be guarantied. Also, all observation stations are located around -30 degrees latitude. Making it not possible to verify that the latitude of the station has impact on the inclination of the satellites observed. Further research and computer modelling can be used to investigate this relation.

[1] `https://www.youtube.com/watch?v=Ke_-_mps88Q`, accessed on 17-9-2020.

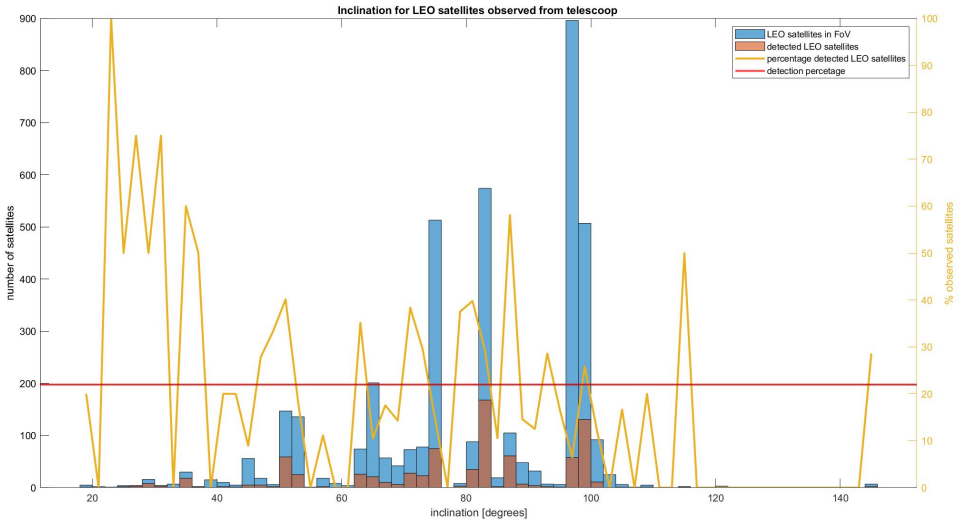

Figure 4.51: Inclination of the observed satellites compared to all satellites which where in the camera's field of view. The yellow line indicated the observed percentage and the red line is the average observed percentage of satellites

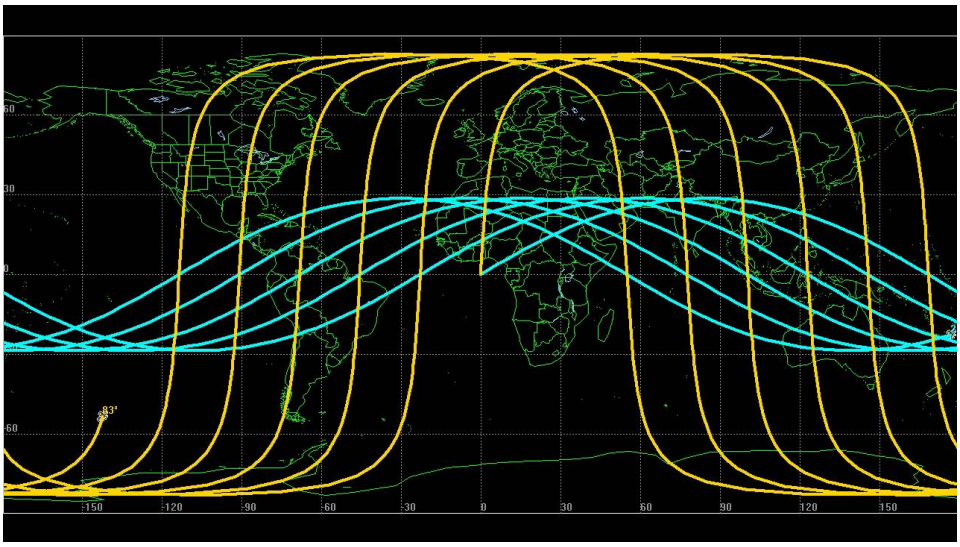

Figure 4.52: Ground track for a satellite with a 83 degrees inclination indicated with the yellow track and a satellite with a 28 degrees inclination indicated with the blue track.

5
Discussion

This section discusses the results presented in chapter 4. The CAR-MHF is discussed in section 5.1. The satellite characteristics are discussed in section 5.2.

5.1. CAR-MHF

The validation showed that the CAR-MHF worked as intended for single arc observations, but started to show unstable behaviour for multiple sequential arcs. When resetting the covariance matrix between arcs resulted in the elimination of this instability. Therefore the problem is expected to be caused by the covariance matrix propagation. And this makes sense since the covariance matrix is propagated with a state transition matrix, which uses linear propagation. For this reason it was already determined to use the RKF4(5) for state propagation, since this variable step size integrator does suffer a lot less from this problem.

The Unscented Kalman filter, which DeMars uses for his implementation of the CAR-MHF, could resolve this problem. The UKF makes use of sigma-points, which are a spread of state vectors, and propagates this with any preferred method. The spread of these sigma-points at the next epoch determines the covariance matrix at this epoch. Therefore there is no need to propagate the covariance matrix. So this will resolve the problem of not being able to use multiple observation arcs, as it can be seen by the work of DeMars [10].

But there is not guaranty that this solves the problem, because poor dynamical models and significant initial errors can also result in an unstable behaviour as described by Murat Gokce Et. al [15]. Section 4.1.6, already made a small site-step to this topic. Here the CAR-MHF solution is only propagated to the next observation arc to assess the magnitude of the error. With the limiting experience it is found that the errors are significant and could resolve in this unstable behaviour.

This unstable behaviour could be resolved by using more perturbing forces for the dynamical model, like the J5 effect, third body perturbations of the Moon and the Sun and atmospheric drag. An added benefit when using the UKF is that no complex partial derivatives of the dynamical equations is needed. Especially with additional perturbing forces these partial derivatives can become complex, sensitive to errors, and linearization errors due to partial derivatives could occur. This last effect was already seen in section 3.3.2, the validation of the state transition matrix.

If further research would provide evidence that stable transitions from one observation arc to another is possible, then the orbit determination solution can gain significant in accuracy. Section 4.1, the CAR-MHF analysis for 10 satellites showed two satellites which found another semi-stable behaviour for the short observation arc. This problem can quickly be resolved if there would be another observation arc, ideally, on the opposite side of the first observation arc. Then it would quickly be apparent that the found combination of eccentricity and semi-major axis were off by a large fraction.

But additional observation arcs would not only solve the problem of these large errors. In this research it was found that in general the orbital plane, and the position within the orbital plane with a few degrees accurately

determined. The shape of the orbit, defined by the semi-major axis and eccentricity had the largest errors. So with the same logic as presented in the previous paragraph, additional observation arcs would greatly improve the semi-major axis and eccentricity error.

Of course if stable behaviour, when transitioning from one to another observation arc, can be achieved. If this cannot be achieved the CAR-MHF would not be the best choic for IOD/OD problems. In this research it is found that Gauss' method and this implementation of the CAR-MHF showed similar performance for for single arc orbit determination. The CAR-MHF was able to find 242 OD valid solutions, where Gauss' method was only able to find 204 valid solutions. Giving a slight advantage to the CAR-MHF over Gauss' method.

The CAR-MHF is a much more complex algorithm to properly set-up compared to Gauss' method. A proper assessment of the initial covariance, model uncertainty, and measurement uncertainty needs to be researched. Also the elimination criteria, grid size and constrains for the admissible region are all variables which can be tuned. In an earlier stage of this research only 16 CAR-MHF solutions were found for exactly the same data set. Therefore it would be my recommendations to only use the CAR-MHF method when it is proven that the CAR-MHF, with improvements, is able to transition from one observation arc to another. Then one has an IOD and OD in one neat algorithm.

An alternative would be to investigate batch methods to improve the IOD solutions. The accuracy performance of Gauss' method was similar to that of the CAR-MHF, and is therefore alike. The advantage of the using batch method is that one does not need to propagate from one observation arc to another, thus not introduce propagation errors.

With this best estimate from a batch method, it would also be possible to use this as a starting point for a sequential orbit determination algorithm, like a Kalman filter. The advantage of this combination is that the initial state has a smaller initial error, therefore the propagation error is smaller, which makes it more likely that the sequential method would be stable.

5.2. Analysis of the observed satellites

This sections discusses the results about the observations made for the different orbital regimes in section 5.2.1. Section 5.2.2 discusses the results of the radar cross sections and the nuances of linking the RCS to the physical size. Section 5.2.3 discuses the orbital parameters of the observed satellites with respect to the observation stations.

5.2.1. orbit regimes

The analysis of the observed satellites showed that the IPA flagged LEO, MEO and GEO satellites, where it was found that MEO and GEO satellites were a result of noise in the images, So these were false positives. The detection of MEO and GEO satellites where coincidence and therefore the satellite itself was not really detected.

For this research the data points were already linked to the satellite for which it belonged. Therefore it is possible to filter the observed data for only LEO satellites for the application of the CAR-MHF. When these routines need to be used to determine the orbits of satellites which are not available in the CSpOC data base, and therefore require data correlation to determine the data points belonging to a single satellite, the false positives add unwanted noise to the system. Therefore the IPA can be improved on the filter out these MEO and GEO false detections.

5.2.2. Radar cross section

The analysis of the radar cross sections showed the effect when removing the satellites from your data set that were not in the field of view. Since they were not in the field of view it is impossible to have detected these satellites. Therefore removing these satellites gives a more realistic analysis. This was then later applied for all other analysis.

Also the increased detection probability during twilight is expected when thinking of the dynamics. During

twilight the ground station is already in the dark but the Earth does not yet block the sunlight between the sun and the satellite. Therefore the light of the sun can still reflect from the satellite to the camera. The contrast between the dark sky in combination with the reflected sunlight creates the perfect conditions.

In this research the RCS is used to find an indication of the physical size of the satellite. This is due to the fact that the CSpOC had a list of satellites available were the RCS is given, en a database of the physical size of the satellites is not available.

This relation needs more clarifications in order to prevent wrong conclusions. The RCS is also dependent on the aspect angle, dependent by the phase angle and attitude of the satellite[20]. The frequency of the observer and the polarisation. The frequency of the radar stations CSpOC was 108 MHz in the past and is later changed to 216-217 MHz, according to Dr. Ir. E.J.O Schrama, Associate Professor at the TU Delft, section space exploration. Since it is not known which of the two installations is used for our data base, both frequencies are looked ad. The wavelength is 1.4 and 2.8 meters, for 217 MHz and 108 MHz, respectively.

Nadav Levanon describes that the RCS can be a 1000 times later then the physical surface area if the wave length is 10 times smaller then the physical dimensions for flat plates[19]. This is an approximation made for this analysis. For satellites of 10 square meters plus this effect needs to be taken into account. The RCS used in this research is based on multiple observations, making it reasonable to assume that effects from the phase angle and attitude of the satellite are averaged out and are therefore no significant error source. When a small data set is used for the determination of the RCS, the RCS needs to be taken with an uncertainty due to this effect.

Due to these effects no conclusive parallels can be drawn between the RCS and the physical size of the satellite, but it can be used as an indication in the absence of a database of the physical size of the satellites.

5.2.3. Observations trends in the orbital elements

In the result section 4.4.3 it is investigated if for the current camera set-up shows a trend for the observability of the satellites. For the eccentricity, inclination and semi-major axis showed no clear trend. This research is limited due to the relative short observation window of three days. More data would make it possible to observe more satellites and see a statistical more clear trend.

All three ground stations are also located around the same latitude of -30 degrees. This makes it impossible to determine what the effect of the latitude of the ground station w.r.t. the observed satellite.

The available orbits is limited to the satellites that are orbiting the Earth in LEO. In the graphs in section 4.4.3, for the eccentricity, semi-major axis and inclination shows groupings of satellites around certain values. The eccentricity is centred close to zero. Therefore there as a low amount of satellites with a larger eccentricity. The semi-major axis shows a low concentration for an altitude lower then 400 km, between 1000 and 1400 km altitude, and larger then 1600 km. The inclination for the given satellites show 5 peaks around 50, 65, 78, 82, and 98 degrees. The last one is the largest and is due to the fact that this is needed sun-synchronous orbits. All these regions makes it statistical impossible to draw parallels to the position of the ground station and the observed orbits.

In order to determine the best position of the ground station the approach used in this research is not the best approach. In order to determine the optimal ground stations positions and configuration simulation would need to be made, where the ground station is a variable and a wide range of different orbits can be simulated and checked if the satellites pass the field of view of the camera, desirable during twilight for optimal observation conditions. Also with this simulation conclusions can be drawn over the limitations of the current ground stations MASCARA and bRing.

The graphs do show the spread in the population of LEO satellites for the orbital elements; eccentricity, semi-major axis, and inclination. The regions where most LEO satellites are located. This can give insight for the starting conditions of designing the optimal ground station position and configuration.

6

Conclusion & recommendation

The chapter first presents the conclusion in section 6.1, where the conclusions following this research are presented. Following the conclusions, the recommendations for future work are presented in section 6.2.

6.1. Conclusion

The Constrained Admissible Region Multiple Hypothesis Filter (CAR-MHF), as proposed by DeMars has until now only been tested in simulated environments where the detection rate is a 100% when in the field of view of the camera and random errors are given to the data. In this research an adoption of the described CAR-MHF of DeMars is developed and is tested based on observations made by the MASCARA and bRing telescopes as part of an investigation into the limitations of orbit determination based on observations made by these telescopes. The CAR-MHF showed a promising concept which is able to perform the IOD without relying on fundamental assumptions like Gauss' method. After finding the IOD solution the method should smoothly move over from IOD to OD, where the IOD solution is improved on by a Kalman filter based on available observations.

During the validation in, section 3.3, it is found that the Extended Kalman Filter (EKF), as part of the CAR-MHF, showed showed unstable behaviour when moving from one observation arc to another. The solution from the previous observation arc is propagated to the next observation arc, resulting in propagation errors. These propagation error then result in a larger difference between the predicted and measured observations. The state covariance matrix is not accurately propagated over the time span between the two observation arcs due to the use of a linearized state transition matrix. The increased error between the predicted and measured observation in combination with an inaccurately propagated covariance matrix leads to unstable behaviour between observation arcs. Therefore the research limited to only analysing the performance of the self modified CAR-MHF for single observation arcs.

The first research goal is given below:

Compare the accuracy performance of the CAR-MHF with the accuracy performance of Gauss' method.

The instability of the EKF when propagating from one observation arc to another, removed the advantage of the CAR-MHF to continuously improve the estimated state based on available data point. Where Gauss's method is only able to construct is single best initial estimate of the state. A detailed performance of the

Now that both methods only perform on a single observation arc, a fair assessment between the two methods can be made. This comparison is shown in section 4.3. It was found that the performance of the CAR-MHF was better for the semi-major axis with an average error of 1282 km, versus an average error of 2192 km for Gauss's method. Both methods have an average error of less then one degree for the inclination and Right ascension of the ascending node, defining the orbital plane. The eccentricity shows an error of around 0.1. The Argument of Periapsis and True Anomaly show significant errors, but when adding those two values, the error is also less then one degree. From this it can be concluded that the the position in the orbit is determined with an accuracy of less then one degree. It also shows, in combination with the semi-major axis and

eccentricity error, that a single observation arc is not sufficient to accurately determine the shape of the orbit.

The CAR-MHF is able to find a valid solution for 242 satellites, where Gauss' method is only able to find the solution for 204 satellites. The expected cause of the difference is also presented in section 4.3. The satellite for which the CAR-MHF found a solution, and Gauss' method did not showed an lower then average observation arc duration of 1:38 minutes. The average observation arc duration of the 204 satellites is 2:04 minutes. Therefore concluding that the CAR-MHF is better equipped to find a valid solution for short arc observations.

Concluding; The CAR-MHF and Gauss' method show similar performance w.r.t. accuracy, with the exception of the semi-major axis. The CAR-MHF is able to produce more solutions, making it a more versatile method.

The second research goal is given below:

Analyse the detected satellites as a function of the following characteristics: orbital parameters, orbit type, and Observability.

The analysis of the detected satellite focuses it attention of finding trends in the observed satellite. The results can be found in section 4.4. There is no correlation found for the orbital element: Eccentricity, semi-major axis, or inclination. No statistical significant correlation was found whereby specific orbits where detected more significantly.

The observed data did show detection of MEO and GEO satellites and were investigated. These observations, as showed in section 4.4.3, where noisy pixel accidentally linked to the position of these MEO and GEO satellites. Therefore it is concluded that the Image processing algorithm, which generated the observation data from the image, is not able to detect MEO and GEO satellites

The analysis of the Radar Cross Section of the satellites, showed in section 4.4.1, found that satellites with a RCS of three square meters or larger have a 80% detection probability. But the RCS can not directly linked to the physical size, as discussed in section 5.2.2. The RCS is next to physical size, depended on the phase angle, wavelength, attitude of the satellite. Therefore no conclusions can be drawn about the physical size of the satellite which the camera set-up is able to detect. It was found that most observations are made during twilight, where the conditions are ideal for optical observations, where the observer is in the dark, and the satellite is still in the field of view of the sun, making it able to reflect sunlight to the observer.

Answering the research question of this master thesis:

Investigating the limitations of the MASCARA & bRing optical instrument for the detection & orbit determination of LEO satellites with the constrained admissible region multiple hypotheses filter.

The data obtained from the bRing and MASCARA optical instruments made it possible to perform initial orbit determination for the observed satellites. After filtering the data for LEO satellites only and applying the Image Processing Algorithm (IPA), the data provides sufficient accurate data to use as input for an IOD algorithm. Looking back this is also expected due to the fact that the IPA links data points to satellites with the pixel position of the track end-point is withing 10 pixels of the SGP4-based determines pixel position. Making the maximum error approximate 0.2 degrees, as discussed in section 3.3.3.

Conclusions about the limitations of the position of the optical instruments could not be drawn. Due to limited observation of different orbits of satellites and the fact that all three stations are located around -30 degrees latitude. This discussion is presented in 5.2.3. To answer this question a simulation should be made, where the position and configuration of the ground station, and the satellite orbits are variable. With this simulation trends between ground station position and configuration and different orbital characteristics can be found.

The current implementation of the CAR-MHF makes it not possible to perform orbit determination for multiple consecutive observation arcs, as discussed in the validation, section 3.3.2. Chapter 4 showed that the CAR-MHF is able to determine the orbital plane, determined by the inclination and Right ascension of the ascending node, with an average accuracy of less then one degree. The position in the orbital plane, given by

the combined value of the Argument of periapsis and true anomaly is determined with an average accuracy of less then one degree. The eccentricity does still show significant error of with an average error of 0.11. This large error also results in an average error of more then 100 degrees for the separate Argument of periapsis and True anomaly. From this observations, it is concluded that a single observation arc is not sufficient to accurately determine the eccentricity.

Therefore it is concluded that the CAR-MHF is the most limiting factor for accurate and reliable orbit determination. The data provided by the MASCARA and bRing provide excellent input and insight in real-world problems, and can therefore again be used for future work, to improve the orbit determination solution.

6.2. recommendations

During this research a vast amount of experience was obtained on the area of initial orbit determination, Kalman filters and the experience of handling non-simulated data. This has resulted in a set of recommendations for future research.

The FOTOS study worked out their algorithms in a Python environment. This study is a follow up from that study, and therefore it would be recommended to code in Python instead of the Matlab program the author has used. Python is the faster programming language for handling large data sets and it does not require the import and export of data between the two coding platforms.

On paper the CAR-MHF is an elegant algorithm when having plenty of observations. The algorithm is able to start as a initial orbit determination algorithm and smoothly transition to a orbit determination algorithm after having eliminated all but one hypothesis. Improving the state when new observations are available, even when the satellite manoeuvred.

In order to demonstrate this elegance, the extended Kalman filter needs to be replaced, probably by the Unscented Kalman filter, which does not show theoretical shortcoming to be able to handle gabs in the data. With longer observation data a proper analysis of the required perturbing forces in the dynamical model is recommended, to improve the stable behaviour when propagating from one observation arc to another.

An alternative is the use Gauss' method to perform the IOD solution per observation arc, and then use a batch method to determine the state more accurately.
An alternative would be Gauss' method to determine the initial orbit solution in combination with the batch least square in order to compensate for measurement uncertainties. The advantage is that the algorithm is of a less complex compared the CAR-MHF. The disadvantage is that the algorithm can not handle manoeuvres of a satellite. This can be resolved by using a batch method to accurately calculate the initial condition for a sequential method. Combining both methods to obtain the best of both worlds.

The satellite characteristics analysis could become a separate research subject when a thorough analysis needs to be achieved. This research only addressed the tip of the iceberg. Larger observation data sets can be used to better draw statistical relations. Additional research to determine the best observation conditions would also be needed. Hereby looking at the different elements like reflective area of the satellite, albedo and phase angle.

The different camera positions available for this research, in combination with simulations, can be used to determine the effects of the position and viewing direction on the detection probability of satellites. This can be further expanded on by performing a more thorough analysis on the relation between the type of orbit (orbital plane and orbital period) and the position of the camera for the detection probability. Here the dependency of the time of day can be research in more detail.

Bibliography

[1] UCS Satellite Database. https://www.ucsusa.org/resources/what-are-satellites-used#:~:text=Satellites%20provide%20in%2Dflight%20phone,for%20cell%20phones%20and%20pagers., 2015 (accessed August 20, 2020).

[2] Earth orientation data. www.iers.org, accessed at August 26, 2020.

[3] Astrodynamics software. https://celestrak.com/software/vallado-sw.php, accessed at August 27, 2020. Version as of 2020 Nov 09.

[4] The kessler effect and how to stop it. http://www.esa.int/Enabling_Support/Space_Engineering_Technology/The_Kessler_Effect_and_how_to_stop_it, accessed August 20, 2020.

[5] Sandip Tukaram Aghav and Shashikala Achyut Gangal. Simplified orbit determination algorithm for low earth orbit satellites using spaceborne gps navigation sensor. *Artificial Satellites*, 49(2):81 – 99, 2014. doi: 10.2478/arsa-2014-0007.

[6] Ana Paula Marins Chiaradia, Hélio Koiti Kuga, and Antonio Fernando Bertachini de Almeida Prado. Comparison between Two Methods to Calculate the Transition Matrix of Orbit Motion. *Mathematical Problems in Engineering*, 2012:768973, October 2011. ISSN 1024-123X. doi: 10.1155/2012/768973. URL https://doi.org/10.1155/2012/768973. Publisher: Hindawi Publishing Corporation.

[7] INTER-AGENCY SPACE DEBRIS COORDINATION COMMITTEE. Iadc space debris mitigation guidelines. Technical report, 2007.

[8] Howard Curtis. *Orbital Mechanics for Engineering Students*. Elsevier Butterworth-Heinemann, first edition, 2005. ISBN 0 7506 6169 0.

[9] K DeMars and M Jah. Passive multi-target tracking with application to orbit determination for geosynchronous objects. *Presented at the 19th AAS/AIAA Space Flight Mechanics Meeting,Savannah, GA*, pages 09–108, 2009.

[10] K. J. DeMars, M. K. Jah, and P. W. Schumacher. Initial Orbit Determination using Short-Arc Angle and Angle Rate Data. *IEEE Transactions on Aerospace and Electronic Systems*, 48(3):2628–2637, July 2012. doi: 10.1109/TAES.2012.6237613.

[11] Kyle J. DeMars and Moriba K. Jah. Probabilistic Initial Orbit Determination Using Gaussian Mixture Models. *Journal of Guidance, Control, and Dynamics*, 36(5):1324–1335, 2013. URL https://doi.org/10.2514/1.59844. doi: 10.2514/1.59844.

[12] G. Der. New Angles-only Algorithms for Initial Orbit Determination. *Advanced Maui Optical and Space Surveillance Technologies Conference*, page 53, September 2012. URL https://ui.adsabs.harvard.edu/abs/2012amos.confE..53D/abstract.

[13] Wei Dong and Zhao Chang-yin. An Accuracy Analysis of the SGP4/SDP4 Model. *Chinese Astronomy and Astrophysics*, 34(1):69–76, 2010. ISSN 0275-1062. doi: https://doi.org/10.1016/j.chinastron.2009.12.009. URL https://www.sciencedirect.com/science/article/pii/S0275106209001404.

[14] P. Fortescue, G. Swinerd, and J. Stark. *Spacecraft Systems Engineering*. Wiley, 2011. ISBN 9781119978367.

[15] Murat Gokce, Ferhat Arberkli, Seda Aydın, and Mehmet Geden. Improved orbit estimation using angles-only observations and its application to low earth orbit satellites. pages 267–271, 06 2019. doi: 10.1109/RAST.2019.8767829.

[16] Alexander Mordvintsev & Abid K. cv2 python package describing the probabilistic hough transform., 2013. URL https://opencv-python-tutroals.readthedocs.io/en/latest/py_tutorials/py_imgproc/py_houghlines/py_houghlines.html.

[17] Tom Kelecy, Michael Shoemaker, and Moriba Jah. Application of the constrained admissible region multiple hypothesis filter to initial orbit determination of a break-up. In *6th European Conference on Space Debris*, volume 723, 2013.

[18] Systems Tool Kit. Stk: Sgp4 propagator, 2016. URL https://help.agi.com/stk/11.0.1/Content/stk/vehSat_orbitProp_msgp4.htm.

[19] Nadav Levanon. Radar. In Robert A. Meyers, editor, *Encyclopedia of Physical Science and Technology*, pages 497–510. Academic Press, Burlington, 2003. ISBN 978-0-12-227410-7.

[20] Hsueh-Jyh Li and Yean-Woei Kiang. 10 - radar and inverse scattering. In WAI-KAI CHEN, editor, *The Electrical Engineering Handbook*, pages 671–690. Academic Press, Burlington, 2005. ISBN 978-0-12-170960-0. doi: https://doi.org/10.1016/B978-012170960-0/50047-5. URL https://www.sciencedirect.com/science/article/pii/B9780121709600500475.

[21] John H. Mathews and Kurtis K. Fink. *Numerical Methods Using Matlab (4th Edition)*. Pearson, 4 edition, January 2004. ISBN 9788120327658. URL http://www.amazon.com/exec/obidos/redirect?tag=citeulike07-20&path=ASIN/0130652482.

[22] Jonathan C. McDowell. The Low Earth Orbit Satellite Population and Impacts of the SpaceX Starlink Constellation. *The Astrophysical Journal*, 892(2):L36, April 2020. ISSN 2041-8213. doi: 10.3847/2041-8213/ab8016. URL http://arxiv.org/abs/2003.07446. arXiv: 2003.07446.

[23] Caleb Henry Space news. Spacex submits paperwork for 30,000 more starlink satellites, 2019. URL https://spacenews.com/spacex-submits-paperwork-for-30000-more-starlink-satellites/.

[24] ESA Space Debris Office. Esa's annual space environment report. Technical Report 4.0, ESA, September 2020.

[25] ESA's Space Debris Office. Space environment statistics, 2021. URL https://sdup.esoc.esa.int/discosweb/statistics/.

[26] R.P. Rikken. Literature study on optical satellitedetection and orbit determination withinfotos2. *Literature study for MSc Thesis - TU Delft*, 2019.

[27] John Seago and David Vallado. Coordinate frames of the u.s. space object catalogs. 08 2000. doi: 10.2514/6.2000-4025.

[28] R. Stuik, J. I. Bailey, P. Dorval, G. J. J. Talens, I. Laginja, S. N. Mellon, B. B. D. Lomberg, S. M. Crawford, M. J. Ireland, E. E. Mamajek, and M. A. Kenworthy. bRing: An observatory dedicated to monitoring the β Pictoris b Hill sphere transit. *Astronomy & Astrophysics*, 607:A45, nov 2017. ISSN 0004-6361, 1432-0746. URL https://www.aanda.org/articles/aa/abs/2017/11/aa31679-17/aa31679-17.html. doi: 10.1051/0004-6361/201731679.

[29] G. J. J. Talens, J. F. P. Spronck, A.-L. Lesage, G. P. P. L. Otten, R. Stuik, D. Pollacco, and I. a. G. Snellen. The Multi-site All-Sky CAmeRA (MASCARA) - Finding transiting exoplanets around bright (mV < 8) stars. *Astronomy & Astrophysics*, 601:A11, May 2017. ISSN 0004-6361, 1432-0746. URL https://www.aanda.org/articles/aa/abs/2017/05/aa30319-16/aa30319-16.html. doi: 10.1051/0004-6361/201630319.

[30] David A. Vallado. *Fundamentals of Astrodynamics and applications*. McGraw-Hill, 1 edition, 1997. ISBN 0070668345.

[31] David A. Vallado. *Fundamentals of Astrodynamics and applications - erratave1*. McGraw-Hill, 2000.

[32] kerel F. Wakker. *Fundamentals of Astrodynamics - AE4874*. Institutional Repository - TU Delft, 1 edition, 2015. ISBN 978-94-6186-419-2.

[33] Thomas Wijnen, Remko Stuik, Michiel Rodenhuis, Marco langbroek, and Petra Wijnja. Using all-sky optical observations for automated orbit determination and prediction for satellites in low earth orbit. *1st NEO and Debris Detection Conference*, 1(1), 2019.

A

Grid size analysis

Four satellites where analysed on for different grid sizes. In order to make a trade of between performance, accuracy, computation time in order to determine the best grid size for the application used in this research.

The tables show the grid sizes for which the method was tested on the first row. The second row, hypotheses, show the number of generated hypotheses after the CAR part. Epoch to conversion, the third row, shows the number of observations required for the CAR-MHF to converge to a single solution. The errors are defined as the difference between the SGP4 reference and the CAR-MHF solution. Where at conversion point means at the point where the second to last hypotheses was eliminated and at the end of arc means at the end of the observation arc. Time stands for the computation time the algorithm needed for a single observation arc and the last row, converged, is a Boolean that stats if a single solution was found, yes or no.

Table A.1: Satellite 10793U, observed from station LSN on the third of januari, 2020, 48 data points spread out over 05:38 minutes.

Grid size	5	10	15	20	25
hypotheses	6	43	105	199	315
epochs to conversion	16	27	33	39	41
At conversion point					
Position error [km]	1.85	1.08	0.71	0.99	1.2
Velocity error [m/s]	4.89	3.42	0.9	1.5	1.8
At end of arc					
Position error [km]	0.95	1.23	1.01	1.06	1.18
Velocity error [m/s]	1.25	1.97	1.63	1.54	1.84
Time [second]	11.2	59.8	136	269	425
converged?	yes	Yes	yes	Yes	Yes

Table A.2: Satellite 36095U, observed from multiple camera's of station LS on the third of januari, 2020, 50 data points spread out over 04:34 minutes.

Grid size	5	10	15	20	25
hypotheses	6	17	42	79	131
epochs to conversion	7	32	40	45	
At conversion point					
Position error [km]	18.16	0.69	0.99	0.076	
Velocity error [m/s]	124.97	4.2	0.67	0.37	
At end of arc					
Position error [km]	3.83	0.9	0.97	0.11	
Velocity error [m/s]	2.21	0.4	0.39	0.43	
Time [second]	8.2	38.96	100	191	
converged?	Yes	Yes	Yes	Yes	NO

Table A.3: Satellite 6257U, observed from station LSE on the third of January, 2020, 28 data points spread out over 02:52 minutes.

Grid size	5	10	15
hypotheses	6	20	48
epochs to conversion	7		
At conversion point			
Position error [km]	14.8		
Velocity error [m/s]	78.32		
At end of arc			
Position error [km]	3.75		
Velocity error [m/s]	18.97		
Time [second]	6.68		
converged?	Yes	No	No

Table A.4: Satellite 404113, observed from multiple camera's of station LS on the third of January, 2020, 46 data points spread out over 04:34 minutes.

Grid size	5	10	15	20	25
hypotheses	2	16	38	69	114
epochs to conversion	7	26	33	44	
At conversion point					
Position error [km]	54.81	0.87	1.22	0.21	
Velocity error [m/s]	3.37	3.91	6.26	0.56	
At end of arc					
Position error [km]	20.55	0.33	0.32	0.21	
Velocity error [m/s]	1.07	1.44	1.24	0.56	
Time [second]	7.84	29.68	75.42	150	
converged?	Yes	Yes	Yes	Yes	No

B

Constrained admissible region validation data

The validation results for the constrained admissible region are presented in this appendix. Table B.1 shows the input data for each satellite. The figures below show the results on which the CAR validation is based.

Table B.1: Validation inputs for the constrained admissible region for satellites: 39260U, 26083U, 38771U, 22803U, 39177U and 22284U.

Satellite	39260U	26083U	38771U	22803U	39177U	29110U
Right ascension [deg]	338.33	78.11	151.07	57.89	139.21	209.37
Declination [deg]	-63.65	8.45	-75.54	-66.47	-52.92	-57.45
Right ascension rate [deg/s]	0.36	0.13	-0.82	0.51	-0.32	-0.44
Declination rate [deg/s]	0.14	-0.14	0.02	0.25	0.11	0.12
Camera latitude [deg]	-29.26	-29.26	-31.27	-29.26	-31.27	-32.38
Camera longitude [deg]	-70.74	-70.74	149.06	-70.74	149.06	20.81
Camera altitude [m]	2369.40	2369.40	1165.00	2369.40	1165.00	1798.00
Camera ID	LSS	LSN	AUE	LSS	AUE	SAE
Time [Julian day]	2458851.620937	2458851.593899	2458851.992660	2458851.628028	2458851.942871	2458852.504592
Minimum range constrained [km]	250.00	250.00	250.00	250.00	250.00	250.00
Track length [pixels]	73.06	44.82	84.38	98.08	70.94	82.93
minimum semi-major axis [km]	250.00	250.00	250.00	250.00	250.00	250.00
maximum semi-major axis [km]	2000.00	2000.00	2000.00	2000.00	2000.00	2000.00
maximum eccentricity [-]	0.30	0.30	0.30	0.30	0.30	0.30

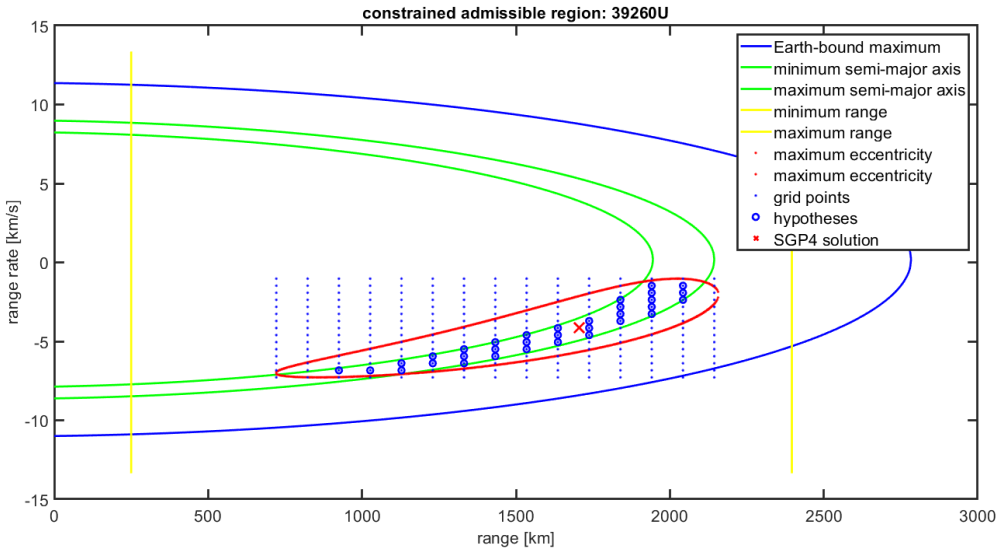

Figure B.1: CAR validation data for satellite 39260U, where it is shown that the satellite state, represented with the red cross, is within the constrained admissible region, were constraints are represented with the green, yellow and red lines. the area with the blue circles around the blue dots represents the constrained admissible region. With a projected grid of 15 by 15.

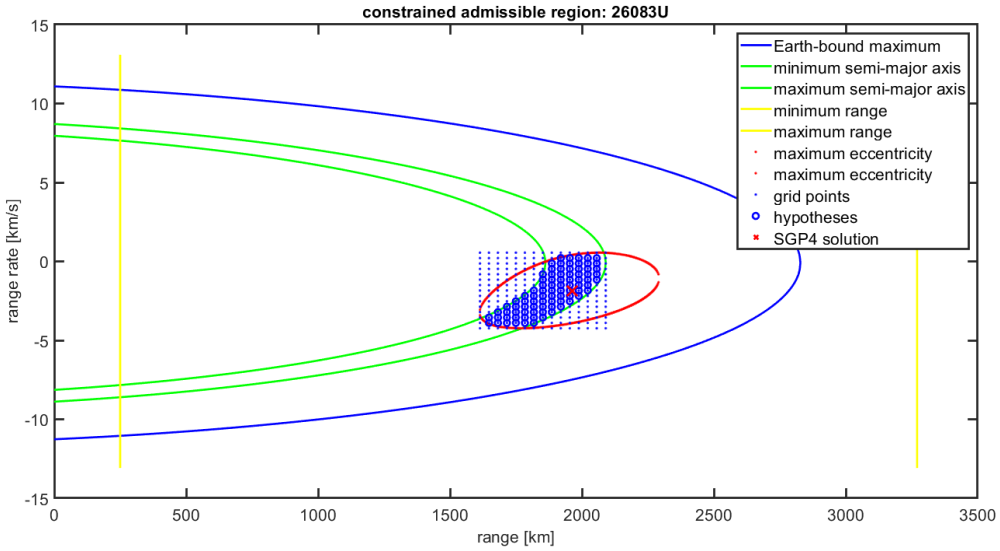

Figure B.2: CAR validation data for satellite 26083U, where it is shown that the satellite state, represented with the red cross, is within the constrained admissible region, were constraints are represented with the green, yellow and red lines. the area with the blue circles around the blue dots represents the constrained admissible region. With a projected grid of 15 by 15.

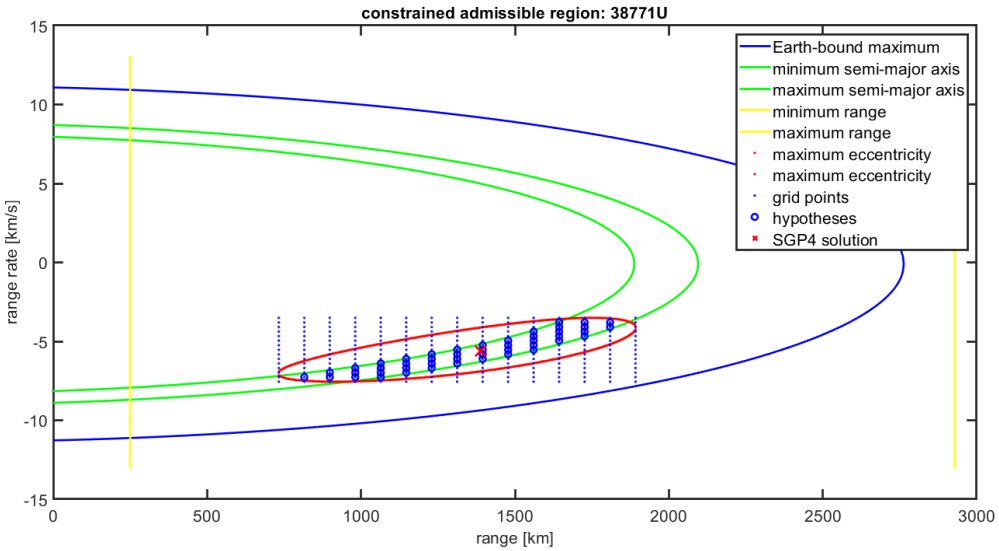

Figure B.3: CAR validation data for satellite 38771U, where it is shown that the satellite state, represented with the red cross, is within the constrained admissible region, were constraints are represented with the green, yellow and red lines. the area with the blue circles around the blue dots represents the constrained admissible region. With a projected grid of 15 by 15.

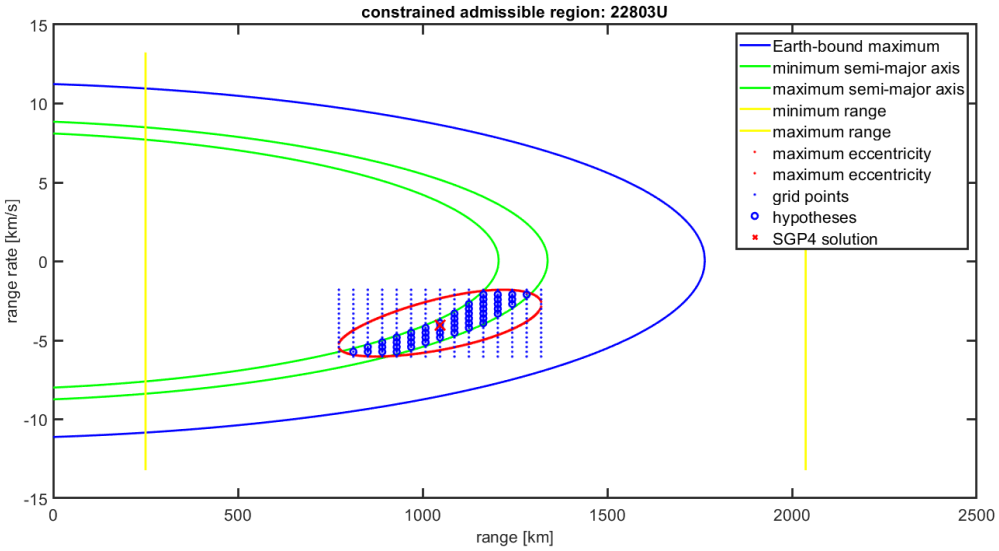

Figure B.4: CAR validation data for satellite 22803U, where it is shown that the satellite state, represented with the red cross, is within the constrained admissible region, were constraints are represented with the green, yellow and red lines. the area with the blue circles around the blue dots represents the constrained admissible region. With a projected grid of 15 by 15.

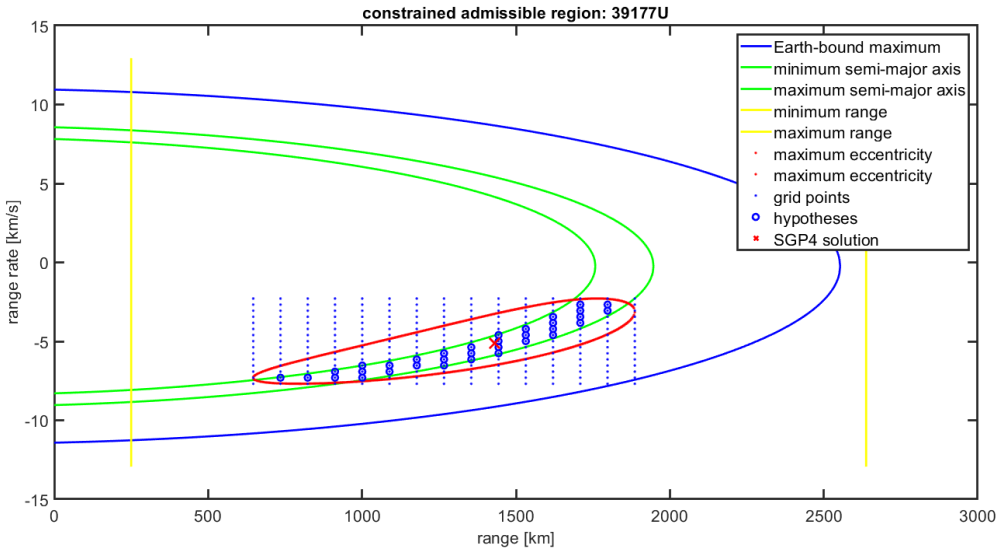

Figure B.5: CAR validation data for satellite 39177U, where it is shown that the satellite state, represented with the red cross, is within the constrained admissible region, were constraints are represented with the green, yellow and red lines. the area with the blue circles around the blue dots represents the constrained admissible region. With a projected grid of 15 by 15.

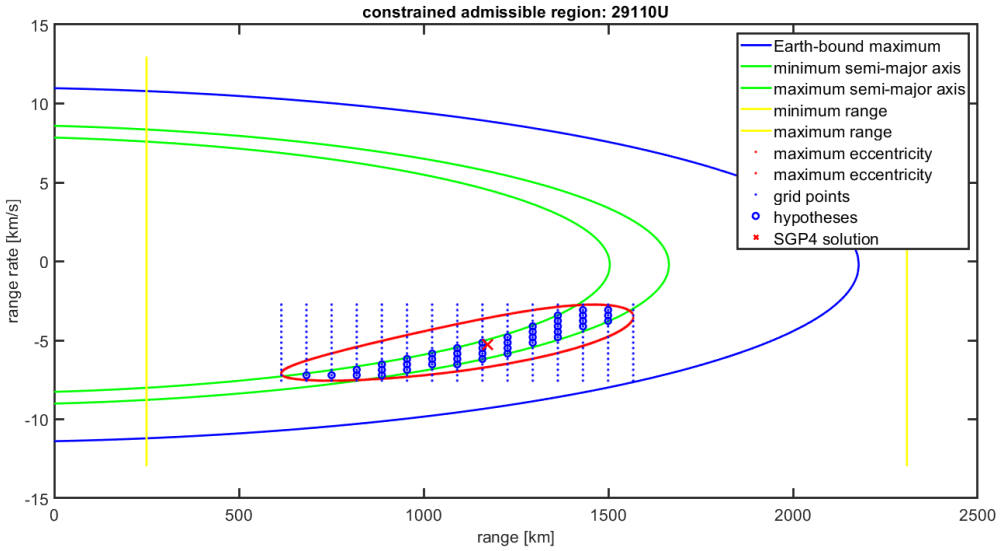

Figure B.6: CAR validation data for satellite 29110U, where it is shown that the satellite state, represented with the red cross, is within the constrained admissible region, were constraints are represented with the green, yellow and red lines. the area with the blue circles around the blue dots represents the constrained admissible region. With a projected grid of 15 by 15.

C

Elimination criteria Verification

The appendix shows the data of the elimination criteria verification, to provide the information needed to assess if the elimination criteria is working as intended. The elimination criteria is first tested with SGP4-based measurements. Value n, given in equation 2.98 is set to one. The grid size is set to 10.

The following satellites are used to test the elimination criteria:

- Satellite 4794U, station LS, 03-01-2020, 58 data points, 05:38 minute time span.
- Satellite 6257U, station LSE, 03-01-2020, 25 data points, 02:52 minute time span.
- Satellite 10793U, station LSN, 03-01-2020, 48 data points, 05:38 minute time span.
- Satellite 22284U, station SAE, 03-01-2020, 30 data points, 03:05 minute time span.
- Satellite 23404U, station AUE, 03-01-2020, 26 data points, 02:52 minute time span.

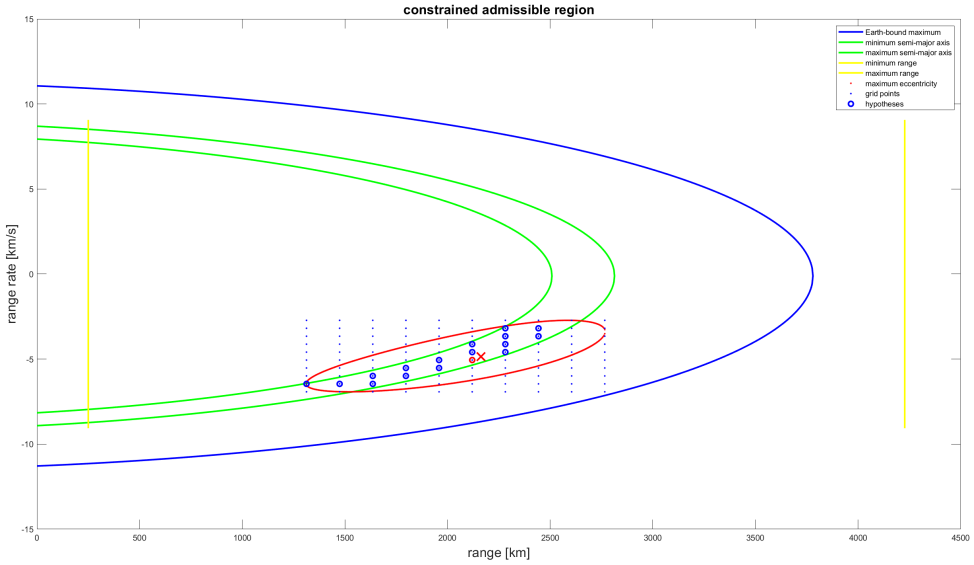

Figure C.1: Satellite 4794U, constrained admissible region with the range, semi-major axis and eccentricity constraint. The blue dots represents the grid, and the blue circled dots represents the selected hypotheses. The red dot is the resulting hypotheses after the CAR-MHF with the described elimination criteria, and the red cross represents the SGP4-based correct state.

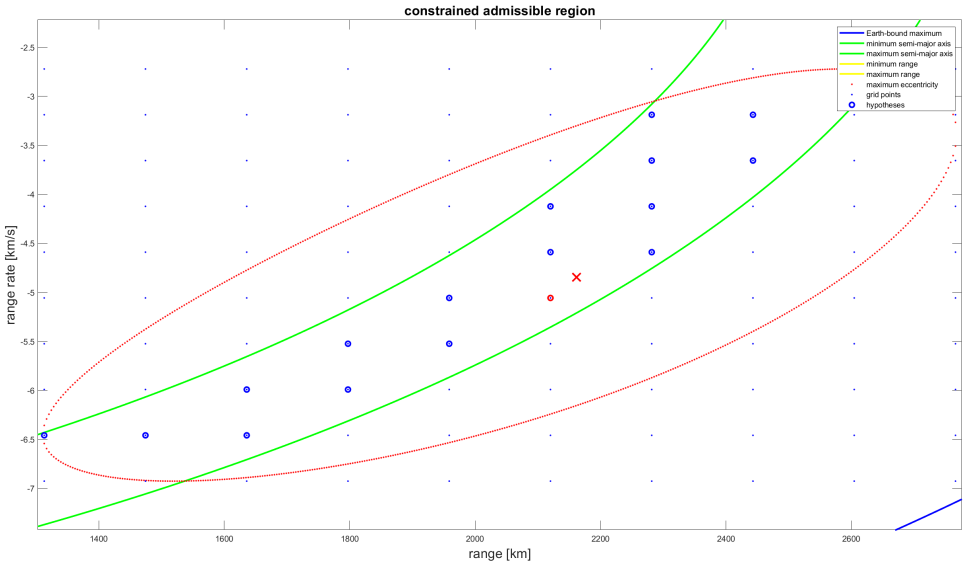

Figure C.2: Satellite 4794U, constrained admissible region with the range, semi-major axis and eccentricity constraint. The blue dots represents the grid, and the blue circled dots represents the selected hypotheses. The red dot is the resulting hypotheses after the CAR-MHF with the described elimination criteria, and the red cross represents the SGP4-based correct state.

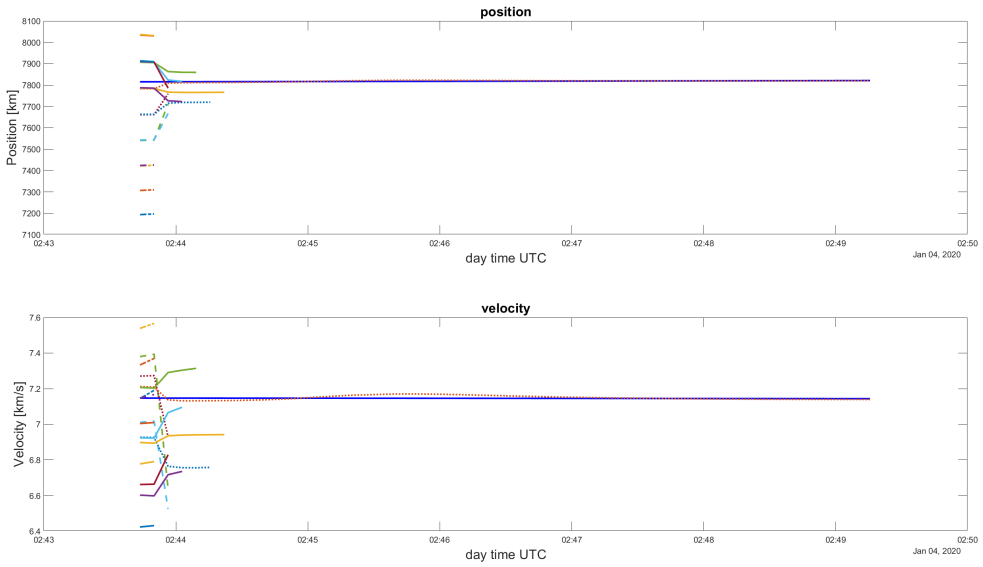

Figure C.3: Satellite 4794U resulting position and velocity at each epoch for each hypothesis selected from the CAR over the duration of an observation arc. The blue line is the SGP4 state of the satellite, the expected solution. Hypothesis line stop when the hypothesis is eliminated.

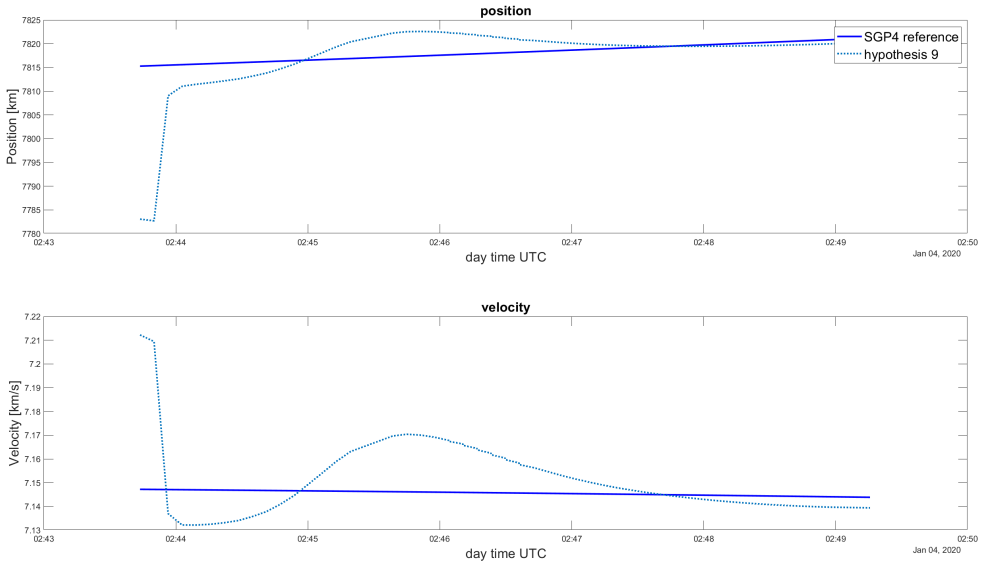

Figure C.4: Satellite 4794U, where the found solution its position and velocity is plotted individually over the span of the observation arc. The dark blue line is the SGP4-based orbit, which is used as a reference.

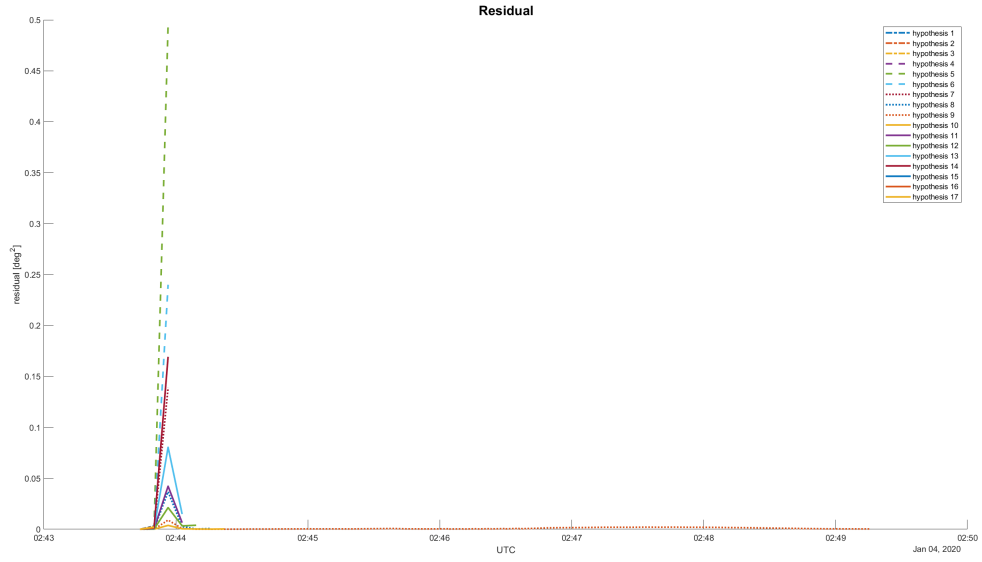

Figure C.5: Satellite 4794U residual during the first observation arc. The residual line stops when the hypothesis is eliminated

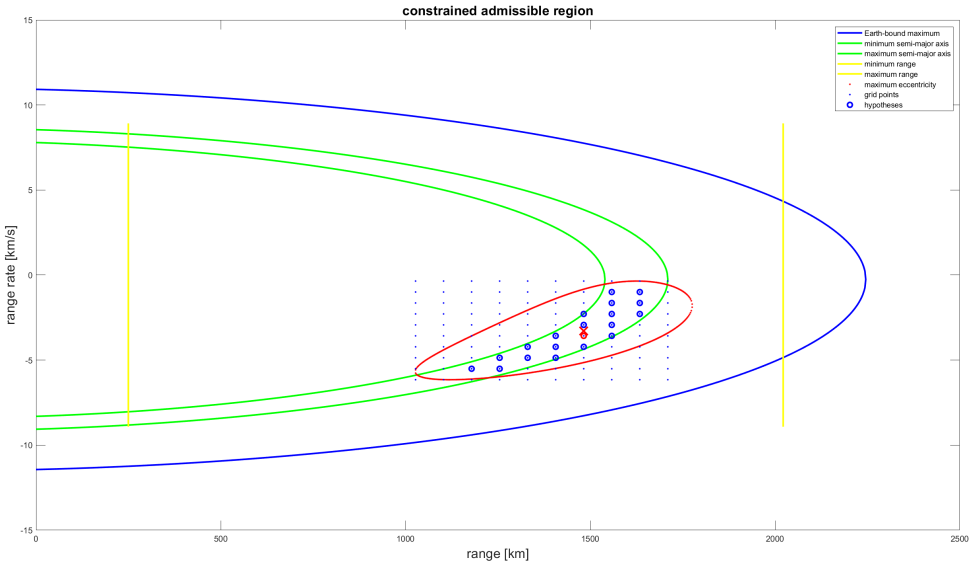

Figure C.6: Satellite 6257U, constrained admissible region with the range, semi-major axis and eccentricity constraint. The blue dots represents the grid, and the blue circled dots represents the selected hypotheses. The red dot is the resulting hypotheses after the CAR-MHF with the described elimination criteria, and the red cross represents the SGP4-based correct state.

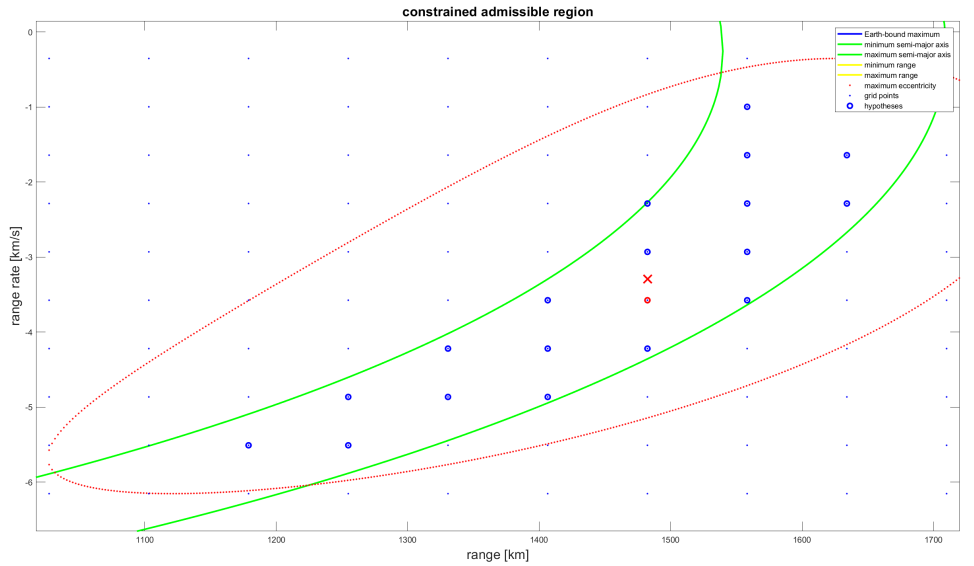

Figure C.7: Satellite 6257U, constrained admissible region with the range, semi-major axis and eccentricity constraint. The blue dots represents the grid, and the blue circled dots represents the selected hypotheses. The red dot is the resulting hypotheses after the CAR-MHF with the described elimination criteria, and the red cross represents the SGP4-based correct state.

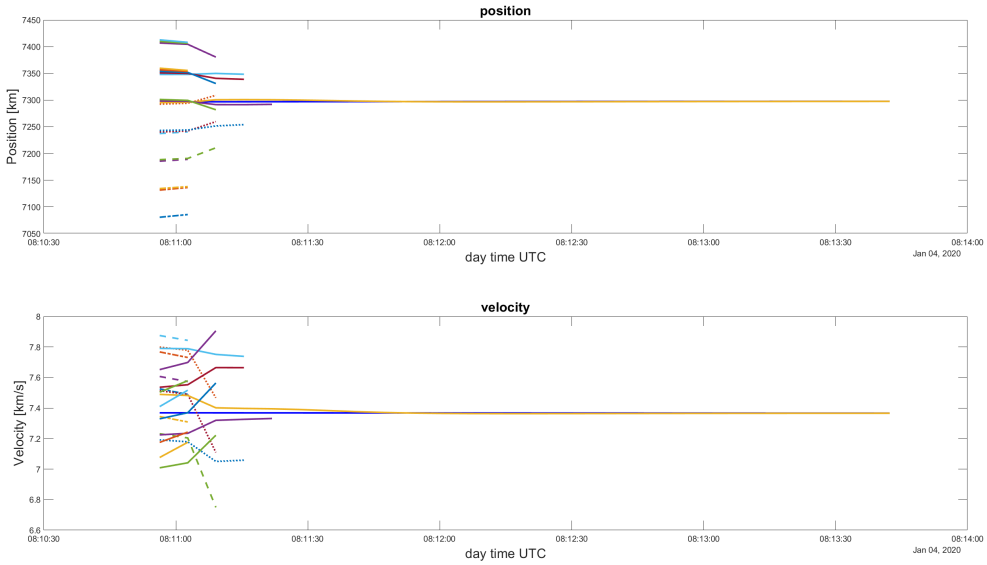

Figure C.8: Satellite 6257U resulting position and velocity at each epoch for each hypothesis selected from the CAR over the duration of an observation arc. The blue line is the SGP4 state of the satellite, the expected solution. Hypothesis line stop when the hypothesis is eliminated.

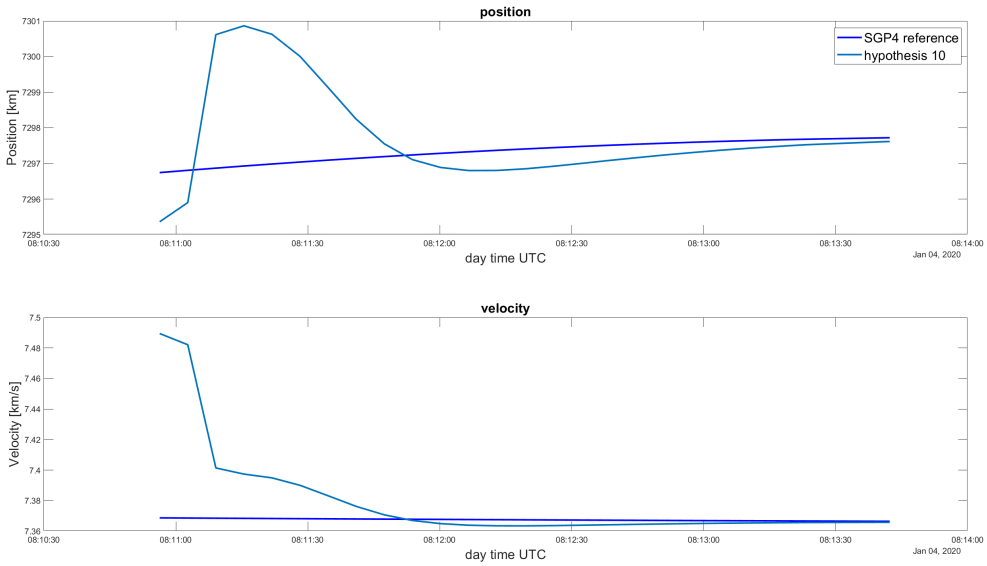

Figure C.9: Satellite 6257u, where the found solution its position and velocity is plotted individually over the span of the observation arc. The dark blue line is the SGP4-based orbit, which is used as a reference.

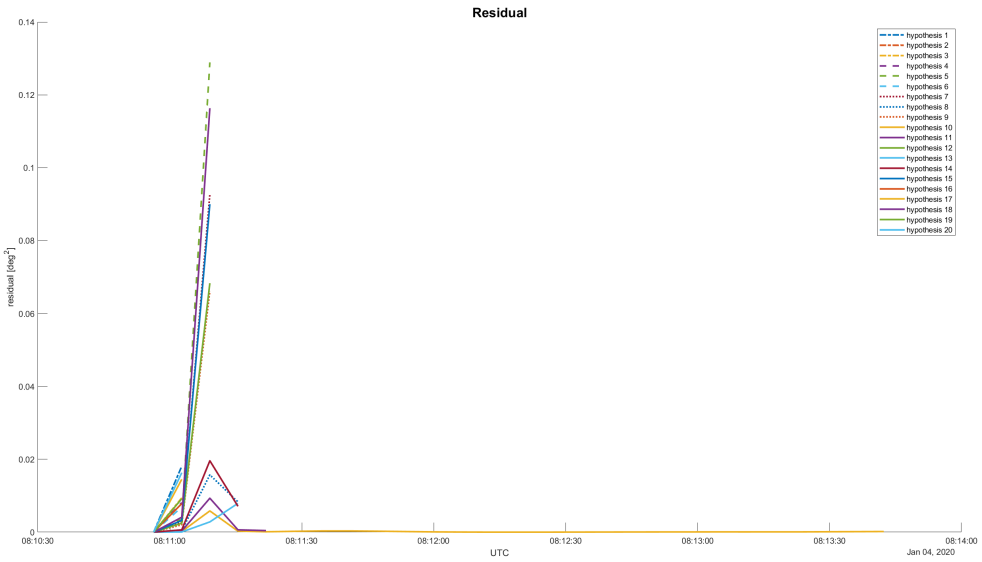

Figure C.10: Satellite 6257U residual during the first observation arc. The residual line stops when the hypothesis is eliminated

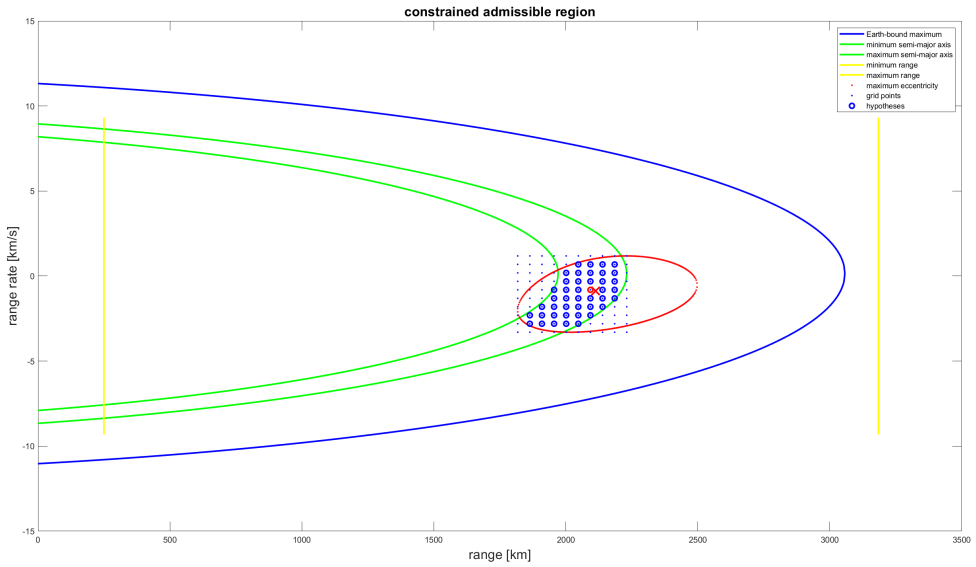

Figure C.11: Satellite 10793U, constrained admissible region with the range, semi-major axis and eccentricity constraint. The blue dots represents the grid, and the blue circled dots represents the selected hypotheses. The red dot is the resulting hypotheses after the CAR-MHF with the described elimination criteria, and the red cross represents the SGP4-based correct state.

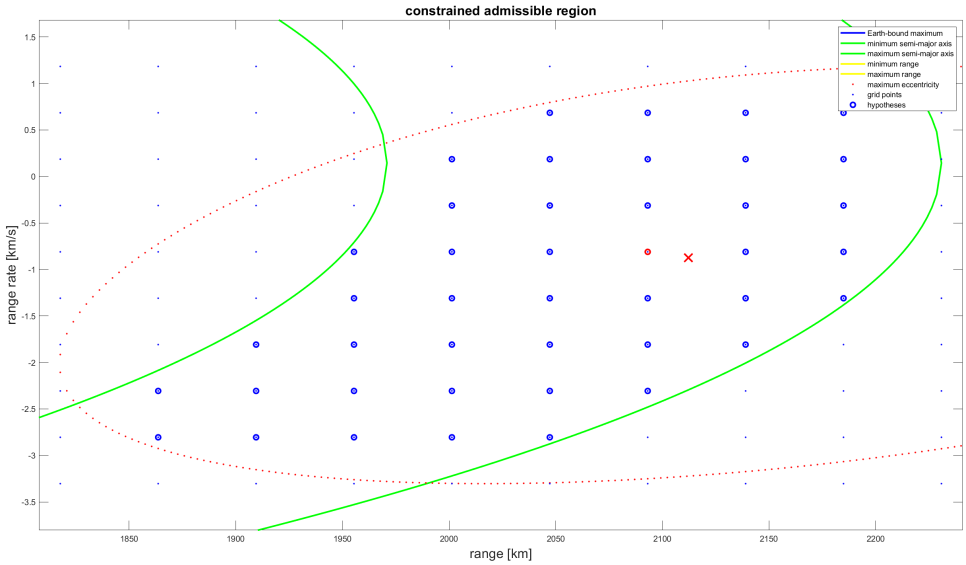

Figure C.12: Satellite 10793U, constrained admissible region with the range, semi-major axis and eccentricity constraint. The blue dots represents the grid, and the blue circled dots represents the selected hypotheses. The red dot is the resulting hypotheses after the CAR-MHF with the described elimination criteria, and the red cross represents the SGP4-based correct state.

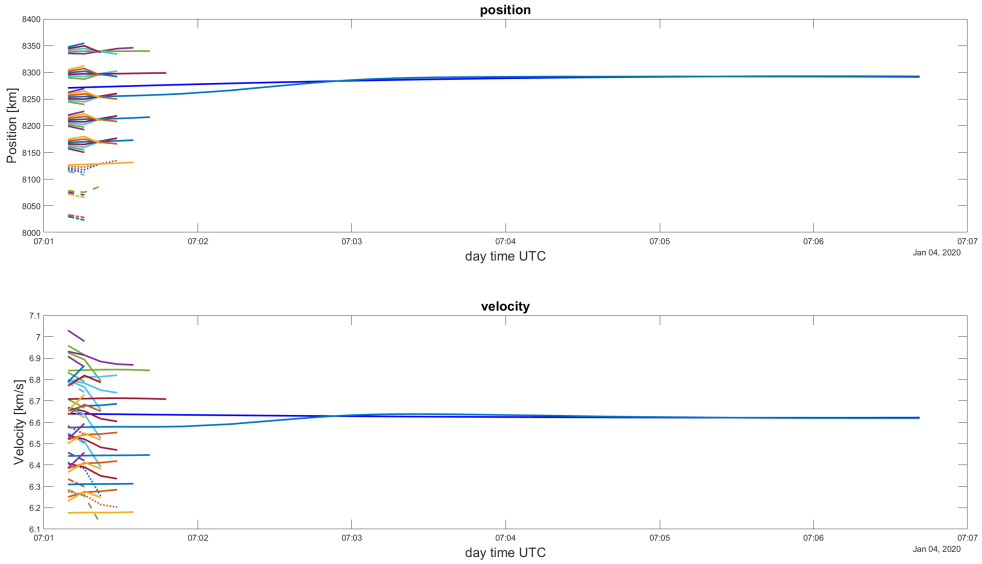

Figure C.13: Satellite 10793U resulting position and velocity at each epoch for each hypothesis selected from the CAR over the duration of an observation arc. The blue line is the SGP4 state of the satellite, the expected solution. Hypothesis line stop when the hypothesis is eliminated.

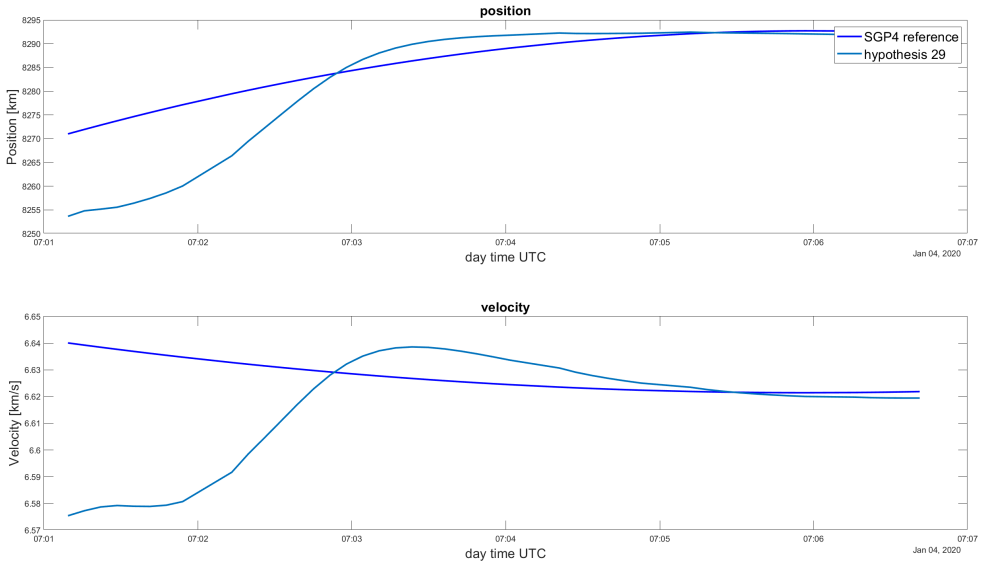

Figure C.14: Satellite 10793U, where the found solution its position and velocity is plotted individually over the span of the observation arc. The dark blue line is the SGP4-based orbit, which is used as a reference.

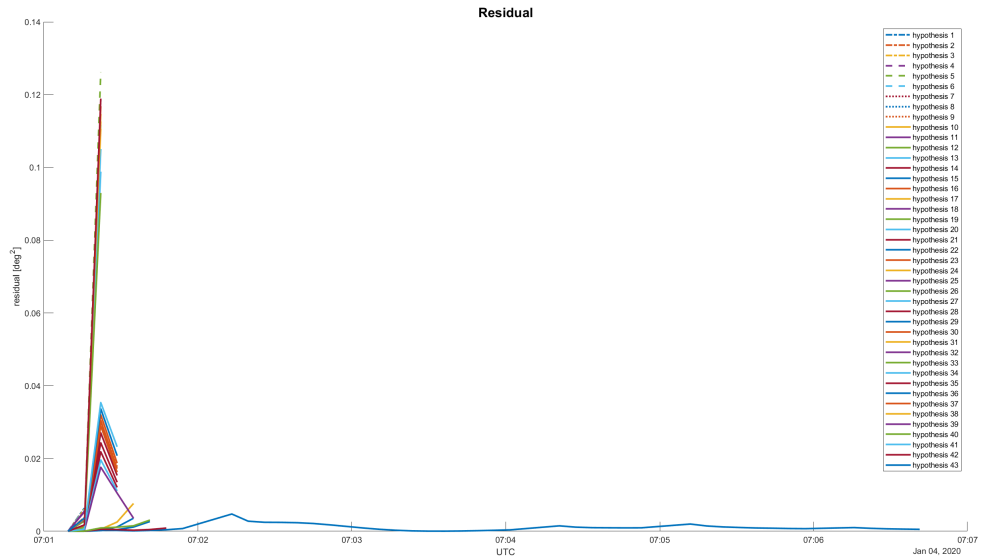

Figure C.15: Satellite 10793U residual during the first observation arc. The residual line stops when the hypothesis is eliminated.

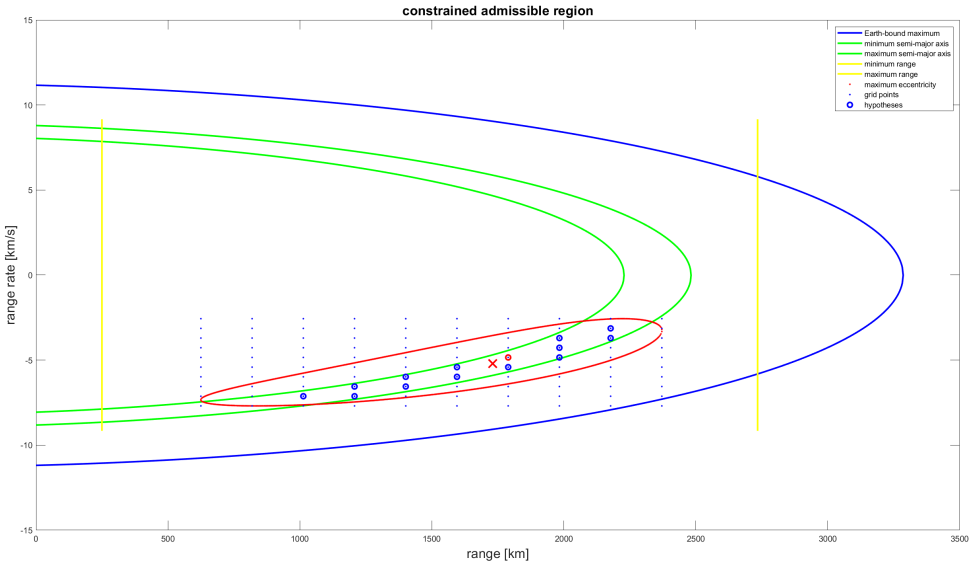

Figure C.16: Satellite 22284U, constrained admissible region with the range, semi-major axis and eccentricity constraint. The blue dots represents the grid, and the blue circled dots represents the selected hypotheses. The red dot is the resulting hypotheses after the CAR-MHF with the described elimination criteria, and the red cross represents the SGP4-based correct state.

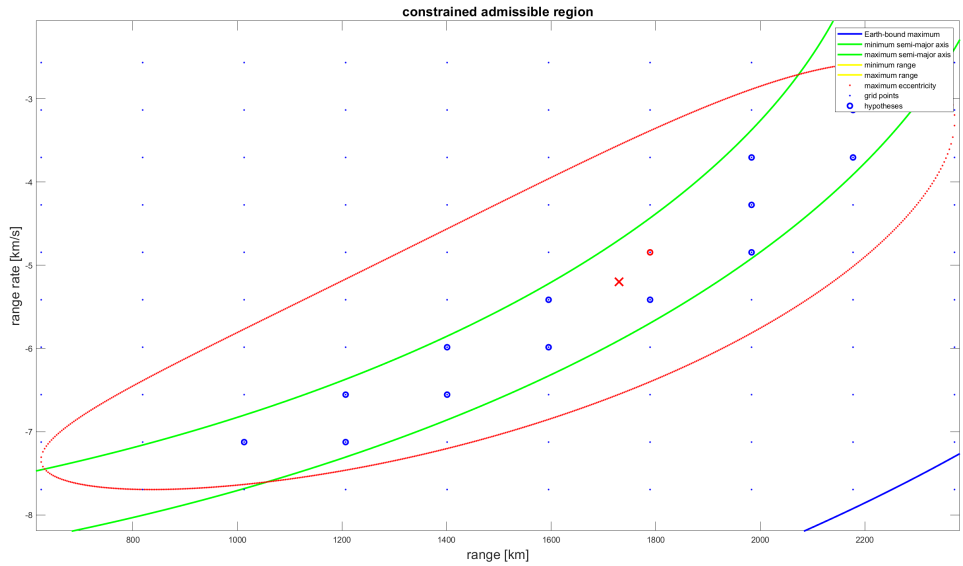

Figure C.17: Satellite 22284U, constrained admissible region with the range, semi-major axis and eccentricity constraint. The blue dots represents the grid, and the blue circled dots represents the selected hypotheses. The red dot is the resulting hypotheses after the CAR-MHF with the described elimination criteria, and the red cross represents the SGP4-based correct state.

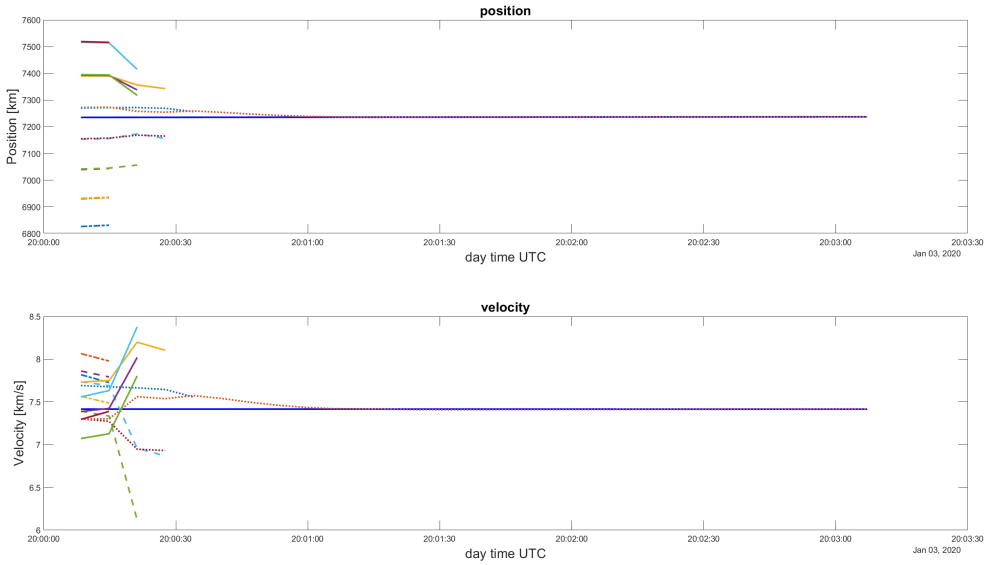

Figure C.18: Satellite 22284U resulting position and velocity at each epoch for each hypothesis selected from the CAR over the duration of an observation arc. The blue line is the SGP4 state of the satellite, the expected solution. Hypothesis line stop when the hypothesis is eliminated.

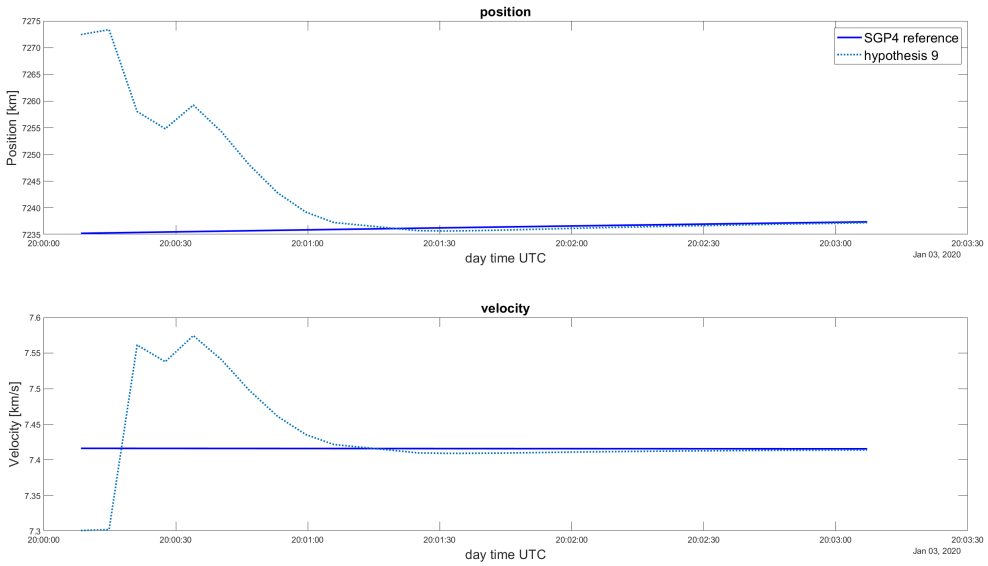

Figure C.19: Satellite 22284U, where the found solution its position and velocity is plotted individually over the span of the observation arc. The dark blue line is the SGP4-based orbit, which is used as a reference.

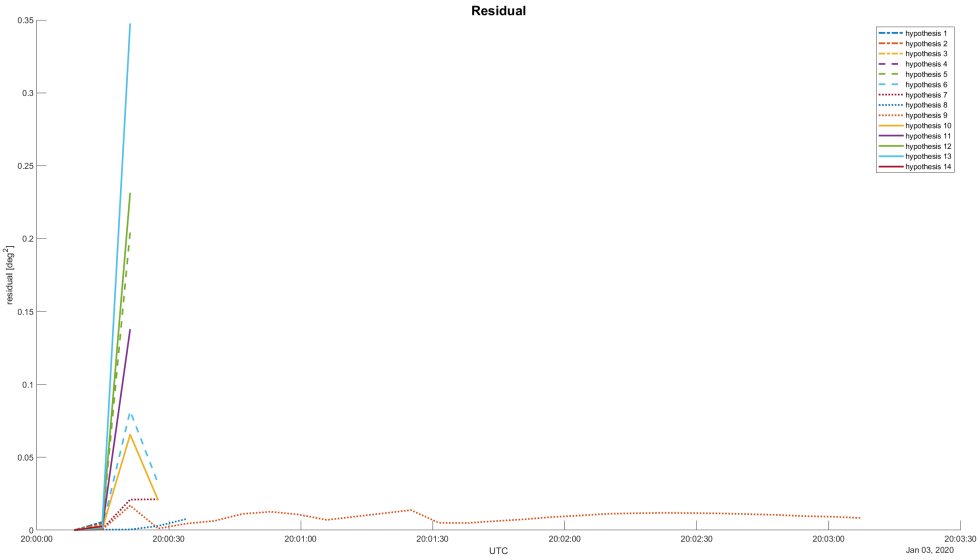

Figure C.20: Satellite 22284U residual during the first observation arc. The residual line stops when the hypothesis is eliminated

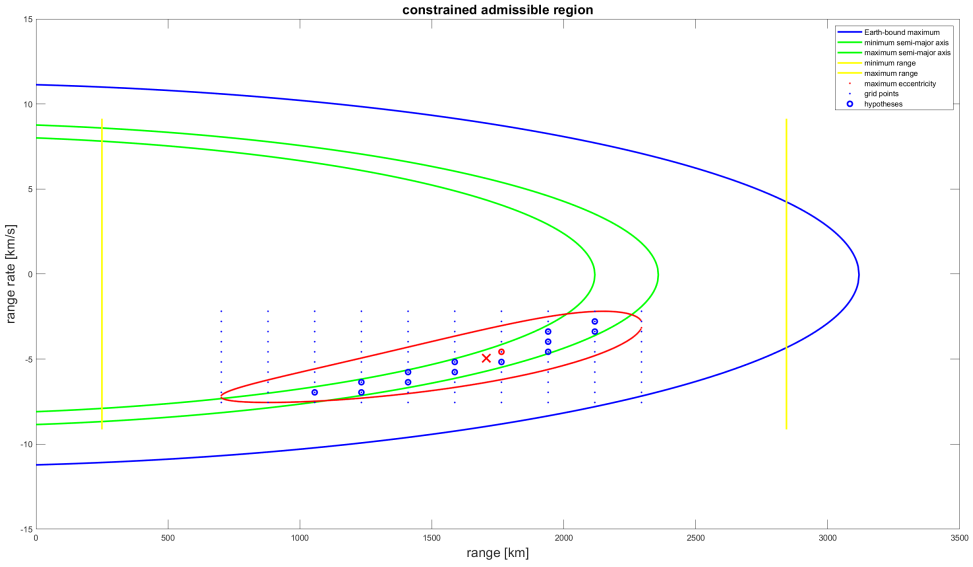

Figure C.21: Satellite 23404U, constrained admissible region with the range, semi-major axis and eccentricity constraint. The blue dots represents the grid, and the blue circled dots represents the selected hypotheses. The red dot is the resulting hypotheses after the CAR-MHF with the described elimination criteria, and the red cross represents the SGP4-based correct state.

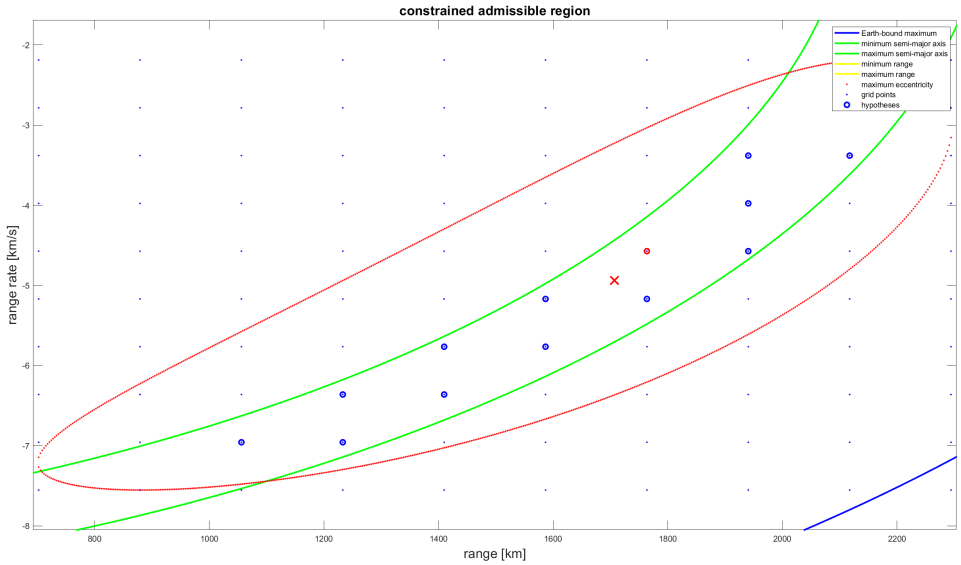

Figure C.22: Satellite 23404U, constrained admissible region with the range, semi-major axis and eccentricity constraint. The blue dots represents the grid, and the blue circled dots represents the selected hypotheses. The red dot is the resulting hypotheses after the CAR-MHF with the described elimination criteria, and the red cross represents the SGP4-based correct state.

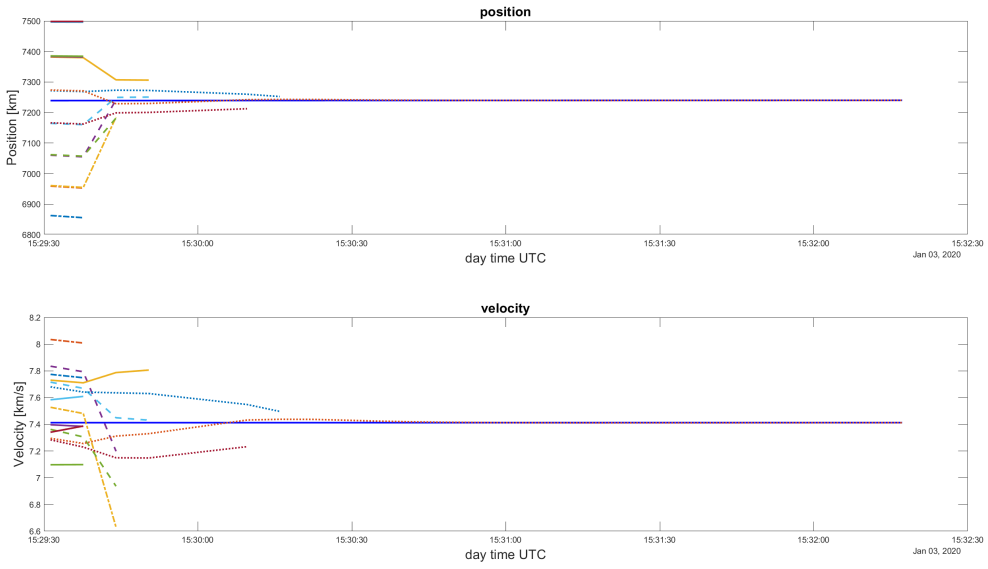

Figure C.23: Satellite 23404U resulting position and velocity at each epoch for each hypothesis selected from the CAR over the duration of an observation arc. The blue line is the SGP4 state of the satellite, the expected solution. Hypothesis line stop when the hypothesis is eliminated.

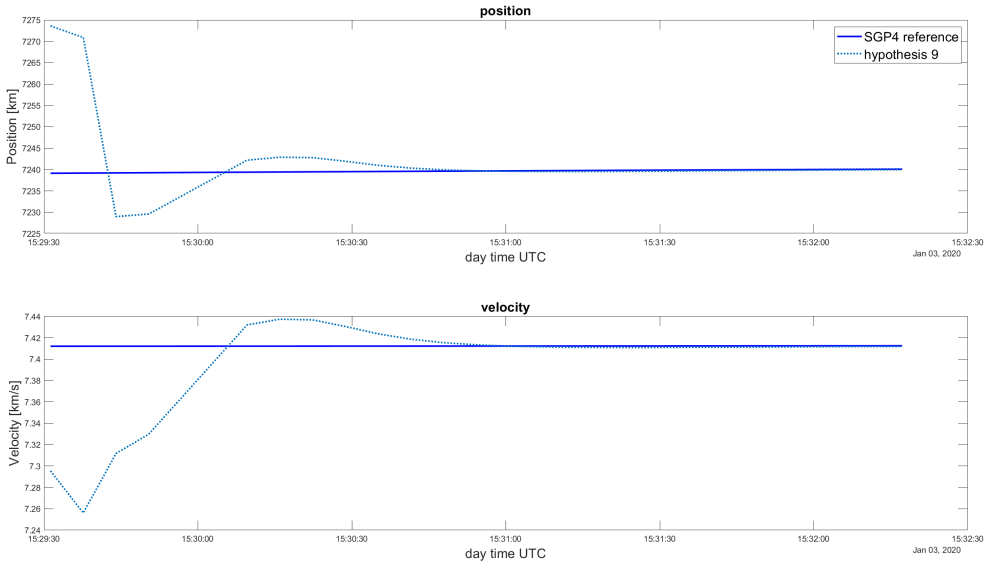

Figure C.24: Satellite 23404U, where the found solution its position and velocity is plotted individually over the span of the observation arc. The dark blue line is the SGP4-based orbit, which is used as a reference.

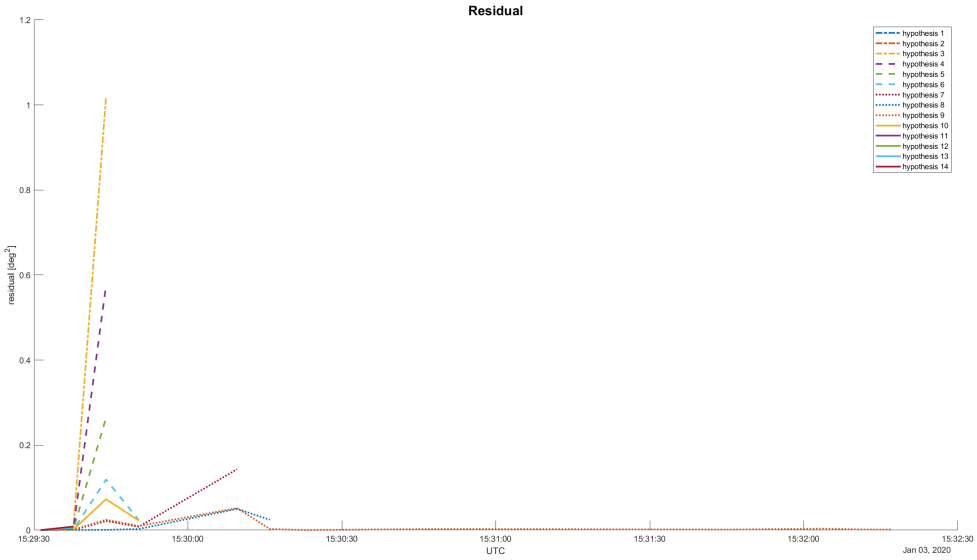

Figure C.25: Satellite 23404U residual during the first observation arc. The residual line stops when the hypothesis is eliminated

D

Elimination criteria validation

This chapter gives the data for the validation results for the elimination criteria. As part of this validation, it was investigated how much observations needed to be grouped together in order to make the method resistant to measurement uncertainties.

Table D.1: Satellite 10793U, station LSN, date 01-03-2020, validation of the elimination criteria for different values for, n, the number for which the average is taken.

n	1	3	5	7	9
hypotheses	43	43	43	43	43
epochs to conversion	6	6	14	41	39
At conv point					
Position error [km]	123.0	12.0	80.0	67.0	23.0
Velocity error [m/s]	701.7	608.0	242.0	191.1	58.0
At end of arc					
Position error [km]	2.8	26.5	34.5	32.8	16.0
Velocity error [m/s]	9.2	64.8	81.6	77.8	39.7
Time [second]	18.5	27.3	41.9	59.7	74.0
converged	Yes	Yes	Yes	Yes	Yes

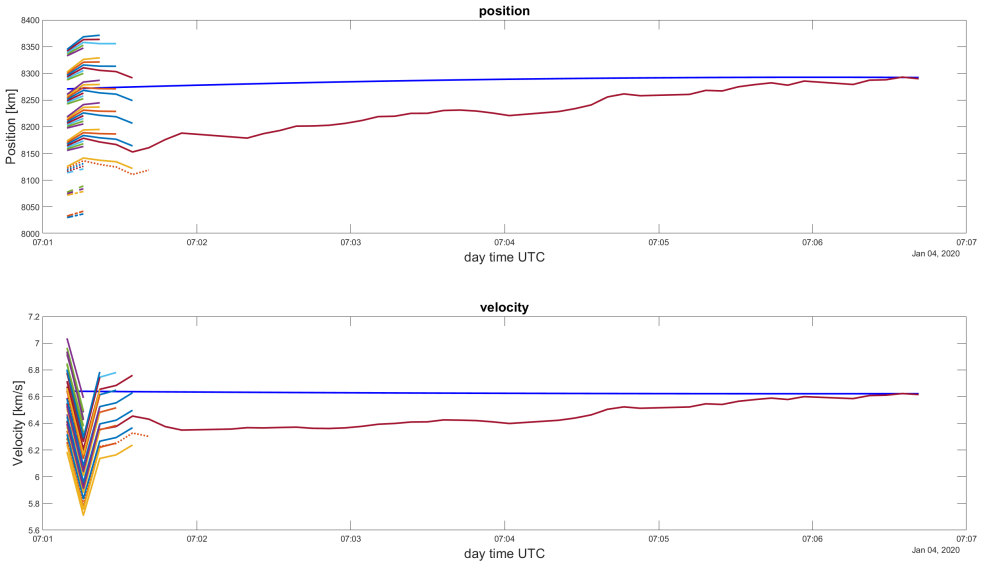

Figure D.1: Satellite 10793U resulting position and velocity at each epoch for each hypothesis selected from the CAR over the duration of an observation arc. The blue line is the SGP4 state of the satellite, the expected solution. Hypothesis line stop when the hypothesis is eliminated. Elimination criteria with average weighting 1.

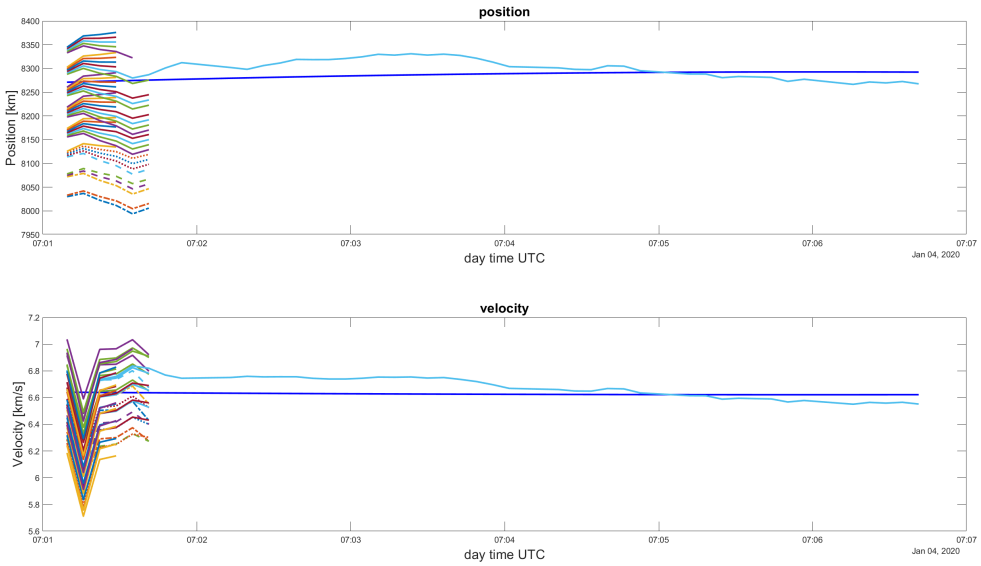

Figure D.2: Satellite 10793U resulting position and velocity at each epoch for each hypothesis selected from the CAR over the duration of an observation arc. The blue line is the SGP4 state of the satellite, the expected solution. Hypothesis line stop when the hypothesis is eliminated. Elimination criteria with average weighting 3.

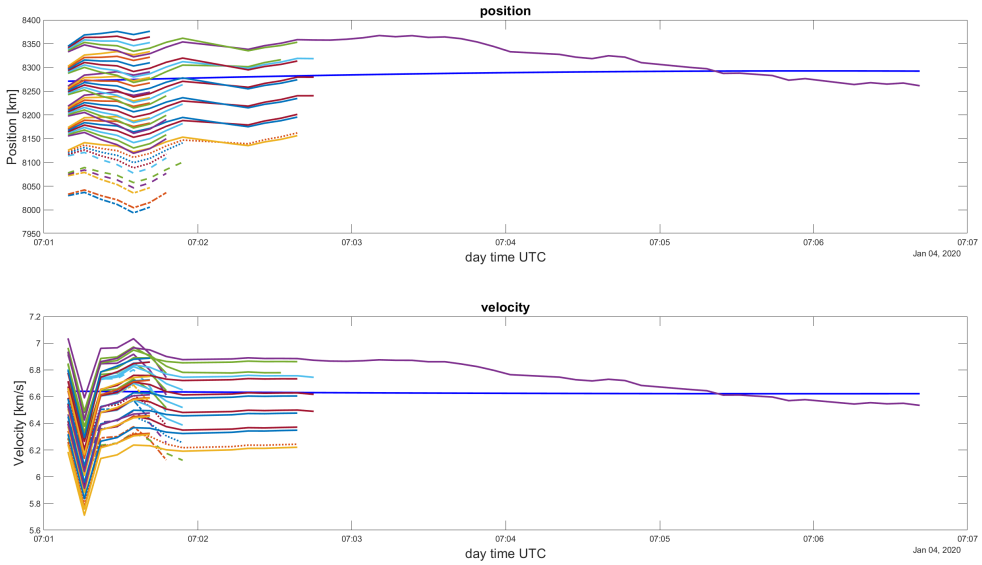

Figure D.3: Satellite 10793U resulting position and velocity at each epoch for each hypothesis selected from the CAR over the duration of an observation arc. The blue line is the SGP4 state of the satellite, the expected solution. Hypothesis line stop when the hypothesis is eliminated. Elimination criteria with average weighting 5.

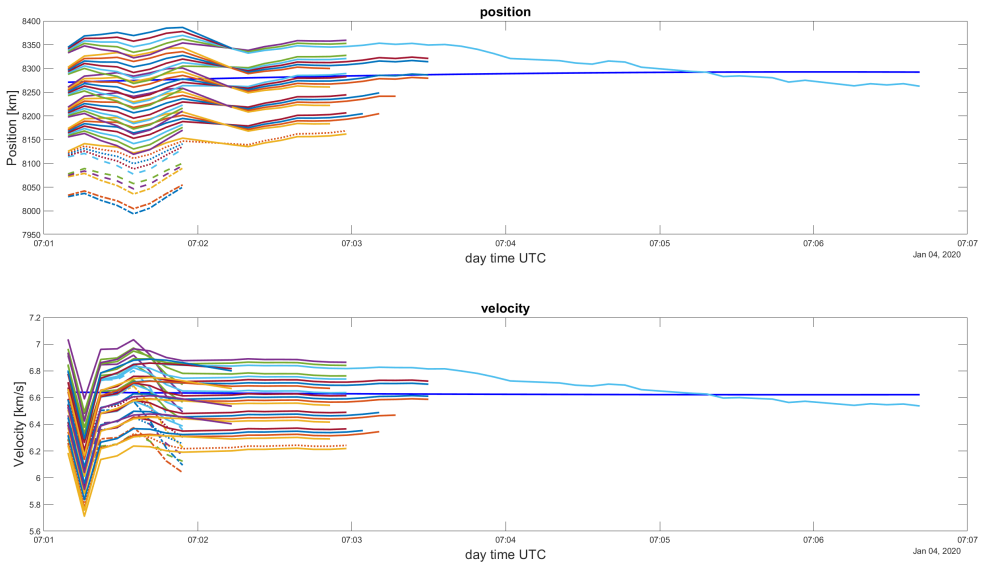

Figure D.4: Satellite 10793U resulting position and velocity at each epoch for each hypothesis selected from the CAR over the duration of an observation arc. The blue line is the SGP4 state of the satellite, the expected solution. Hypothesis line stop when the hypothesis is eliminated. Elimination criteria with average weighting 7.

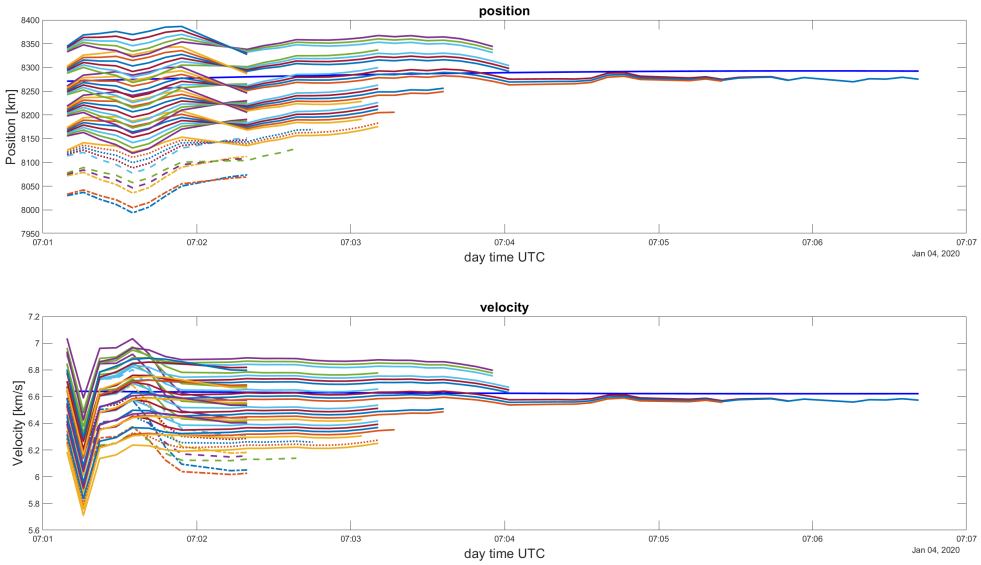

Figure D.5: Satellite 10793U resulting position and velocity at each epoch for each hypothesis selected from the CAR over the duration of an observation arc. The blue line is the SGP4 state of the satellite, the expected solution. Hypothesis line stop when the hypothesis is eliminated. Elimination criteria with average weighting 9.

Table D.2: Satellite 23404U, station AUE, date 01-03-2020, validation of the elimination criteria for different values for, n, the number for which the average is taken.

n	1	3	5	7	9
hypotheses	15	15	15	15	15
epochs to conversion	5	9	11	19	22
At conv point					
Position error [km]	56	69,6	68.4	7.4	16.7
Velocity error [m/s]	171.8	386,7	377.2	36.5	84
At end of arc					
Position error [km]	5.5	5.8	2.54	3.4	2.5
Velocity error [m/s]	53.5	26.3	36.7	15.6	36.7
Time [second]	8.7	13.4	16.6	21.9	25.5
converged	Yes	Yes	Yes	Yes	Yes

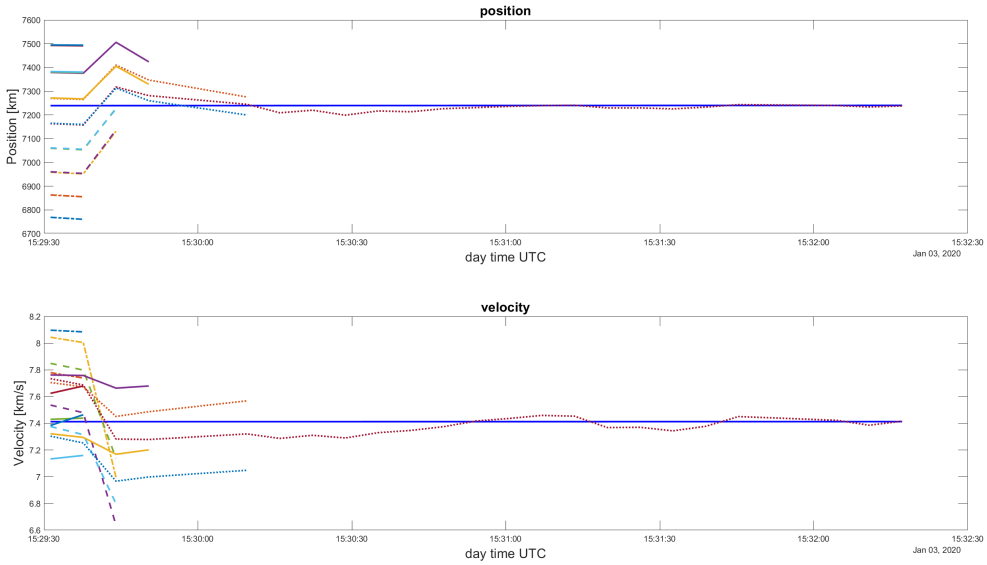

Figure D.6: Satellite 23404U resulting position and velocity at each epoch for each hypothesis selected from the CAR over the duration of an observation arc. The blue line is the SGP4 state of the satellite, the expected solution. Hypothesis line stop when the hypothesis is eliminated. Elimination criteria with average weighting 1.

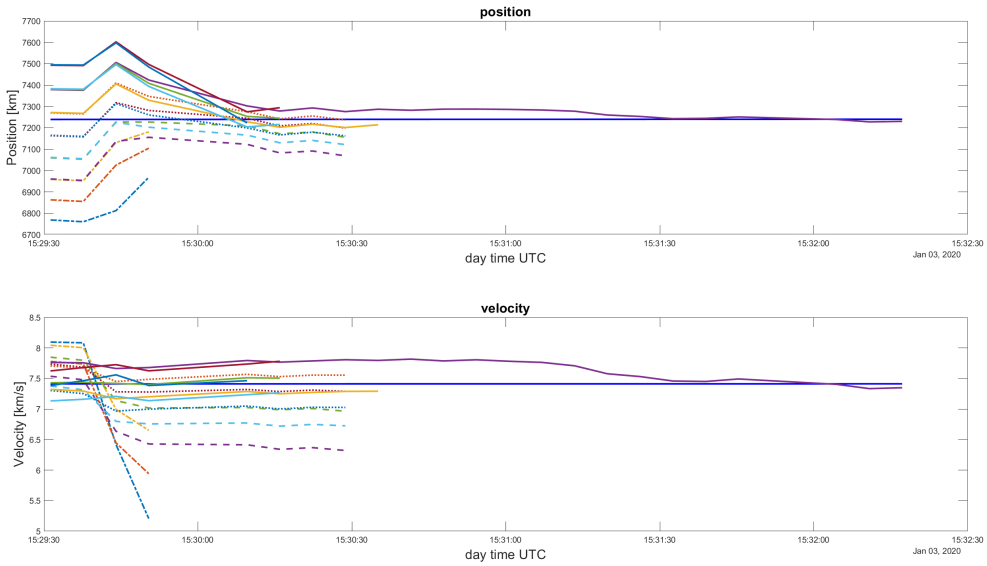

Figure D.7: Satellite 23404U resulting position and velocity at each epoch for each hypothesis selected from the CAR over the duration of an observation arc. The blue line is the SGP4 state of the satellite, the expected solution. Hypothesis line stop when the hypothesis is eliminated. Elimination criteria with average weighting 3.

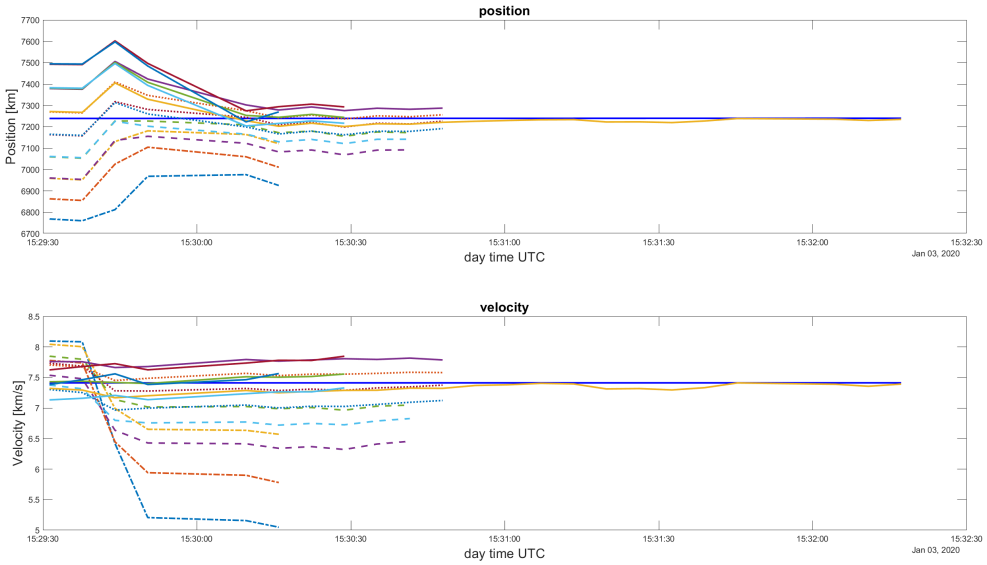

Figure D.8: Satellite 23404U resulting position and velocity at each epoch for each hypothesis selected from the CAR over the duration of an observation arc. The blue line is the SGP4 state of the satellite, the expected solution. Hypothesis line stop when the hypothesis is eliminated. Elimination criteria with average weighting 5.

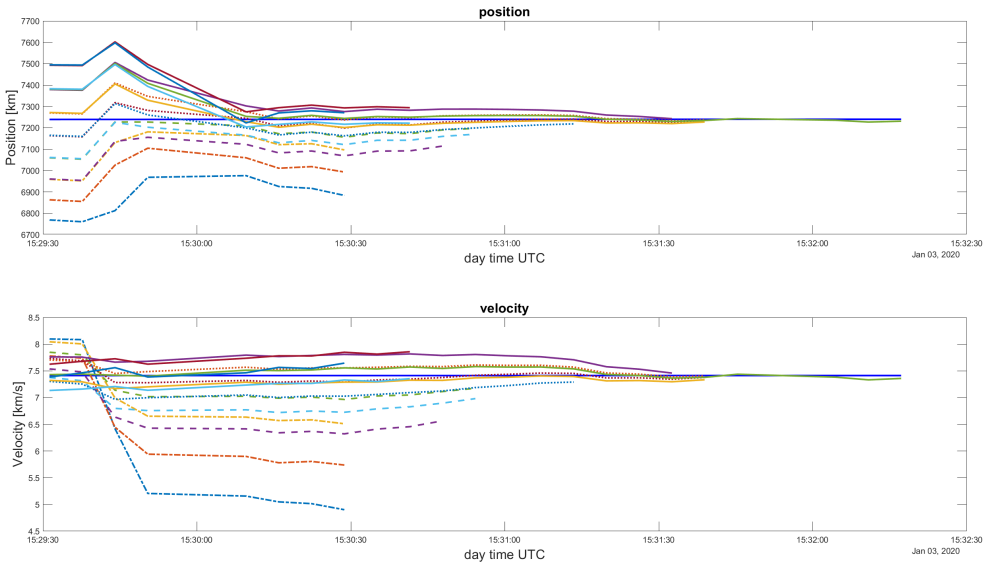

Figure D.9: Satellite 23404U resulting position and velocity at each epoch for each hypothesis selected from the CAR over the duration of an observation arc. The blue line is the SGP4 state of the satellite, the expected solution. Hypothesis line stop when the hypothesis is eliminated. Elimination criteria with average weighting 7.

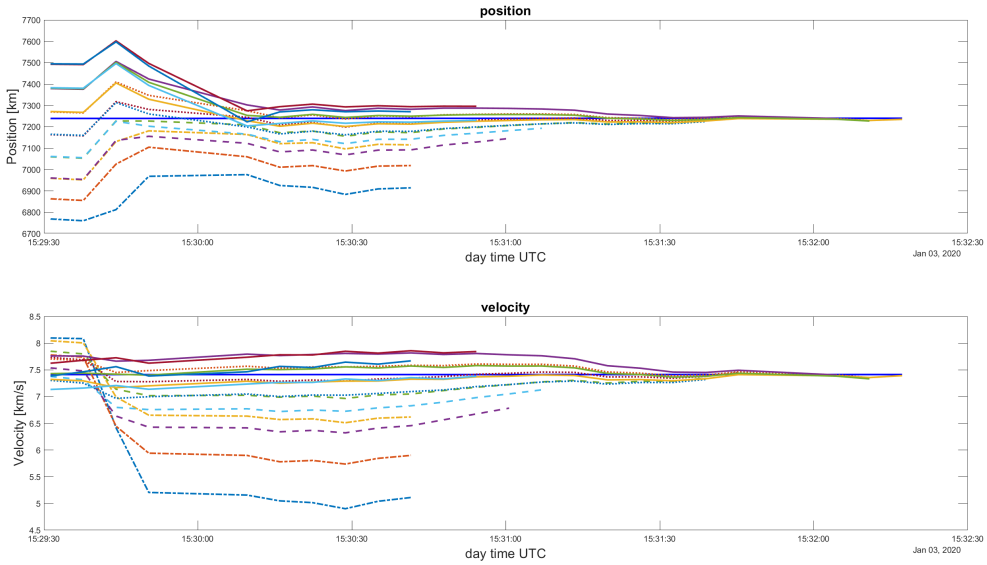

Figure D.10: Satellite 23404U resulting position and velocity at each epoch for each hypothesis selected from the CAR over the duration of an observation arc. The blue line is the SGP4 state of the satellite, the expected solution. Hypothesis line stop when the hypothesis is eliminated. Elimination criteria with average weighting 9.

Table D.3: Satellite 36095U, station LS, date 01-03-2020, validation of the elimination criteria for different values for, n, the number for which the average is taken.

n	1	3	5	7	9
hypotheses	17	17	17	17	17
epochs to conversion	5	11	13	23	17
At conv point					
Position error [km]	74.3	154.7	107.8	80.7	42.2
Velocity error [m/s]	8.3	905.5	674.9	527.8	296.0
At end of arc					
Position error [km]	24.9	24.8	6.9	4.1	18.1
Velocity error [m/s]	132.2	132.2	43.2	30.7	84.6
Time [second]	11	16	21	28	27.9
converged	Yes	Yes	Yes	Yes	Yes

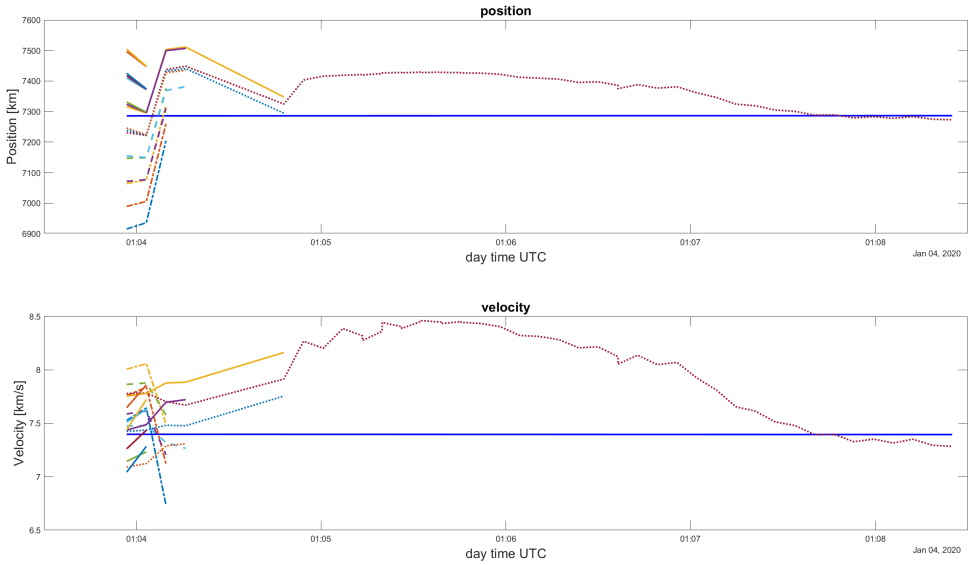

Figure D.11: Satellite 36095U resulting position and velocity at each epoch for each hypothesis selected from the CAR over the duration of an observation arc. The blue line is the SGP4 state of the satellite, the expected solution. Hypothesis line stop when the hypothesis is eliminated. Elimination criteria with average weighting 1.

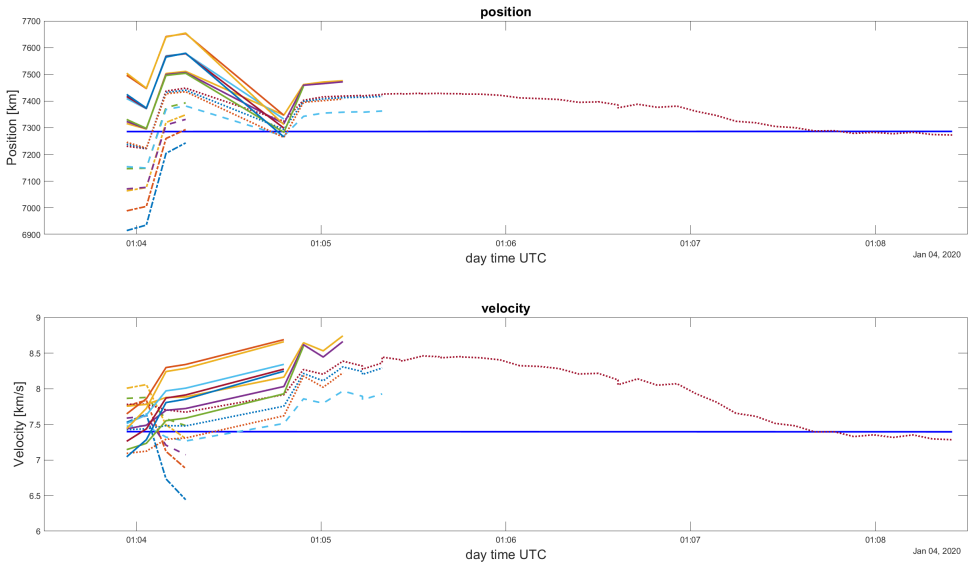

Figure D.12: Satellite 36095U resulting position and velocity at each epoch for each hypothesis selected from the CAR over the duration of an observation arc. The blue line is the SGP4 state of the satellite, the expected solution. Hypothesis line stop when the hypothesis is eliminated. Elimination criteria with average weighting 3.

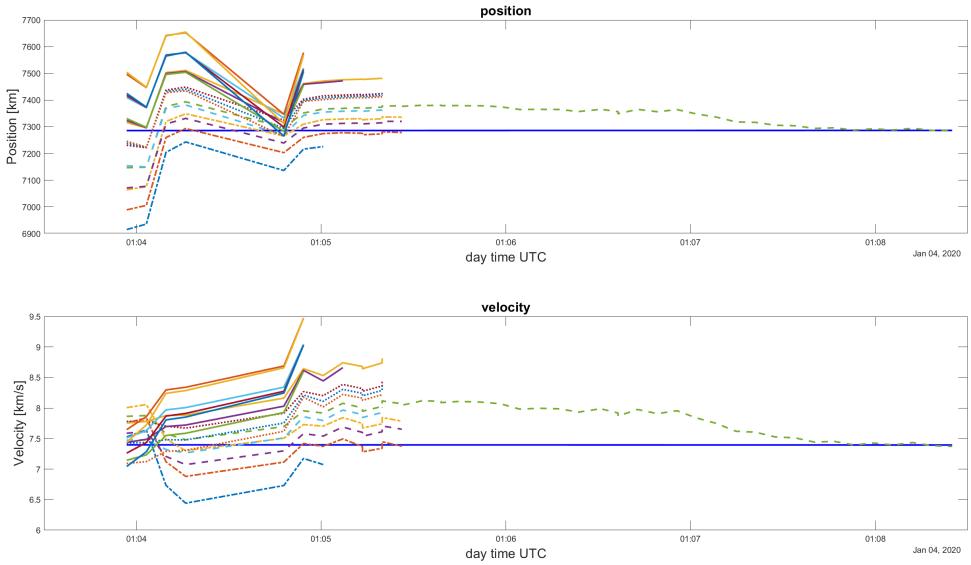

Figure D.13: Satellite 36095U resulting position and velocity at each epoch for each hypothesis selected from the CAR over the duration of an observation arc. The blue line is the SGP4 state of the satellite, the expected solution. Hypothesis line stop when the hypothesis is eliminated. Elimination criteria with average weighting 5.

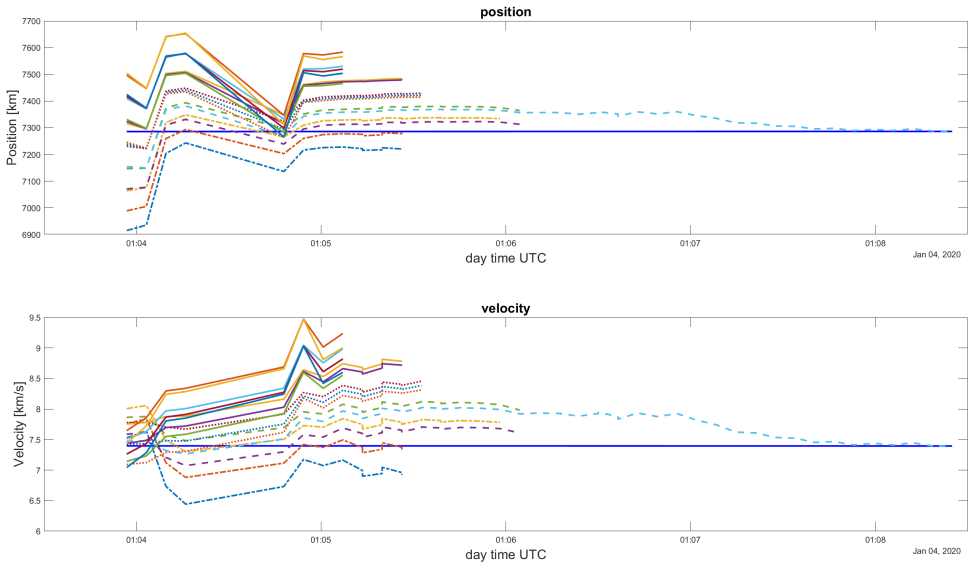

Figure D.14: Satellite 36095U resulting position and velocity at each epoch for each hypothesis selected from the CAR over the duration of an observation arc. The blue line is the SGP4 state of the satellite, the expected solution. Hypothesis line stop when the hypothesis is eliminated. Elimination criteria with average weighting 7.

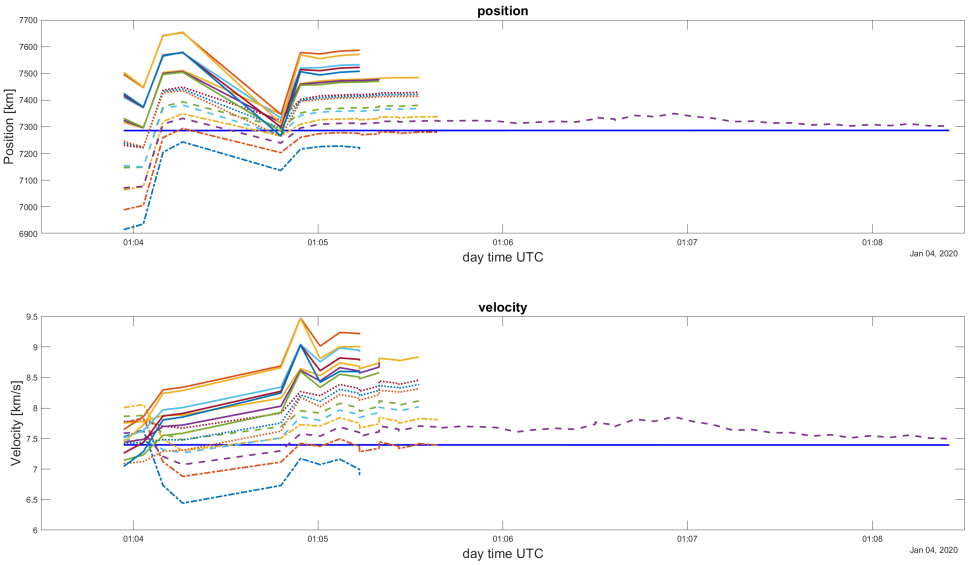

Figure D.15: Satellite 36095U resulting position and velocity at each epoch for each hypothesis selected from the CAR over the duration of an observation arc. The blue line is the SGP4 state of the satellite, the expected solution. Hypothesis line stop when the hypothesis is eliminated. Elimination criteria with average weighting 9.

Table D.4: Satellite 40113U, station LS, date 01-03-2020, validation of the elimination criteria for different values for, n, the number for which the average is taken.

n	1	3	5	7	9
hypotheses	16	16	16	16	16
epochs to conversion	6	15	13	17	17
At conv point					
Position error [km]	276.3	76.7	103.4	14.8	14.8
Velocity error [m/s]	975.8	202.3	277.3	135.3	135.3
At end of arc					
Position error [km]	15.2	30.1	30.1	15.2	15.2
Velocity error [m/s]	76.7	1.6	153.1	76.7	76.7
Time [second]	10.7	16.9	20.2	23.13	25.07
converged	Yes	Yes	Yes	Yes	Yes

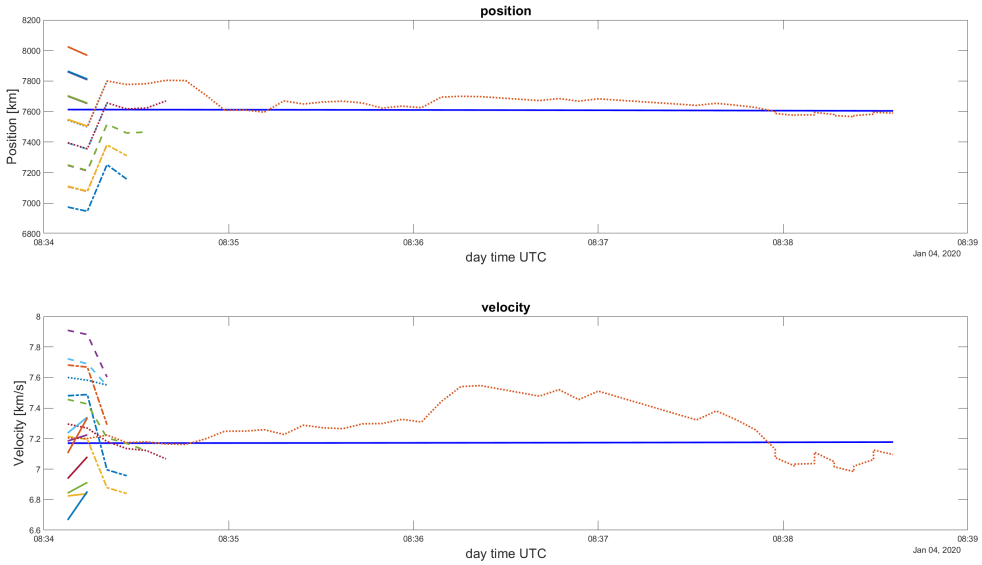

Figure D.16: Satellite 40113U resulting position and velocity at each epoch for each hypothesis selected from the CAR over the duration of an observation arc. The blue line is the SGP4 state of the satellite, the expected solution. Hypothesis line stop when the hypothesis is eliminated. Elimination criteria with average weighting 1.

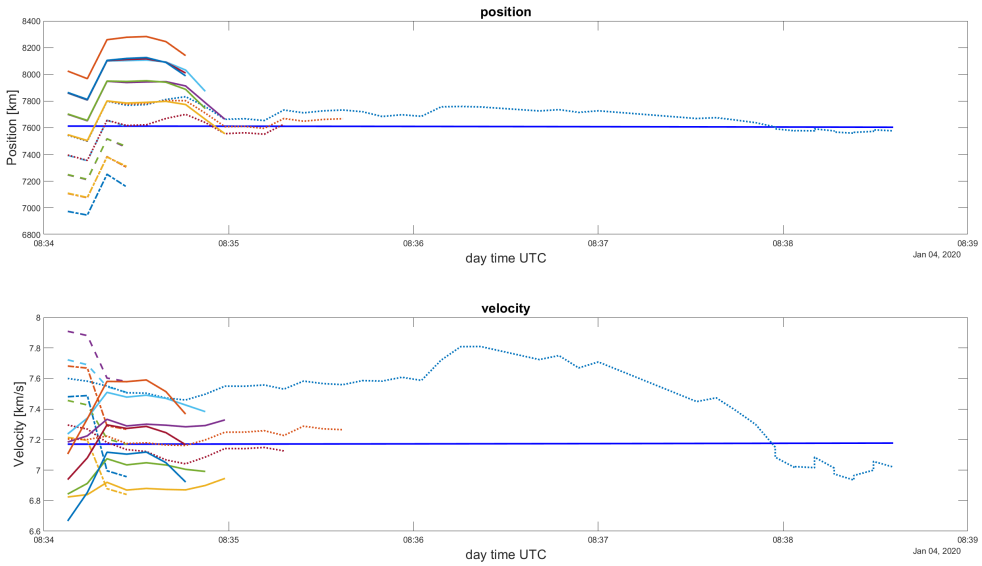

Figure D.17: Satellite 40113U resulting position and velocity at each epoch for each hypothesis selected from the CAR over the duration of an observation arc. The blue line is the SGP4 state of the satellite, the expected solution. Hypothesis line stop when the hypothesis is eliminated. Elimination criteria with average weighting 3.

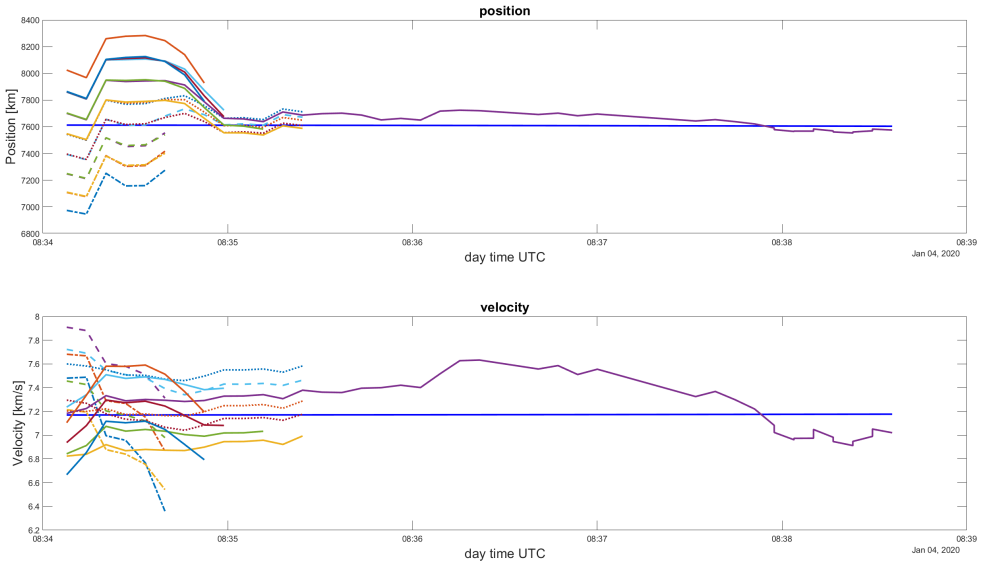

Figure D.18: Satellite 40113U resulting position and velocity at each epoch for each hypothesis selected from the CAR over the duration of an observation arc. The blue line is the SGP4 state of the satellite, the expected solution. Hypothesis line stop when the hypothesis is eliminated. Elimination criteria with average weighting 5.

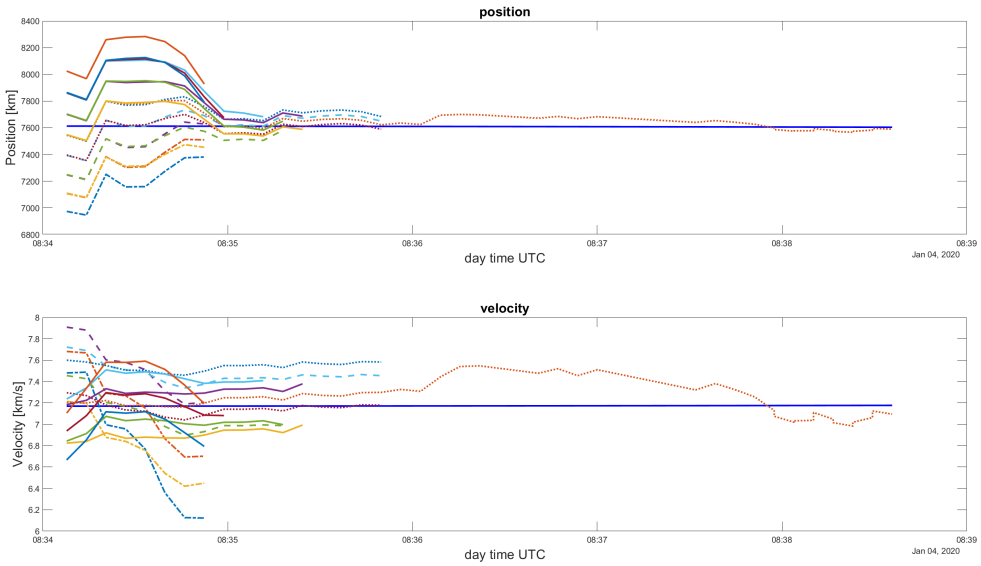

Figure D.19: Satellite 40113U resulting position and velocity at each epoch for each hypothesis selected from the CAR over the duration of an observation arc. The blue line is the SGP4 state of the satellite, the expected solution. Hypothesis line stop when the hypothesis is eliminated. Elimination criteria with average weighting 7.

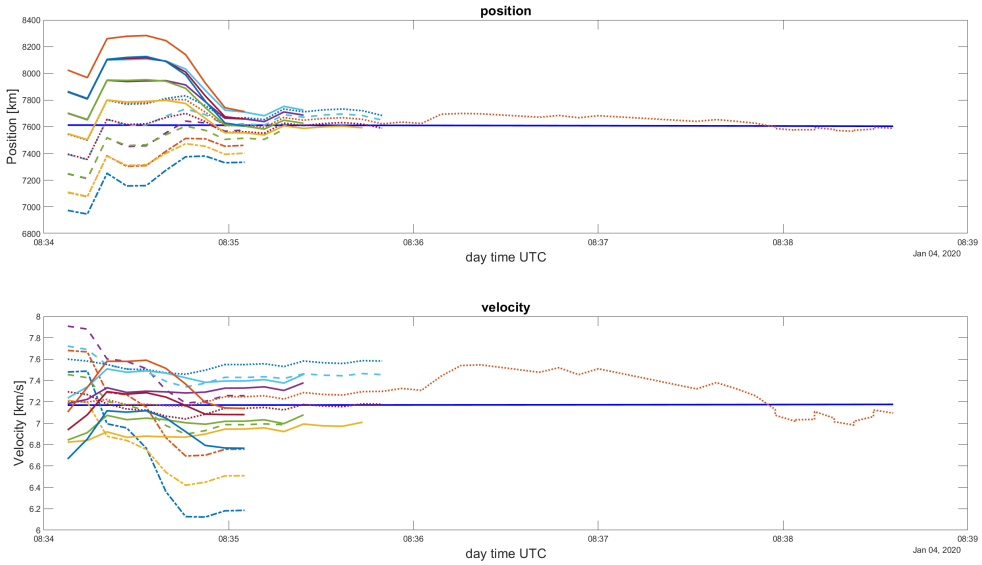

Figure D.20: Satellite 40113U resulting position and velocity at each epoch for each hypothesis selected from the CAR over the duration of an observation arc. The blue line is the SGP4 state of the satellite, the expected solution. Hypothesis line stop when the hypothesis is eliminated. Elimination criteria with average weighting 9.

E

Validation: RKF4(5)

This chapter shows the different graphs for validation data used for the RKF4(5) method.

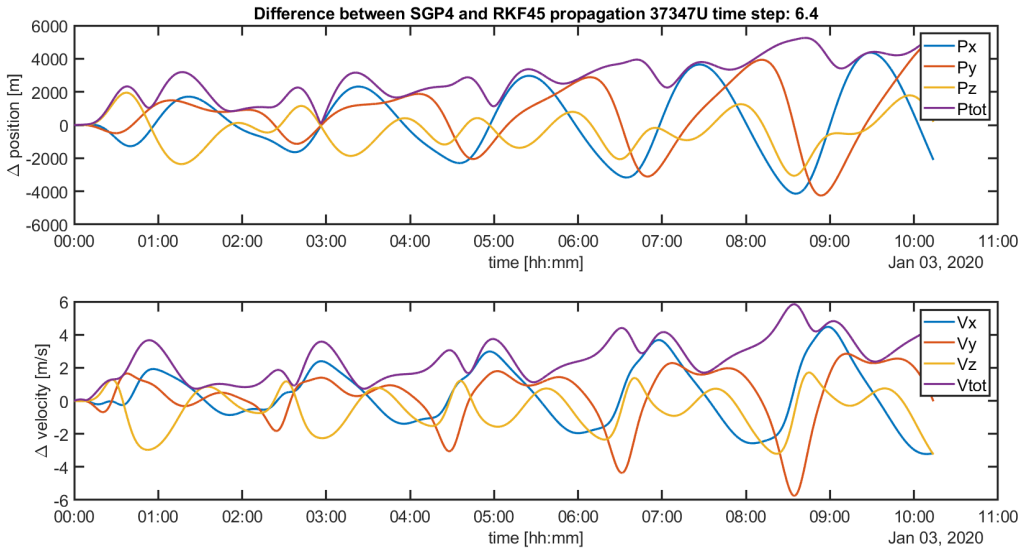

Figure E.1: Satellite 37347U propagated for 5 orbits with the RKF4(5) propagator with a time step of 6.4 seconds, stating from 03-01-2020 00:00:00, with the last know TLE at that time as starting condition. The total error is shown.

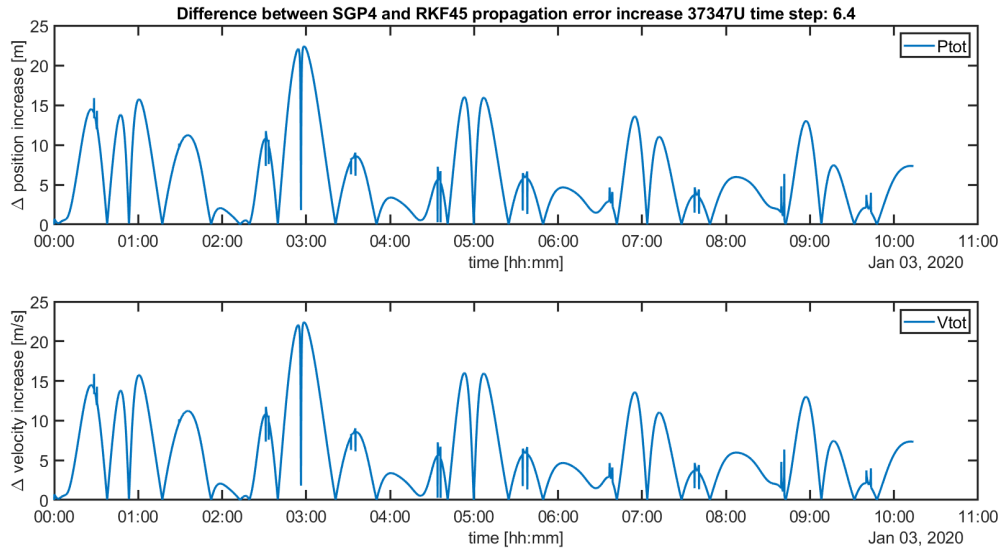

Figure E.2: Satellite 37347U propagated for 5 orbits with the RKF4(5) propagator with a time step of 6.4 seconds, stating from 03-01-2020 00:00:00, with the last know TLE at that time as starting condition. The error increase per epoch is shown

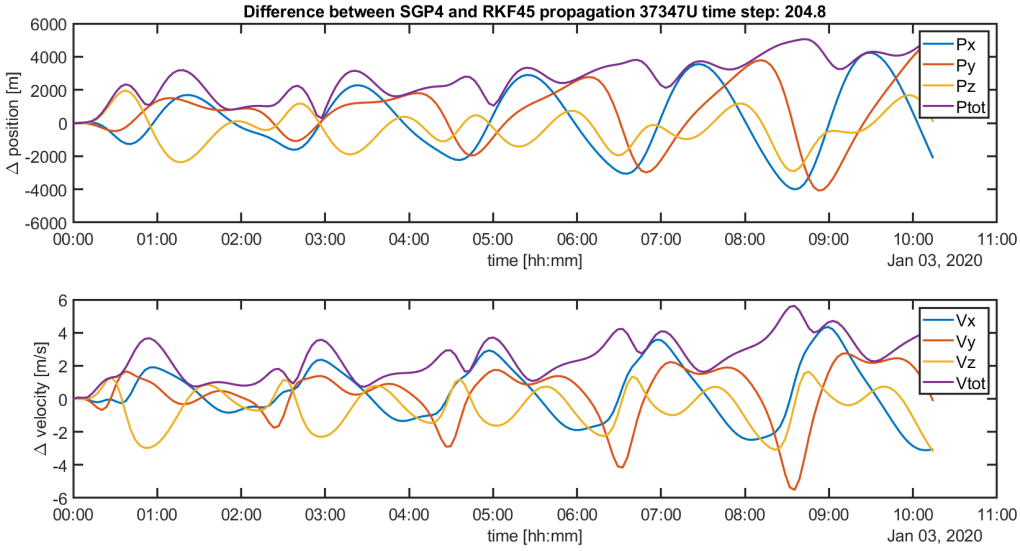

Figure E.3: Satellite 37347U propagated for 5 orbits with the RKF4(5) propagator with a time step of 204.8 seconds, stating from 03-01-2020 00:00:00, with the last know TLE at that time as starting condition. The total error is shown.

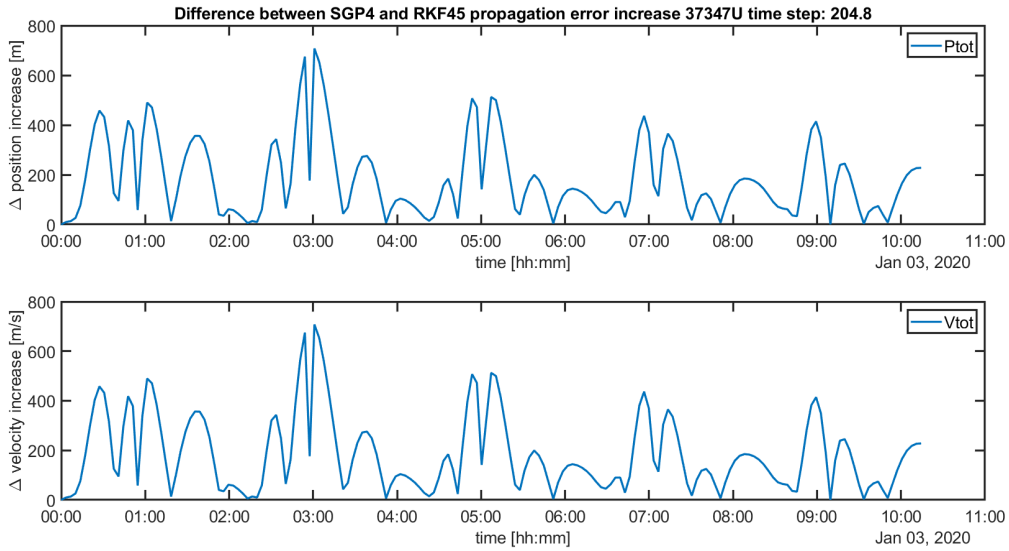

Figure E.4: Satellite 37347U propagated for 5 orbits with the RKF4(5) propagator with a time step of 204.8 seconds, stating from 03-01-2020 00:00:00, with the last know TLE at that time as starting condition. The error increase per epoch is shown

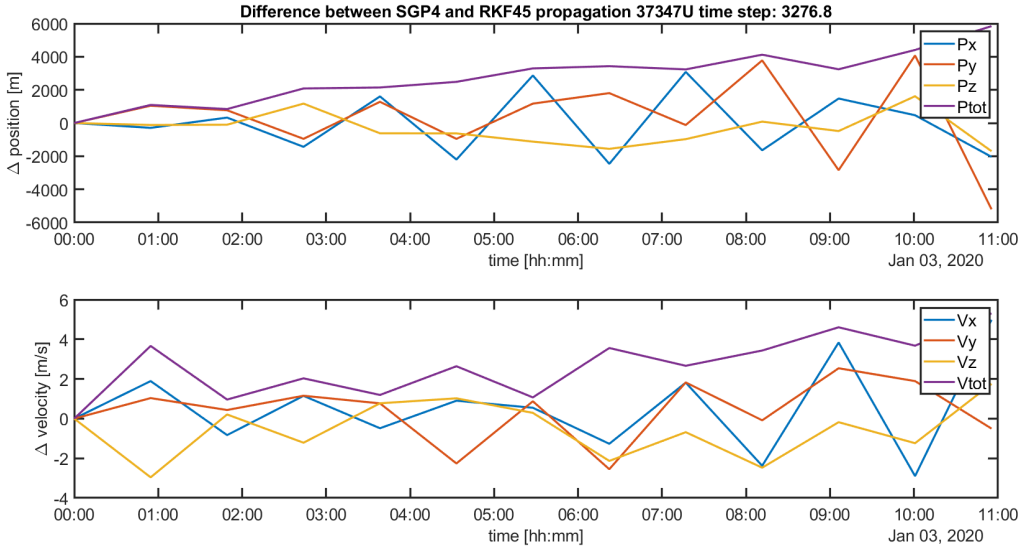

Figure E.5: Satellite 37347U propagated for 5 orbits with the RKF4(5) propagator with a time step of 3276.8 seconds, stating from 03-01-2020 00:00:00, with the last know TLE at that time as starting condition. The total error is shown.

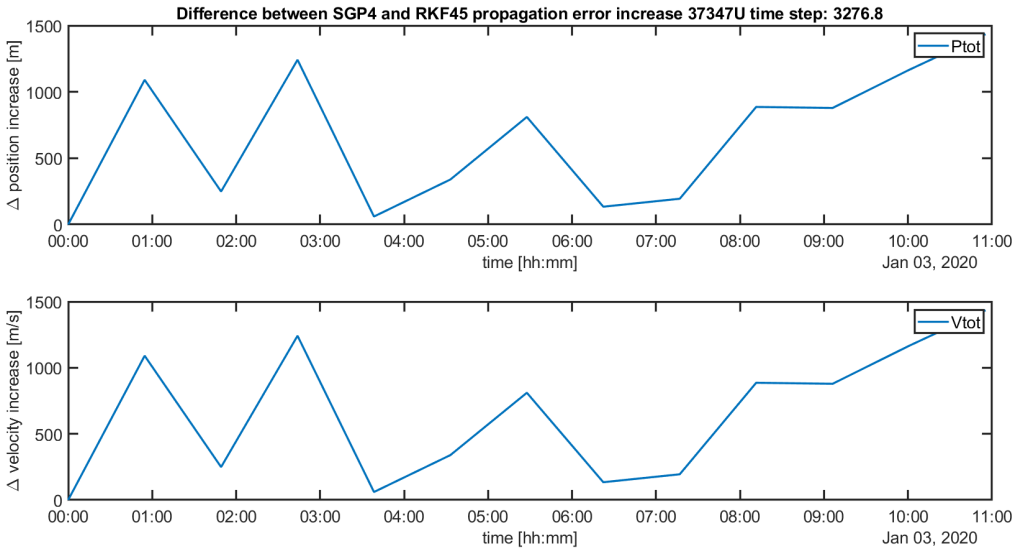

Figure E.6: Satellite 37347U propagated for 5 orbits with the RKF4(5) propagator with a time step of 3276.8 seconds, stating from 03-01-2020 00:00:00, with the last know TLE at that time as starting condition. The error increase per epoch is shown

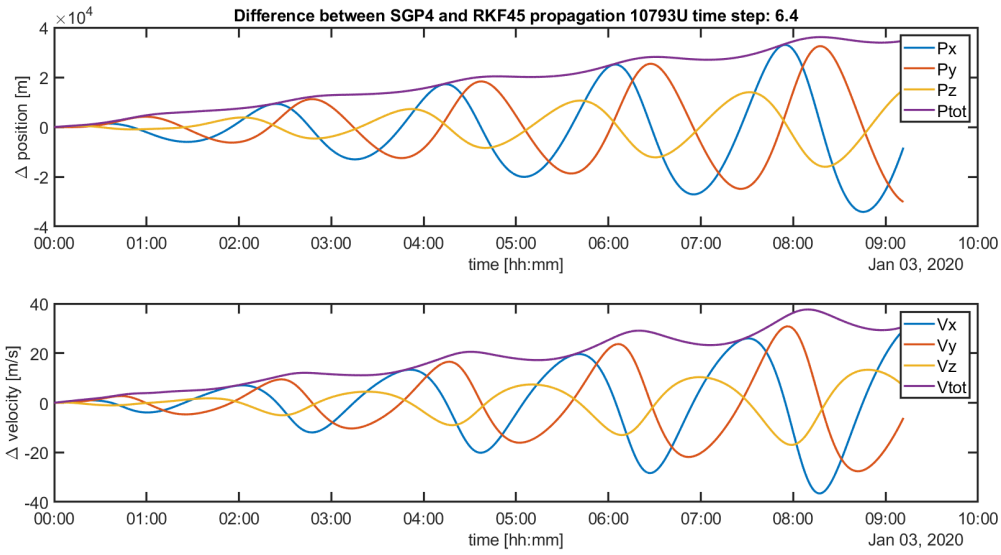

Figure E.7: Satellite 10793U propagated for 5 orbits with the RKF4(5) propagator with a time step of 6.4 seconds, stating from 03-01-2020 00:00:00, with the last know TLE at that time as starting condition. The total error is shown.

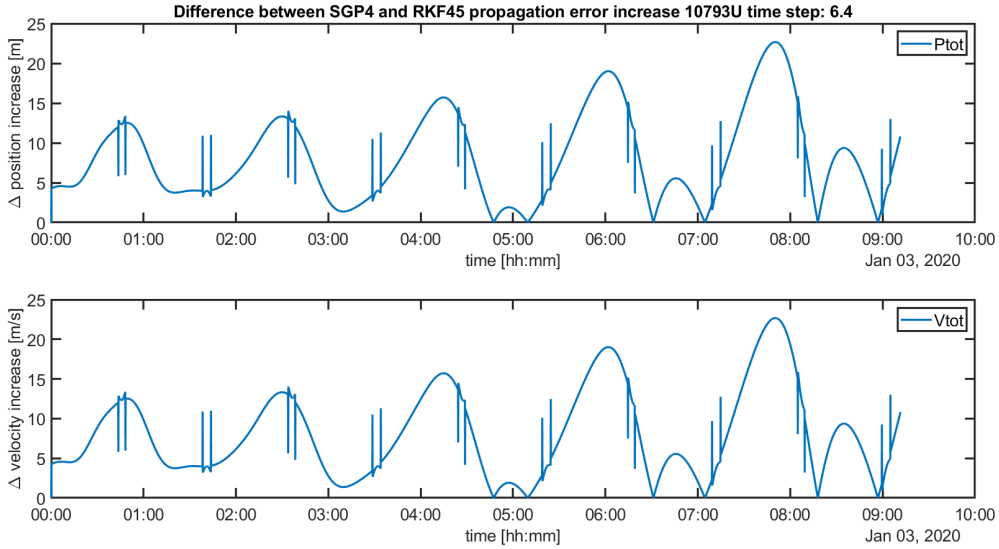

Figure E.8: Satellite 10793U propagated for 5 orbits with the RKF4(5) propagator with a time step of 6.4 seconds, stating from 03-01-2020 00:00:00, with the last know TLE at that time as starting condition. The error increase per epoch is shown

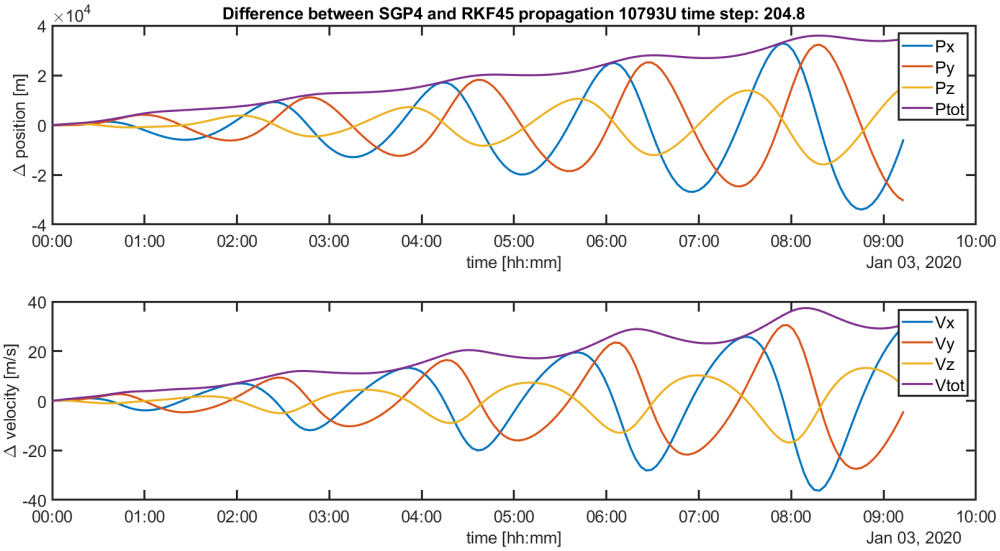

Figure E.9: Satellite 10793U propagated for 5 orbits with the RKF4(5) propagator with a time step of 204.8 seconds, stating from 03-01-2020 00:00:00, with the last know TLE at that time as starting condition. The total error is shown.

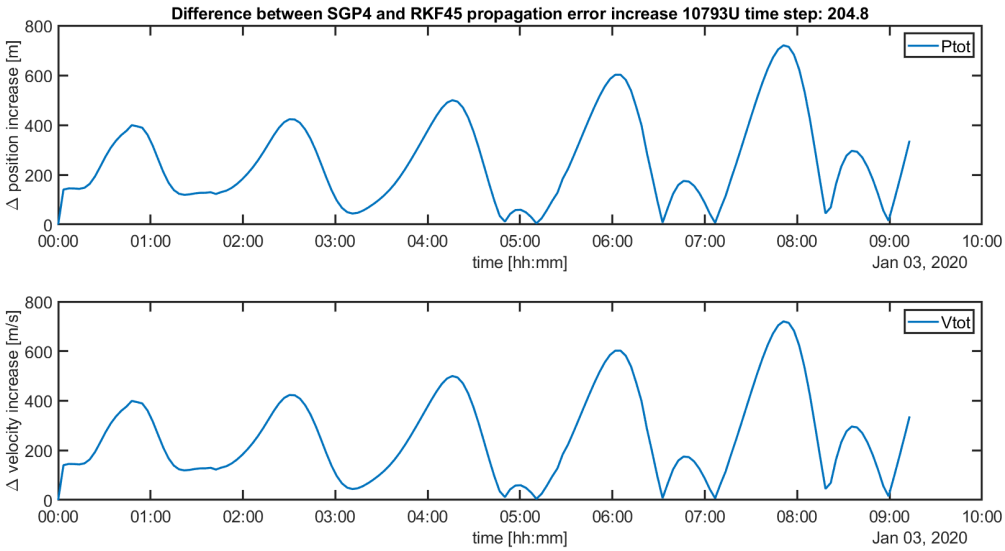

Figure E.10: Satellite 10793U propagated for 5 orbits with the RKF4(5) propagator with a time step of 204.8 seconds, stating from 03-01-2020 00:00:00, with the last know TLE at that time as starting condition. The error increase per epoch is shown

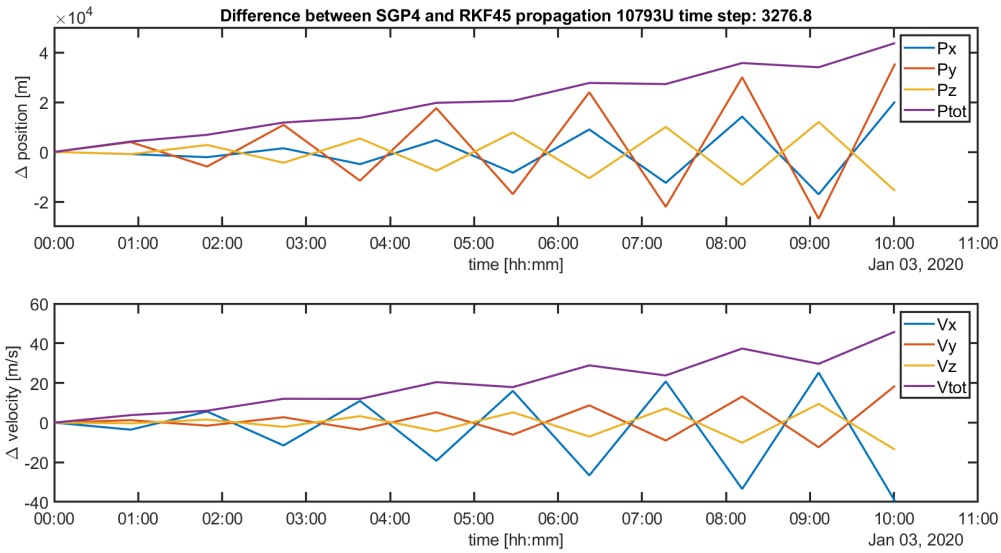

Figure E.11: Satellite 10793U propagated for 5 orbits with the RKF4(5) propagator with a time step of 3276.8 seconds, stating from 03-01-2020 00:00:00, with the last know TLE at that time as starting condition. The total error is shown.

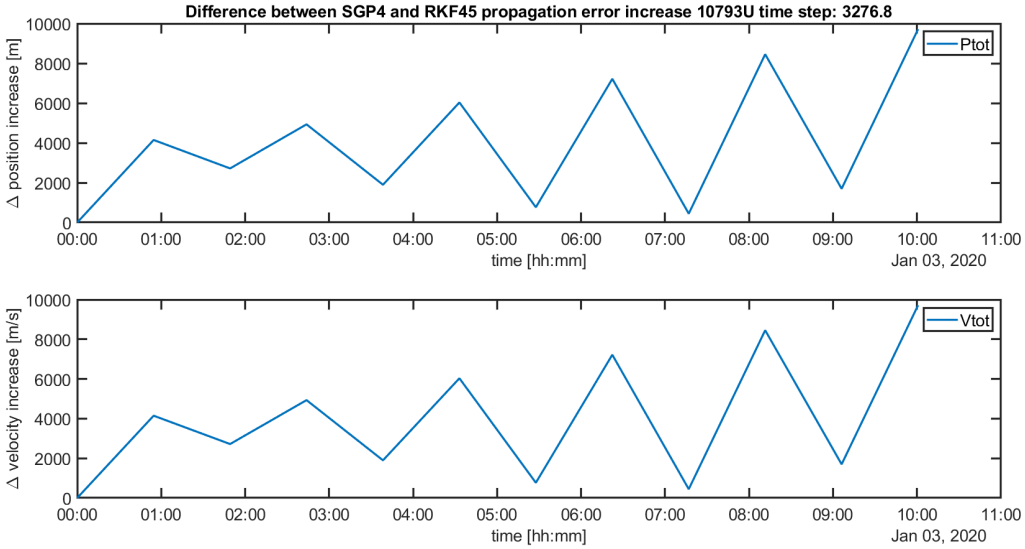

Figure E.12: Satellite 37347U propagated for 5 orbits with the RKF4(5) propagator with a time step of 3276.8 seconds, stating from 03-01-2020 00:00:00, with the last know TLE at that time as starting condition. The error increase per epoch is shown

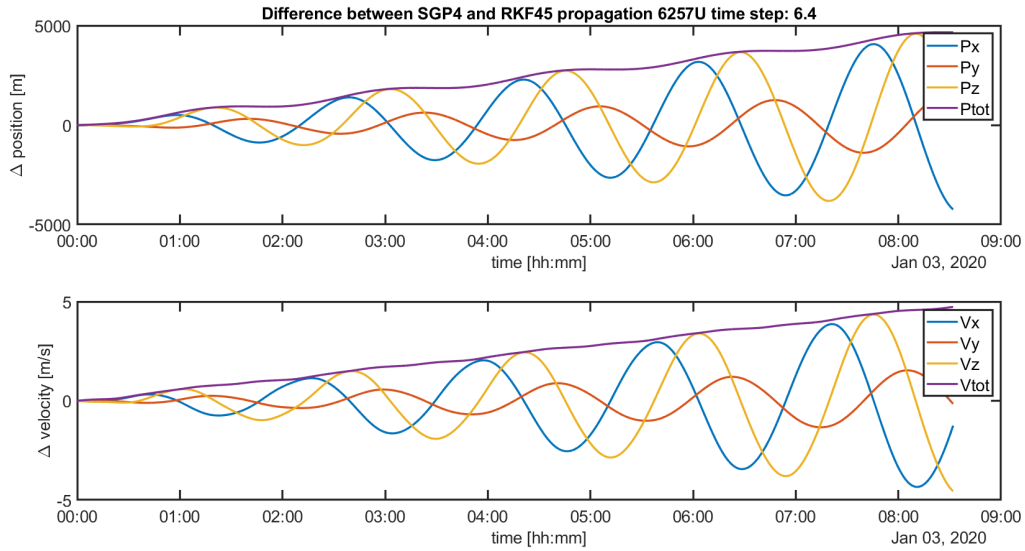

Figure E.13: Satellite 6257 propagated for 5 orbits with the RKF4(5) propagator with a time step of 6.4 seconds, stating from 03-01-2020 00:00:00, with the last know TLE at that time as starting condition. The total error is shown.

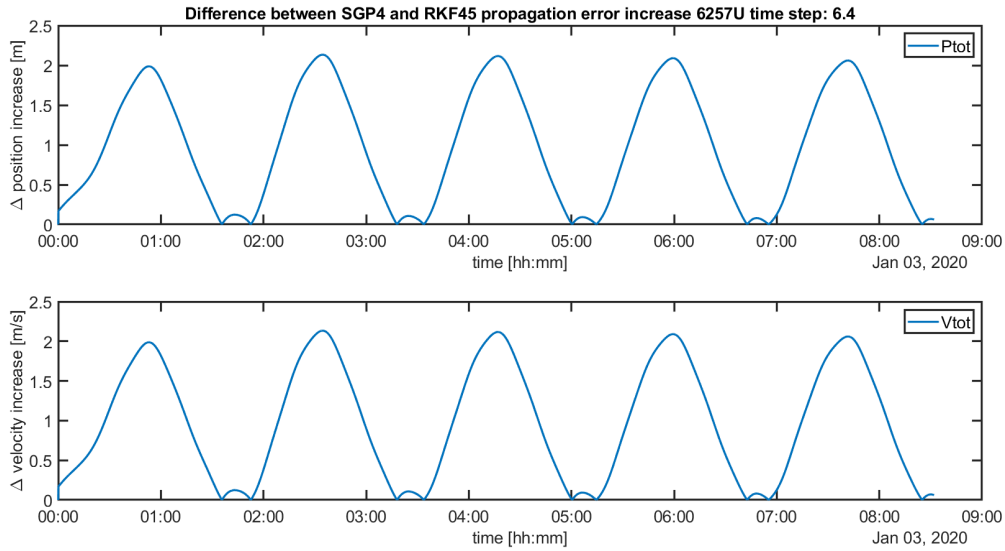

Figure E.14: Satellite 6257 propagated for 5 orbits with the RKF4(5) propagator with a time step of 6.4 seconds, stating from 03-01-2020 00:00:00, with the last know TLE at that time as starting condition. The error increase per epoch is shown

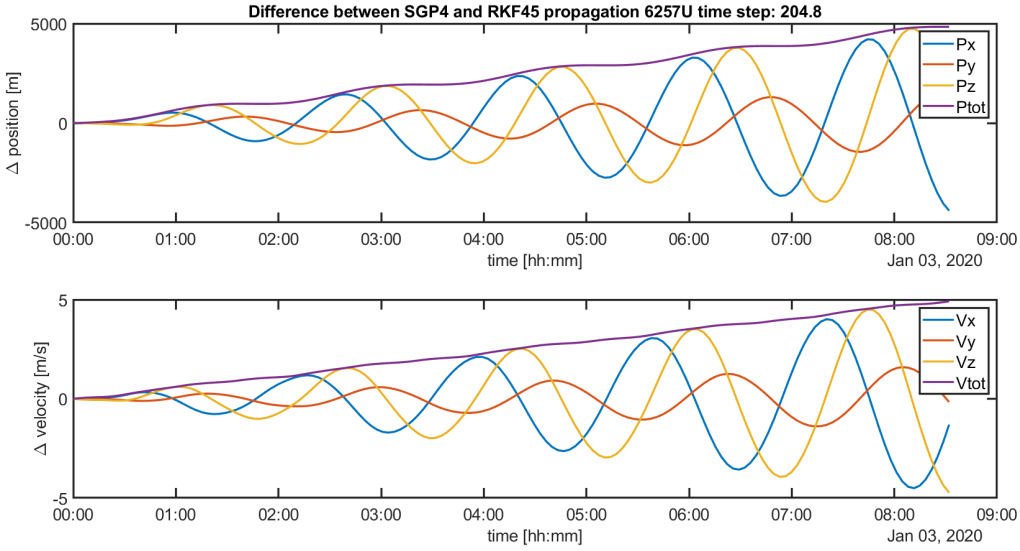

Figure E.15: Satellite 6257 propagated for 5 orbits with the RKF4(5) propagator with a time step of 204.8 seconds, stating from 03-01-2020 00:00:00, with the last know TLE at that time as starting condition. The total error is shown.

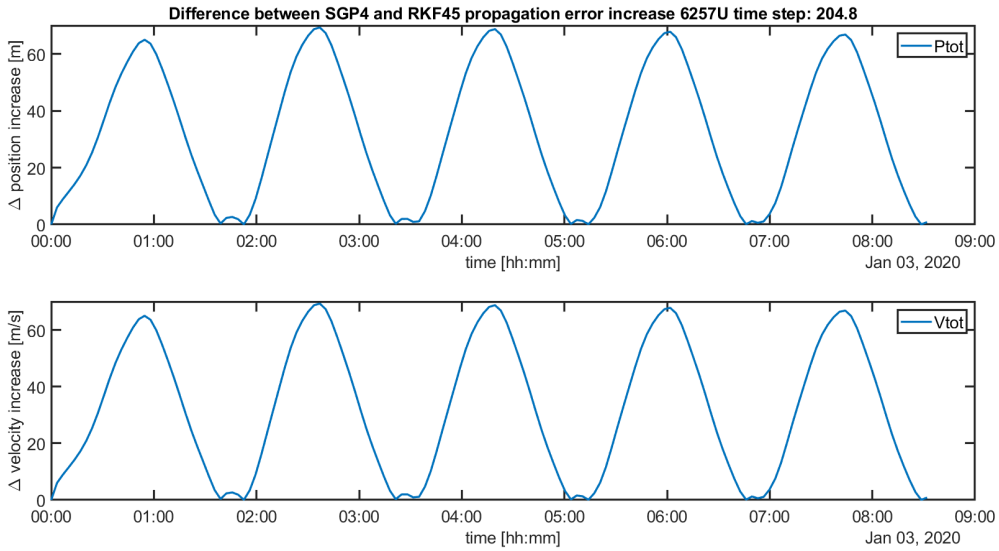

Figure E.16: Satellite 6257 propagated for 5 orbits with the RKF4(5) propagator with a time step of 204.8 seconds, stating from 03-01-2020 00:00:00, with the last know TLE at that time as starting condition. The error increase per epoch is shown

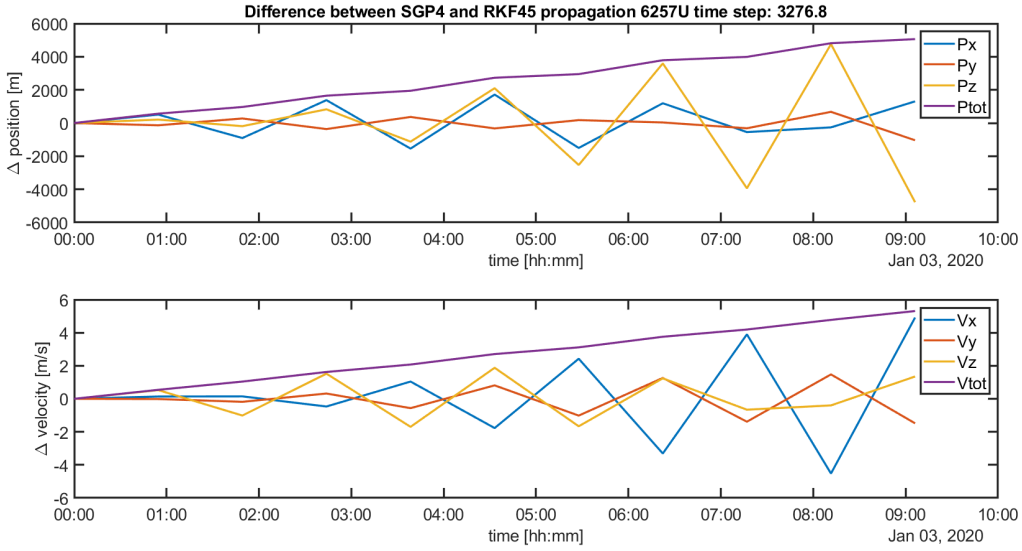

Figure E.17: Satellite 6257 propagated for 5 orbits with the RKF4(5) propagator with a time step of 3276.8 seconds, stating from 03-01-2020 00:00:00, with the last know TLE at that time as starting condition. The total error is shown.

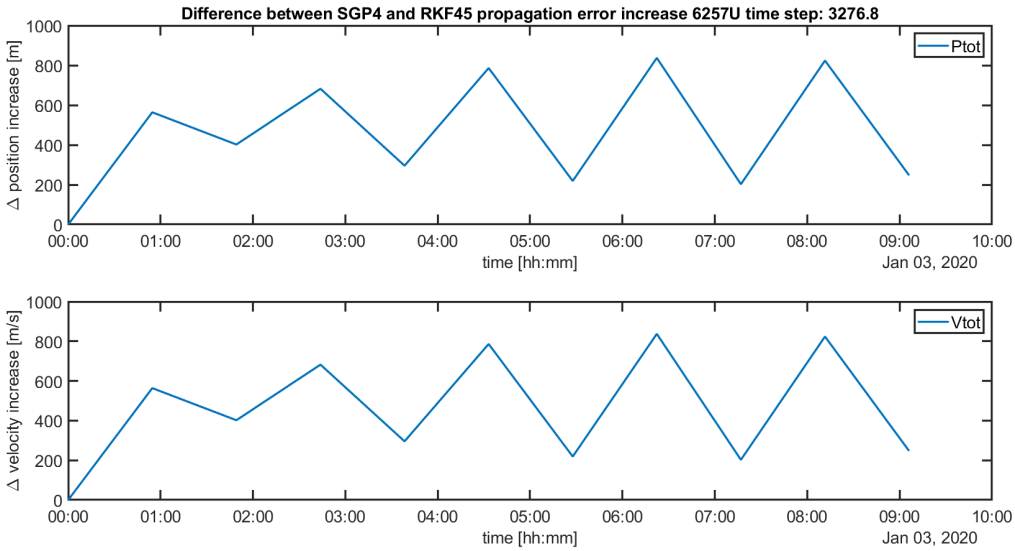

Figure E.18: Satellite 6257 propagated for 5 orbits with the RKF4(5) propagator with a time step of 3276.8 seconds, stating from 03-01-2020 00:00:00, with the last know TLE at that time as starting condition. The error increase per epoch is shown

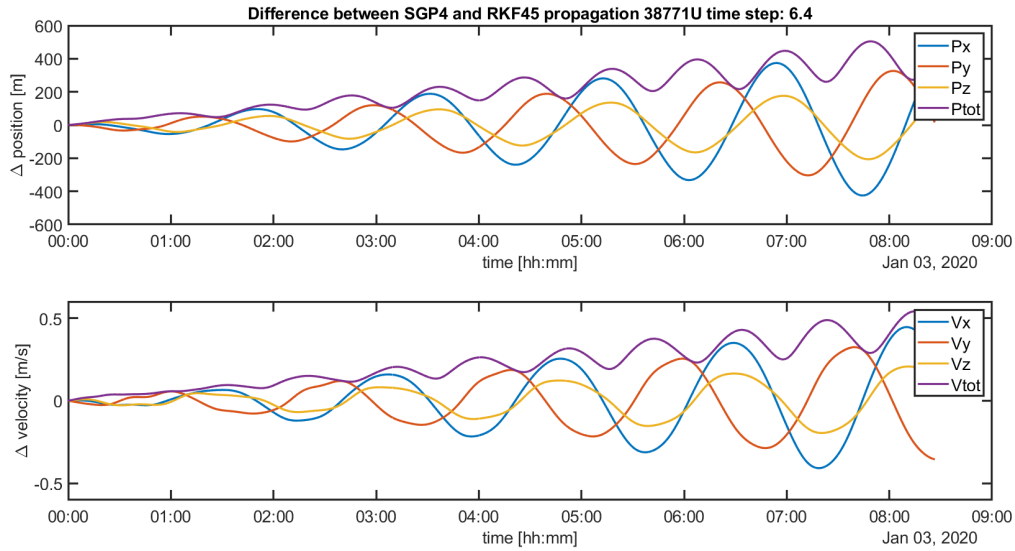

Figure E.19: Satellite 38771 propagated for 5 orbits with the RKF4(5) propagator with a time step of 6.4 seconds, stating from 03-01-2020 00:00:00, with the last know TLE at that time as starting condition. The total error is shown.

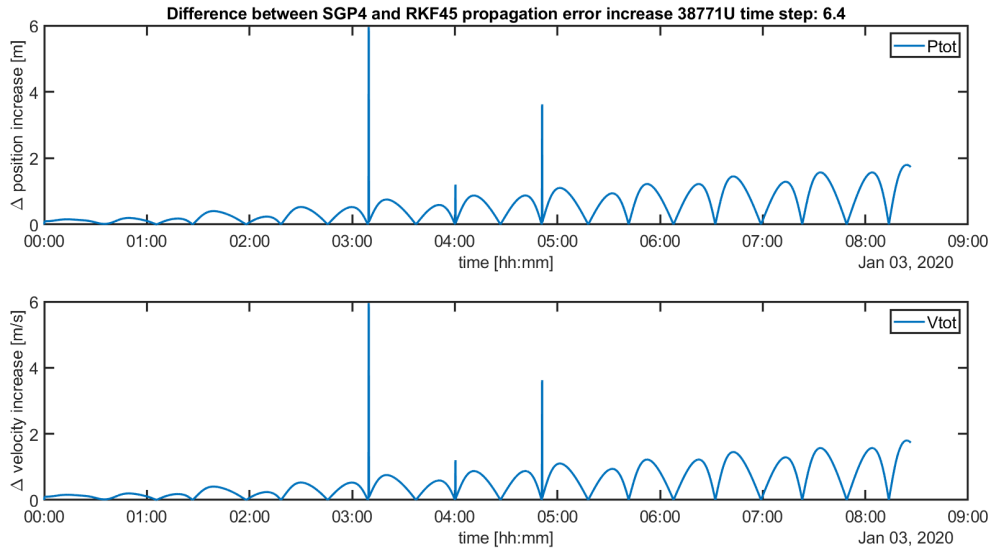

Figure E.20: Satellite 38771 propagated for 5 orbits with the RKF4(5) propagator with a time step of 6.4 seconds, stating from 03-01-2020 00:00:00, with the last know TLE at that time as starting condition. The error increase per epoch is shown

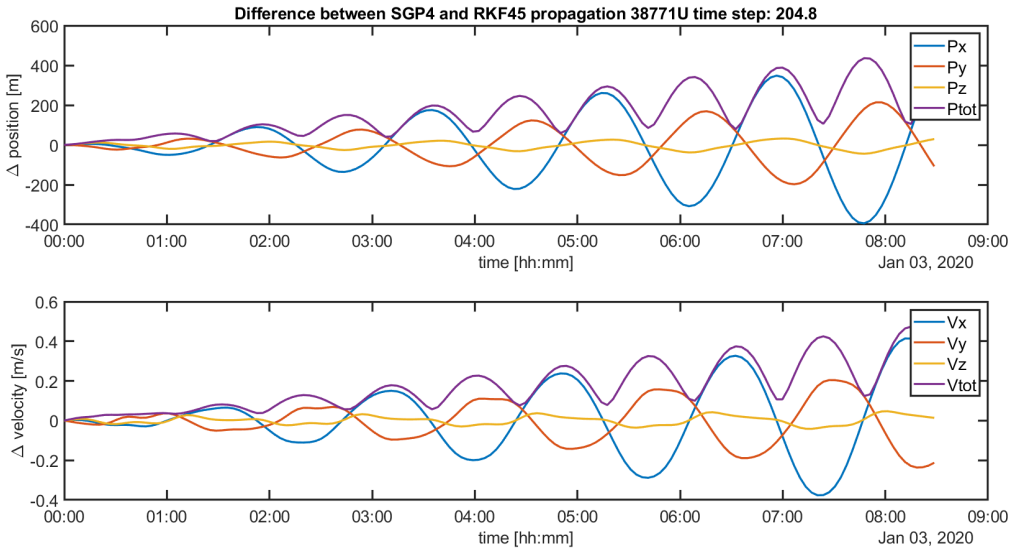

Figure E.21: Satellite 38771 propagated for 5 orbits with the RKF4(5) propagator with a time step of 204.8 seconds, stating from 03-01-2020 00:00:00, with the last know TLE at that time as starting condition. The total error is shown.

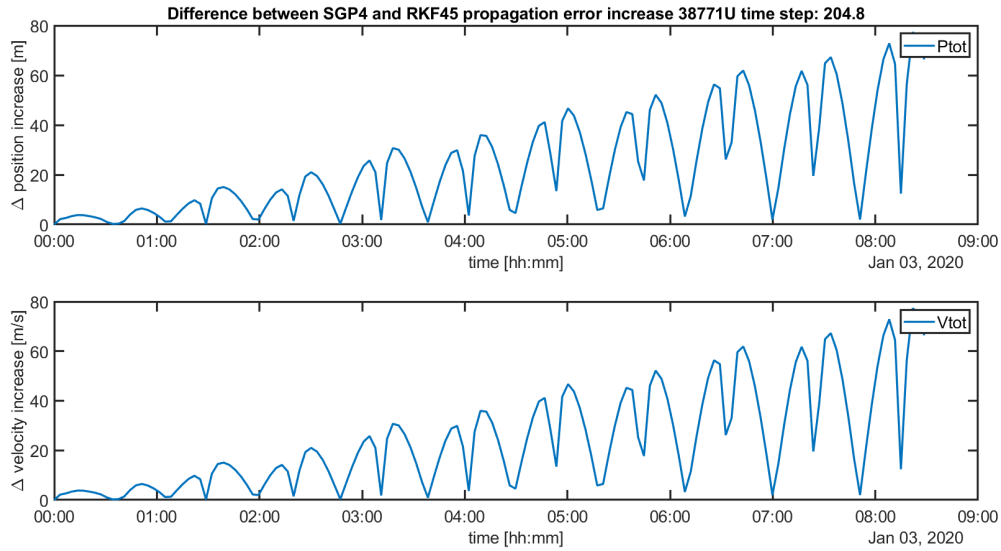

Figure E.22: Satellite 38771 propagated for 5 orbits with the RKF4(5) propagator with a time step of 204.8 seconds, stating from 03-01-2020 00:00:00, with the last know TLE at that time as starting condition. The error increase per epoch is shown

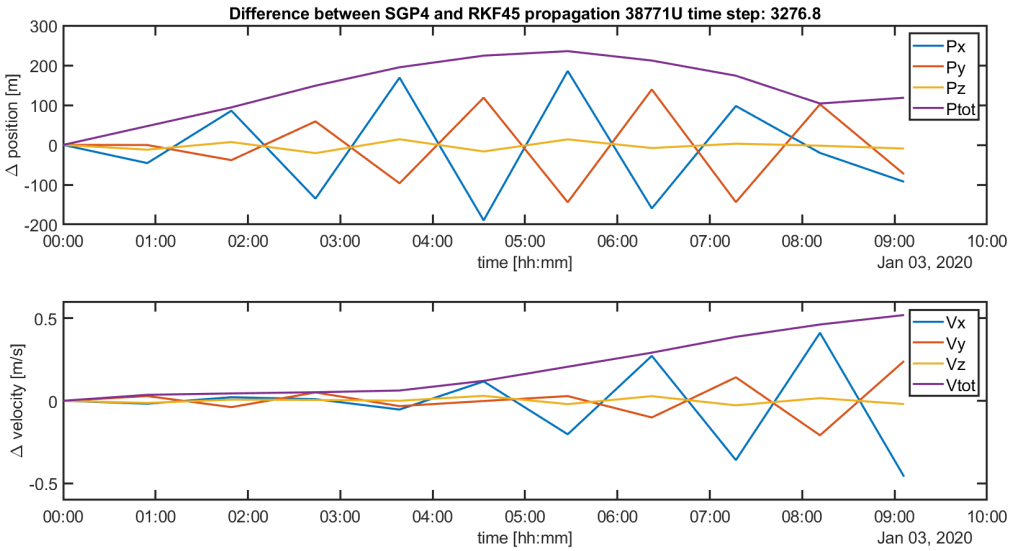

Figure E.23: Satellite 38771 propagated for 5 orbits with the RKF4(5) propagator with a time step of 3276.8 seconds, stating from 03-01-2020 00:00:00, with the last know TLE at that time as starting condition. The total error is shown.

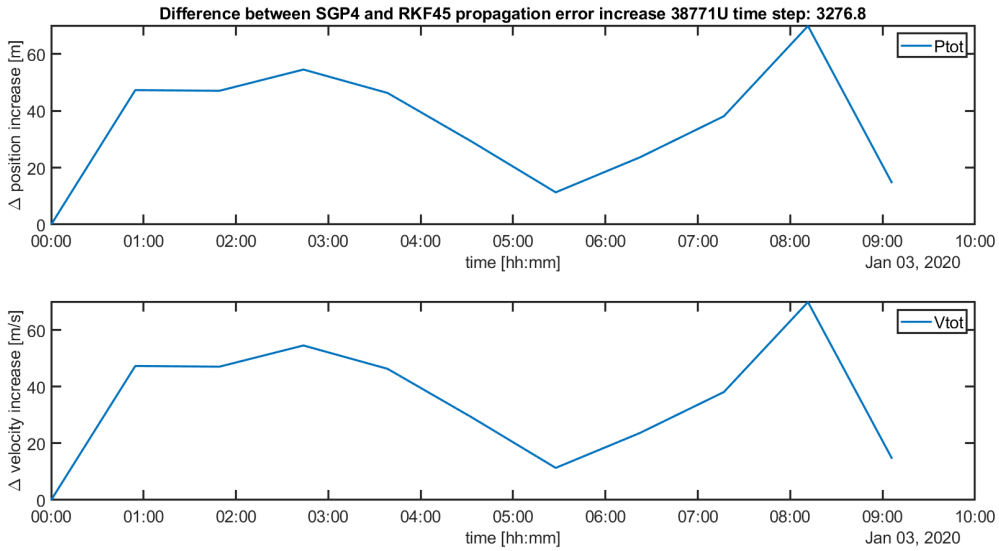

Figure E.24: Satellite 38771 propagated for 5 orbits with the RKF4(5) propagator with a time step of 3276.8 seconds, stating from 03-01-2020 00:00:00, with the last know TLE at that time as starting condition. The error increase per epoch is shown

F

Validation: Extended Kalman filter

The appendix show the different graphs for all satellites that are used to validate the Extended Kalman Filter.

F.1. Single observation arc validation

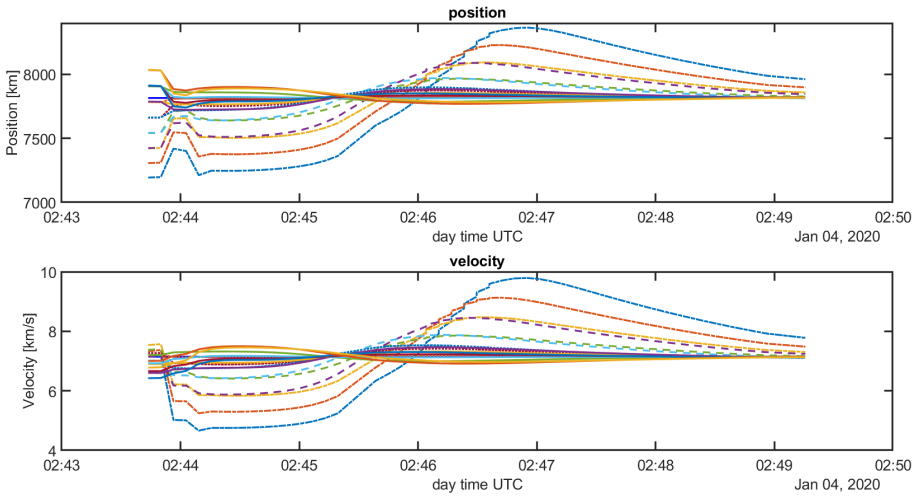

Figure F.1: The hypotheses generated for satellite 4794U propagated and corrected with the EKF with SPG4-based observations. The EKF is applied on a single observation arc.

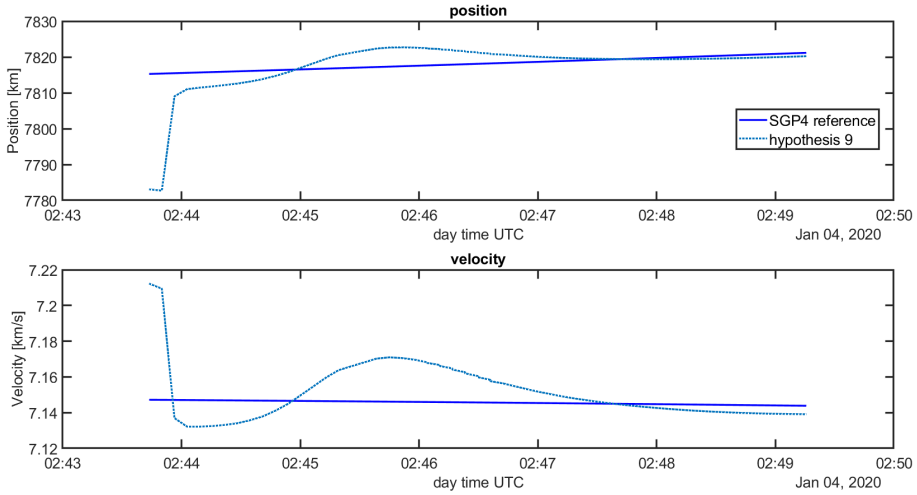

Figure F.2: The best hypothesis generated for satellite 4794U propagated and corrected with the EKF with SPG4-based observations. The EKF is applied on a single observation arc.

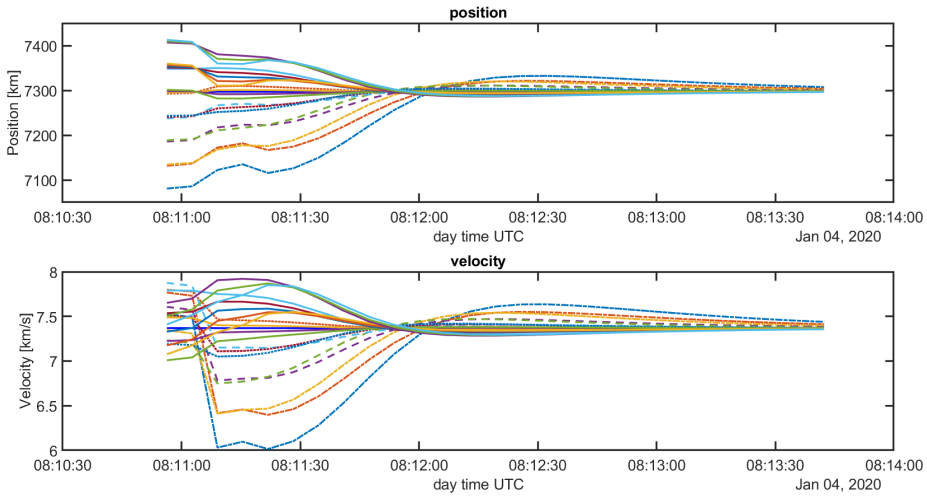

Figure F.3: The hypotheses generated for satellite 6257U propagated and corrected with the EKF with SPG4-based observations. The EKF is applied on a single observation arc.

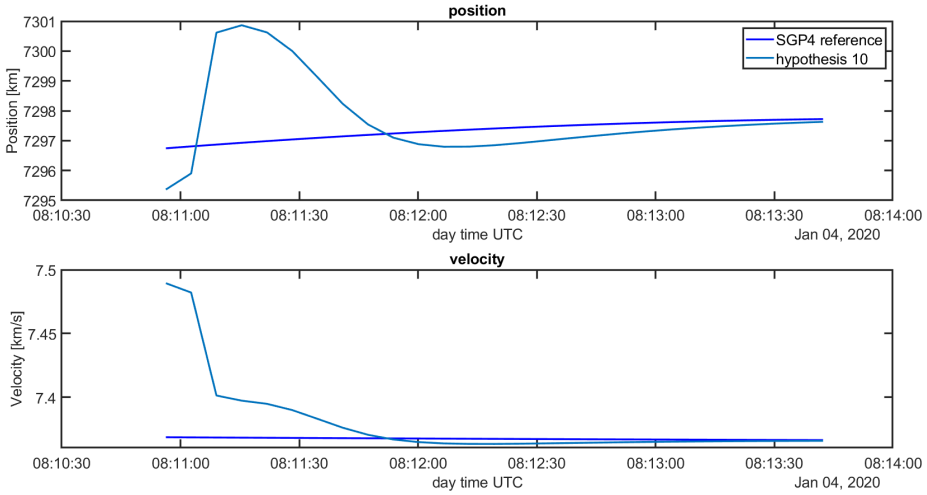

Figure F.4: The best hypothesis generated for satellite 6257U propagated and corrected with the EKF with SPG4-based observations. The EKF is applied on a single observation arc.

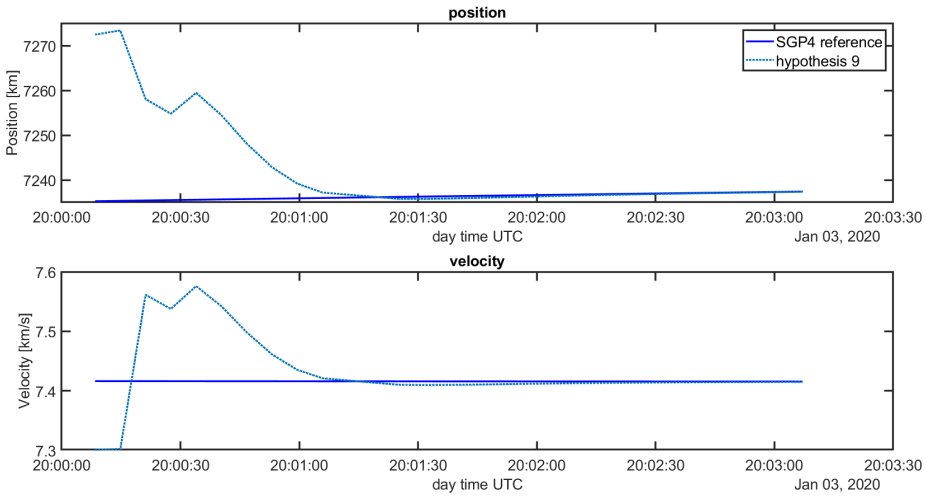

Figure F.5: The hypotheses generated for satellite 22284U propagated and corrected with the EKF with SPG4-based observations. The EKF is applied on a single observation arc.

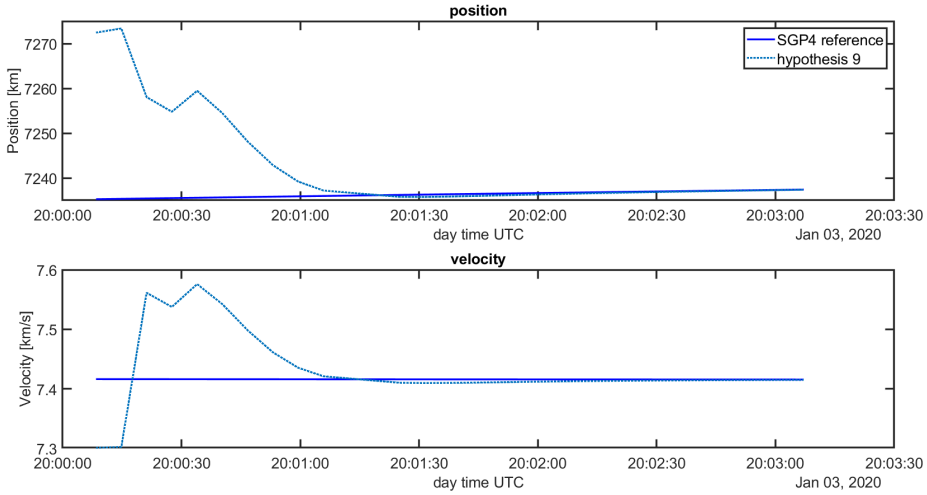

Figure F.6: The best hypothesis generated for satellite 22284U propagated and corrected with the EKF with SPG4-based observations. The EKF is applied on a single observation arc.

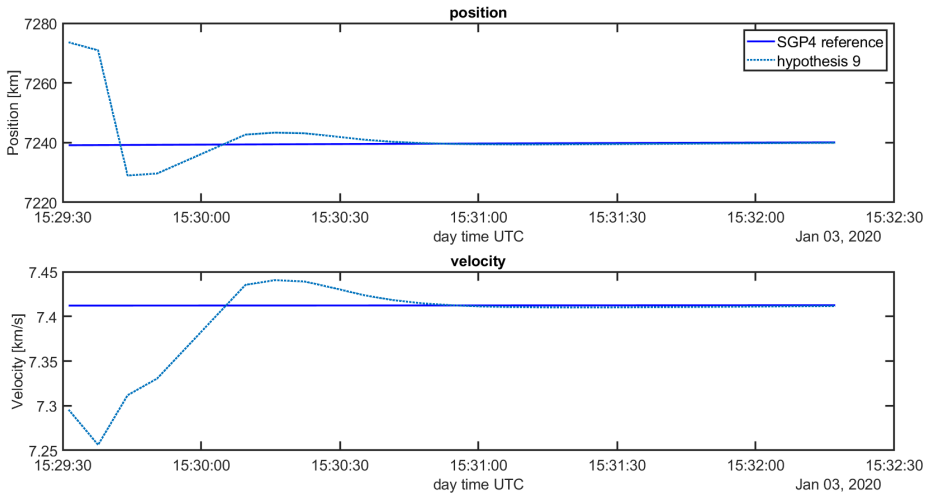

Figure F.7: The hypotheses generated for satellite 23404U propagated and corrected with the EKF with SPG4-based observations. The EKF is applied on a single observation arc.

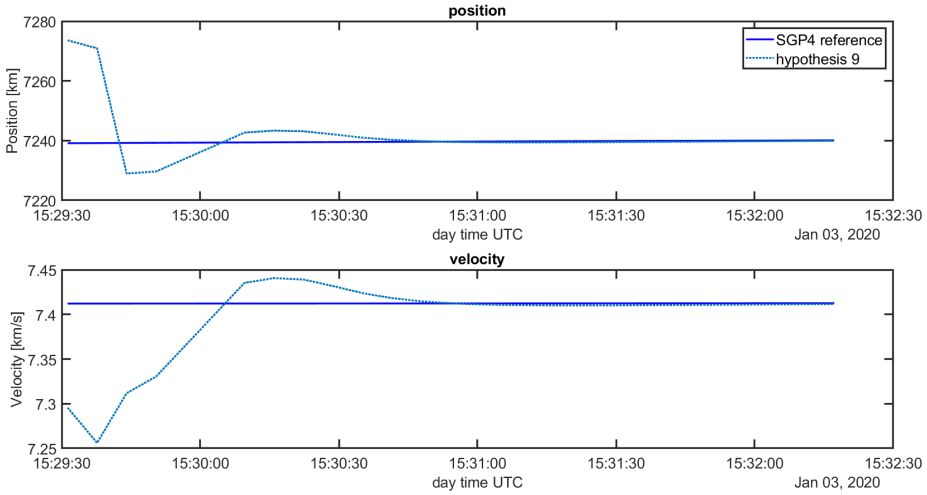

Figure F.8: The best hypothesis generated for satellite 23404U propagated and corrected with the EKF with SPG4-based observations. The EKF is applied on a single observation arc.

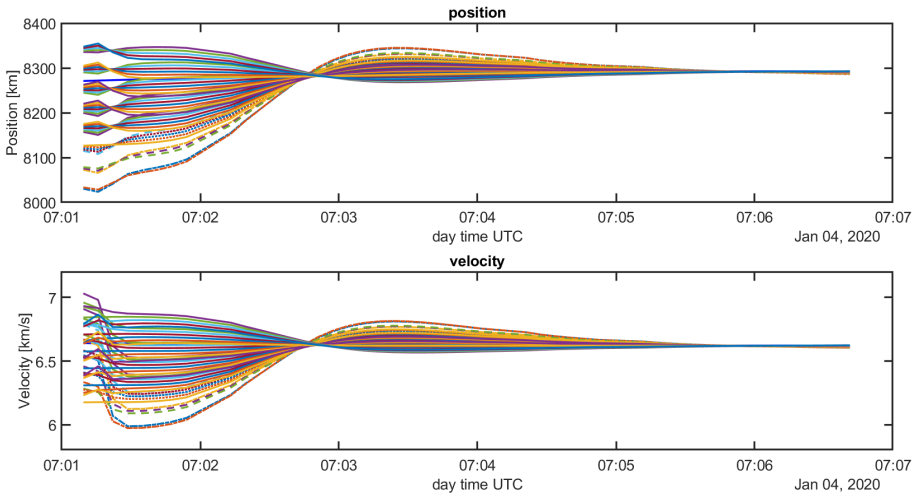

Figure F.9: The hypotheses generated for satellite 10793U propagated and corrected with the EKF with SPG4-based observations. The EKF is applied on a single observation arc.

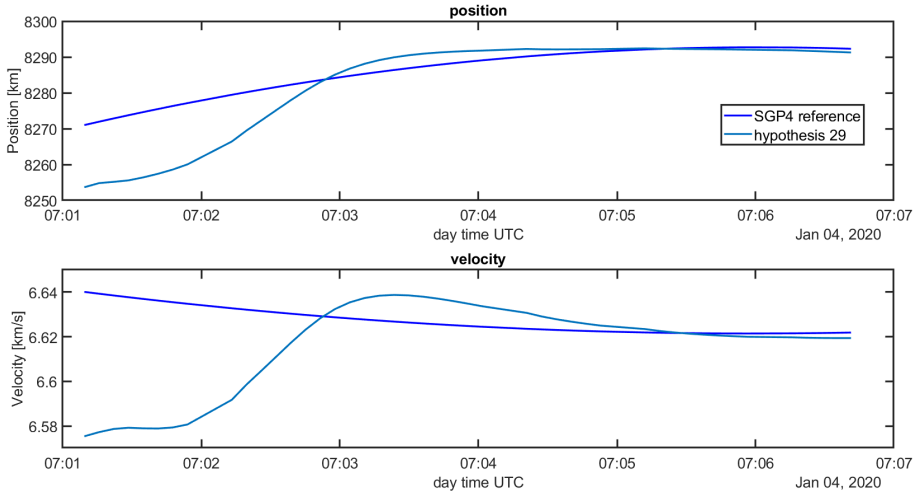

Figure F.10: The best hypothesis generated for satellite 10793U propagated and corrected with the EKF with SPG4-based observations. The EKF is applied on a single observation arc.

F.2. Multiple observation arc validation

F.2.1. Satellite 38771U

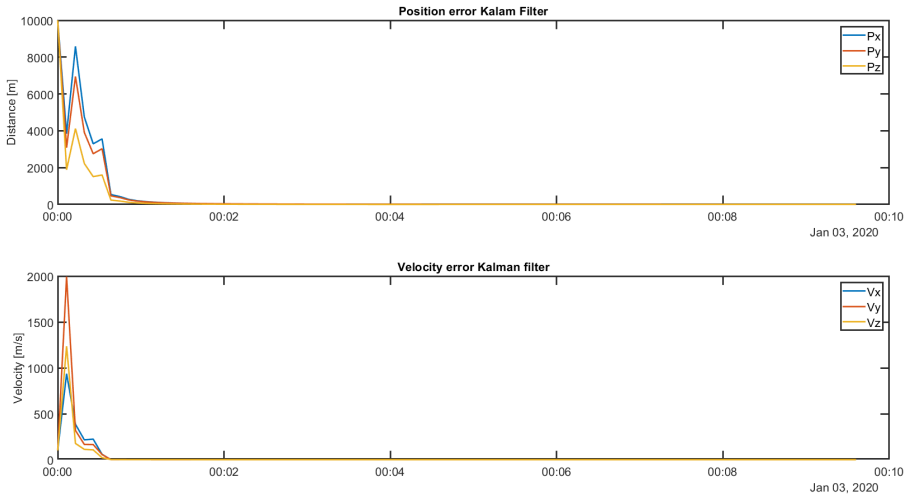

Figure F.11: First observation arc for satellite 38711U, where the position and velocity difference between the SGP4-based reference state and EKF solution per epoch is visualised, for each separate element.

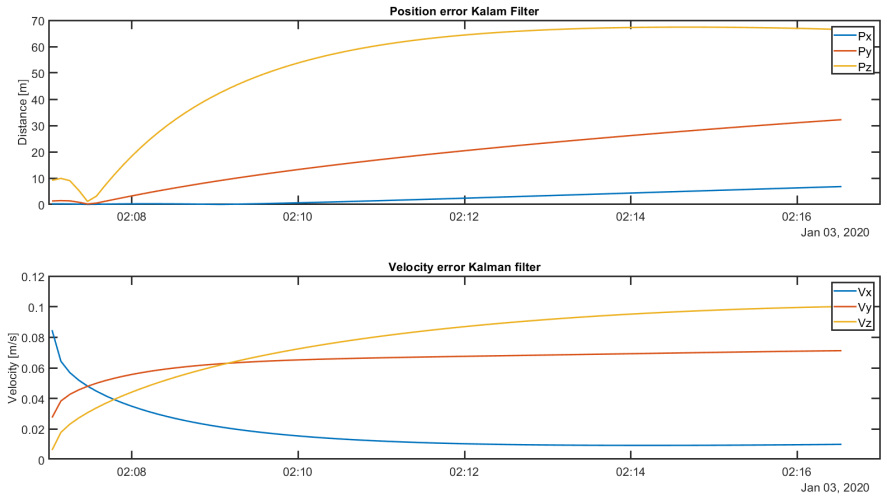

Figure F.12: Second observation arc for satellite 38711U, where the position and velocity difference between the SGP4-based reference state and EKF solution per epoch is visualised, for each separate element.

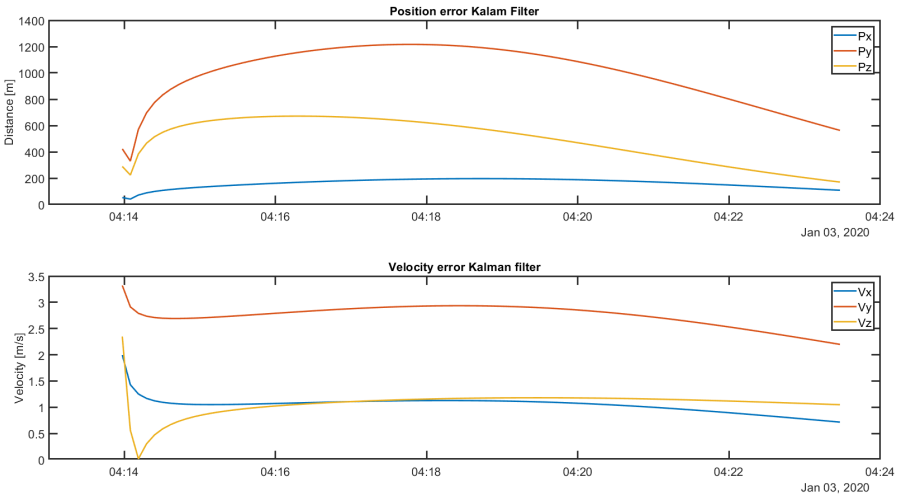

Figure F.13: Third observation arc for satellite 38711U, where the position and velocity difference between the SGP4-based reference state and EKF solution per epoch is visualised, for each separate element.

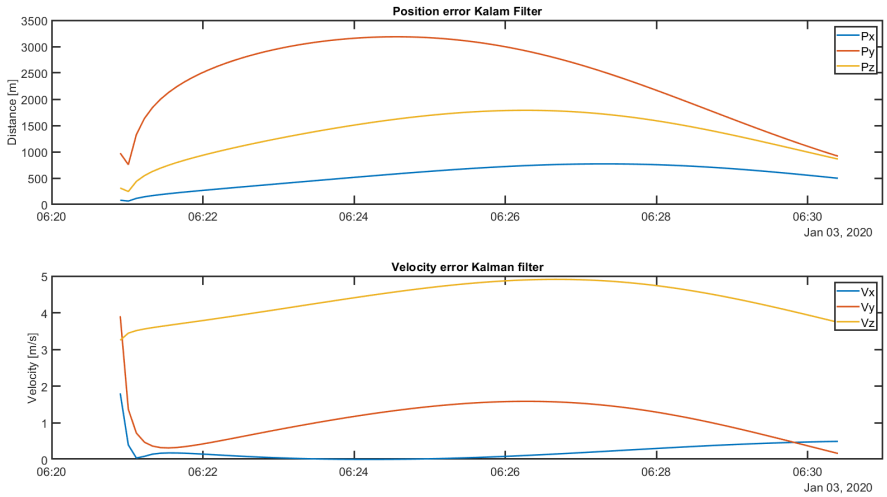

Figure F.14: Fourth observation arc for satellite 38711U, where the position and velocity difference between the SGP4-based reference state and EKF solution per epoch is visualised, for each separate element.

F.2.2. satellite 6257U

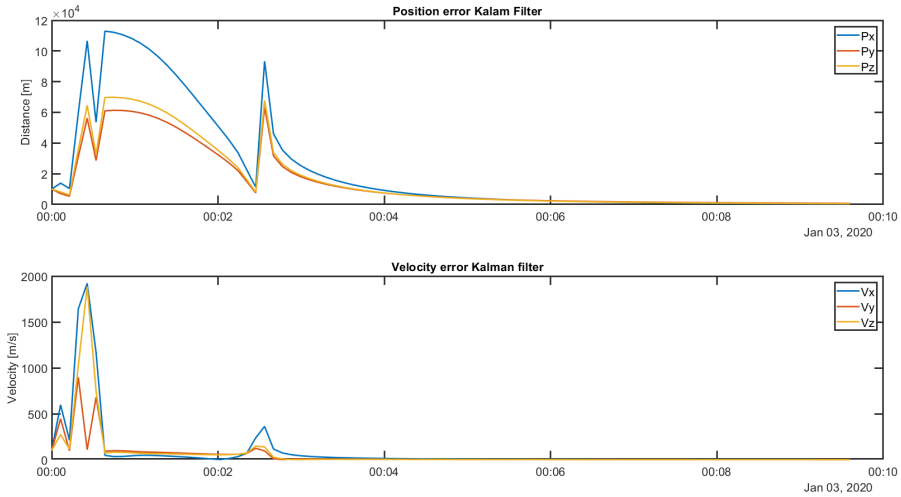

Figure F.15: First observation arc for satellite 6257U, where the position and velocity difference between the SGP4-based reference state and EKF solution per epoch is visualised, for each separate element.

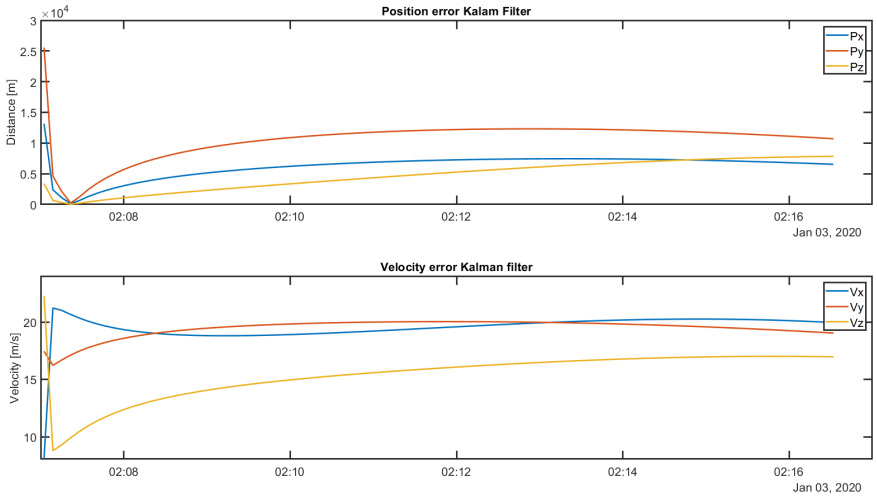

Figure F.16: Second observation arc for satellite 6257U, where the position and velocity difference between the SGP4-based reference state and EKF solution per epoch is visualised, for each separate element.

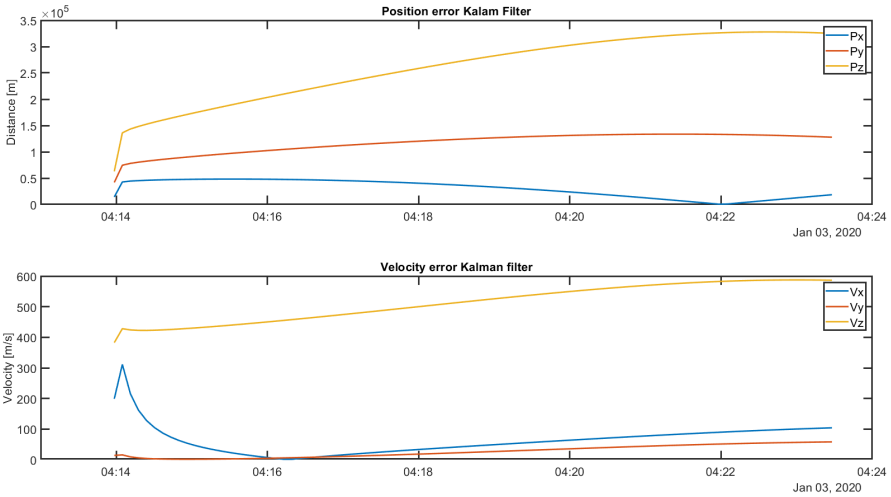

Figure F.17: Third observation arc for satellite 6257U, where the position and velocity difference between the SGP4-based reference state and EKF solution per epoch is visualised, for each separate element.

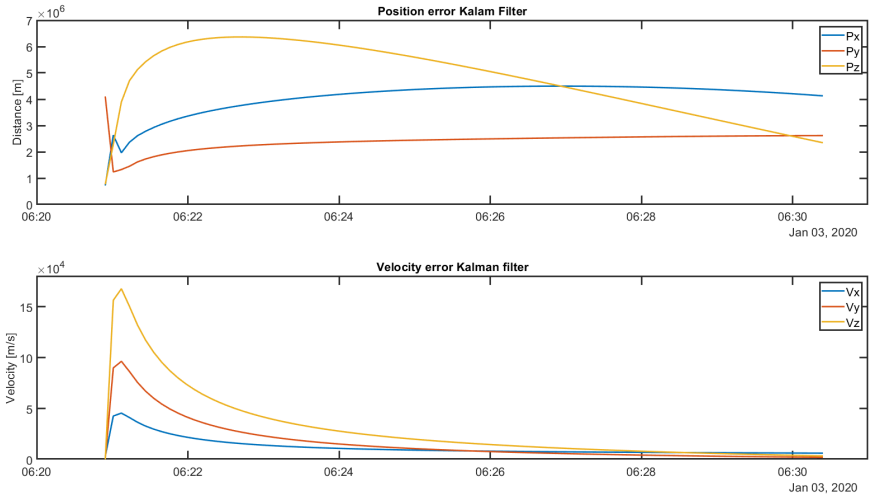

Figure F.18: Fourth observation arc for satellite 6257U, where the position and velocity difference between the SGP4-based reference state and EKF solution per epoch is visualised, for each separate element.

F.2.3. Satellite 10793U

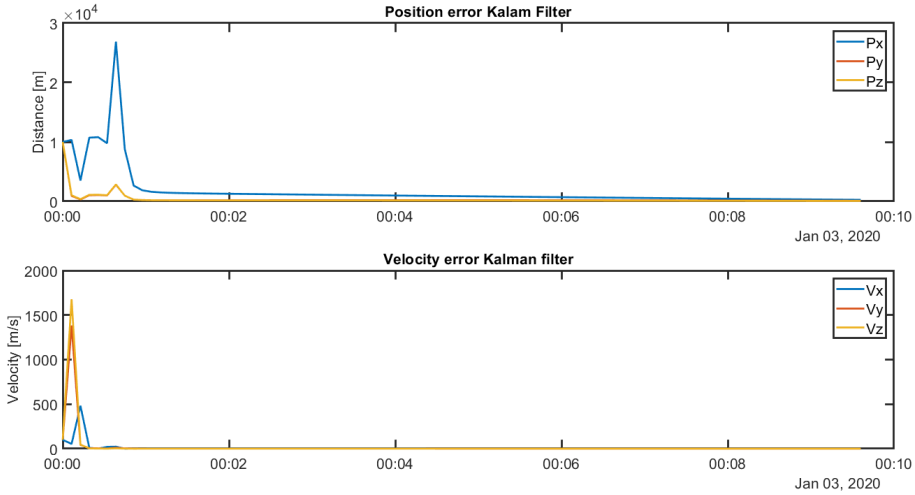

Figure F.19: First observation arc for satellite 10793U, where the position and velocity difference between the SGP4-based reference state and EKF solution per epoch is visualised, for each separate element.

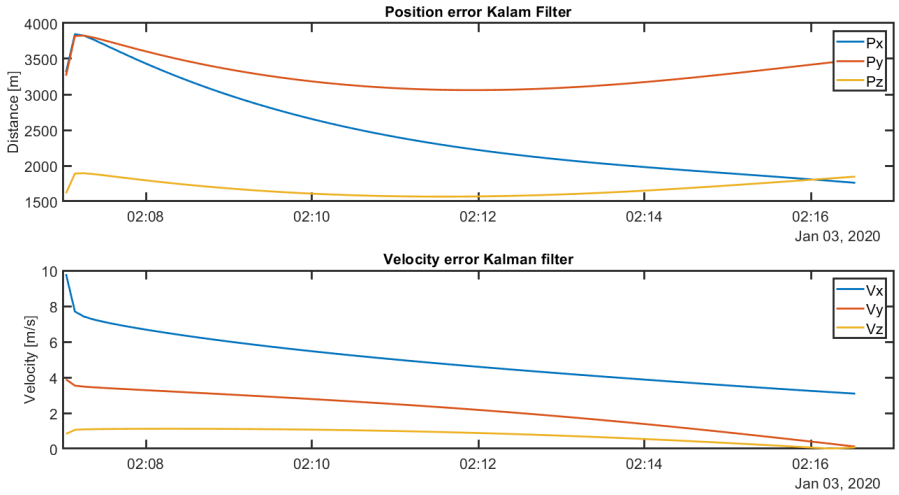

Figure F.20: Second observation arc for satellite 10793U, where the position and velocity difference between the SGP4-based reference state and EKF solution per epoch is visualised, for each separate element.

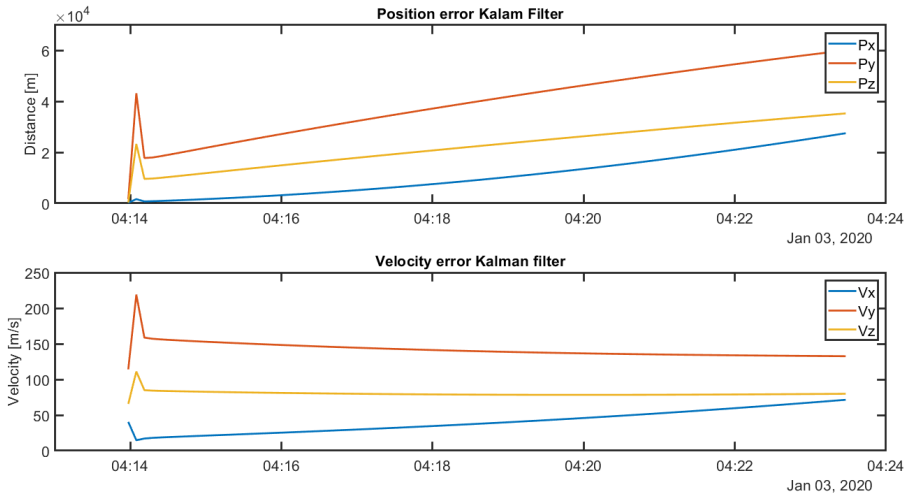

Figure F.21: Third observation arc for satellite 10793U, where the position and velocity difference between the SGP4-based reference state and EKF solution per epoch is visualised, for each separate element.

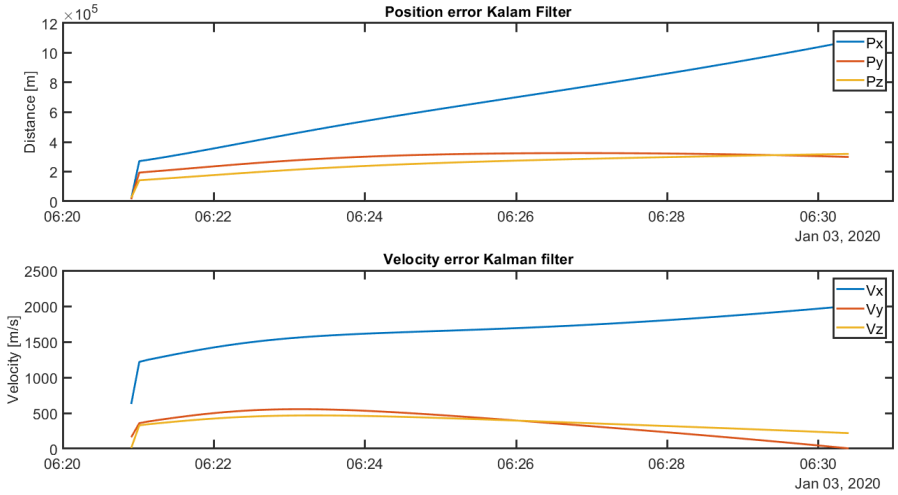

Figure F.22: Fourth observation arc for satellite 10793U, where the position and velocity difference between the SGP4-based reference state and EKF solution per epoch is visualised, for each separate element.

F.3. Multiple observation arc validation - with covarience reset

F.3.1. Satellite 38771U

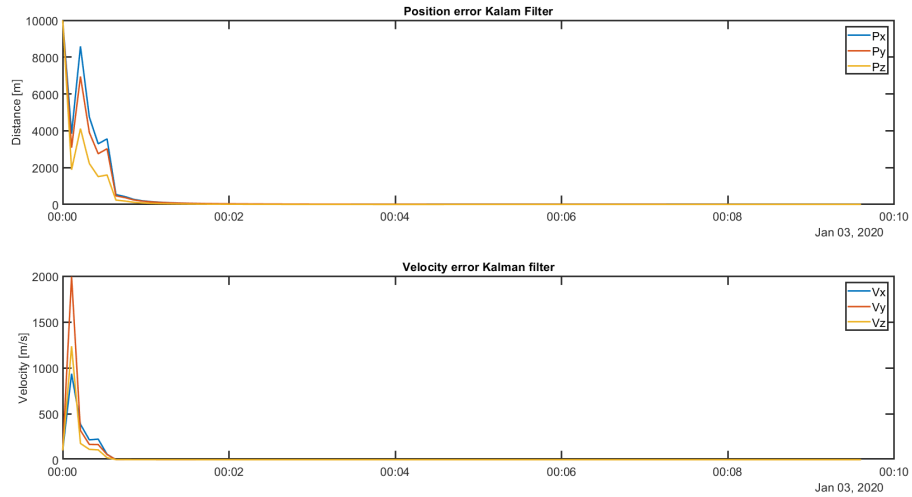

Figure F.23: First observation arc for satellite 38711U, where the position and velocity difference between the SGP4-based reference state and EKF solution per epoch is visualised, for each separate element. Starting with an initialise covariance matrix.

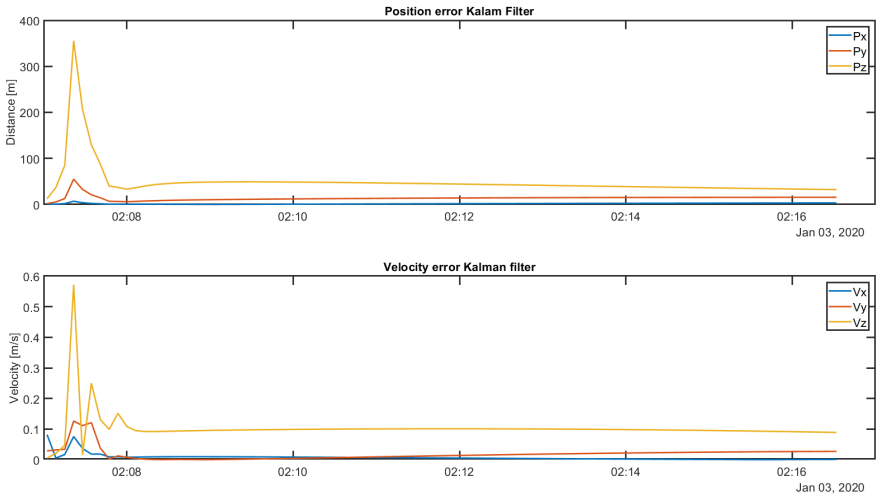

Figure F.24: Second observation arc for satellite 38711U, where the position and velocity difference between the SGP4-based reference state and EKF solution per epoch is visualised, for each separate element. Starting with an initialise covariance matrix.

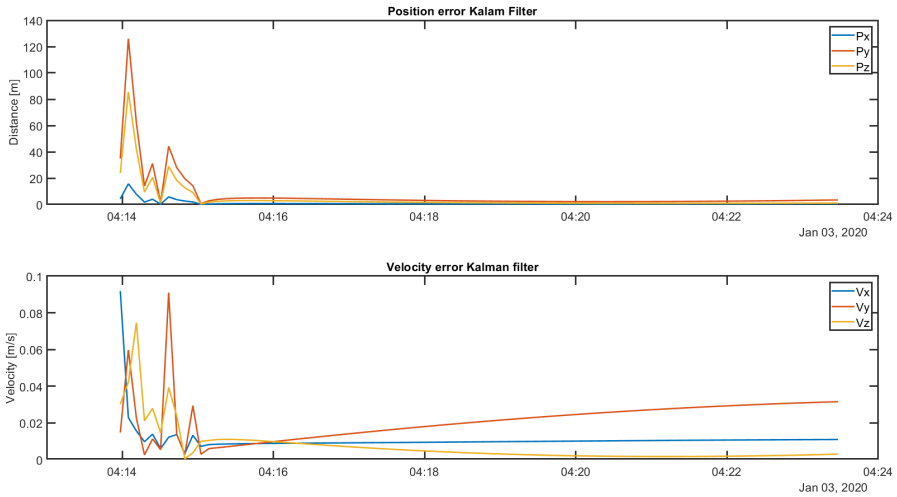

Figure F.25: Third observation arc for satellite 38711U, where the position and velocity difference between the SGP4-based reference state and EKF solution per epoch is visualised, for each separate element. Starting with an initialise covariance matrix.

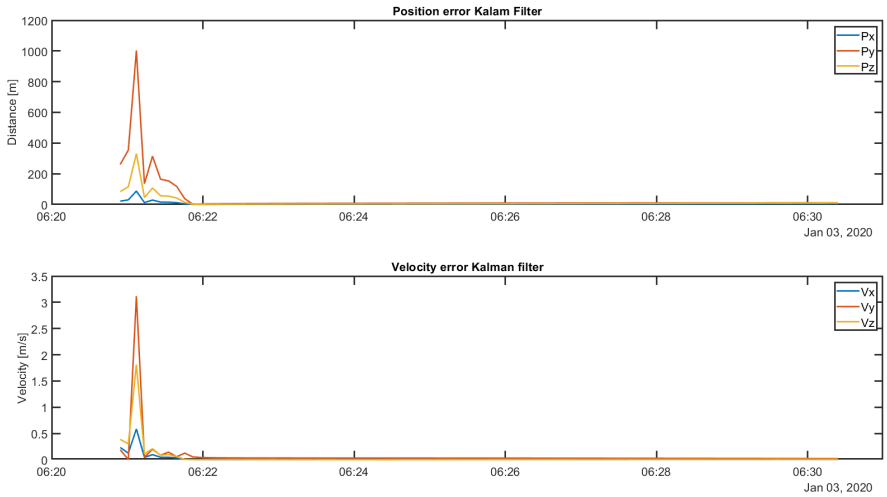

Figure F.26: Fourth observation arc for satellite 38711U, where the position and velocity difference between the SGP4-based reference state and EKF solution per epoch is visualised, for each separate element. Starting with an initialise covariance matrix.

F.3.2. satellite 6257U

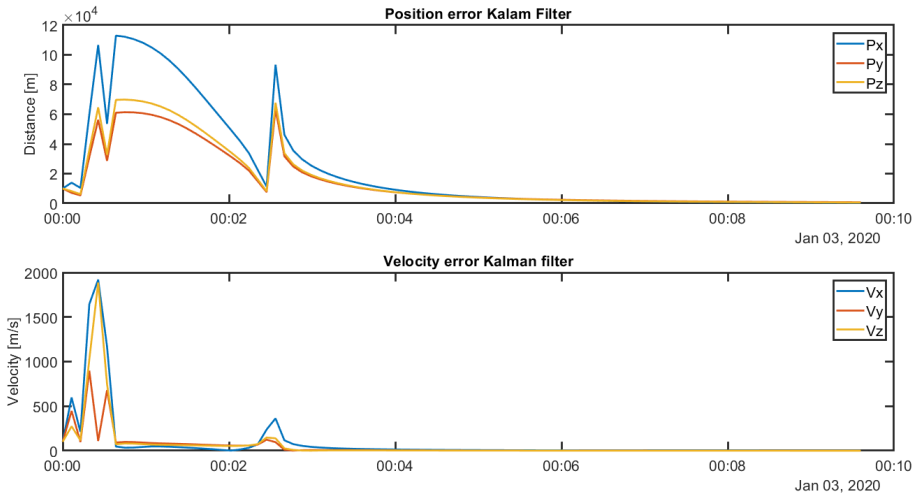

Figure F.27: First observation arc for satellite 6257U, where the position and velocity difference between the SGP4-based reference state and EKF solution per epoch is visualised, for each separate element. Starting with an initialise covariance matrix.

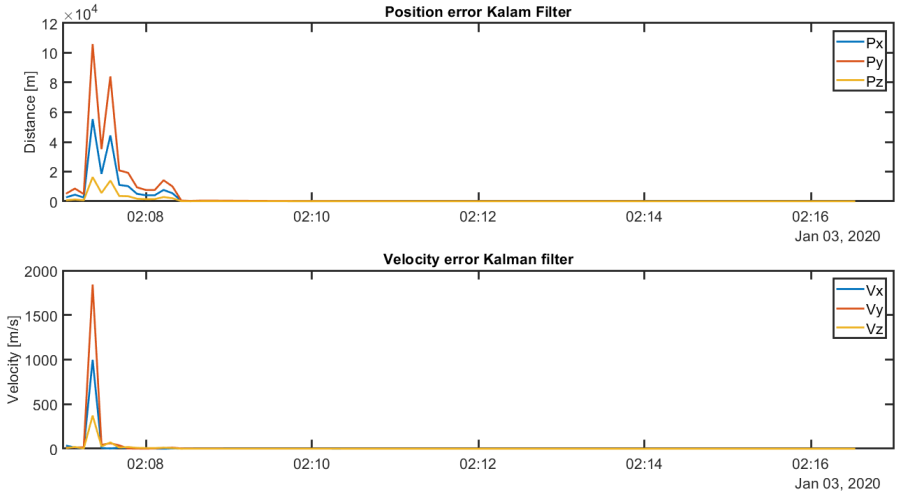

Figure F.28: Second observation arc for satellite 6257U, where the position and velocity difference between the SGP4-based reference state and EKF solution per epoch is visualised, for each separate element. Starting with an initialise covariance matrix.

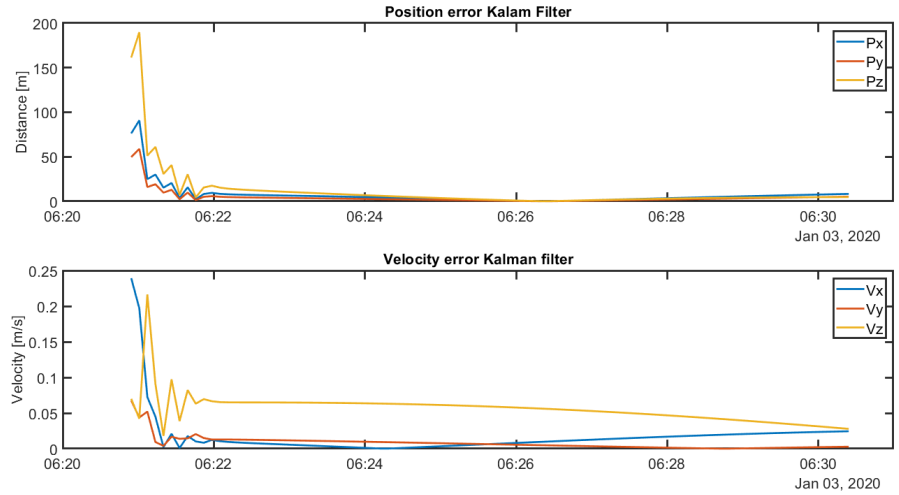

Figure F.29: Third observation arc for satellite 6257U, where the position and velocity difference between the SGP4-based reference state and EKF solution per epoch is visualised, for each separate element. Starting with an initialise covariance matrix.

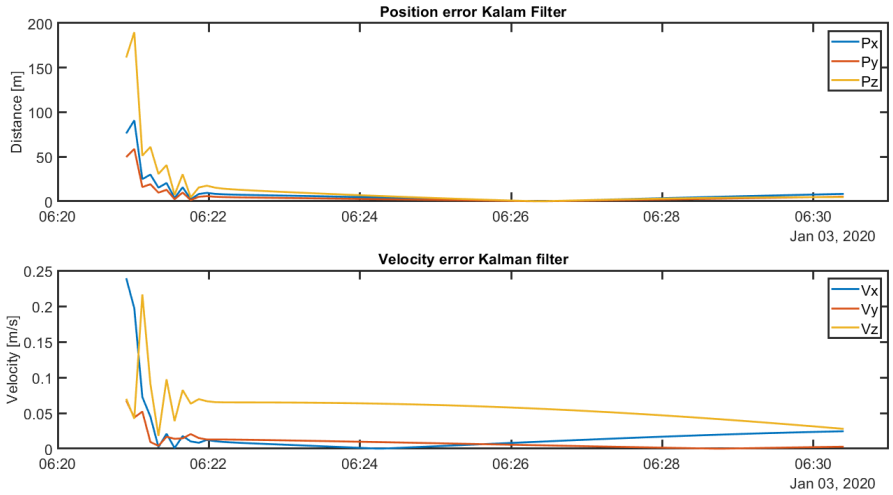

Figure F.30: Fourth observation arc for satellite 6257U, where the position and velocity difference between the SGP4-based reference state and EKF solution per epoch is visualised, for each separate element. Starting with an initialise covariance matrix.

F.3.3. Satellite 10793U

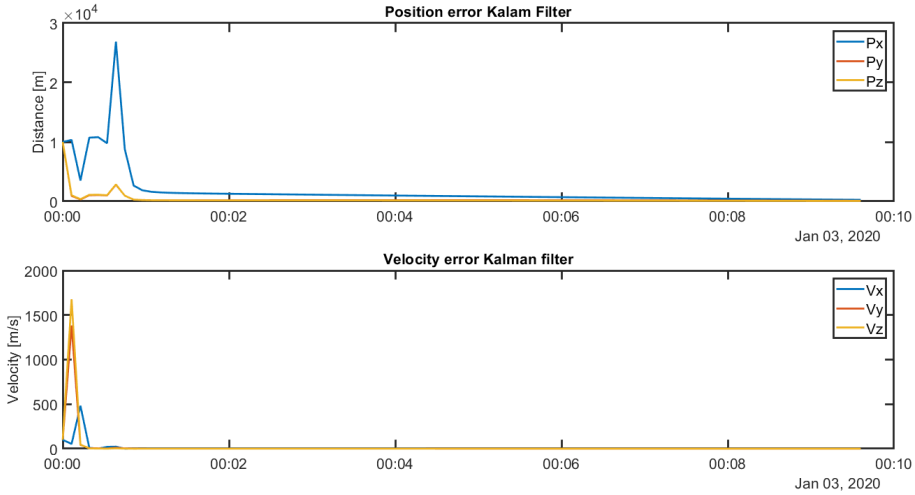

Figure F.31: First observation arc for satellite 10793U, where the position and velocity difference between the SGP4-based reference state and EKF solution per epoch is visualised, for each separate element. Starting with an initialise covariance matrix.

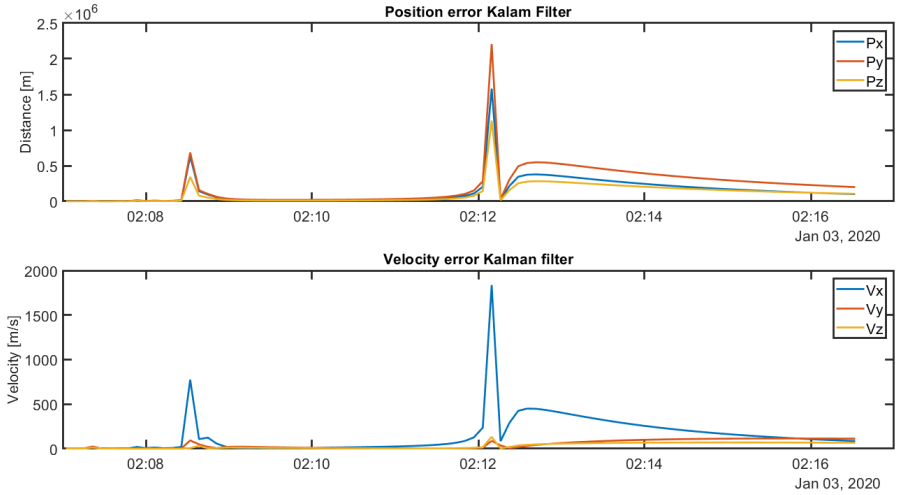

Figure F.32: Second observation arc for satellite 10793U, where the position and velocity difference between the SGP4-based reference state and EKF solution per epoch is visualised, for each separate element. Starting with an initialise covariance matrix.

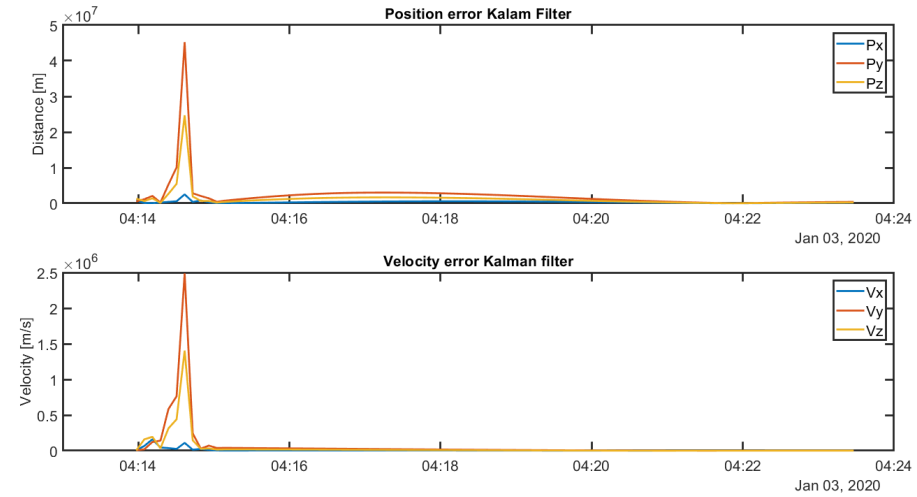

Figure F.33: Third observation arc for satellite 10793U, where the position and velocity difference between the SGP4-based reference state and EKF solution per epoch is visualised, for each separate element. Starting with an initialise covariance matrix.

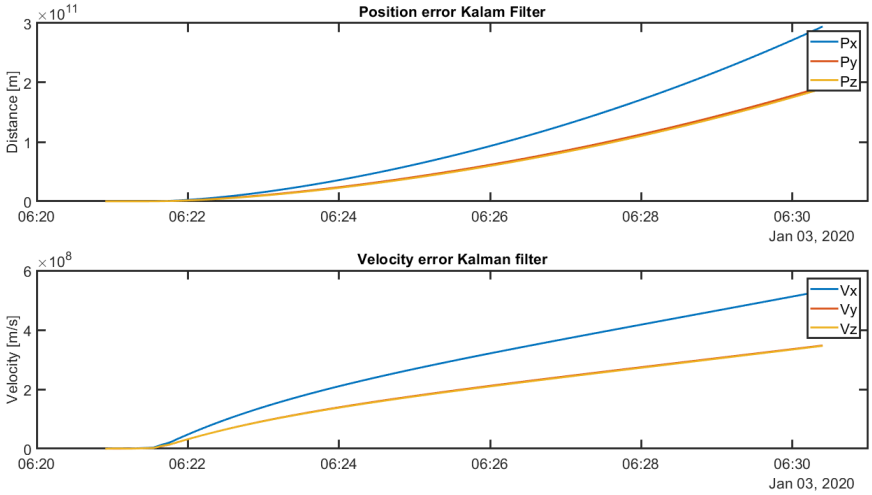

Figure F.34: Fourth observation arc for satellite 10793U, where the position and velocity difference between the SGP4-based reference state and EKF solution per epoch is visualised, for each separate element. Starting with an initialise covariance matrix.

G

Validation: RKF4(5) analysis comparing the error for high and low inclination orbits.

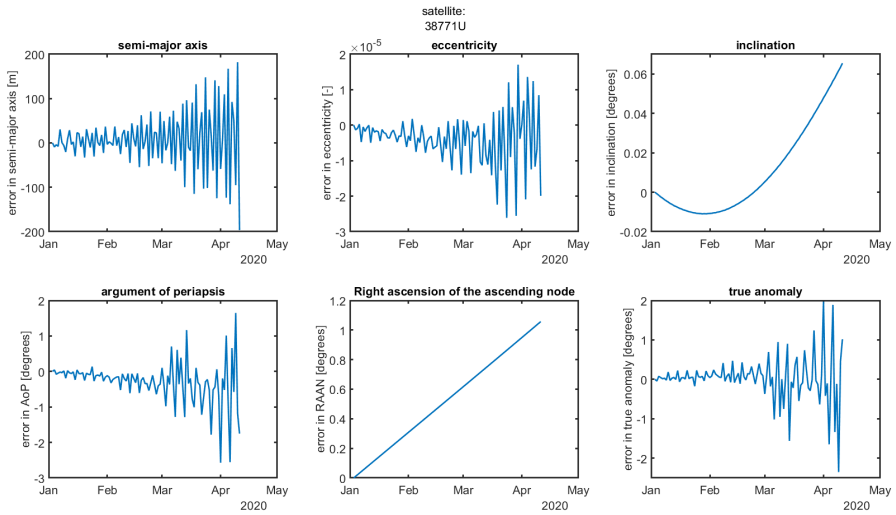

Figure G.1: Propagation difference in Kepler elements between the SGP4 orbit and the RKF4(5) method. Analysed from the start of January 2020, for three months. Here it shows a satellite with a high inclined orbit.

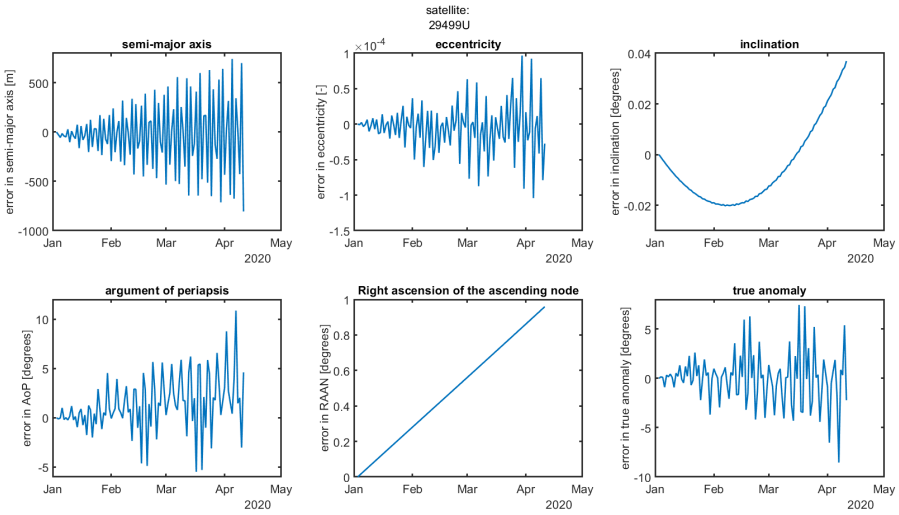

Figure G.2: Propagation difference in Kepler elements between the SGP4 orbit and the RKF4(5) method. Analysed from the start of January 2020, for three months. Here it shows a satellite with a high inclined orbit.

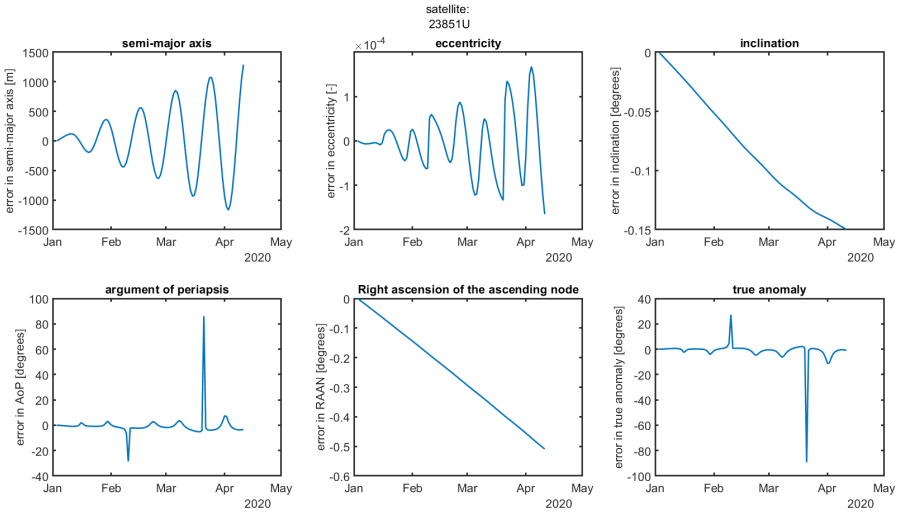

Figure G.3: Propagation difference in Kepler elements between the SGP4 orbit and the RKF4(5) method. Analysed from the start of January 2020, for three months. Here it shows a satellite with a high inclined orbit.

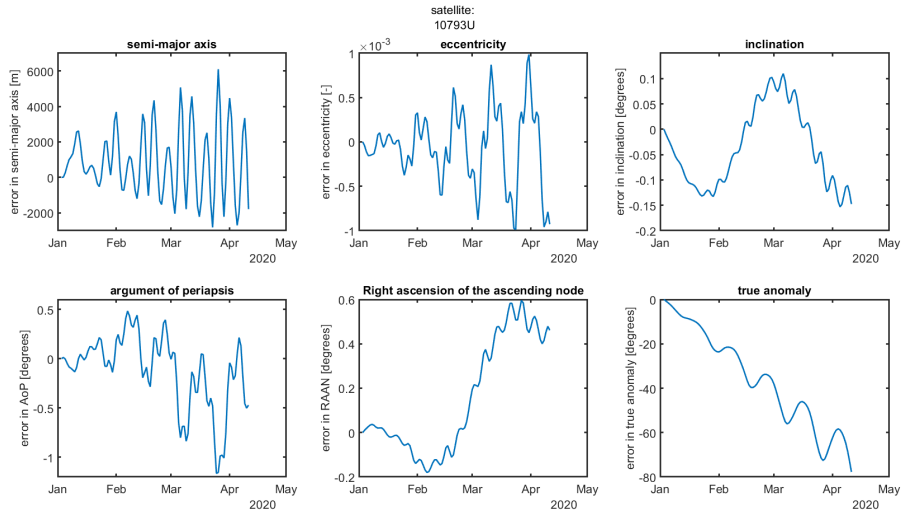

Figure G.4: Propagation difference in Kepler elements between the SGP4 orbit and the RKF4(5) method. Analysed from the start of January 2020, for three months. Here it shows a satellite with a low inclined orbit.

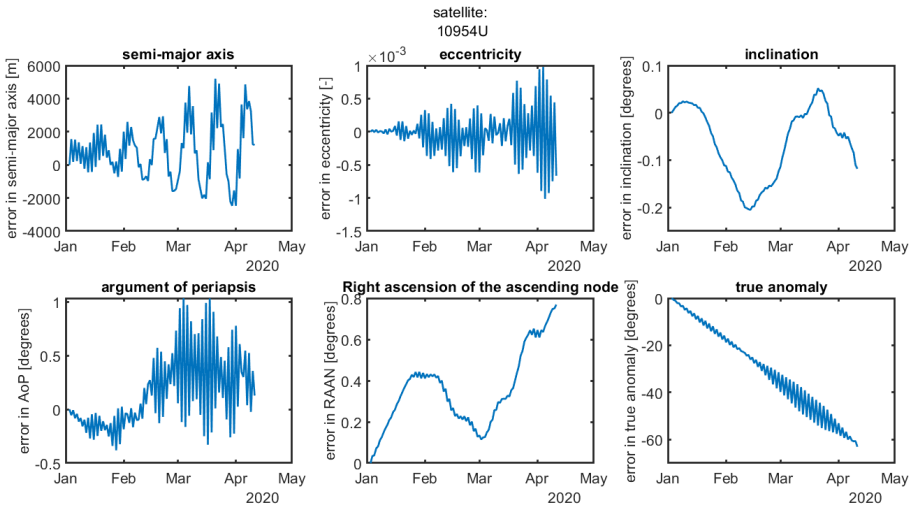

Figure G.5: Propagation difference in Kepler elements between the SGP4 orbit and the RKF4(5) method. Analysed from the start of January 2020, for three months. Here it shows a satellite with a low inclined orbit.

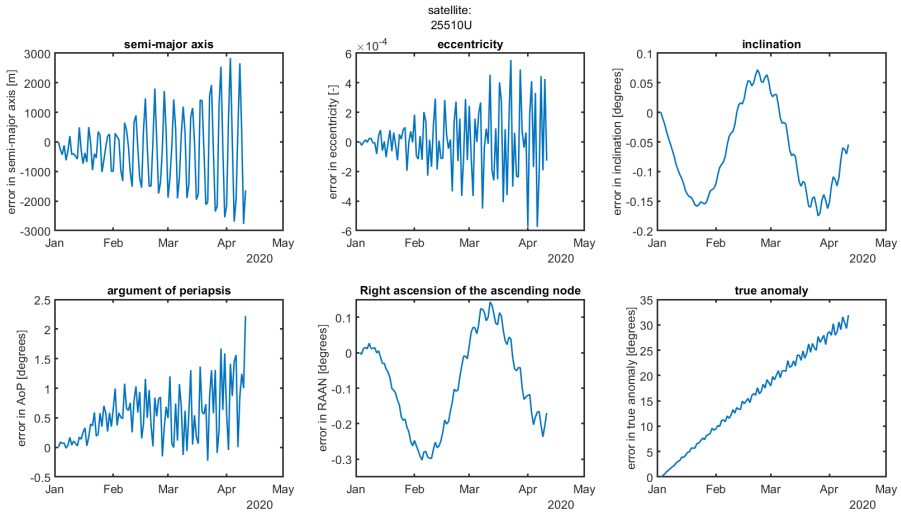

Figure G.6: Propagation difference in Kepler elements between the SGP4 orbit and the RKF4(5) method. Analysed from the start of January 2020, for three months. Here it shows a satellite with a low inclined orbit.

H

Mathematically ambiguity for applying atmospheric drag to the Extended Kalman filter for shart arc, angle only, observations

Looking at the normal scenario where the extended Kalman filter is used to increase the accuracy of the state vector, based on angle only observations for a short arc of the total orbit. The right ascension and declination is observed, but the range is not directly observed. The time between the observations, the observations itself, and the orbital mechanics makes it possible to deduce the range.

The mathematics that support this relation will be explained in words. A satellite with a large range moves relatively slowly across the night sky, as seen from an observer on Earth, and a satellite with a small range moves relatively fast. Therefore when consecutive observations in a single observation arc are closely grouped together, c.q. small difference in angles, the range of the satellite will need to be large, based on orbital mechanics. Assuming no active propulsion, or large drag terms.

A mathematical ambiguity arise when the atmospheric drag is added to the dynamics, where the ballistic coefficient is added to the state vector as seventh element and determined by the Kalman filter. The drag term can mathematically "add" acceleration, and consequently, velocities to the state vector. Therefore the range cannot be reliably determined on the basis of the spread of the observations. An example will be discussed to visualise the problem, all circular orbits are assumed and the observer is positioned in the middle of the Earth. These assumptions are made to make the example more easy to understand. The image below shows three orbits, where the middle, orange, orbit is the reference orbit, where the twee red dot represent observations. Orbit one is an orbit with a smaller radius, where the red dots are the project observation of the reference orbit.

When the observation angles are the same for the reference orbit and orbit 1, the angular velocity of the satellite, w.r.t. the middle of the Earth, is equal. Where the radius of the reference orbit is larger then orbit 1. Therefore the velocity of the reference orbit needs to be larger then orbit 1. Only looking at the orbital mechanics, this is not possible. Only looking at a point mass gravity, the velocity of the satellite in orbit 1 is larger than the velocity of the satellite in the reference orbit. But when drag acceleration is added to the dynamics of orbit 1 and propagated, a solution can be found where the proper velocity of the satellite in orbit 1 is achieved in a way that both angular velocities are equal to each other and thus orbit 1 is fitted through the projected observations. Similarly an added 'negative' drag acceleration (propelling force), makes it possible to fit orbit 2 through the projected observation angles.

Because of this mathematical ambiguity, multiple orbits with different ranges can be found for different values of drag acceleration for the same set of observed angles. For this reason there is no single solution anymore. This problem would not occurred if range observations where available. Therefore adding drag acceleration to the extended Kalman filter, where the ballistic coefficient is one of variables in the state vector will

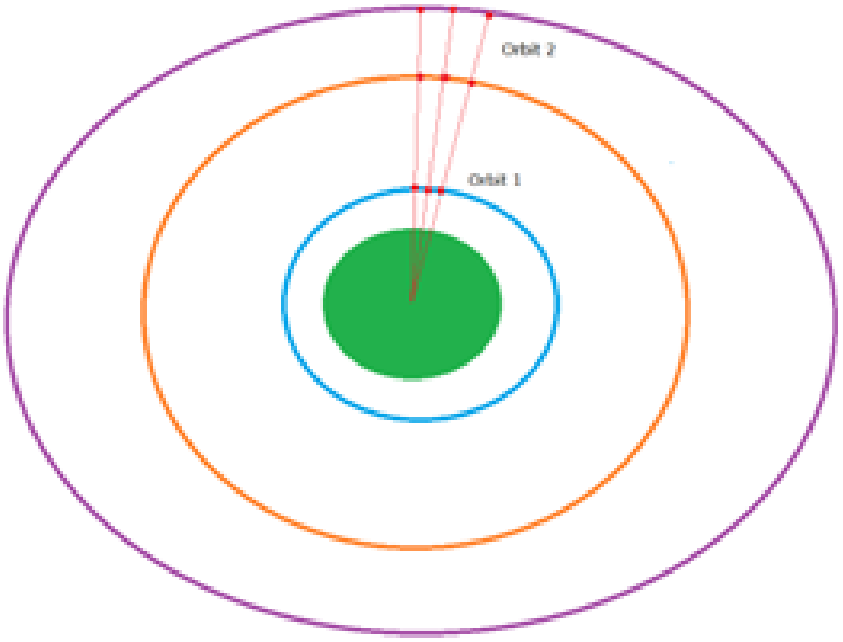

Figure H.1: Schemtatic representation of projected observations on lower and higher orbits, to illustrate the mathematical ambiguity for drag acceleration as part of the extended kalman filter.

not improve the performance of the Kalman filter for a single observation arc with angle only observations.

Secondly this insight came in the last stage of the thesis which did not make it possible to test the earlier mentioned theory to be sure. So, within the scope of this research, the atmospheric drag is not added to the dynamics, and more importantly, the ballistic coefficient is not added to the state vector.

Due to the earlier mentioned conclusions it is not advised to add atmospheric drag to the dynamical model. For this reason the research will focus on satellites that do not experience significant atmospheric drag, in order to mitigate this shortcoming. For small time steps the propagation errors are smaller then the SGP4 model uncertainty, therefore the error is acceptable for small time steps. With this side note the RKF4(5) with the prescribed dynamical model is validated.

CAR-MHF results

Showing the results of the CAR-MHF filter for observation obtained from the IPA algorithm. The analysis is performed for 10 different satellites. Showing the CAR-MHF compared to the SGP4-based reference state, where the CAR-MHF is applied on a single observation arc.

I.1. Satellite 10793U

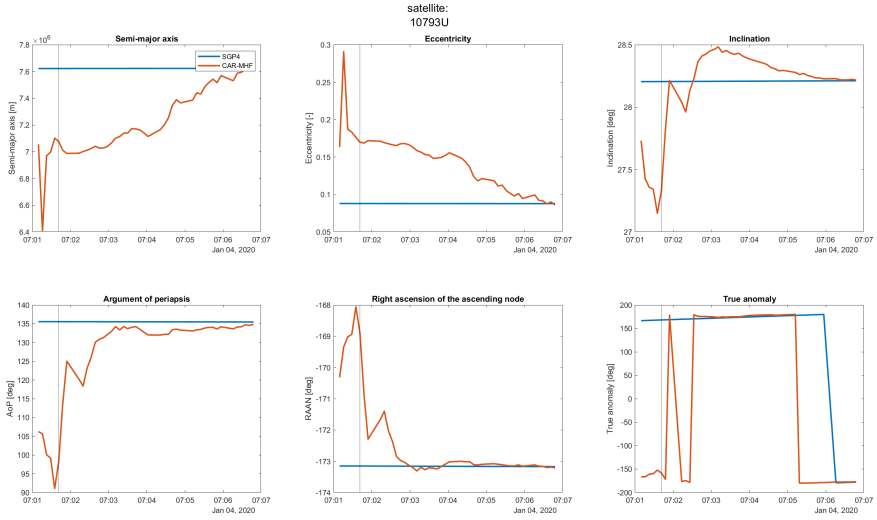

Figure I.1: The solution of the CAR-MHF for a single observation arc for satellite 10793U on the third of January over ground station La Silla. The track-based observations are the measurements used for the EKF. Here the blue line is the SGP4-based reference and the orange line is the CAR-MHF solution. The grey line is the convergence point of the CAR-MHF filter.

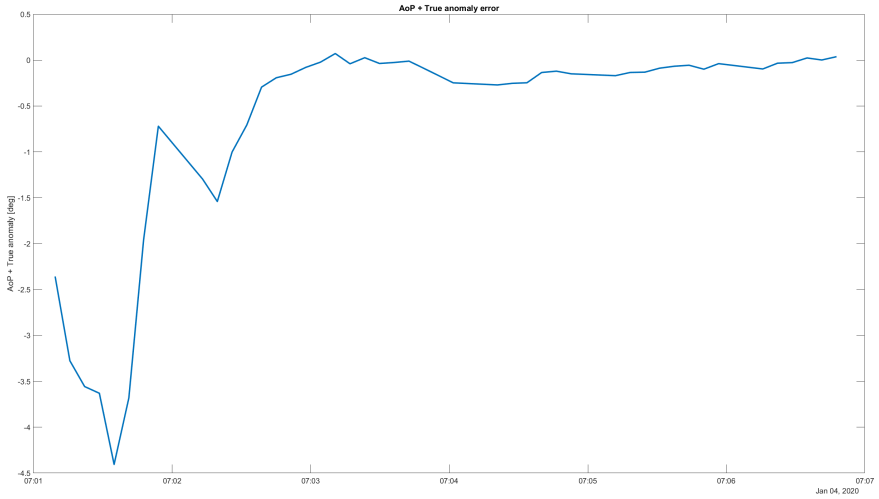

Figure I.2: The addition of the Argument of periapsis and the True anomaly errors over the short arc observation of satellite 10793U, on the night of the third of January, by the ground station in Australia.

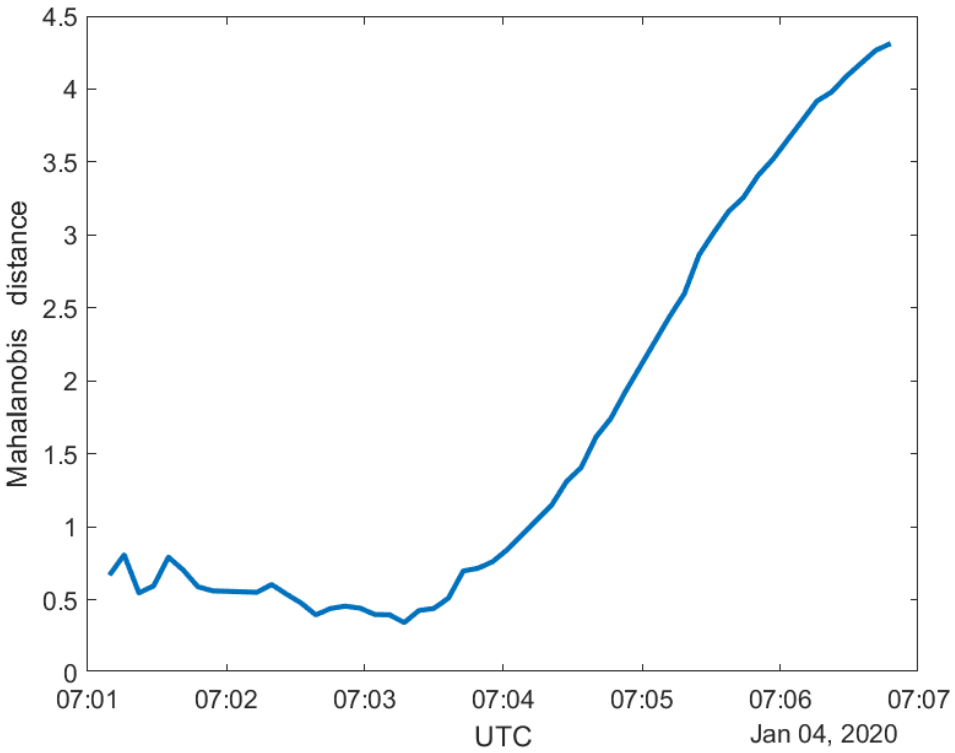

Figure I.3: The Mahalanobis distance for satellite 10793U, on the night of the third of January, by the ground station in Australia.

I.2. Satellite 23404U

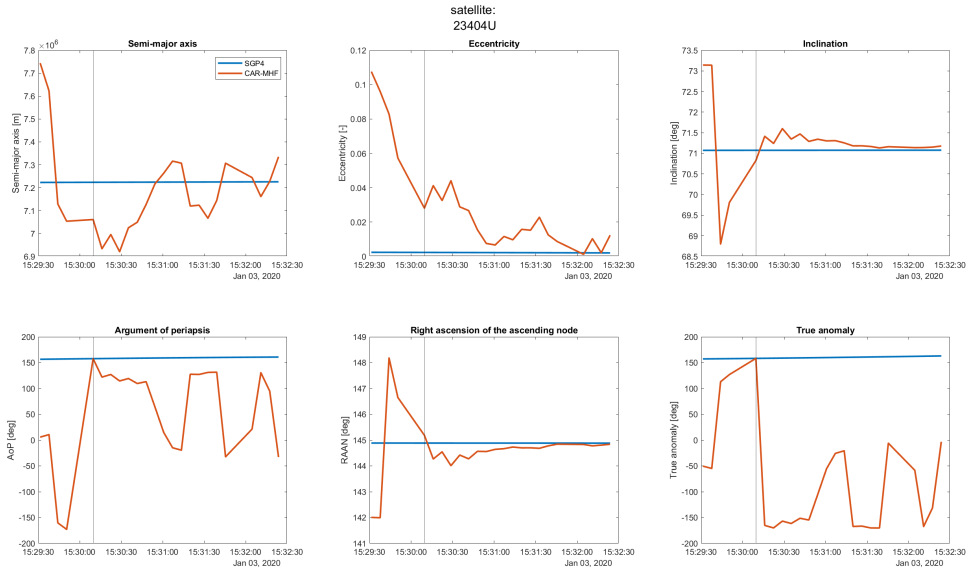

Figure I.4: The solution of the CAR-MHF for a single observation arc for satellite 23404U on the third of January over ground station La Silla. The track-based observations are the measurements used for the EKF. Here the blue line is the SGP4-based reference and the orange line is the CAR-MHF solution. The grey line is the convergence point of the CAR-MHF filter.

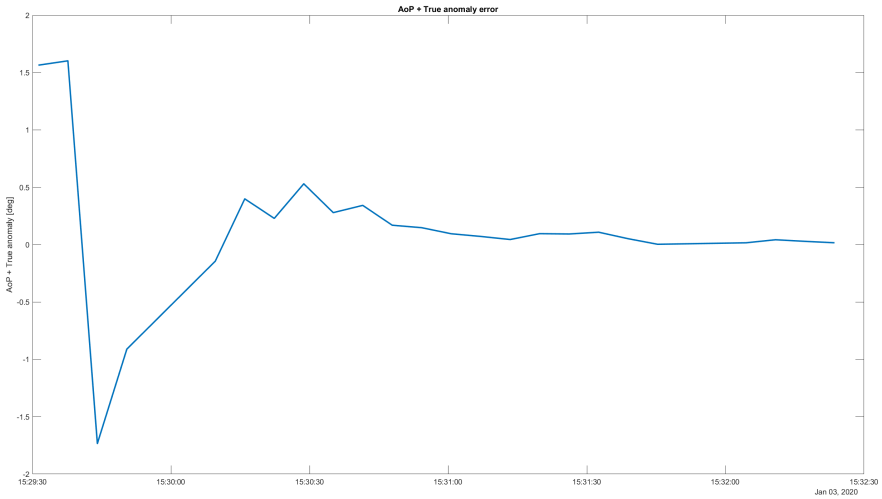

Figure I.5: The addition of the Argument of periapsis and the True anomaly errors over the short arc observation of satellite 23404U, on the night of the third of January, by the ground station in Australia.

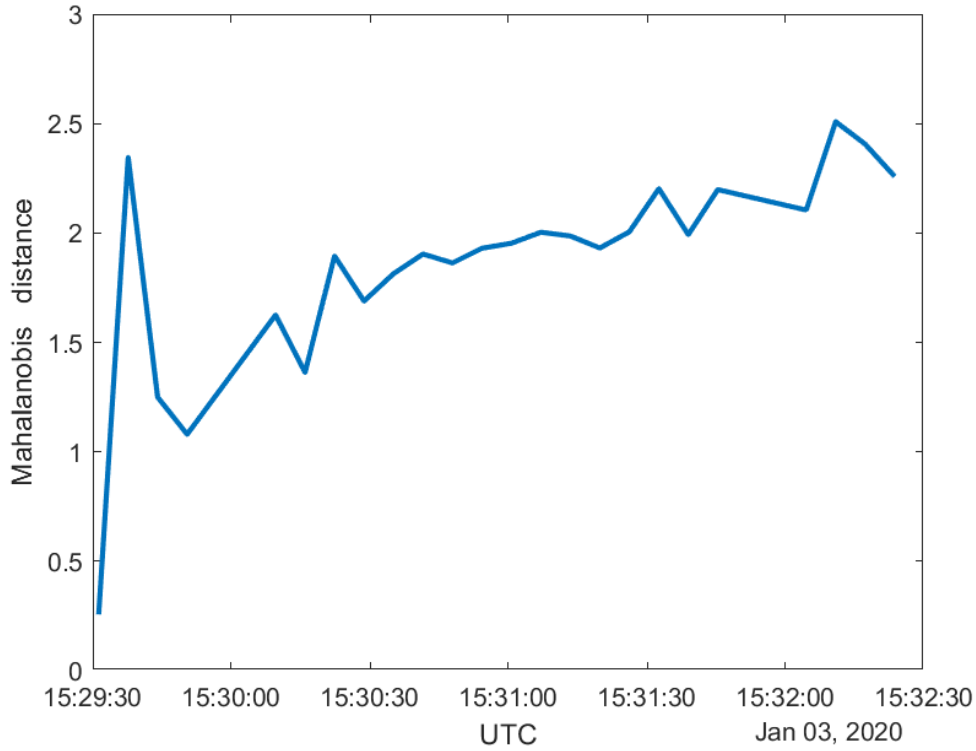

Figure I.6: The Mahalanobis distance for satellite 23404U, on the night of the third of January, by the ground station in Australia.

I.3. Satellite 38771U

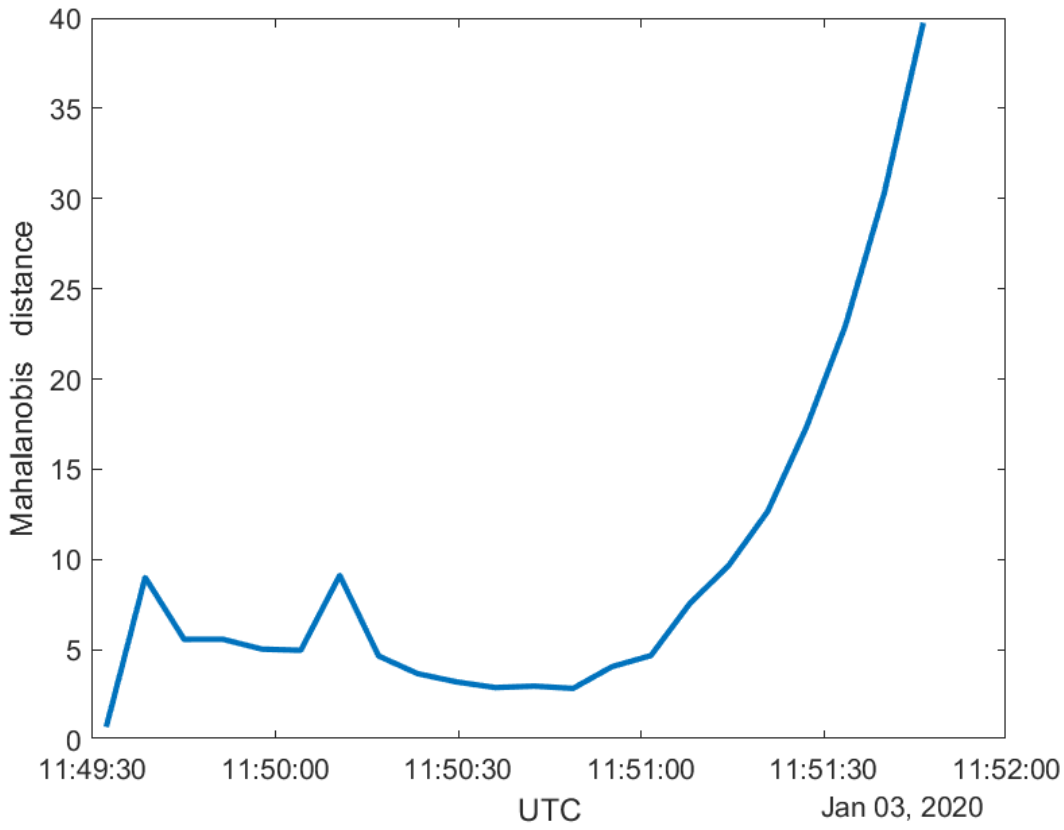

Figure I.7: The solution of the CAR-MHF for a single observation arc for satellite 38771U on the third of January over ground station La Silla. The track-based observations are the measurements used for the EKF. Here the blue line is the SGP4-based reference and the orange line is the CAR-MHF solution. The grey line is the convergence point of the CAR-MHF filter.

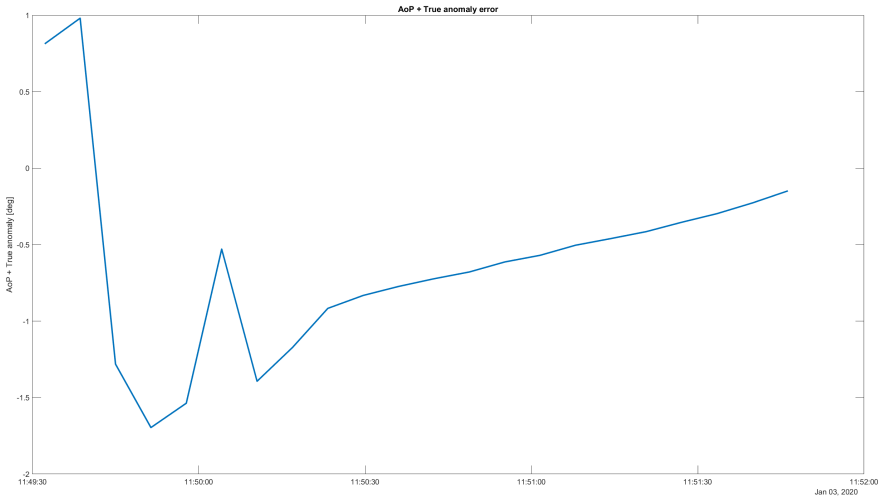

Figure I.8: The addition of the Argument of periapsis and the True anomaly errors over the short arc observation of satellite 38771U, on the night of the third of January, by the ground station in Australia.

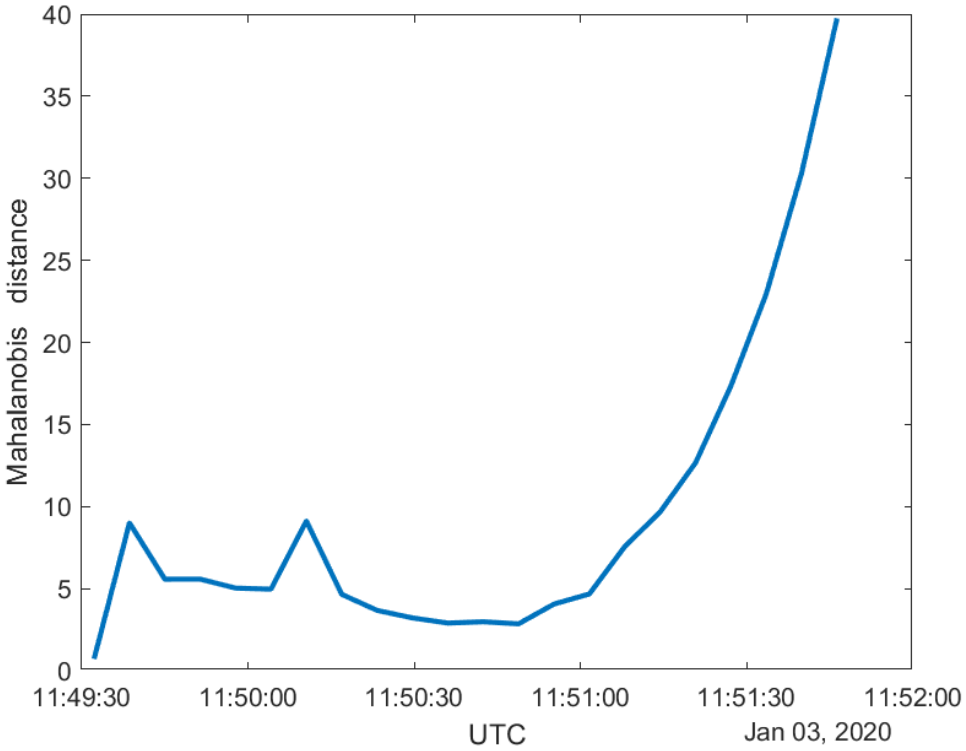

Figure I.9: The Mahalanobis distance for satellite 38771U, on the night of the third of January, by the ground station in Australia.

I.4. Satellite 10954U

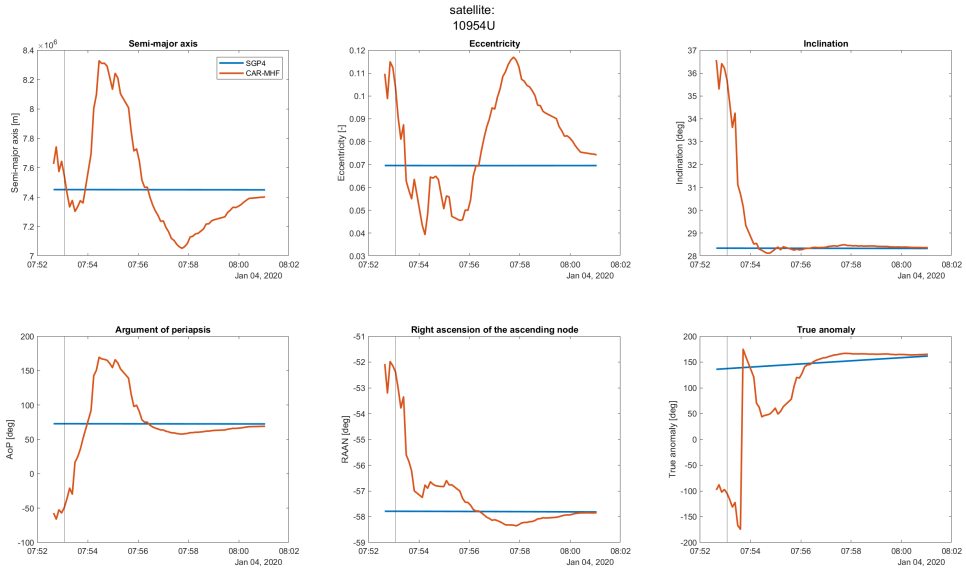

Figure I.10: The solution of the CAR-MHF for a single observation arc for satellite 10954U on the third of January over ground station La Silla. The track-based observations are the measurements used for the EKF. Here the blue line is the SGP4-based reference and the orange line is the CAR-MHF solution. The grey line is the convergence point of the CAR-MHF filter.

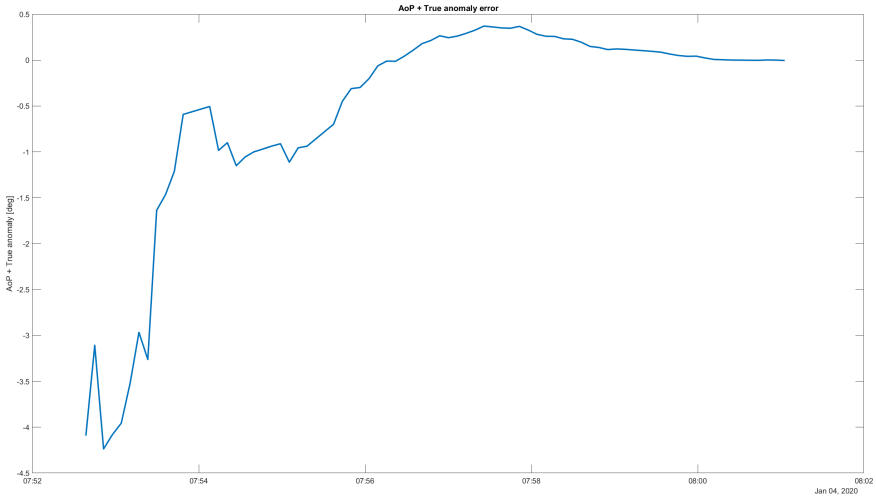

Figure I.11: The addition of the Argument of periapsis and the True anomaly errors over the short arc observation of satellite 10954U, on the night of the third of January, by the ground station in Australia.

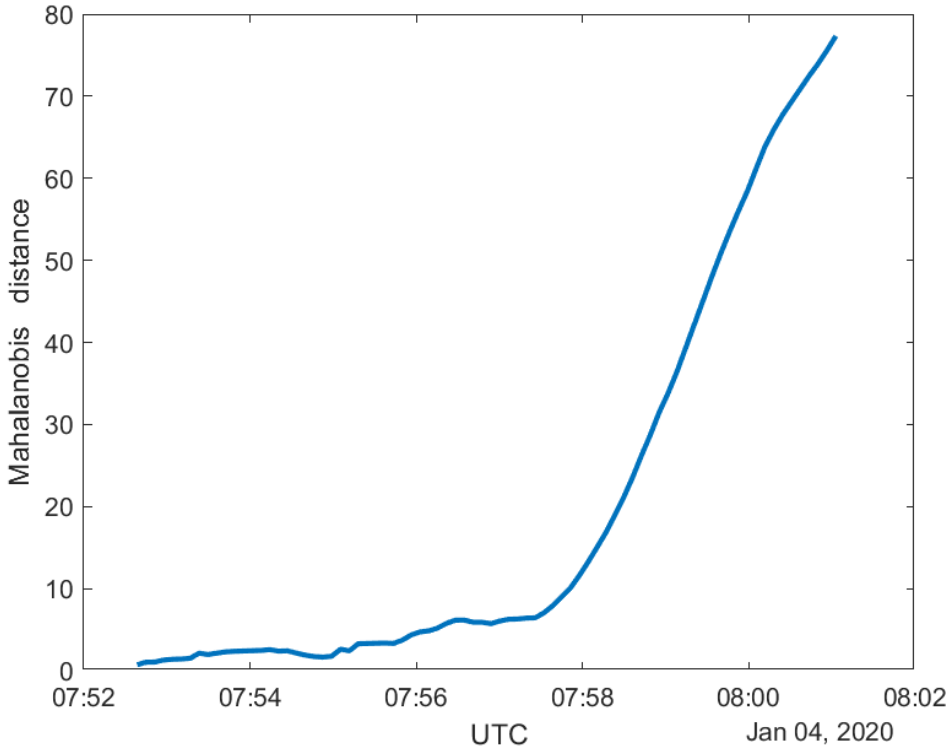

Figure I.12: The Mahalanobis distance for satellite 10954U, on the night of the third of January, by the ground station in Australia.

I.5. Satellite 25510U

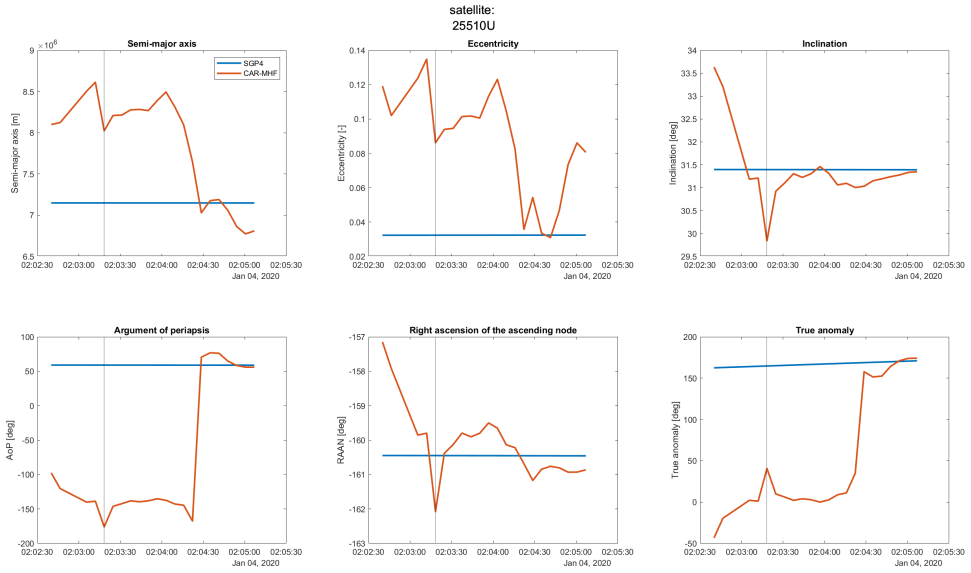

Figure I.13: The solution of the CAR-MHF for a single observation arc for satellite 25510U on the third of January over ground station La Silla. The track-based observations are the measurements used for the EKF. Here the blue line is the SGP4-based reference and the orange line is the CAR-MHF solution. The grey line is the convergence point of the CAR-MHF filter.

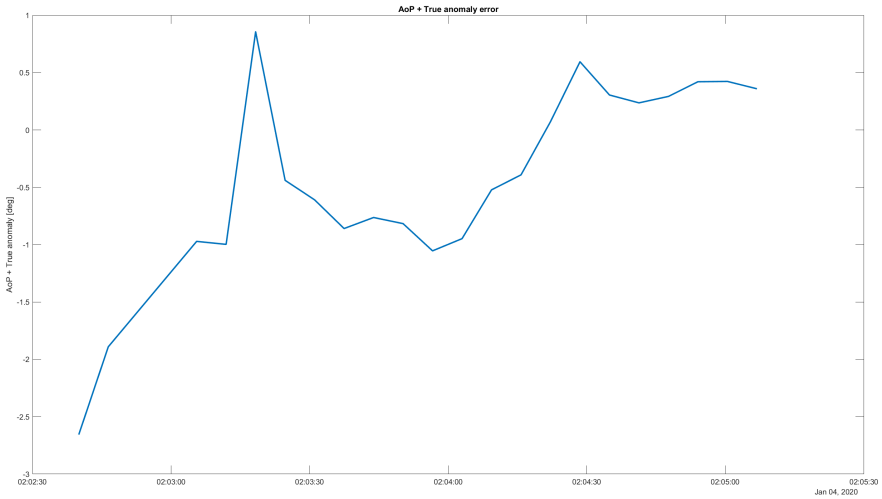

Figure I.14: The addition of the Argument of periapsis and the True anomaly errors over the short arc observation of satellite 25510U, on the night of the third of January, by the ground station in Australia.

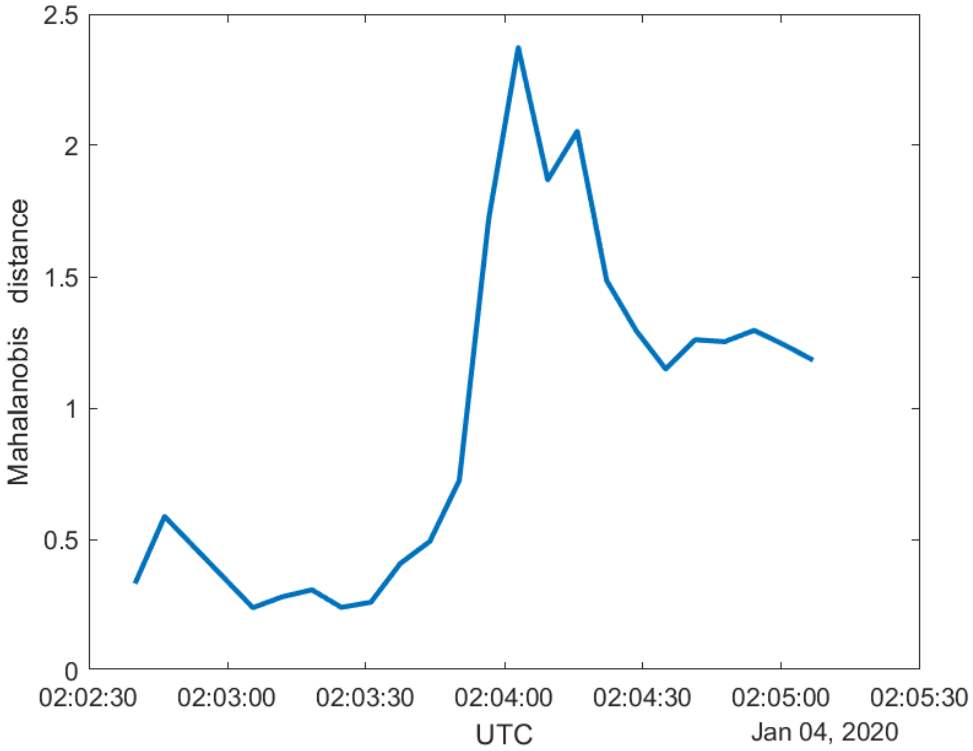

Figure I.15: The Mahalanobis distance for satellite 25510U, on the night of the third of January, by the ground station in Australia.

I.6. Satellite 29499U

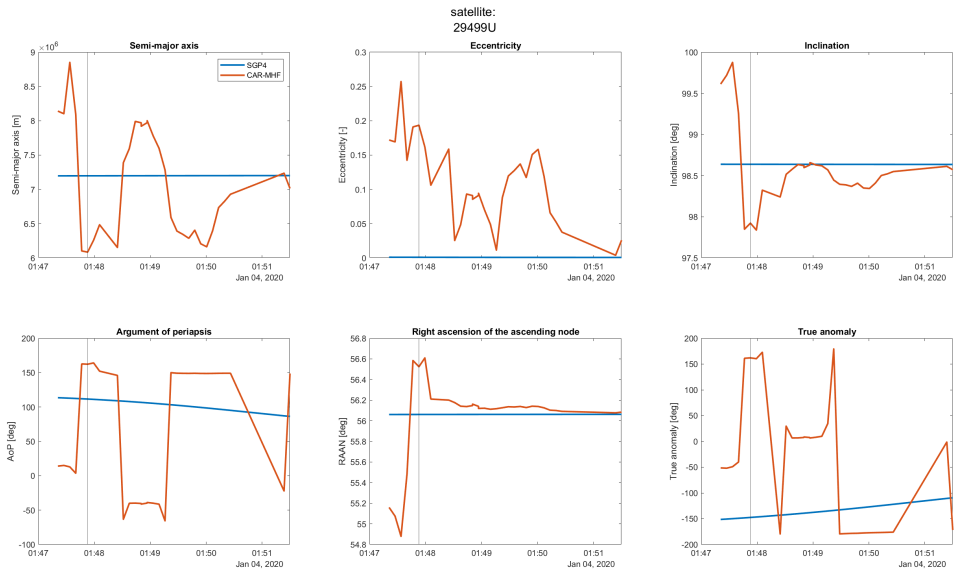

Figure I.16: The solution of the CAR-MHF for a single observation arc for satellite 29499U on the third of January over ground station La Silla. The track-based observations are the measurements used for the EKF. Here the blue line is the SGP4-based reference and the orange line is the CAR-MHF solution. The grey line is the convergence point of the CAR-MHF filter.

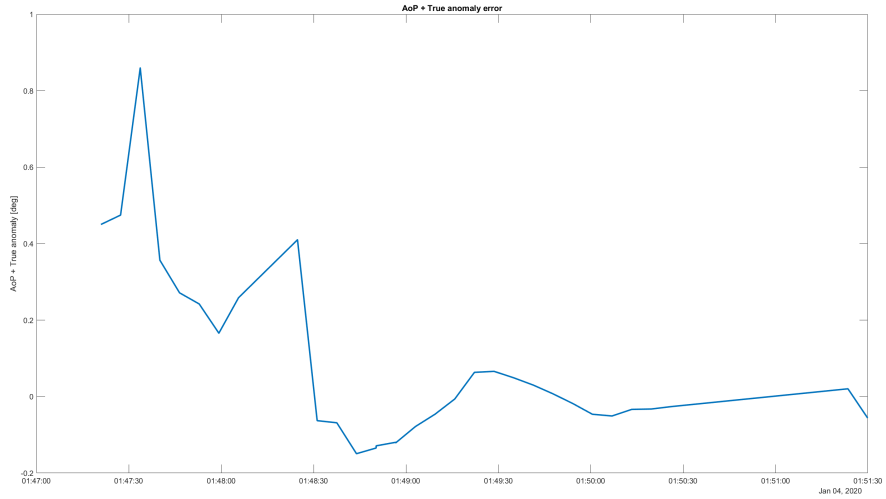

Figure I.17: The addition of the Argument of periapsis and the True anomaly errors over the short arc observation of satellite 29499U, on the night of the third of January, by the ground station in Australia.

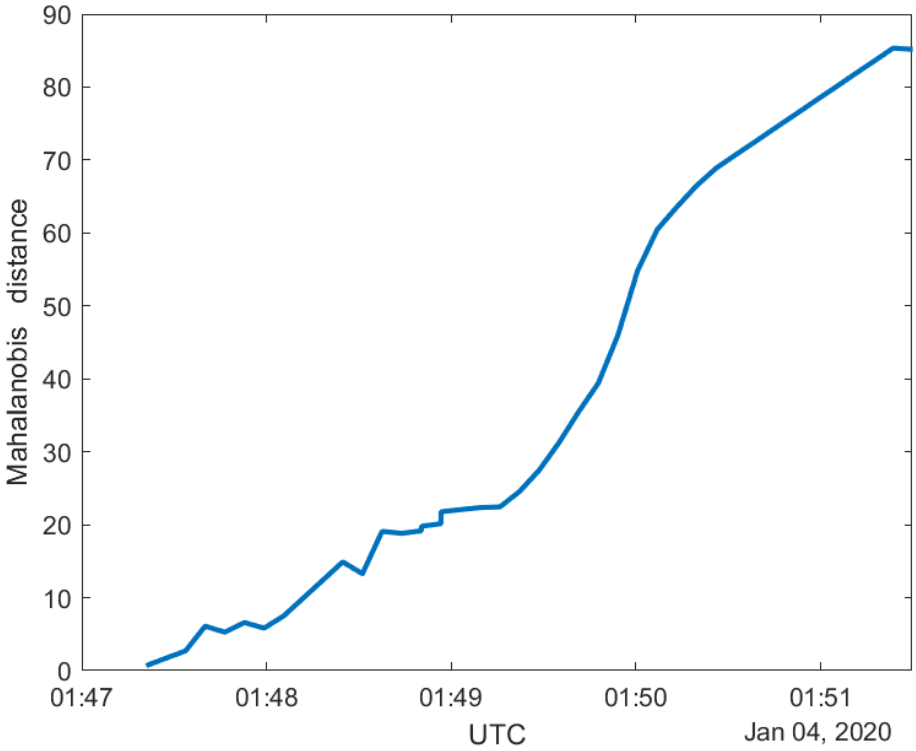

Figure I.18: The Mahalanobis distance for satellite 29499U, on the night of the third of January, by the ground station in Australia.

I.7. Satellite 4794U

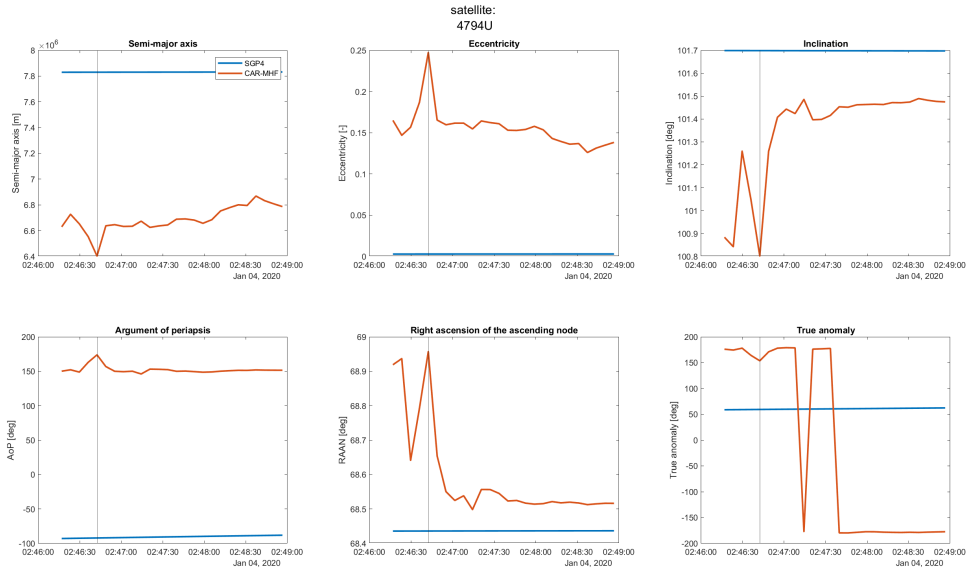

Figure I.19: The solution of the CAR-MHF for a single observation arc for satellite 4794U on the third of January over ground station La Silla. The track-based observations are the measurements used for the EKF. Here the blue line is the SGP4-based reference and the orange line is the CAR-MHF solution. The grey line is the convergence point of the CAR-MHF filter.

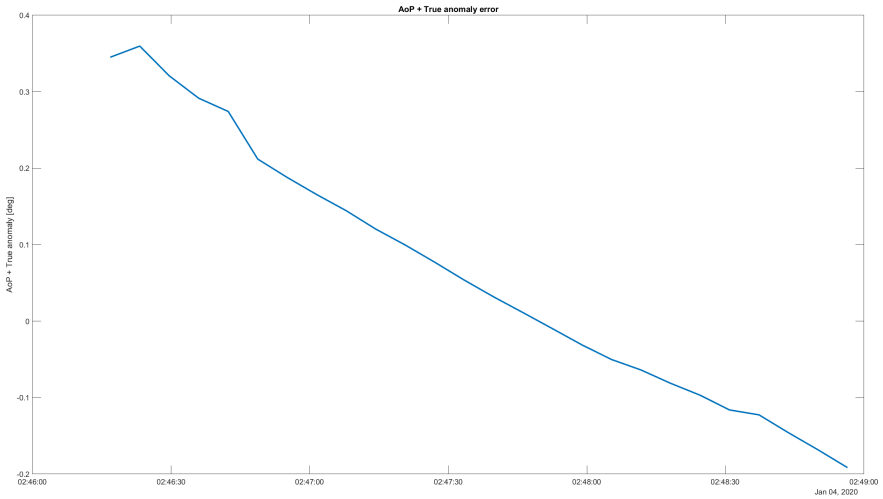

Figure I.20: The addition of the Argument of periapsis and the True anomaly errors over the short arc observation of satellite 4794U, on the night of the third of January, by the ground station in Australia.

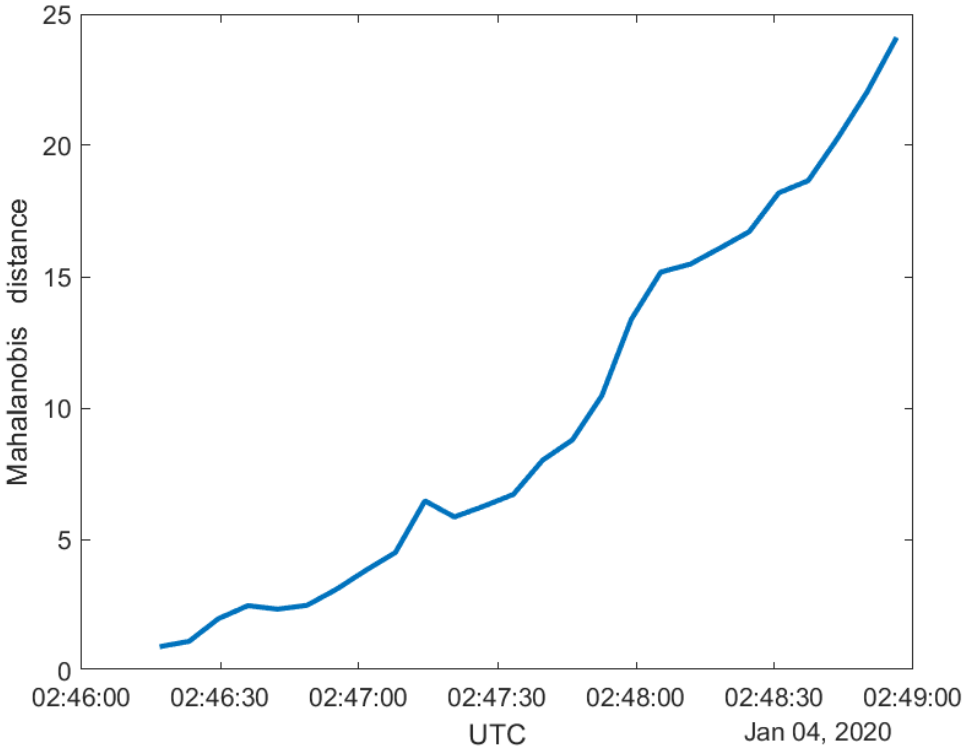

Figure I.21: The Mahalanobis distance for satellite 4794U, on the night of the third of January, by the ground station in Australia.

I.8. Satellite 25885U

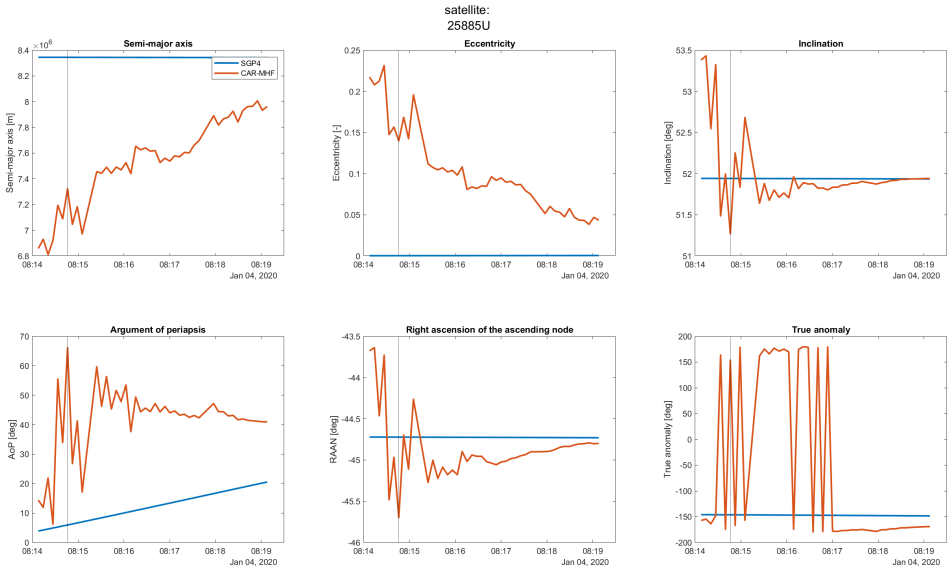

Figure I.22: The solution of the CAR-MHF for a single observation arc for satellite 25885U on the third of January over ground station La Silla. The track-based observations are the measurements used for the EKF. Here the blue line is the SGP4-based reference and the orange line is the CAR-MHF solution. The grey line is the convergence point of the CAR-MHF filter.

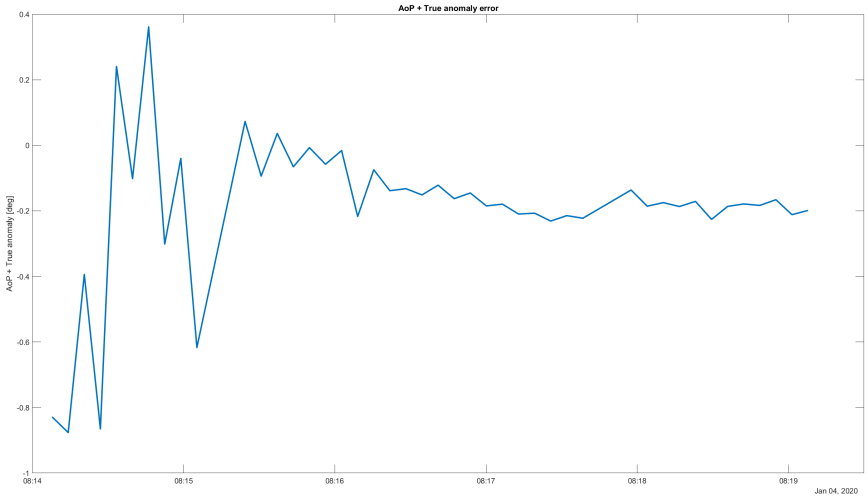

Figure I.23: The addition of the Argument of periapsis and the True anomaly errors over the short arc observation of satellite 25885U, on the night of the third of January, by the ground station in Australia.

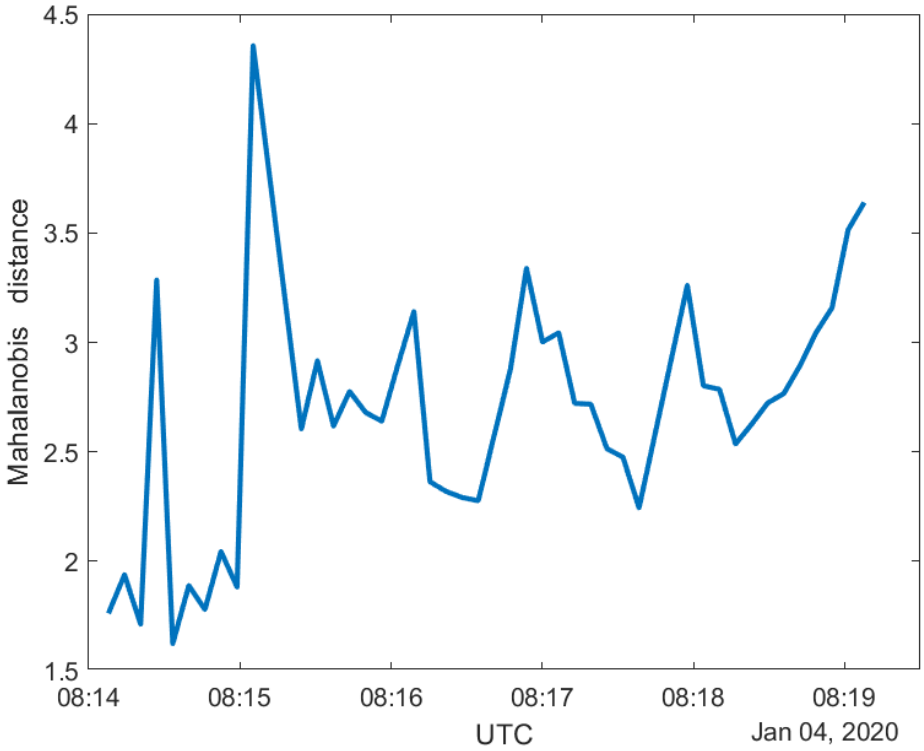

Figure I.24: The Mahalanobis distance for satellite 25885U, on the night of the third of January, by the ground station in Australia.

I.9. Satellite 22284U

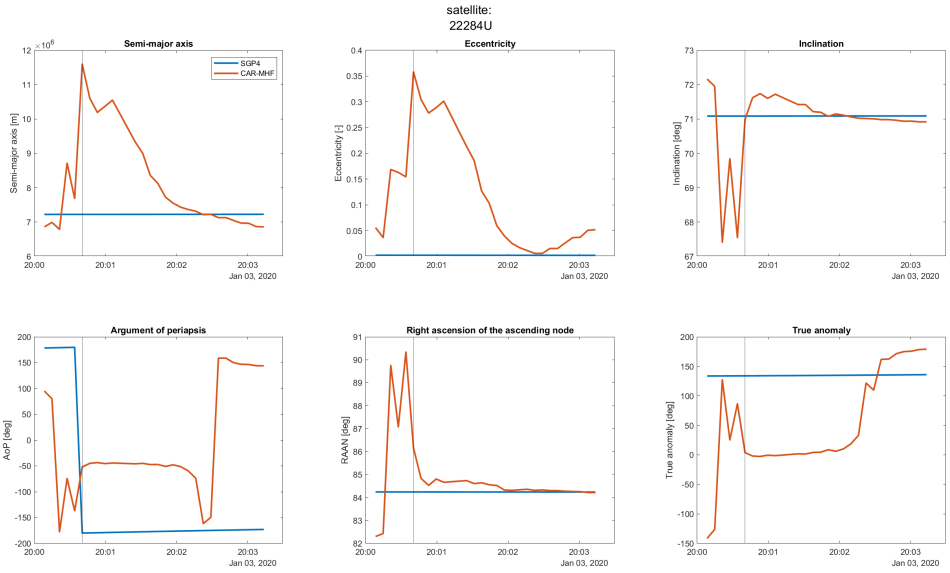

Figure I.25: The solution of the CAR-MHF for a single observation arc for satellite 22284U on the third of January over ground station La Silla. The track-based observations are the measurements used for the EKF. Here the blue line is the SGP4-based reference and the orange line is the CAR-MHF solution. The grey line is the convergence point of the CAR-MHF filter.

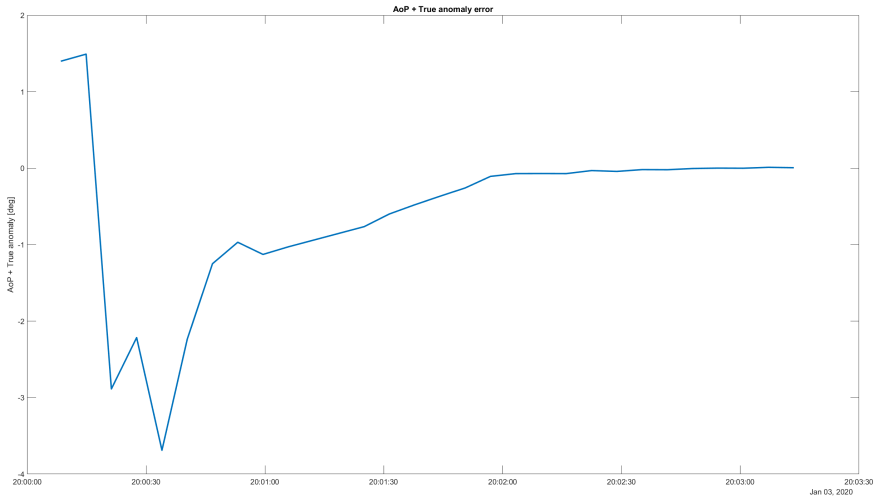

Figure I.26: The addition of the Argument of periapsis and the True anomaly errors over the short arc observation of satellite 22284U, on the night of the third of January, by the ground station in Australia.

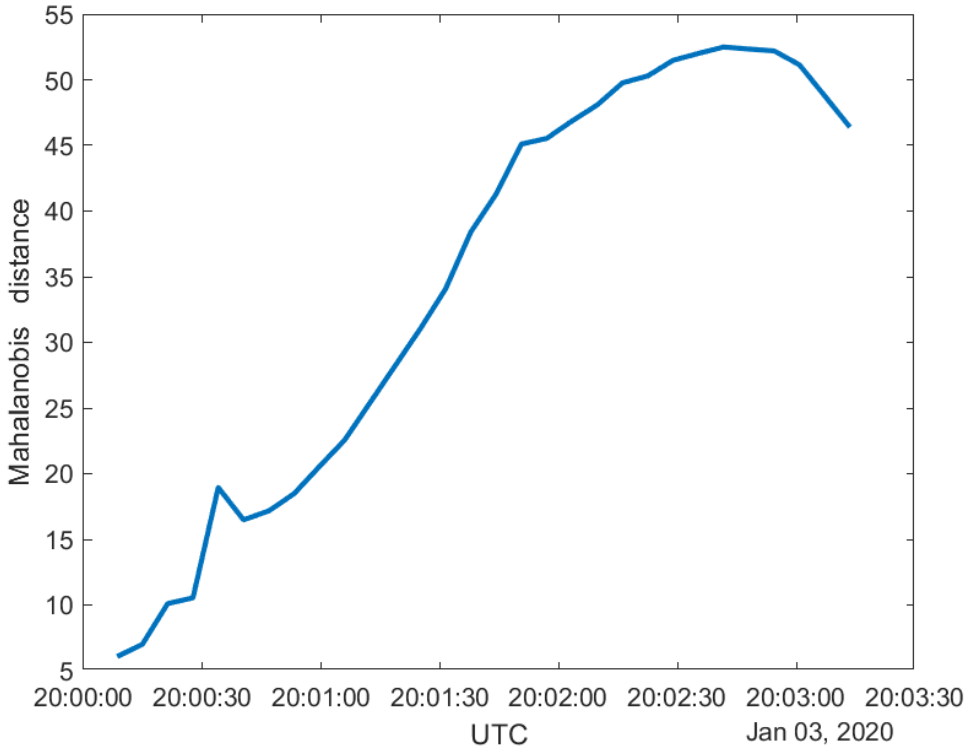

Figure I.27: The Mahalanobis distance for satellite 22284U, on the night of the third of January, by the ground station in Australia.

I.10. Satellite 39260U

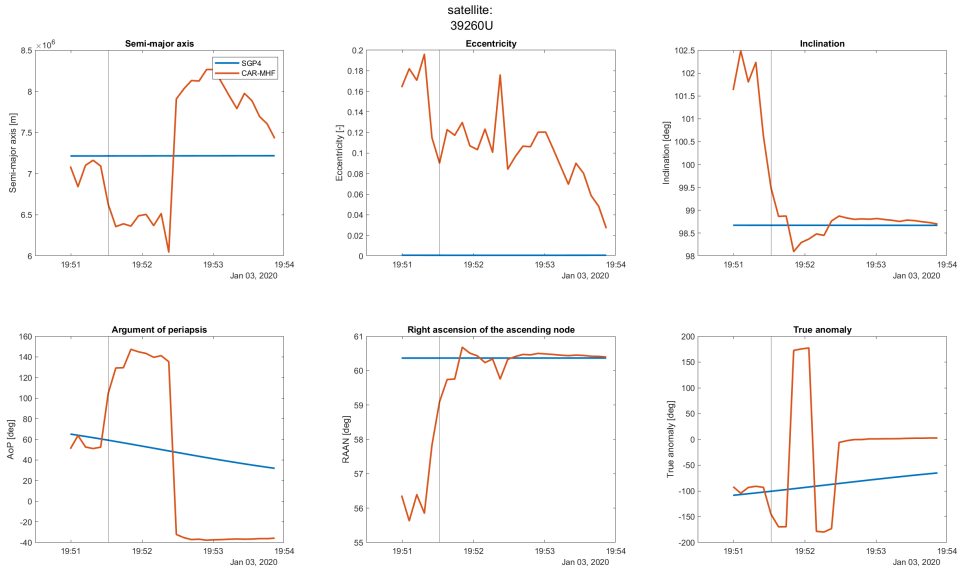

Figure I.28: The solution of the CAR-MHF for a single observation arc for satellite 39260U on the third of January over ground station La Silla. The track-based observations are the measurements used for the EKF. Here the blue line is the SGP4-based reference and the orange line is the CAR-MHF solution. The grey line is the convergence point of the CAR-MHF filter.

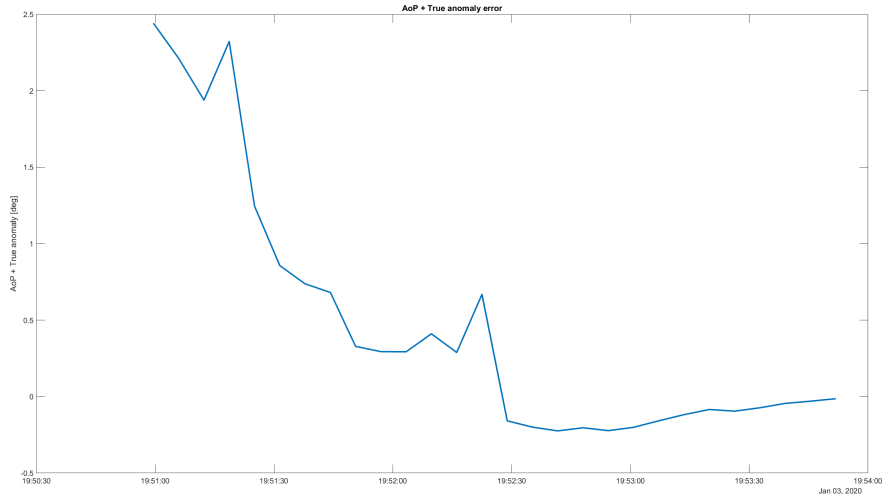

Figure I.29: The addition of the Argument of periapsis and the True anomaly errors over the short arc observation of satellite 39260U, on the night of the third of January, by the ground station in Australia.

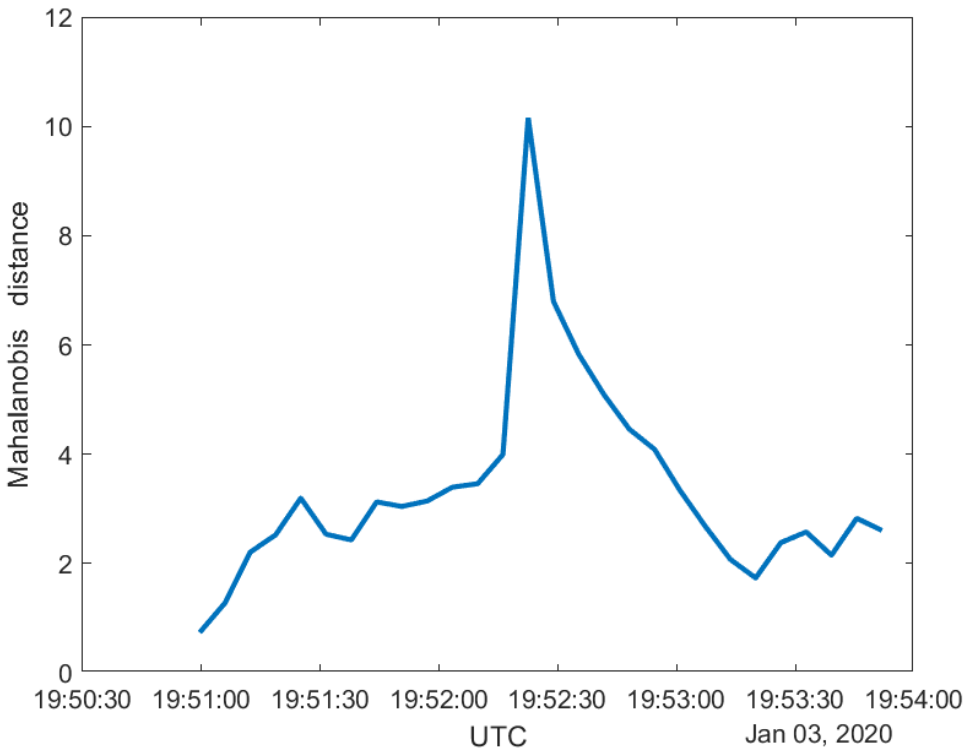

Figure I.30: The Mahalanobis distance for satellite 39260U, on the night of the third of January, by the ground station in Australia.